An Investigation into Acoustics and Vibration Characteristics of CPAP Devices

By

Tung Xuan VUONG

A Thesis submitted to Auckland University of Technology

in fulfilment of requirements for the degree of

Doctor of Philosophy (PhD)

February 2015

Faculty of Design & Creative Technology

School of Engineering

Institute of Biomedical Technologies

Auckland, New Zealand

Primary Supervisor: Professor Ahmed Al-Jumaily

DECLARATIONS

‘I hereby declare that this submission is my own work and that, to the best of my knowledge and belief, it contains no material previously published or written by another person nor material which to a substantial extent has been accepted for the qualification of any other degree or diploma of a university or other institution of higher learning, except where due acknowledgment is made in the acknowledgements.’

Signature **Date**
Tung Xuan VUONG

I further authorise the Auckland University of Technology to reproduce this thesis by photocopying or by other means, in total or in part, at the request of other institutions or individuals for the sole purpose of scholarly research.

Signature **Date**
Tung Xuan VUONG

BORROWERS PAGE

The Auckland University of Technology requires the signatures of all people using or photocopying this thesis. Accordingly, all borrowers are required to fill out this page.

DATE	NAME	ADDRESS	SIGNATURE

ACKNOWLEDGEMENT

I am grateful and would like to thank Professor Ahmed Al-Jumaily, who is like a father figure to me in New Zealand, for giving me the opportunity to work on this research project at the Institute of Biomedical Technologies at the Auckland University of Technology (AUT University). Your guidance, generosity and patience have allowed me to complete this project. Your successful career has always inspired me. Thank you Dr Robert Paxton for your enthusiasm toward me and wish you a very successful in your professional career.

I also wish to thank Fisher & Paykel Healthcare Ltd Company and especially Mr Adam Darby, for helping and allowing me to use all the available equipment, materials and documents during this PhD project. Thanks for all other engineers at Fisher & Paykel Healthcare Ltd whom had helped me during the experimental studies at the company. Thank you the Technology New Zealand Funding programme from New Zealand Government for financial support during this project. Thank you all colleagues at the Institute of Biomedical Technologies (IBTec), who have known me and be friendly toward me.

I wish to express my love and gratitude to my beloved family, especially my beautiful wife who always understands and supports me during the difficult times. Without your supports I will not achieve many things in life. There are no words could say enough of my appreciations toward you. It is now my turn to support you unconditionally to complete your goals.

Finally, to VUONG's family and my DEAR FATHER, thank you all for your unlimited supports. Without your supports, I would not even be here in New Zealand to fulfil my dreams, so THANK YOU VERY MUCH FROM THE BOTTOM OF MY HEART.

ABSTRACT

High demand for lower noise generation in the CPAP device industries necessitates the need to have a computational modelling for obtaining in-depth understanding of internal aerodynamic flows and aero-acoustic characteristics that can be used during the product development process. In this thesis, a comprehensive numerical study is conducted to investigate flow-induced noise and vibration of the CPAP devices with supports of experimental investigations for validations.

A 3-D flow system of a CPAP device is originally developed and then re-constructed and simplified for numerical simulation purposes. The CPAP flow system consists of inlet and outlet ducts, a centrifugal fan and a humidifier. A numerical simulation, which is a combination of well-established computational fluid dynamics (CFD) techniques with acoustic analogies (AA) and finite element analysis (FEA), is adopted and applied to each primary component of the CPAP devices to investigate noise and vibration generated by internal turbulent flows. The numerical results are compared with the experimental data for validations.

Significant insights into the noise and vibration characteristics of the CPAP components are obtained and compared with each other to identify the noise source power and its locations. The contribution of each element to the overall noise generation level is estimated.

Prior to the numerical studies, a thorough experimental investigation was conducted to investigate the flow performances, noise radiations and surfaces vibration of the CPAP devices and its main components. The results from the experimental investigation can be used for validation purposes as well as the boundary conditions for numerical studies.

Numerical results has found that the uneven flow structure or asymmetric internal flow is identified as the main cause of the noise generation. The specific geometry designed for the CPAP flow system has created flow patterns which contain many aerodynamic characteristics that are related to the aerodynamic noise generation such as flow attachment and separation, flow recirculation or rotation, etc.

Furthermore, individual noise power level at each components are estimated and compared with each other. It is found that the noise power generated from the centrifugal fan is the most contributed source to the overall noise level radiated from the CPAP device.

TABLES OF CONTENTS

LIST OF FIGURES

LIST OF TABLES

LIST OF UNIT, SYMBOLS AND ABBREVIATIONS

Abbreviation

2-D	Two dimensional
3-D	Three-dimensional
AA	Aero-acoustic analogy
ALE	Arbitrary Lagrangian-Eulerian
AV	Acoustic and Vibration
B&K	Bruel & Kjaer
BNS	Broadband noise source
BPF	Blade passing frequency
CAA	Computational aero-acoustic
CFD	Computational fluid dynamics
CPAP	Continuous positive air pressure
DNS	Direct numerical simulation
DVM	Discrete vortex method
FEM	Finite Element Method
FSI	Fluid-structure interaction
FVM	Finite Volume Method
FW-H	Ffowcs Williams and Hawking
HVAC	Heating, ventilating and air conditioning
ISO	International standard organization
LES	Large eddy simulation
N-S	Navier-Stokes
OSA	Obstructive sleep apnoea
PWL	Sound power level
RANS	Reynolds-averaged Navier-Stokes
RF	Rotational frequency
RNG	Renormalization group theory

SPL	Sound pressure level
SST	Shear stress transport

Symbols

θ	Angle
$\vec{\omega}$	Angular velocity vector
q_T	Body heat source term
p_{ij}	Compressive stress tenor
$C_{1,2,3,\varepsilon}$	constant values
x, y, z	coordinates
A_c	correlation area
$\delta(f)$	Dirac delta function
r	Distance between observer and source
D_{ij}	elastic tensor
U	flow velocity
u_n	flow velocity normal to surface
ρ_0	Fluid density at rest
F	force
C_v	Heat capacity
$H(f)$	Heaviside function
δ_{ij}	Kronecker delta
p	Pressure
W_{ref}	reference sound power
τ	retarded time
I	sound intensity
L_p, L_w	sound pressure level, sound power level
y	Source position

V_y	Source volume
ε_{ij}	strain tensor
σ_{ij}	Stress tensor
S	surface area
W_s	surface sound power
T	Temperature
υ_n	the normal velocity of the surface
t	Time
G_k	Turbulence kinetic energy by mean velocity gradients
ε	Turbulent dissipation rate
k	Turbulent kinetic energy, thermal conductivity (eq. 3.3)
S_k, S_ε	user-defined source term
u	Velocity component
u_r	Velocity related to rotating frame
$G(\vec{x}, \vec{y}; t, \tau)$	Green function
$Q(\mathrm{y}, \tau)$	source strength
ρ	Fluid density
T_{ij}	Lighthill stress tensor
$\vec{r}$	Radius respected to radius direction
c	Speed of sound
τ_{ij}	Stress tensor

Chapter 1: **Introduction**

1.1 Background

In recent years, the challenges in the medical device manufacturing industry have been to ensure that the noise level is sufficiently low under all operating conditions. This is because the demands from customers for quieter medical devices are becoming more important criteria. From a product design point of view, this issue needs to be addressed at an early stage of development to ensure that the products comply with regulations and succeed in market competition worldwide. The research study in this thesis focuses on the continuous positive air pressure (CPAP) device. The CPAP device is used to generate a pressurized airflow to support Obstructive Sleep Apnoea (OSA) patients to breathe comfortably and easily. Figure 1.1 shows the CPAP model considered in this thesis.

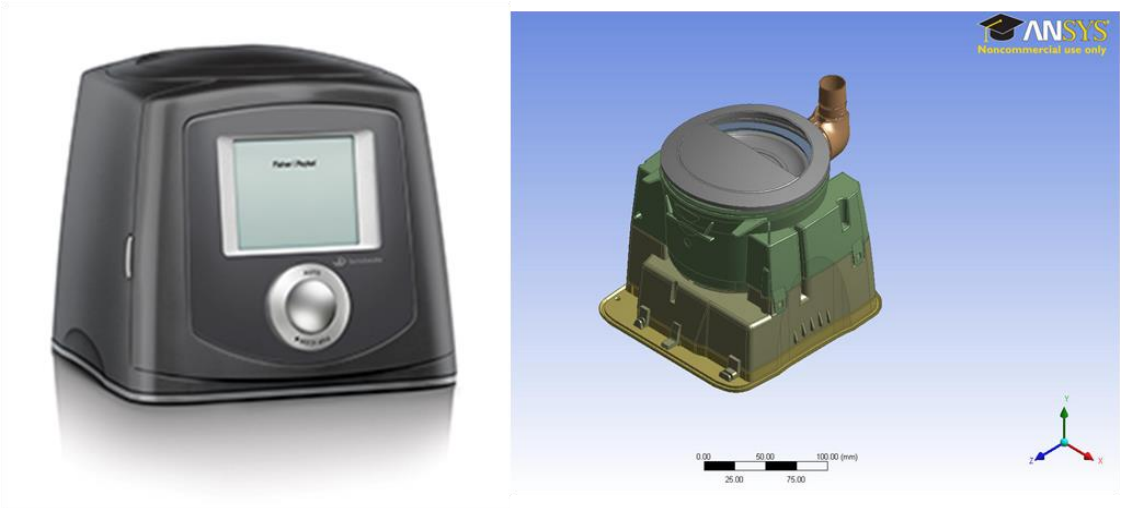

Figure 1.1: A CPAP model: (a) CPAP model, (b) internal solid parts

In a CPAP device, the flow system is the main contributor to the total noise levels produced during operation. The flow system is very complicated with complex-shaped corners, short ducts, different cross-sectional areas, etc. This system could result in a complicated noise generation and radiation to the far-field as there could be many sources of noise inside the device. Amongst these noise sources, the aerodynamic sources are the most difficult ones to identify and predict due to the complexity and non-linear relationships between the flow and the noise fields. In order to reduce the noise level generated from the CPAP devices, there is a need to thoroughly understand the aerodynamic noise generated inside the CPAP flow system by asking, for instance, where are these sources? What are their characteristics? How does each noise source contribute to the overall noise levels? And how can it be reduced? Once the understandings of the internal flow are fully covered and the dominant noise sources identified and addressed, noise reduction techniques can be developed and implemented.

Currently, product design engineers are heavily reliant on an expensive and time consuming experimental approach which is based on the ISO (International Standard Organisation) 3744 method [1] to measure the noise level in the far-field and there are no practically usable numerical methods to predict aerodynamically generated noise in CPAP devices. However, the current measurement method could only provide the overall noise level radiated from the device to the far-field. The measurement method has proven to be very expensive, time consuming and also appears to be very difficult to conduct on the CPAP device due to its small sizes and complexities. The small size of the duct system has made it very difficult not only for noise measurements but also for the vibration measurement.

Hence, the design of a quieter system could encounter difficulties if it can only relied on measurement techniques. As a result, in recent years, product designers have been seeking

new ways to develop quieter CPAP devices, with a focus on the aerodynamic noise, in conjunction with the existing experimental method that mentioned earlier. The research study in this thesis will focus on numerical simulation approaches to predict the flow-induced noise and vibration in CPAP device.

1.2 CPAP Flow System

The CPAP flow system consists of four main elements, namely, inlet duct, a centrifugal fan, outlet duct and a humidifier. These elements are made up from many individual parts that are assembled together to create a flow path. This design leads to a complex flow path which has many short ducts, small size and complicated corners and bends, etc. Figure 1.2 shows a three-dimensional flow model in the CPAP devices.

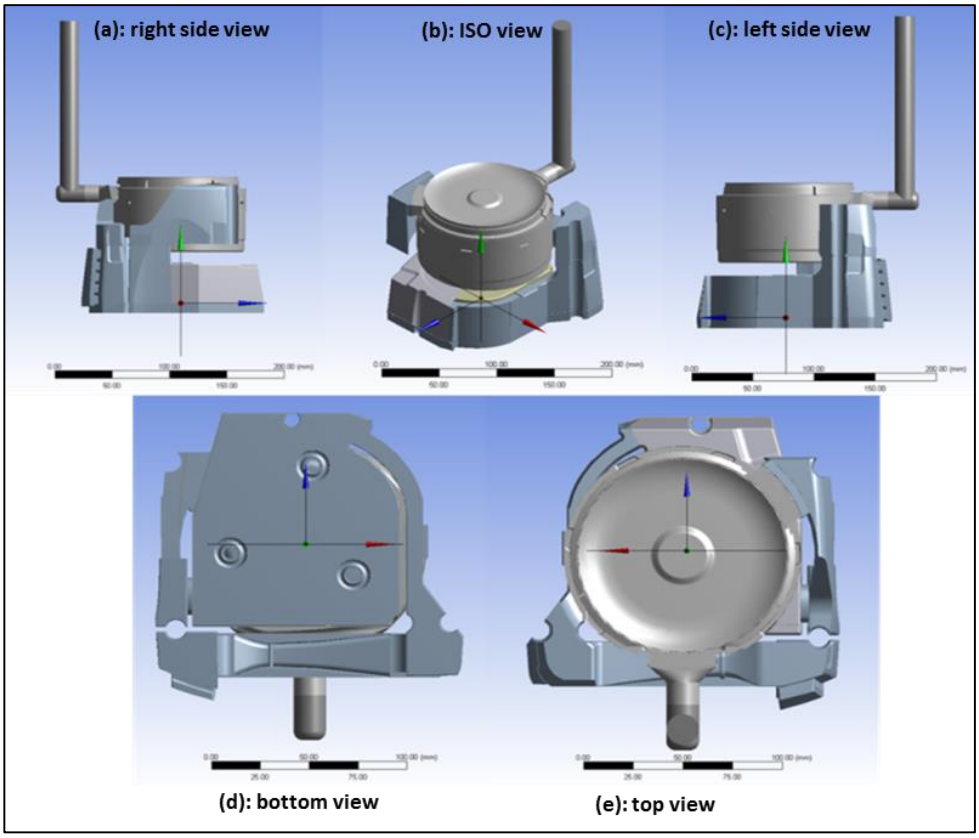

Figure 1.2: 3-D CPAP fluid model

This is a compact and complex flow system; however, the CPAP flow system could be described schematically in a simpler way as shown in Figure 1.3.

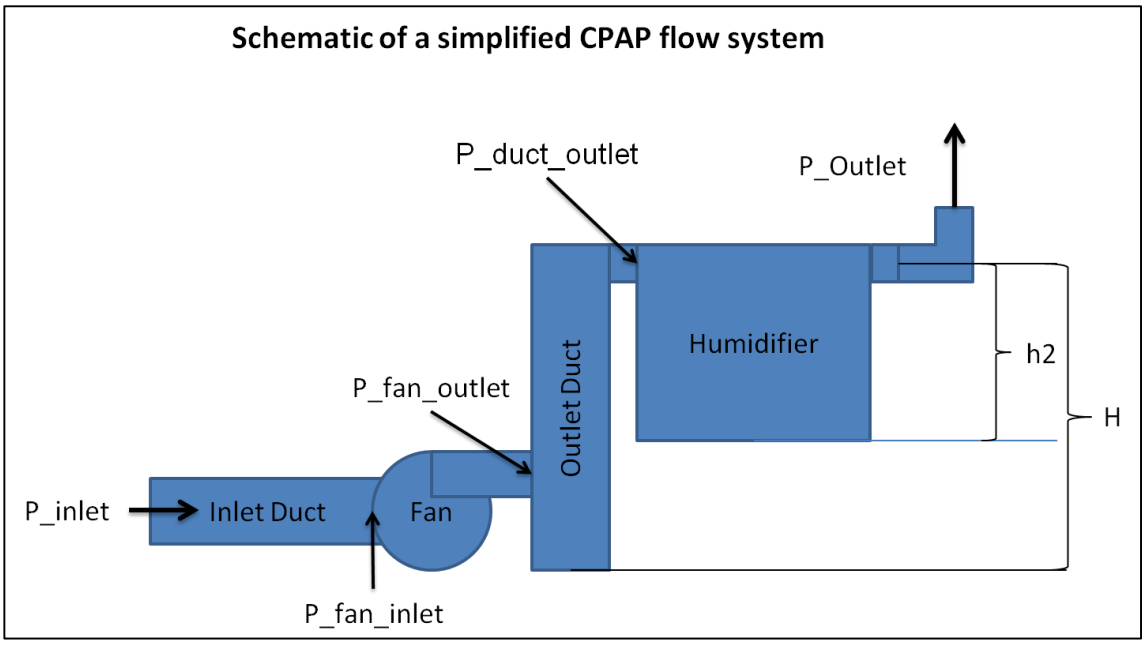

Figure 1.3: A simple flow system of CPAP device

In this figure, the air from outside (P_inlet) is ingested into the device through a complex inlet duct by means of a suction power made by a high-speed rotational centrifugal fan located inside the CPAP device. Inside the fan, the impeller imparts a radial and rotary motion to the air, which results in increasing both pressure and kinetic energy. The air pressure and its kinetic energy force its way into the volute casing through the impeller outlet. The vane-less diffuser in the volute casing collects and redirects discharged air from the periphery of the impeller at high velocity and gradually causes a reduction in air velocity by increasing the flow area. This converts the velocity head to a static pressure head or pressure rise. The air is then discharged from the centrifugal fan through the outlet (P_fan_outlet). The desired continuous pressurized airflow will continue to travel through an outlet path to a humidifier (P_duct_outlet). The humidifier, which is used to improve the air humidity, has a complicated internal flow structure. The humidifier unit consists of a flow chamber and a turbulent baffle. The flow chamber acts like a mixing chamber, where the air flow is kept and cycled inside the chamber for a period of time before releasing and the turbulent baffle is used to increase the turbulent flow inside the humidifier unit. The combined process allows turbulent air to mix with water vapour to

improve the air humidity. The final stage is the pressurized air with improved humidity (P_outlet) continues to travel through a heated hose to the mask interface, where it connects to the patient.

1.3 CPAP Flow System Noise

In the CPAP devices, the centrifugal fan or blower is used as the main driving force to generate flow and pressure within the device. Therefore, it is logical to say that the centrifugal fan is the main contributor of noise to the overall noise radiation level of the CPAP device. However, fan noise is not the only source that contributes to the total noise level emitted to the environment, as the inlet, outlet and humidifier, etc., are also other contributors.

The CPAP device considered in this thesis is small and compact in design. It has limited space and size. The limitations have led to complicated configurations in the internal flow system. In particular, the inlet and outlet ducts have many changes in size, length, shape and corners, etc., which might cause a number of serious noise issues. For example, the duct may be too short to allow a full development and expansion of air flow throughout the entire duct length. As a result, the noise contributing factor can be sudden changes in duct dimensions and/or flow direction that could cause flow to separate, develop vortex shedding and create an unwanted flow circulation as well as other complicated internal turbulent flow structure inside the duct. Complications in the duct shapes result in aerodynamic noise which could be generated at many locations. For instance, at duct elbows, duct constriction and expansion and/or other duct elements, where there is a sudden change in direction, cross-sectional area can cause pressure fluctuation and therefore noise generation. The noise levels have different characteristics depending on the duct element geometry and the level of air turbulence flow and its velocity.

Another contributing factor to the overall noise level to be considered in this CPAP device is the noise generated from the humidifier component which could also be brought to attention as an additional noise source. The humidifier consists of a heating element, a container covered by a lid and a turbulent baffle. This turbulent baffle is designed in a special way to produce turbulent flow for better humidification. When the air with high velocity and pressure comes from the centrifugal fan enters the humidifier unit, it impacts on the baffle wall and create more air turbulence inside the humidifier. This process allows the air to be scattered around to combine with water vapour to increase the air humidity. As a result of this process, air turbulence inside the humidifier could be counted as an important noise generation source that contributes to the overall noise level.

Structure-borne noise could also contribute to the noise radiation level in the CPAP device. This noise is normally induced by the fluid-structure interaction (FSI). This is because, in the CPAP device, most of the solid parts are made from thin elastic material, i.e., polycarbonate, which could be excited by vibrations or by the noise and flow fields present in the flow path, and so could transmit structural vibration. Therefore, the flow pressure fluctuation combined with some mechanical vibration could contribute to the structural vibration and, in turn, produce noise which radiating to the environment. The vibration of various components in the CPAP device, which include mechanical as well as flow-induced vibration, can be a problem if it is not treated carefully.

1.4 Thesis Motivation

As indicated in section 1.1, there is a desire to understand the aerodynamic noise generated from the CPAP internal flow system in order to improve the future product. However, to date, no comprehensive study has been conducted on determining the noise and vibration characteristics of CPAP devices. Previously, there were several computer-based CPAP simulation models developed to investigate various dynamic behaviours of

the CPAP devices [2-5]; however, they failed to take acoustic and vibration characteristics into account. Therefore, it is highly desirable to develop a simulation programme for predicting the noise and vibration from CPAP device.

Apart from measurement method mentioned earlier, analytical methods could be considered as potential methods to predict the noise and vibration. However, in reality, the analytical methods are only limited to simple models and rarely coincide with actual physical problems. The closest analytical method is the noise power prediction of heating, ventilating and air conditioning (HVAC) systems. This method is mostly based on empirical models, which were developed by experimental researchers. However, this method was developed directly for the HVAC system which functions on a much larger scale compared to the CPAP flow system. Therefore, it cannot be used directly to predict the noise generated from the CPAP flow system unless clarifications are made.

Alternatively, despite some limitations and difficulties, the numerical simulation methods have proven to be very useful approaches for product designers or engineers to obtain an insight for product improvements. The numerical simulation methods use mathematical equations to govern and solve physical behaviours of studied models computationally. The numerical methods for predicting noise generated from flows is known as the computational aero-acoustics (CAA) methodology, and the numerical methods for predicting the flow-induced vibration is called fluid-structure interface (FSI) simulation. To the best of the author's knowledge, there is no specific study that has been previously conducted numerically to investigate the flow-induced noise and vibration in the internal CPAP flow system. This thesis is the first attempt to investigate the flow-induced noise and vibration characteristics of the CPAP devices using the numerical simulation approaches. A comprehensive computational approach supported by experimental

validation will give a better understanding of the noise and vibration generation in the current CPAP device in an attempt to propose some improvements.

1.5 Thesis Objectives

Inspired by the need to obtain insights into the internal flow-induced noise and vibration of the CPAP device under dynamic conditions, the objectives of this research are:

- to gain an understanding of the influences of internal turbulent flow on noise sources, its locations and contributions to structural vibration,
- to gain information on the contribution of noise generated by individual elements to the overall noise level of the CPAP device, and
- to assist product designers to understand how aero-acoustic noise is generated and how it can be reduced.

The objectives are attained by numerical investigations of the sources and locations of the flow-induced noise and vibration inside the CPAP device by:

- performing computational aero-acoustic (CAA) simulation, and
- performing flow-structure interaction (FSI) simulation.

1.5.1 Proposed Numerical Frameworks

The complexity of the 3-D CPAP fluid model makes it very difficult if not impossible to develop a computational simulation model as a whole. Also, by calculating the overall noise generated from a whole system, the result does not provide information on the contribution of each individual element to the overall noise generation. Therefore, noise reduction techniques might not provide a good solution, where it is needed the most, to solve the current noise problems. In order to obtain the information on flow-induced noise and vibration for each component of the CPAP flow system and also to determine the

contribution of each local noise level to the overall noise level, the flow system of each element needs to be investigated independently from one another. One possible solution for this problem is to divide the 3-D CPAP fluid flow system into four simplified sub-models namely inlet duct fluid model, centrifugal fan fluid model, outlet duct fluid model and the humidifier fluid model, as shown in Figure 1.4.

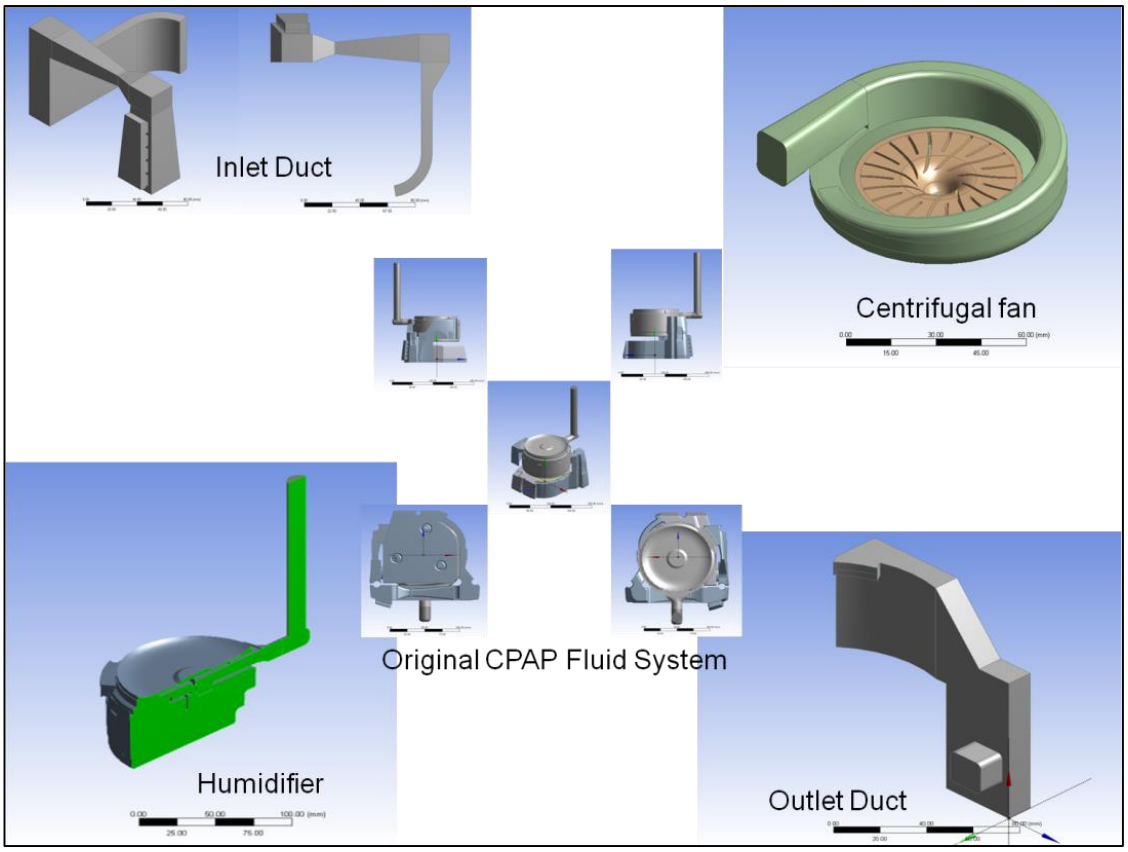

Figure 1.4: Four main components in the CPAP flow system

Numerical investigations will be conducted for each model using the numerical framework as shown in Figure 1.5. The simulation starts with the boundary condition and path-design intents, which are acting as controlled inputs. Physical values such as flow rates, velocity or pressure values, or geometry characters such as the shapes or the lengths of the model can be designed or modified before inputting into the simulation models. The values of the boundary conditions can be obtained from the experimental results. Once all the conditions are fulfil, 3-D computer models are then used to analyse the noise generation using the numerical "TOOL" simulations. The predicted results could be

compared and analysed to find any correlations between the local to the overall noise level. The findings would reveal dominant sources and solutions to solve identified problems which can easily be addressed. In order to confidently use a model in design process, a thorough assessment and validation of the model is required. This usually involves validating the method using experimental data or by other theoretical models already available. In this thesis, experimental investigations are used to validate the numerical results.

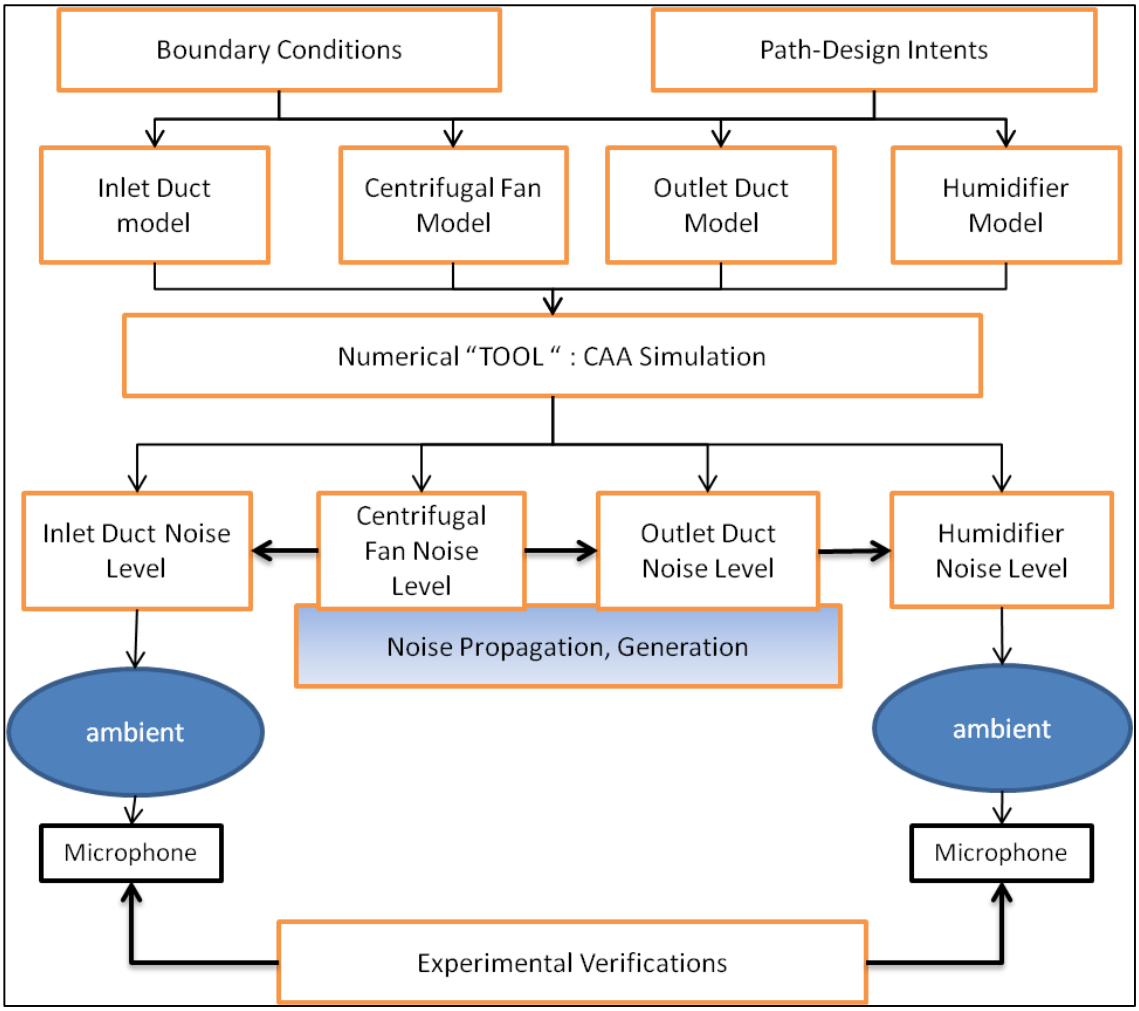

Figure 1.5: CAA Simulation Framework for CPAP flow system

1.5.2 Research Outlines

In order to accomplish the objectives, several necessary steps are undertaken as follows:

- Conduct a thorough experimental study on the CPAP device to

    - Observe an overview of how noise and vibration is generated from the CPAP devices,
    - Obtain the boundary conditions for numerical simulation models,
    - Compare with numerical results for validations.
- Develop simplified 3-D CPAP model consists of:
    - Centrifugal fan model,
    - Inlet and Outlet duct model,
    - Humidifier model.
- Use computer simulation to predict flow-induced noise to
    - Identify the dominant noise sources,
    - Identify critical source locations,
    - Determine source contribution on the overall noise pressure level (SPL).
- Use computer simulation to predict flow-induced vibration at
    - Centrifugal fan solid model,
    - Inlet and outlet solid duct models,
    - Humidifier solid model.
- Correlate the numerical and experimental results in order to give an overall assessment of the noise generated from the CPAP devices.

1.6 The Relevance, Significant, Contribution of this Research

The relevance of this research could be viewed as the first to develop a 3-D fluid model to numerically investigate the noise and vibration characteristics of the CPAP device. This research is carried out in collaboration with Fisher & Paykel Healthcare Ltd. The potential important key of using the computational simulation approach is to assist product designers to have a deeper view and thorough understanding of internal flow

dynamics and its noise generation. Knowledge obtained from this research, in turn, could be further developed as a guideline for noise reduction concepts.

Due to the lack of existing literature discussed specifically on the CPAP flow system, the significance of this research could be considered as contributions to the knowledge of the field of industrial design in an area where no documented research presently exists. Additionally, the development of a computer aided model (CAD) will minimize the effort in current CPAP testing and evaluation processes as it will provide an alternative solution and a useful tool to guide the development for better and quieter CPAP devices.

The research involves with current CPAP product of Fisher & Paykel Healthcare Ltd in the search of and advanced computational tool for predicting and improving the noise propagation and generation in the CPAP device. The successful completion of this research project will contribute to reducing or eliminating unwanted noise related to aerodynamic problems, which will possibly make the CPAP devices more attractive and comfortable to Obstructive Sleep Apnoea (OSA) patients.

This thesis is conducted using a commercial ANSYS software package for several reasons. Firstly, the commercial ANSYS software package provides variety of numerical solutions that are suitable for this research topic. For example, ANSYS software packages provide the 2-D and 3-D flow field simulations through several CFD software, i.e., FLUENT, CFX, etc. Secondly, the ANSYS FLUENT software provides some solutions for acoustic prediction, i.e., Ffowcs-Williams and Hawking (FW-H) acoustic model, broadband noise source models, etc. Thirdly, it also provides some FSI solutions for flow-induced vibration problems through its implemented coupling solutions such as one-way and two-way solutions. Finally, the software has been widely used and been proven reasonably accurate in industrial applications.

1.7 Thesis Outlines

Following the objectives, this thesis is set out into several chapters as follows:

Chapter 1 covers introduction on the CPAP device, motivation, relevance and objectives. Chapter 2 surveys the existing literature on aerodynamic noise theory, numerical simulation methods that can be considered to apply in this research thesis. The literature in this chapter also presents how those numerical simulation methods can be applied to predicting aerodynamic noise in duct, cavity and centrifugal fan, etc. Also, some of the key findings which are relevant and contribute to this research will be made and discussed.

Chapter 3 presents the background governing equations of numerical simulation methods that are identified and used for predicting flow-induced noise and vibration in the CPAP devices. In this chapter, numerical formulations are presented in general forms.

Chapter 4 presents the preliminary studies conducted throughout a series of experimental investigations on the noise and vibration of the CPAP device and its primary components. This chapter provides some helpful understandings as well as overviews of how the studied CPAP works and behaves during working conditions. Measured results could also be used for numerical validations.

As the various components of the CPAP devices have different nature, i.e., rotating, fixed with various shapes and sizes, etc., therefore they are structured to discuss in separate chapters in chapters 5, 6 and 7. In these chapters, numerical simulations are conducted for the centrifugal fan, the duct and the humidifier components respectively. Each component from the CPAP device can be treated independently and will represent a stand-alone chapter, which includes computational simulations, experimental validations, results and discussions o that particular component.

Chapter 8 discusses the noise sources locations, the power levels and its contributions. In this chapter, the validated numerical results are used to predict the locations and estimate the local sound power level as well as their contributions for individual component.

Finally, the research project is completed in chapter 9 where some conclusions are made and future works are recommended.

Chapter 2: **Literature Survey**

2.1 Introduction

For the purpose of searching available numerical simulation methods that are suitable for predicting the internal flow-induced noise and vibration in the CPAP device as proposed earlier in Chapter 1, this literature review consists of two main research areas. The first part, section 2.2 covers the reviews of available numerical methodologies used for flow-induced noise. In this section, aero-acoustic models are briefly discussed and presented. Also, some literature reviews on how those numerical methods are used to determine the centrifugal fan noise, duct noise, etc., which are relevant to the thesis objectives.

The second part, section 2.3 focuses on reviewing numerical studies on flow-induced vibration. In this section, reviews of the fluid-structure interaction methods are presented. Some reviews of how the numerical methods are applied to solve some flow-induced vibration problems. Finally, a summary of the literature Chapter is presented in section 2.4 to highlight some of the key findings that are relevant and contribute to this research.

2.2 Prediction Methods for Flow-induced Noise

Flow-induced noise is defined as the interaction of flow and solid structure that generate noise. In principle, experimental, analytical and numerical methods can be used to predict the aero-acoustic generation. However, for the purpose of this thesis, the numerical simulation methods are only considered and discussed in this section.

2.2.1 Computational Aero-acoustics Methods

The numerical simulation methods used for predicting flow-induced noise is called computational aero-acoustics (CAA) method [6, 7]. This is a numerical method used to compute the aero-acoustics noise generated from aerodynamic sources that propagate through the medium (air) to the receivers at some distance in the far-field, i.e., microphones or human ears, etc.

In CAA, there are two approaches that can be used to predict the aerodynamic noise generated to the far-field called direct and indirect (or hybrid) approaches [8]. The direct approach or direct numerical simulation (DNS) is a method used to calculate the noise field simultaneously with flow field using the compressible Euler or Navier-Stokes (N-S) equations [9]. In this method, the unsteady flow and noise generation are both included and computed simultaneously in the same model. However, this inclusion will create a computer problem because of the large disparities of length and energy scales between fluid and acoustic fields. The DNS needs very large computational resources in order to complete a direct simulation to predict noise [10]. This appears to be a very big challenge to computer technology even with the current advanced computer technology and it is not suitable for industrial research [11]. Consequently, the second approach, i.e., indirect or hybrid approach, is more preferable and widely used to predict the aerodynamic noise problems especially in the centrifugal applications [12, 13]. In this approach, the fluid models are coupled with the acoustic models to predict the acoustic pressure generation. The simulation consists of a two-step procedure: (i) firstly, the noise sources are obtained by solving turbulent flows using computational fluids dynamic (CFD) simulation and (ii) secondly, the acoustic pressure in the far-field is then computed from resulted sources on source region surfaces by means of analytical expressions through available acoustic analogies (AA).

2.2.2 Acoustic Analogies

In regard to acoustic analogies (AA), the development of the AA models have been considered as early as 1950's. In 1952, an acoustic model was developed by Lighthill (known as Lighthill's analogy) to aerodynamically compute the noise generated [14, 15]. In his model, the time derivative of the continuity equation and the divergence of the momentum equation were combined and then subtracted the term of $c^2 \frac{\partial^2 \rho}{\partial x_i^2}$ on both sides of the equation to obtain the governing equation.

$$\frac{\partial^2 \rho}{\partial t^2} - c^2 \frac{\partial^2 \rho}{\partial x_i^2} = \frac{\partial^2 T_{ij}}{\partial x_i x_j} \tag{2.1}$$

$$T_{ij} = \rho u_i u_j + P_{ij} - c^2(\rho - \rho_0)\delta_{ij} \tag{2.2}$$

Where T_{ij} is Lighthill stress tensor, c is speed of sound, ρ is fluid density, ρ_0 is fluid density at rest. $P_{ij} = p\delta_{ij} + \sigma_{ij}$ is compressive stress tensor, p is pressure, σ_{ij} is stress tensor , δ_{ij} is Kronecker delta (vanishing if i and j differ and unity if they are equal to each other), t is time, u and x are the velocity and directional component of the flow. The subscripts i and j describe the direction associated with u, T, p and x.

Equation 2.1 is known as the inhomogeneous wave equation. The term on the right hand of equation 2.1 describes the noise source terms including the pressure and velocity fluctuation as well as the stress tensor and force terms defined in equation 2.2. The Lighthill's equation can be solved by applying the general solution from Green's function. The acoustic pressure at the far-field is computed

$$\rho(x,t) - \rho_0 = \frac{1}{4\pi c^2} \frac{\partial^2}{\partial x_i \partial x_j} \int_{V_y} \left[\frac{T_{ij}}{r} \right]_{RET} dV_y \tag{2.3}$$

Where r is distance from source to receiver, V_y is source volume integration. ρ_0 is fluid density at rest.

The development of Lighthill's analogy model was originally developed for the jet noise problems in the aircraft industry [16]. However, it was considered as an anchor of the new era for the aero-acoustic research fields as many researchers have followed, applied or even further developed into different acoustic models including more complex aerodynamic problems [17]. For example, Proudman [18] developed an acoustic model for predicting broadband noise generation. In his model, Proudman combined the Lighthill's methods with techniques from the statistical theory of the isotropic turbulence to obtain the local and instantaneous expression for the acoustic power per mass. The broadband noise source models derived their noise radiation predictions using the turbulent kinetic energy k and dissipation rate ε. Broadband model was a quick solution to determine the loudness of the object of interest, e.g. duct noise etc., and could be considered to determine the pre-design stage to obtain the quick solution in modification.

Curle [19] extended the Lighthill's acoustic analogy to include the influences of a solid boundary at rest on the noise field. In this model, acoustic pressure fluctuation was computed by solving the Curle's equation using the Green's transfer function. The noise pressure level (SPL) was obtained from the resulting pressure fluctuation. This study revealed that a solid boundary can be an efficient noise source, especially at low speeds, which behave like a dipole. In Curle's equation, the effect of steady solid boundaries was included in the form of surface integrals. The Curle's equation was further developed to another broadband prediction model called boundary layer noise sources. In 1964, Powell [20] proposed a model for computing the aerodynamic noise, which considered vortex dynamics as main noise source generation. By rearranging the Lighthill's equation, he introduced the vortex noise theory that considers vortex eddy motion as an acoustic

source. Powell's theory was further developed by Howe [21] by considering the vortex noise method. In the following year, another acoustic model was proposed by Lowson [22]. In this model the Lighthill's equation was modified to form an expression for the noise field of a point force in an arbitrary motion. In particular, he derived a general expression for the equivalent sources of arbitrary moving aerodynamic bounding surfaces with adjacent turbulent flow.

In 1969, Ffowcs Williams and Hawkings (FW-H) [23] extended the Curle's equation by including the effects of moving surfaces as noise sources. In FW-H, three noise source components were presented as quadrupole, dipole and monopole. The solution of the FW-H equation was obtained from the integral solution based on the free-space Green's function solution. Further modifications of the FW-H acoustic equation have been developed by Farassat *et al.* [24-28] to get an easily applied version that can be implemented to the calculation of noise generation. These formulations are currently used in many software applications including the ANSYS FLUENT software [29].

In summary, the development of the AA family has provided great tools for researchers to deal with many aerodynamic noise related problems. Many researchers have combined the AA with the flow simulation methods to solve many aerodynamic noise problems, especially in the turbo-machinery industry. Some critical reviews of these techniques can also be found in reference [30]. In the following subsection, discussions of the noise generated from centrifugal applications are made with the focus on centrifugal fan in order to find suitable solutions for solving the noise generation in the centrifugal blower used in the CPAP devices.

2.2.3 Centrifugal Fan Noise Prediction

As previously stated, the development of the computational simulation models, i.e., CAA simulation, has helped researchers to deal with more complicated realistic models,

especially in many centrifugal applications. The study of noise generated from centrifugal applications has been extensively reported in the literature.

At earlier stages of determining the noise generated from centrifugal applications, most researchers conducted studies on noise radiation and generation using experimental techniques. The review of those techniques can be found in Neise's paper [31]. Based on experimental techniques, Choi [32] conducted an experimental study on the noise generated from centrifugal turbo-machinery. His study was focused on broadband noise sources. The noise generated from impeller was measured using the B&K condenser microphone and noise measurement system at both inlet and outlet of the centrifugal fan. It was found that the radiated noise from the studied impeller dominated by harmonically related broad humps, which were related to the low frequency noise spectrum. Another experimental paper presented by Choi *et al.* [33], they conducted an experimental study on unsteady flow and noise generated from centrifugal impeller of the pump. They used the hot-wire sensors to measure the flow and pressure transducers to measure surface pressure. The sensors were attached to the impeller surface at several locations. The noise analysis in frequency domain revealed that unsteady flow separation at the suction side of the impeller interacted with the impeller blades near the trailing edge generated noise that radiate to the environment. Suarez *et al.* [34, 35] also conducted experimental studies to determine the tonal noise generated in centrifugal fans with backward and forward-curved impeller models. In their study, a microphone was placed at one meter away from the fan outlet in the fan outlet direction. The acoustic pressure radiated to the free field was measured using the B&K sound measurement system. Near-field acoustic pressure fluctuations at the volute surfaces were also measured using flush-mounted microphones placed on the volute surfaces. Correlation studies of both measured data were conducted to explain aerodynamic behaviours of noise generated from studied fans. It was found

strong sources of noise caused by interactions between the fluctuating flow leaving the impeller and the volute tongue regions.

From experimental studies, it was found that the fan noise was a complex phenomenon because of the aerodynamic noise is mostly influenced by the interaction between the turbulent flow from a rotating part with other solid objects, known as stationary parts, in the close vicinity of the rotating part. The noise spectrum observed from experimental study showed both tonal components and broadband components. The tonal components were dominant sources of the fan noise and it was produced by the interaction of impeller blades with the stationary object and often seen at the blade passing frequency. The broadband noise was produced by the impingement of the turbulent flow stream on the volute casing.

The availabilities of numerical simulation method has contributed significantly to the advancement of noise predictions. Researchers have combined both experimental and numerical approaches to investigate the noise generated from centrifugal applications to obtain a deeper understanding of how the noise generated inside the fan and to identify the location of the noise sources. In these studies, the experimental approaches were mostly used for validating numerical results. Cho and Moon [36] developed a two-dimensional (2-D) cross-flow fan (different type of centrifugal fan) and used the computational aero-acoustic (CAA) with hybrid approach to study the acoustic pressure generation. In this study, they first used 2-D incompressible Navier-Stokes equations in moving coordinates to compute the unsteady viscous flow field to obtain pressure fluctuation as noise sources. Pressure fluctuations were used to calculate the acoustic pressure using the Ffowcs-Williams and Hawkings (FW-H) equation. The predicted acoustic pressure was validated using experimental results.

Mao *et al.* [37] developed a 2-D fluid model to investigate the tonal noise generated by a centrifugal fan. In this study, the flow field simulation was performed in commercial ANSYS FLUENT software. The simulated results were incorporated into the acoustic model based on FW-H equation to compute the noise propagation. The numerical results were compared well with experimental results. A similar hybrid approach was presented by Mao *et al.*[38]. They first performed a flow analysis for a centrifugal fan in ANSYS FLUENT software to generate noise sources. However, in their second steps, they used a thin-body boundary element method (BEM) to reduce the boundary integral equations from the governing equations and boundary conditions using the fundamental solution and Green's transfer function. The numerical results were compared well to the exact solution of the plane wave scattered by a rigid flat plate. The numerical results for the blades noise showed that the scattering of the volute casing not only changed the directivity pattern of the blades noise but also increased the noise pressure level at the outlet of the volute casing.

Langthjem *et al.*[39, 40] used the CAA with the hybrid approach to study aero-acoustics generated from a 2-D centrifugal pump model. In this study, the flow analysis was performed with a discrete vortex method (DVM), which is a numerical technique for solving the two-dimensional Navier-Stokes equations in vorticity-transport form, to calculate unsteady velocity fields. The forces exerted on the impeller blades were estimated by the unsteady Bernoulli's equation and the results were fed into the FW-H model to compute the noise propagate to the far-field. Data was validated with the experimental results and an agreement was made.

Researchers have not only used the 2-D model but also used a 3-D model to predict the noise generation from the turbo-machinery applications. Liu *et al.* [41] used the large eddy simulation (LES) to simulate the unsteady flow of the centrifugal fan and used the

FW-H equation to predict the dipole and quadrupole noises. The results showed that the noise pressure level of the dipole noise generated from the volute casing was much higher than the one from the impeller blades. Sun and Lee [42, 43] used the FW-H equation to evaluate the noise source of the centrifugal compressor impeller. Turbulent flow fields were computed by the three-dimensional Euler's formulation and the three-dimensional unsteady compressible N-S equation respectively. The simulated results were fed into the acoustic model to compute the aerodynamic noise generated from the impeller. Spectrum analysis showed that the dominant frequency was associated with blade passing frequency (BPF) and matched well with the experimental results.

Several research studies conducted by Khelladi *et al.* [44, 45], who also used the FW-H equation to predict the dipole and monopole aerodynamic tonal noise generated from a high speed centrifugal fan. The unsteady flow inside the fan was computed by solving the unsteady Reynolds averaged Navier-Stokes (RANS) equations. The models were validated by experimental data. Similarly, Younsi *et al.* [46, 47] used the hybrid approach where the CFD simulation coupled with the FW-H equation to calculate aerodynamic tonal noise generated from the centrifugal fan. The dynamic performance of the fan was predicted and validated at different flow rates. They computed the near field wall pressure fluctuations at different strategic points on the volute surface and applied to the FW-H acoustic equation to estimate the aerodynamic tonal noise. The numerical results were compared with the experimental results. The spectral analysis of the noise pressure also showed that the main source of the tonal noise was the aerodynamic interactions between the impeller and the volute tongue. Studies described above were performed using commercial ANSYS FLUENT software.

Several researchers used Lowson's model [22] to calculate the aerodynamic noise generation due to the internal unsteady flow which related to the blade passing frequency

in centrifugal machinery principles [48-51]. They used the incompressible Discrete Vortex Method (DVM) to calculate the unsteady flow fields and unsteady force fluctuations. The DVM is a numerical technique for the solution of the two-dimensional Navier-Stokes equations in vorticity-transport form [52]. The resulted forces were used to calculate the noise field by solving the Lowson's equation. The spectrum analysis showed that the peak frequency and its amplitude of the tonal noise were similar to the experimental data. It was found that the source of blade passing frequency (BPF) was an unsteady force fluctuation at impeller blades. This force was fluctuated by the periodic interaction between the impeller blade and the volute tongue.

Choi and Lee [53] used the Lowson's equation to predict the acoustic pressure generated from the rotating dipole source. Initially, a numerical method based on thin-body boundary element method (BEM) combined with Kirchhoff-Helmholtz equation, was developed to compute the flow field around the rotating source. Later, the predicted results from flow simulation were used as input to the Lowson's equation to compute acoustic pressures. Acoustic pressure radiation was compared to the experimental results and showed that the wave propagation was dependent on the cut-off frequency travelling in an inlet duct. It also showed that the acoustic pressure radiation could be changed according to the relation between the cut-off frequency and the rotating frequency of the source. Similarly, Liu *et al.* [54] also used Lowson's model to calculate the aerodynamic noise generated from the unsteady flow in a centrifugal fan. In this study, they developed a three-dimensional numerical simulation model to compute unsteady flow fields generated from a forwarded-curved centrifugal fan. The simulation model was solved by the finite element method (FEM) and higher order discretization schemes. The numerical results compared well with experimental results, and showed that the force acting on the volute casing was the dominant source of the aerodynamic noise. It also found that a

clearance between the blade tip and the volute tongue combined with a moderate slope of the volute tongue had a significant impact on noise reduction of the centrifugal fan.

Other researchers have also used different acoustic models to predict the noise generated from centrifugal applications. Moon *et al.* [55] used the Curle's model to predict the aerodynamic tonal noise generated from a cross flow fan. In their study, the 2-D incompressible Navier-Stokes equations were used to simulate the unsteady flow interactions between the rotating impeller blades and the fan casing. The numerical results were fed into the acoustic model, which was based on the Curle's model to predict the acoustic pressure fluctuations. Numerical methods were verified by experimental results as it showed a good outcome. Lee *et al.* [56] also used the Curle's model to predict the internal blade passing frequency (BPF) noise generated from a centrifugal fan in a refrigerator. The unsteady flow was computed by solving the incompressible RANS equations with conventional CFD techniques. The BPF noise was predicted using the acoustic model combined with the boundary element method. Based on the results obtained from the acoustic model, they proposed a technique to reduce noise and achieved an approximate 3 dB noise reduction in comparison to the original fan model.

The Powell's acoustic model [20] was also used in references [34, 35, 57-60]. In these studies, researchers used the Powell's model to analyse the effects of the distance between the impeller and the volute tongue on the aerodynamic noise generated from a centrifugal fan. They used three-dimensional unsteady Reynolds averaged Navier-Stokes (URANS) equations to obtain the flow fields. The resulted forces were fed into the Powell's model to calculate the acoustic pressures. Numerical results were compared with experimental results and obtained good agreements.

2.2.4 Duct Noise Prediction

The field of internal duct noise has also got much attention in the literature. Unlike the fan noise, the internal flow generated noise in the duct has different physical background. When airflow is obstructed or diverted by a change of geometry, i.e., corner, constriction area, etc., the flow instabilities and vortices are generated. As the vortices continuously impact on the wall boundaries, it will generate noise. The two main generating mechanisms in internal flow are turbulence noise and noise generated by wall interaction with hydrodynamic pressure fluctuations, with the latter being more efficient for low Mach number. Many published papers have presented several methods to determine the duct noise. Some fundamental aspects of the sound generated aerodynamically in theory can be seen in reference [61].

Similar to the fan noise prediction, both the DNS and CAA with hybrid approach have also been applied to determine the noise generated by ducts. Several researchers used the direct numerical simulation (DNS) method to predict the noise generated in the flow duct system [62, 63]. As mentioned earlier, the DNS method is relatively expensive and not suitable for industrial research. The computational aero-acoustic (CAA) with hybrid approach is again preferable and suitable for industrial research to predict the noise generated from the duct systems as can be seen in references [64-71]. Khondge *et al.* [65] used the CAA with hybrid approach to predict the noise generated from a heating, ventilating and air conditioning (HVAC) ducts. In their study, the CFD simulation was used to generate the noise sources and the noise power level of the duct was predicted using the broadband noise source models. The Proudman's acoustic model [18] was used to predict the broadband noise generated by the flow turbulence in the duct model. The noise generated by dipole source was predicted using the boundary layer source model, which were derived from the Curle's equation [19]. The study was conducted with different duct models and the prediced sound power level (PWL) were compared to each

other. From the findings, they were able to identify which models could be the best options for lower noise generation. They also concluded that the broadband noises model can be used to determine the noise generated from the duct system. A similar approach was also used by Mohamud *et al.* [68] to predict the noise generated from the automotive HVAC centre duct. In this study, they also used the CFD simulation approach to generate noise sources and use the broadband noise sources available in ANSYS FLUENT to predict the noise sources locations that were responsible for the noise generated by the automotive HVAC duct in a automotive ventilation system. The duct model was first simulated with the commercial CFD ANSYS FLUENT software. Generated results were used for calculating the sound powers and its locations inside the duct. The sound powers were used to compute the sound power level in the duct regions. They concluded that the broadband noise source model is a valuable and cost effective tool for the early design process for product development.

Ayar *et al.* [66] studied the flow-induced noise in HVAC duct system using the CAA with hybrid approach. In their study, transient CFD simulation combined with acoustic analogy was used to predict the noise generated from the climate control system in the automotive system. The CFD simulations were conducted with different turbulence models from k-e RNG model to LES model, etc in order to obtain the best solution for acoustic calculations. The study was also conducted in different commercial software, i.e., ANSYS FLUENT and Star-CD. The results showed that using the LES turbulent model could obtain a better noise prediction. The predicted results were validated by experimental results.

In general, the noise generated from the duct system is broadband in nature, however, in several complicated duct design that involves a cavity, there is some tonal frequency occurring in the noise spectrum. Researchers have used numerical simulation to predict

the tonal noise successfully. For instance, Kanna *et al.* [67] used the ANSYS FLUENT to develop a 2-D model of the automotive air-intake duct system to predict a whistle noise generated from a cavity inside the duct. Acoustic pressure was recorded at a monitor point placed inside the cavity and was compared to the acoustic pressure obtained from an inserted microphone at similar location during the sound measurement. It was found that similarity between these frequency spectrums. Using the finding from the numerical simulation, they managed to modify the model to reduce the noise level produced by the whistle noise due to the cavity.

Ashcroft *et al.* [72] used the CAA with hybrid approach to predict the tonal noise radiated from a two-dimensional cavity model under low-speed turbulent flow. In their study, near-field turbulent was generated by k-omega turbulent model. Unsteady flow field recorded with small time step were used to compute acoustic pressure in the far-field using the FW-H equation. The comparisons were made and found to be in good agreement in both the frequency and amplitude of the oscillations within the cavity.

2.2.5 Remarks

Section 2.2 has covered an overview of the numerical simulation methods that could be considered for predicting aerodynamic noise generated from the CPAP device. The CAA methods for predicting aerodynamic noise generation was reviewed including direct and indirect approaches. The direct numerical simulation (DNS) method could provide better and accurate results compared with the indirect approach. However, this approach required very high computational resources. The indirect approach, on the other hand, requires less computational resources and is more preferable in solving many engineering applications as seen by many references in this section. Therefore, the CAA with hybrid approach could be considered for the numerical simulation methods in this thesis.

2.3 Prediction Methods for Flow-induced Vibration

In parallel to the prediction methods for flow-induced noise, the flow-induced vibration or fluid-structure interaction (FSI) study has been around for sometimes. The FSI phenomenon commonly happens in many engineering applications, especially in the flow distribution system. The term FSI is used to define the interactions between the fluid flow and the solid structure, where the solid structure either is being covered in fluids and/or it contains fluids. The interactions could cause dynamic pressure fluctuations which could lead to the solid structure's motion that in turn causes the stress developed in the fluid and vice versa.

In recent years, the fluid-structure interaction (FSI) simulation method has been preferable and actively used due to the recent development of advanced computer technology. In this method, the finite element (FE) solvers are coupled with the flow field solvers to solve the FSI problems through a coupling system. During the simulation, generated data from both models are transferred back and forwards during the simulation time to generate the effects on both sides. For example, the pressure fluctuations at the wall interfaces, which is generated in the CFD simulation, is used as external forces to excite some vibration modes in solid models and in turn, the motion of the solid vibration, displacement motion, will have an effect on the fluid dynamic behaviours. As a result, the FSI modelling has been used to deal with many FSI problems in several engineering industries, for instance, in the biomedical industry [73-76], in the turbo-machinery industry [77, 78], and even in the military industry [79, 80].

A literature review of numerical methods has been developed and applied to solve FSI problems and this can be found in details in reference [81]. The most common method used in the FSI simulation is the continuum theory developed for solid and fluid models as coupling tool. In this way, each of the models is being governed by conservation laws.

An example of this method is the arbitrary Lagrangian-Eulerian (ALE) method [82, 83]. This method is based on two different theories, the Eulerian continuum approach to govern the flow field and the Lagrangian equation to deal with the structural motion. The ALE method is adopted in the commercial software, i.e., ANSYS, for solving the FSI problem.

Figure 2.1 shows the interaction mechanisms between the solid structural simulation and the fluid dynamics simulation. The coupling system acts as a medium that allows the two numerical simulations to communicate with each other and therefore data is transferred between both models during the simulation time.

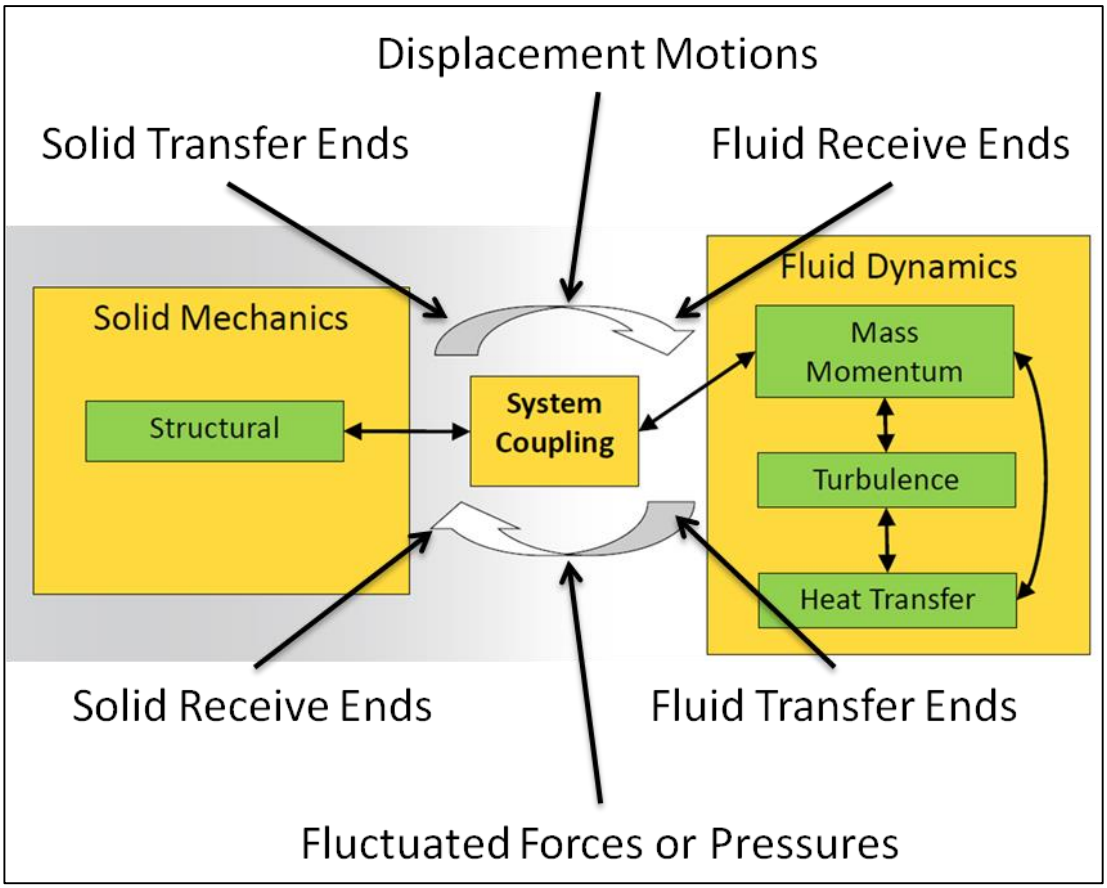

Figure 2.1: Overview of FSI coupling techniques

Figure 2.2 shows the mesh matching and data transferred process during the FSI simulations. In this Figure, pressure data obtained from the CFD simulation was transferred to the solid surface nodes via interpolation. In order to perform the data

transfer, the surface structural nodes need to identify its matching partner from the fluid mesh model. Once the matching process is completed, the force transfers are performed.

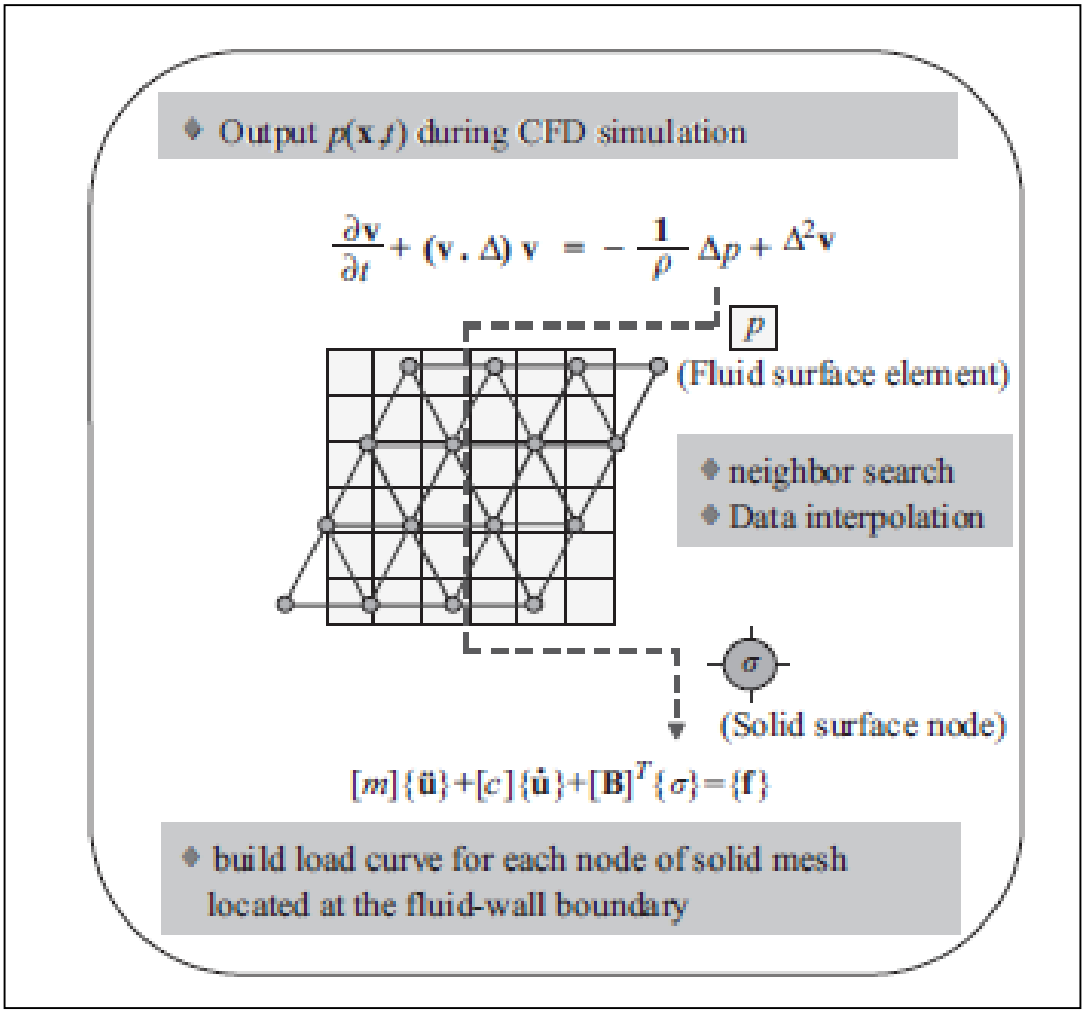

Figure 2.2: Mesh matching and data transferred in FSI simulations adopted from reference [84]

In the FSI simulation method, there are two ways of communication between the solid and fluid models through the coupling technique call one-way FSI and two-way FSI simulation.

2.3.1 One-way Fluid-Structure Interaction Technique

The first coupling technique called one-way FSI simulation [85]. In one-way coupling, it assumes that the structural deformations are small enough that they do not influence the flow field, only sources the fluid model are allowed to transfer to the solid model to generate the excited forces or displacement. For instance, pressure fluctuations at the

fluid-solid interface are transferred to the solid wall as external loads. The structure is then allowed to respond to the loads that are updated each time step. The fluid model, however, does not respond to the structural motions.

2.3.2 Two-way Fluid-Structure Interaction Technique

The second coupling technique is called two-way FSI simulation [86]. In this setting, data transfers in both directions, i.e., from fluid to solid and vice versa at every simulated time steps. The two-way coupling technique considers to be necessary when the structural deformation is affected to the flow field. More often, the two-way FSI simulation is used to validate the one-way FSI simulation by determining the magnitude of the simulated results. if there is no or insignificant differences obtained, the one-way simulation is recommended in considering the significant higher computational cost of the two-way over the one-way simulations.

2.3.3 Fluid-Structure Interaction Applications

As mentioned earlier, the FSI simulation methods have been used by many researchers in many different applications as applications of solid-fluid interaction. In the military industry, Anghileri *et al.* [80] investigated the interaction between the structure and the fluid inside a tank of a helicopter. Zwaan *et al.* [87] used a linear structural model coupled with the non-linear Euler/RANS equation to analyse the elasticity of the aircraft.

In the biomedical industry, Sonntag *et al.* [74] studied an artificial heart by developing a 3-D heart model and used the two-way FSI simulation approach available in ANSYS software package. The fluid dynamics of the heart was generated in CFD CFX software and the solid was simulated by structural solver in ANSYS Mechanical. Hart *et al*. [86] developed a three-dimensional computational analysis to investigate the FSI problems in the aortic valve. In this study, the FSI simulation was conducted in commercial ANSYS

software packages, which employed the ALE algorithm to solve the FSI problems. Chouly *et al.*[88] used the linear elasticity theory for small deformation combined with the fluid dynamics to study the mechanical behaviour of the tongue under upper airway obstructions. The predicted results were compared with the experimental data. It was found that both physical and numerical models could be used to help further understanding of the dynamic behaviours of the airway under obstruction conditions. Nobili *et al.*[89] used FSI simulation methods to study the dynamics of a bi-leaflet prosthetic heart valve. In this study, they reproduced the dynamics of the bi-leaflet mechanical heart valve using the means of the fully implicit fluid-structure interaction method. The fluid dynamics were carried out in the commercial CFD ANSYS FLUENT software and the results were used to compute the structure deformation of the valve model in MDM software. The simulated results were compared with experimental data. It was found the model captures the main feathers of the leaflet motion during the systole. It also confirmed that the applications of FSI models can be a major tool to optimize the heart valve design and could provide useful information to surgeons.

In the centrifugal applications industry, Jiang *et al* [84] performed flow-induced vibration in a centrifugal pump. They first performed unsteady flow simulation via a LES-based CFD program namely FRONTFLOW-Blue. The predicted surface pressure was transferred to the solid model to investigate the structural vibration under flow turbulences. Vibration data was compared to the measured one. It was found the blade passing frequency vibration was well-agreed with the measured results. Liang *et al.* [90] also performed FSI simulation on a Francis turbine runner. In this study, the finite element method (FEM) was carried out to analyse the influence of the water surrounding the runner on the vibration modes of the turbine. The numerical results were compared to the experimental measurements. It was found to be in good agreement with natural frequency values and in mode shapes.

2.3.4 Remarks

This section has covered reviews of the numerical simulation methods for predicting flow-induced vibration that could be applied to solve the flow-induced vibration in the CPAP device. The FSI simulation methods mostly use the ALE methods and are available in many commercial simulation software which includes ANSYS software packages. In FSI simulation, there are two ways of setting that allows the communication between solid and fluid models namely, one-way and two-way FSI simulations. They are proved to be capable in providing the solutions to solve many FSI problems in different industrial applications.

2.4 Summary

The literature study has provided a broad review of the present state of knowledge to which this research can add to and from which this work can benefit. Different approaches were presented in this chapter with focus on what, where and how the available numerical simulation methods can be used to solve noise and vibration problems in practise. Also, a vast number of numerical studies concerning the noise and vibration generation were reviewed in this chapter, for example, from centrifugal fan, from duct as well as cavity, etc. This section will summarise some of the keys findings of the literature review and discuss the relevance

In the first topic covered in this literature review, the fundamental techniques of fluid dynamics, aero-acoustics and structural vibration was presented. The review of these numerical techniques was an educational, learning and researching exercise for the purposes of this thesis. There are several key findings of literature review throughout this learning exercise as follows:

- The CAA with hybrid approach is a preferable numerical simulation method in predicting aero-acoustic noise generation

    - The FW-H acoustic model is suitable for rotating models as well as unbounded models
    - The Broadband Noise Model can be used for predicting noise generated from duct models
- The FSI method is used to predict flow-induced structural vibration
    - One-way FSI approach
    - Two-way FSI approach
- Both the CAA and FSI method used the CFD simulation to generate initial sources to compute the acoustic pressure and vibration values.
- The CFD simulation is governed by the equations of fluids, which are well established but difficult to solve using the direct numerical simulation (DNS) method due to limitations in computational resources.
- The most commonly used form of the governing equations of fluids in practice is the Reynolds-averaged Navier-Stokes (RANS) equation.

The second topic covered in this review chapter was the applications of those numerical techniques to solve flow related problems in many industrial applications. It was learnt that the uses of the CAA with hybrid approach was well applied to solve aero-acoustic problems in turbo-machinery applications. The review of literature on FSI indicated that this is still a field in which research is actively on-going. It was learnt that the diversity of this field is reflected a wide-range of research activities.

More importantly, the literature revealed that there is no study related to the noise and vibration radiated from the CPAP device. Consequently, this works bridges the recognised gap by contributing to the product development with knowledge of practical value obtained from numerical studies.

For the purpose of using the available computational simulations to identify the sources and the locations of the noise generation as well as the characteristics of structural vibration of the CPAP devices, this thesis will attempt to investigate the flow-induced noise and vibration in the CPAP device numerically. The numerical simulations in this thesis is following numerical studies conducted for centrifugal fan and ducts mentioned in literature review. The details of numerical methods are chosen and presented in the next chapter.

Chapter 3: **Numerical Methodology**

3.1 Introduction

The computational simulation methods identified and briefly discussed in Chapter 2 are adopted to investigate the flow-induced noise and vibration in the CPAP devices. The basic governing equations implemented in ANSYS software are briefly presented in this chapter in order to understand how this program is formulated. A combination of the computational aero-acoustic (CAA) and the fluid-structure interaction (FSI) methods is presented in this chapter. It consists of three simulation steps, namely aerodynamic, acoustic and structural-dynamic respectively.

3.2 Governing Equations of Fluid Dynamics

The first and very important simulation step is to generate the sources that can be used to predict noise and vibration. The CPAP device is one of many examples of flow distribution products whose function and performance is closely related to the fluid dynamic behaviours. Therefore, it can be solved using the computational fluid dynamics (CFD) simulation techniques [91-94].

In the CFD simulation techniques, the governing equations are often based on the Navier-Stokes (N-S) equations which are derived from the principles of conservation of mass (or continuity), conservation of momentum and conservation of energy. The basic equations of fluid mechanics present in this section as a starting point for the CFD simulation. In

this chapter, the instantaneous equations of mass, momentum and energy conservation can be written as follows in a stationary frame.

3.2.1 The Continuity Equation

The first equation is the continuity equation or the conservation of mass. Figure 3.1 shows a fluid entering and leaving a differential volume.

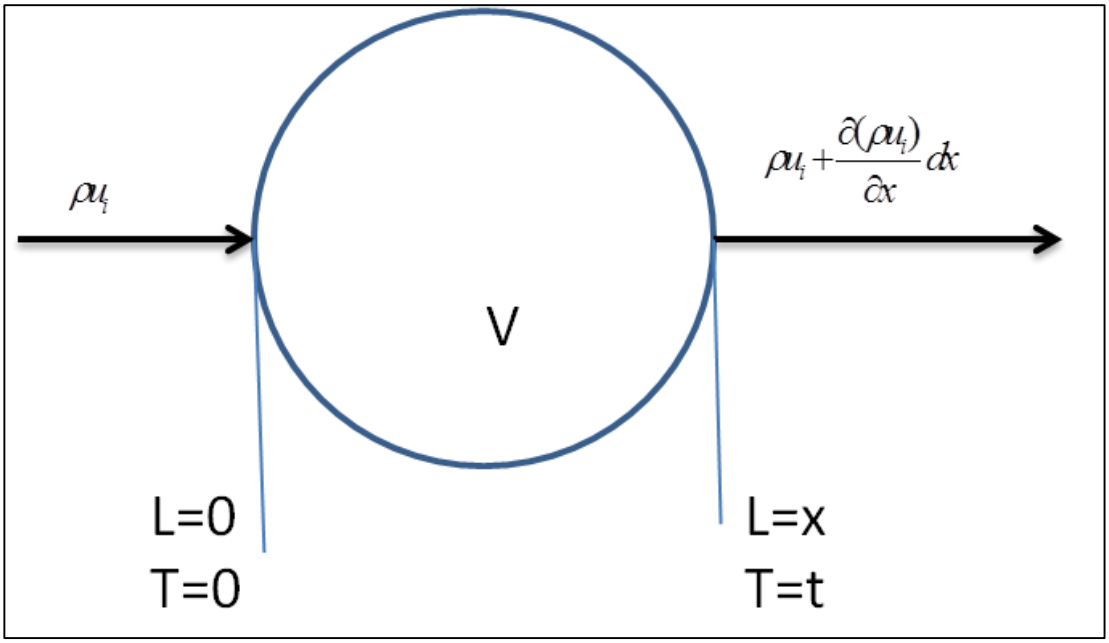

Figure 3.1: Schematic of fundamental fluid dynamics

The mass balance leads to [95]

$$\frac{\partial \rho}{\partial t} + \frac{\partial \rho u_i}{\partial x_i} = 0 \tag{3.1}$$

Where ρ is fluid density, t is time, u_i are the components of the mean velocity vector **u** in the coordinate system, x_i is Cartesian coordinates ($i=1,2,3$).

Equation 3.1 describes the balance between the rate of mass in ($\frac{\partial \rho}{\partial t}$) and the sum of the rate of mass out over the control volume boundaries and the rate of mass is accumulated

within its boundaries ($\frac{\partial \rho u_i}{\partial x_i}$). The velocity u_i and density ρ of the fluid must satisfy the continuity equation to fulfil the conservation of the fluid mass.

3.2.2 The Momentum Equation

The second equation is the momentum equation or the conservation of momentum. This equation expresses the rate of momentum change of a fluid particle equals to pressure gradient and viscous stress gradient as shown [95]

$$\frac{\partial \rho u_i}{\partial t} + \frac{\partial \rho u_i u_j}{\partial x_j} = -\frac{\partial p}{\partial x_i} + \frac{\partial \tau_{ij}}{\partial x_j} \tag{3.2}$$

Where p is the pressure and τ_{ij} is the viscous stress.

Equation 3.2 is derived by applying Newton's second law of motion, which relates the forces on fluid volume to its acceleration. Similar to equation 3.1, the momentum in equation 3.2 must be conversed.

3.2.3 The Energy Equation

The third equation is the called conservation of energy [95]

$$\frac{\partial \rho C_v T}{\partial t} + \frac{\partial \rho u_i C_v T}{\partial x_i} = \frac{\partial}{\partial x_i} k \left(\frac{\partial}{\partial x_i} T \right) + q_T \tag{3.3}$$

Where C_v is heat capacity, T is temperature, k is thermal conductivity of the fluid and q_T is body heat source term.

Equation 3.3 describes the rate of change of the energy in a control volume equals to the rate of heat transfer from the volume and the work is done by the applied forces.

3.2.4 Reynolds Averaged Navier-Stokes (RANS) Equations

In the CFD techniques, the N-S equations are transformed into the averaged formulae namely Reynolds averaged Navier-Stokes (RANS) equations. Consider instantaneous velocity and pressure fields are defined as the sum of the mean components $\bar{u}$, $\bar{p}$ and the fluctuating components u_i', p' as follows

$$u_i = \bar{u}_i + u_i' \tag{3.4}$$

$$p = \bar{p} + p' \tag{3.5}$$

Where mean components are calculated by the time-averaging as

$$\bar{u} = \lim_{T\to\infty} \frac{1}{T} \int_0^T u(x_i, t)dt \tag{3.6}$$

$$\bar{p} = \lim_{T\to\infty} \frac{1}{T} \int_0^T p(x_i, t)dt \tag{3.7}$$

Substituting equations 3.4 and 3.5 into equations 3.1 and 3.2 and taking time average yields the time-averaged momentum equations as shown

$$\frac{\partial \rho u_i}{\partial t} + \frac{\partial \rho u_i u_j}{\partial x_j} = -\frac{\partial p}{\partial x_i} + \frac{\partial}{\partial x_j}\left[\mu\left(\frac{\partial u_i}{\partial x_j} + \frac{\partial u_j}{\partial x_i} - \frac{2}{3}\delta_{ij}\frac{\partial u_j}{\partial x_j}\right)\right] + \frac{\partial\left(-\overline{u_i' u_j'}\right)}{\partial x_j} \tag{3.8}$$

Equation 3.8 is unsteady, non-linear, second-order partial differential equation. By combining this equation with equation 3.1 forms the main governing equations which are implemented in ANSYS FLUENT software. However, when dealing with the rotating system, i.e., the centrifugal fan, the governing equation needs to be changed to the polar form in order to deal with rotating problems. Consider a system that is rotating at a steady angular velocity ω with respect to the stationary reference frame. The relationship between relative and absolute velocities can be described as

$$\vec{u}_r = \vec{u} - (\vec{\omega} \times \vec{r}) \tag{3.9}$$

Where $\vec{\omega}$ is the angular velocity vector which respect to the steadily rotating reference frame and $\vec{r}$ is radius which respect to the radius direction. Apply equation 3.9 to 3.1 and 3.8, the governing equation of the flow in rotating frame are now can be written as

$$\frac{\partial u_r}{\partial x_i} = 0 \tag{3.10}$$

$$\frac{\partial \rho \vec{u}_r}{\partial t} + \frac{\partial \rho \vec{u}_r \vec{u}_r}{\partial x_j} = -\frac{\partial p}{\partial x_i} + \frac{\partial}{\partial x_j}\left[\mu\left(\frac{\partial \vec{u}_r}{\partial x_j} + \frac{\partial \vec{u}_r}{\partial x_i} - \frac{2}{3}\delta_{ij}\frac{\partial \vec{u}_r}{\partial x_j}\right)\right] + \frac{\partial\left(-\overline{u_r' u_r'}\right)}{\partial x_j} \tag{3.11}$$

The Navier-Stokes (N-S) equations presented in this subsequence section are represented as the governing equation for both flow fields in non-rotating and rotating conditions. The governing equations can be solved using the turbulence models as described in the following subsequence section.

3.2.5 Equation of state

The N-S equations described above must be solved with constitutive equations of state in order to form a closed system. In the most general case, these state equations have the form:

$$\rho = \rho(p, T) \tag{3.12}$$

$$dh = \left.\frac{\partial h}{\partial T}\right|_p dT + \left.\frac{\partial h}{\partial p}\right|_T dp = c_p dT + \left.\frac{\partial h}{\partial p}\right|_T dp \tag{3.13}$$

$$c_p = c_p(p, T) \tag{3.14}$$

Where ρ is density, p is pressure, T is temperature, h is enthalpy and c_p is specific heat capacity.

Under incompressible conditions, density ρ is constant and the c_p can be (all most) a function of temperature. Equations 3.12 to 3.14 are written as

$$\rho = \rho_o \tag{3.15}$$

$$dh = c_p dT + \frac{dp}{\rho} \tag{3.16}$$

$$c_p = c_p(T) \tag{3.17}$$

For ideal gas, density is calculated from the ideal gas law and the dh can be (all most) a function of temperature and dp is neglected. Equations 3.12 to 3.14 are written as

$$\rho = \frac{wp_{abs}}{R_o T} \tag{3.18}$$

$$dh = c_p dT \tag{3.19}$$

$$c_p = c_p(T) \tag{3.20}$$

Where w is the molecular weight, p_{abs} is the absolute pressure and R_o is the universal gas constant.

3.2.6 Turbulence Models

To consider the effects of turbulence in the flow fields, the turbulence models are used. The turbulence models have been specifically developed to account for the effects of turbulence without recourse to a prohibitive fine mesh and direct numerical simulation. Most turbulence models are developed in statistical forms except for the large eddy simulation (LES) and the detached eddy simulation model.

In ANSYS FLUENT, The turbulence models are adopted as shown in Figure 3.2. In this Figure, the turbulence models are divided into several groups namely one-equation model, two-equation models, second order closure model and hybrid model respectively.

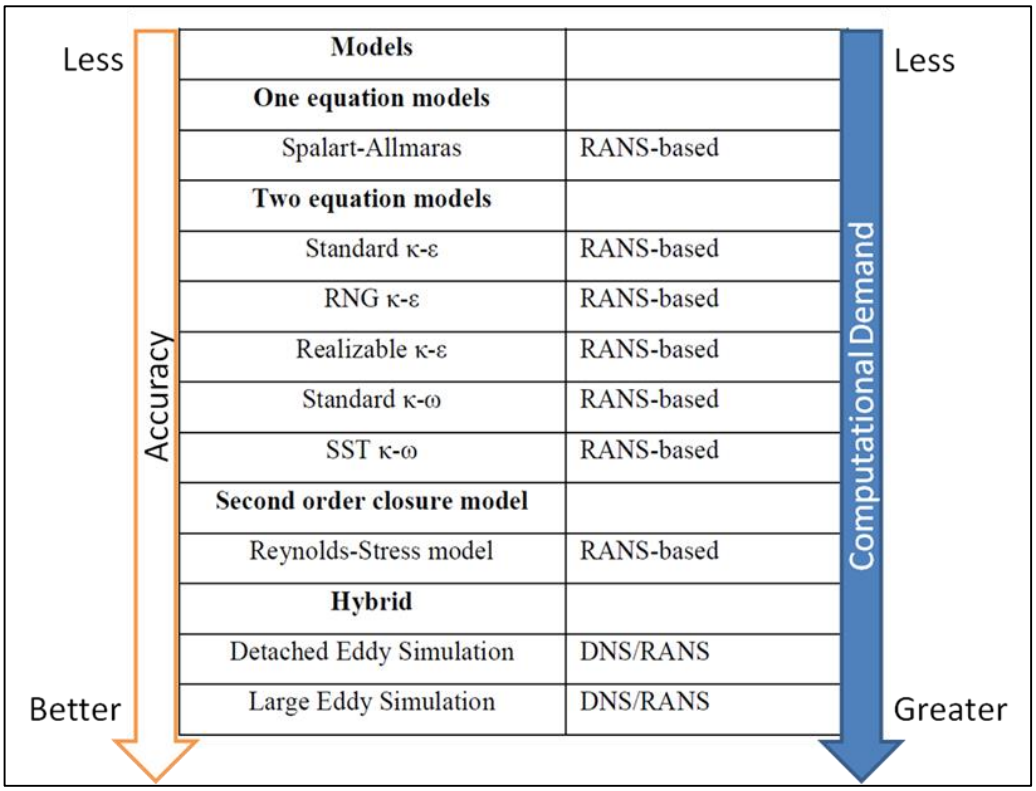

Models	
One equation models	
Spalart-Allmaras	RANS-based
Two equation models	
Standard κ-ε	RANS-based
RNG κ-ε	RANS-based
Realizable κ-ε	RANS-based
Standard κ-ω	RANS-based
SST κ-ω	RANS-based
Second order closure model	
Reynolds-Stress model	RANS-based
Hybrid	
Detached Eddy Simulation	DNS/RANS
Large Eddy Simulation	DNS/RANS

Figure 3.2: Turbulent models adopted from reference [95]

The turbulence models presented in Figure 3.2 are in order from the less to the better accuracy as well as from the less to the greater required computational resources. The Large Eddy Simulation (LES) would provide better predicted results as it was concluded in references [96-98]. However, the LES model also require very high computational resources, therefore, it is often not recommended for the industrial research, where allocated resources and time frames are limited [99]. The two-equation group, on the other hands, is widely used in industrial research due to its stability and convergence. Several papers have identified the $k-\varepsilon$ RNG (renormalization group theory) model is widely used in industry due to its stability and convergence and the $k-\omega$ SST can provide better simulated results [100-102].

Nevertheless, for the purpose of predicting the noise generation and flow-induced vibration in this thesis, several turbulence models are chosen. Firstly, the $k-\varepsilon$ RNG

turbulence model is used for steady state solution and secondly the $k-\omega$ SST turbulence model is used for unsteady simulation.

The $k-\varepsilon$ Renormalization group theory (RNG) Turbulence Model

The first turbulence model used for steady-state simulation in this thesis is the $k-\varepsilon$ RNG turbulence model which was adopted in ANSYS FLUENT. The model consists of two equations as it in the ANSYS FLUENT [29]

$$\frac{\partial \rho k}{\partial t}+\frac{\partial \rho k u_i}{\partial x_i}=\frac{\partial}{\partial x_j}\left[a_k \mu_{eff}\frac{\partial k}{\partial x_j}\right]+G_k+G_b-\rho\varepsilon-Y_M+S_k \tag{3.21}$$

$$\frac{\partial \rho \varepsilon}{\partial t}+\frac{\partial \rho \varepsilon u_i}{\partial x_i}=\frac{\partial}{\partial x_j}\left[a_\varepsilon \mu_{eff}\frac{\partial \varepsilon}{\partial x_j}\right]+C_{1\varepsilon}\frac{\varepsilon}{k}(G_k+C_{3\varepsilon}G_b)-C_{2\varepsilon}\rho\frac{\varepsilon^2}{k}-R_\varepsilon+S_\varepsilon \tag{3.22}$$

In Equation 3.21 and 3.22, S_k and S_ε are user-defined source terms, $C_{1\varepsilon}$, $C_{2\varepsilon}$ and $C_{3\varepsilon}$ are constants, G_k is turbulence kinetic energy generated by the mean velocity gradients

$$G_k=-\rho\overline{u_i'u_j'}\frac{\partial u_j}{\partial x_i} \tag{3.23}$$

G_b is turbulent kinetic energy generated by buoyancy and

$$G_b=\beta g_i\frac{\mu_t}{\mathrm{Pr}_t}\frac{\partial T}{\partial x_i} \tag{3.24}$$

Y_M is dilatation dissipation term

$$Y_M=2\rho\varepsilon M_t^2=2\rho\varepsilon\frac{k}{c^2} \tag{3.25}$$

The $k-\varepsilon$ RNG turbulence model includes the effects of the swirling flow and analytical formulations of the turbulent Prandtl number. The improvements helped the $k-\varepsilon$ RNG turbulence model to be more applicable and accurate for a wider range of flows.

The $k-\omega$ Shear Stress Transport (SST) Turbulence Model

The second turbulence model used for unsteady solution in this thesis is the $k-\omega$ SST turbulence model. The turbulence model adopted in ANSYS FLUENT as similar to the one presented in reference [99]. The $k-\omega$ SST turbulence model was developed by Menter [103] to create a robust and accurate formulation for the $k-\omega$ model in the near-wall region with the free-steam independence. The $k-\omega$ SST model is a production of blending of the $k-\varepsilon$ standard model and the $k-\omega$ standard model as shown

$$\frac{\partial \rho k}{\partial t}+\frac{\partial \rho k \bar{u}_j}{\partial x_j}=\frac{\partial}{\partial x_j}\left(\left[\mu+\frac{\mu_t}{\sigma_{k2}}\right]\frac{\partial k}{\partial x_j}\right)+P_k-\beta'\rho k\omega \tag{3.26}$$

$$\begin{aligned}\frac{\partial \rho \omega}{\partial t}+\frac{\partial \rho \bar{u}_j \omega}{\partial x_j}&=\frac{\partial}{\partial x_j}\left(\left[\mu+\frac{\mu_t}{\sigma_{\omega 2}}\right]\frac{\partial \omega}{\partial x_j}\right)+2\rho\frac{1}{\sigma_{\omega 2}}\frac{\partial k}{\partial x_j}\frac{\partial \omega}{\partial x_j}\\&+\alpha_2\frac{\omega}{k}P_k-\beta_2\rho\omega^2\end{aligned} \tag{3.27}$$

The $k-\omega$ equations are multiplied by a function F_i, and the transformed $k-\varepsilon$ equation some manipulations the SST is obtained as shown

$$\frac{\partial \rho \tilde{\nu}_t}{\partial t}+\frac{\partial \rho \bar{u}_j \tilde{\nu}_t}{\partial x_j}=\frac{\partial}{\partial x_j}\left(\left[\mu+\frac{\rho\tilde{\nu}_t}{\sigma}\right]\frac{\partial \tilde{\nu}}{\partial x_j}\right)+c_1\rho\tilde{\nu}_t S-c_2\rho\left(\frac{\tilde{\nu}_t}{L_{vK}}\right)^2 \tag{3.28}$$

Where $\tilde{\nu}$ is the kinetic eddy viscosity, $\tilde{\nu}_t$ is the turbulent kinematic eddy viscosity, c_1, c_2 and σ are model constant. More details of the $k-\omega$ SST can also be found in reference [29].

3.3 Governing Equations for Acoustic Predictions

The second step of the computational simulation used in this thesis is to predict the noise generation. In this section, the available acoustic models are presented. Firstly, the FW-H acoustic model is introduced and discussed. This model provides the noise signal from the computed unsteady CFD solution and the body kinetics. Secondly, the noise source models due to the turbulence is called broadband noise sources (BNS) models are presented. The BNS models provide the predicted source locations.

3.3.1 Ffowcs -William & Hawking (FW-H) Model

To calculate the sound pressure spectrum generated from sources, the FW-H acoustic analogy is applied. ANSYS FLUENT software adopted the FW-H model in the form of equation that developed by Farassat *et al.* [24-28] as shown as similar to reference [45]

$$\frac{1}{c_0^2}\frac{\partial^2 p'}{\partial t^2}-\frac{\partial^2 p'}{\partial x_i^2}=\frac{\partial^2}{\partial x_i \partial x_j}\left\{T_{ij}H(f)\right\}-\frac{\partial}{\partial x_i}\left\{[P_{ij}n_j+\rho u_i(u_n-v_n)]\delta(f)\right\} + \frac{\partial}{\partial t}\left\{[\rho_0 v_n+\rho(u_n-v_n)]\delta(f)\right\} \tag{3.29}$$

Where ρ is density, u_n is fluid velocity normal to surface, υ_n is the normal velocity of the surface, $\delta(f)$ is Dirac delta function, *H (f)* is the Heaviside function.

Equation 3.29 can be expressed as the acoustic pressure fluctuation in time and space (left term in the equation) is computed by a summation of three main sources as quardupole, dipole and monopole sources (right term in the equation) respectively. Equation 3.29 is obtained by (i) multiplying the Heaviside function to compressible Navier-Stoke equations (equations 3.1 and 3.2); (ii) applying the time derivative to the mass equation and the divergence to the momentum equation and (iii) subtracting the resulting of the

mass and the momentum equations together to form an inhomogeneous wave equation is obtained as shown in equation 3.29.

The general solution of the FW-H equation is obtained by using the free space Green's function ($G(\vec{x},\vec{y};t,\tau)$, which is a wave solution that is generated by an impulsive point source, $\delta(\vec{x}-\vec{y})\delta(t-\tau)$, located at the point $\vec{x}=\vec{y}$ at the time $t=\tau$ in an unbounded space at rest. The Green's function can be written as

$$\left(\frac{1}{c^2}\frac{\partial^2}{\partial t^2}-\frac{\partial^2}{\partial x_i \partial x_j}\right)G(\vec{x},\vec{y};t,\tau)=\delta(\vec{x}-\vec{y})\delta(t-\tau) \tag{3.30}$$

The solution of the Green's function is

$$G(\vec{x},\vec{y};t,\tau)=\frac{1}{4\pi r}\delta(t-\tau-\frac{r}{c}) \tag{3.31}$$

Where $r=|\vec{x}-\vec{y}|$, and $-\infty<\tau<t$ if $\tau>t$ then $G(\vec{x},\vec{y};t,\tau)=0$. Apply equation 3.31 to equation 3. 29 obtained

$$\begin{aligned}4\pi p' &= \frac{\partial^2}{\partial x_i \partial x_j}\iint_{f>0}\frac{\delta(t-\tau-\frac{r}{c})}{r}T_{ij}dVd\tau-\frac{\partial}{\partial x_i}\iint_{f=0}\frac{\delta(t-\tau-\frac{r}{c})}{r}L_i dSd\tau \\ &+\iint_{f=0}\frac{\delta(t-\tau-\frac{r}{c})}{r}QdSd\tau\end{aligned} \tag{3.32}$$

Where Q and L_i are surface sources distribution of mass and linear momentum respectively.

$$Q=\rho_0 U_i\hat{n}_i\,;U_i=(1-\frac{\rho}{\rho_0})v_i+\frac{\rho u_i}{\rho_0}\,;L_i=P_{ij}n_j+\rho u_i(u_n-v_n)\,;\ P_{ij}=(p-p_0)\delta_{ij}-\tau_{ij}$$

Equation 3.32 can be written as

$$4\pi p' = \frac{\partial^2}{\partial x_i \partial x_j}\int_{f>0}\left[\frac{T_{ij}}{r(1-M_r)}\right]_{ret} dV - \frac{\partial}{\partial x_i}\int_{f=0}\left[\frac{L_i}{r(1-M_r)}\right]_{ret} dS + \frac{\partial}{\partial t}\int_{f=0}\left[\frac{Q}{r(1-M_r)}\right]_{ret} dS \tag{3.33}$$

Equation 3.33 presents the solution to compute the acoustic pressure in the far-field from three dominant sources in the aero-acoustic fields. Farassat [24] rewrote the FW-H solution equation in a form of

$$p'(x,t) = p'_m(x,t) + p'_d(x,t) + p'_q(x,t) \tag{3.34}$$

Where

$$p'_m(x,t) = \frac{\partial Q}{\partial t} = \frac{\partial}{\partial t}\left\{\left[\rho u_n - (\rho - \rho_o)\upsilon_n\right]\delta(f)\right\} \tag{3.35}$$

$$p'_d(x,t) = -\frac{\partial F_i}{\partial x_i} = -\frac{\partial}{\partial x_i}\left\{\left[\rho\left(u_n - \upsilon_n\right)u_i + (P - P_o)n_i\right]\delta(f)\right\} \tag{3.36}$$

$$p'_q(x,t) = \frac{\partial^2 T_{ij}}{\partial x_i \partial x_j} = \frac{\partial^2}{\partial x_i \partial x_j}\left[\left(\rho u_i u_j + P_{ij} - c^2(\rho - \rho_0)\delta_{ij}\right)H(f)\right] \tag{3.37}$$

In ANSYS FLUENT, the volute integrals for quadrupole source presented in equation 3.37 is dropped. Therefore, only two sources are considered as monopole and dipole sources. For the solid and impenetrable surface, the term $\left(u_n - \upsilon_n\right) \equiv 0$, equations 3.35 and 3.36 can be written as

$$p'_m(x,t) = \frac{\partial}{\partial t}\left[\rho u_n \delta(f)\right] \tag{3.38}$$

$$p'_d(x,t) = -\frac{\partial}{\partial x_i}\left\{\left[(P - P_o)n_i\right]\delta(f)\right\} \tag{3.39}$$

The general expression for the retarded-time (τ) equation is obtained by considering the generic equation for retarded-time solution as below as similar to references [11, 12, 104]

$$4\pi p(x,t) = \int_S \left[\frac{Q(y,\tau)}{r\left|1-M_r\right|} \right]_{ret} dS \tag{3.40}$$

Where $Q(y,\tau)$ is source strength, which is a function of source position (y) and source time (τ), $\left|1-M_r\right|$ is known as Doppler Effect and r is distance between the source position (y) and the observer position (x). The common numerical evaluation method is to approximate the integral as follows

$$4\pi p(x,t) \approx \sum_{i=1}^{N} \left[\frac{Q(y_i,\tau)}{r_i\left|1-M_r\right|_i} \right]_{ret} \Delta S_i \tag{3.41}$$

Where $i = 1:N$ is number of area ΔS_i. The final expression of the FW-H solution using the retarded time solution is presented in Equation 3.42.

$$p(\vec{x},t) - p_0 \cong \frac{1}{4\pi} \sum_{i=1}^{N} \left[\frac{\dot{p}\delta_{ij}}{cr} + \frac{p\delta_{ij}}{r^2} \right]_{ret} \Delta S_i \tag{3.42}$$

Full details of the FW-H algorithm development can also be found in these references [11, 12, 105]. The coupling approach has been implemented in the ANSYS FLUENT software and is used to predict noise generation.

3.3.2 Broadband Noise Source (BNS) Model

To calculate the broadband noise, the broadband noise models are used. ANSYS FLUENT software adopted two broadband noise models, namely Proudman's model and boundary layer source model.

Quadrupole Source Model

The first noise model used to predict the broadband noise is called the Proundman's broadband model [18]. In this model, Proudman rewrote the Lighthill's acoustic analogy

into a new form which is the local sound power contribution per unit volume due to the isotropic turbulence (quadrupole sound sources) is computed as follows

$$W_Q = \alpha_\varepsilon \rho_0 \varepsilon \left(\frac{\sqrt{2k}}{c} \right)^5 \tag{3.43}$$

$$L_w = 10 \log_{10} \left(\frac{W_Q}{W_{ref}} \right) \tag{3.44}$$

Where W_Q is acoustic power (W/m^3) computed from quadrupole sources, $\alpha_\varepsilon = 0.1$ is the numerical constant, c =340 m/s is speed of sound, ρ_0 is air density, L_w is local sound power level dB and $W_{ref} = 10^{12}$ (W/m^3) is noise power reference.

In term of *k* and ε using the following equations

$$u^2 = \frac{2k}{3} \tag{3.45}$$

$$\varepsilon = \frac{1.5u^3}{l} \tag{3.46}$$

Where *u* is turbulence velocity, *k* is kinetic energy and *l* is turbulence length scale.

Dipole Source Model

The boundary layer noise source model was developed based on Curle's equation [19] . In this model, the noise sources generated by turbulent flow over a solid body is taken into account and the noise generation level is computed based on the surface noise power and the intensity in the far-field is estimated by equation 3.41. The solution of Curle's equations is written as

$$p'(\vec{x},t) = \frac{1}{4\pi c} \int_S \frac{(x_i - y_i) n_i}{r^2} \frac{\partial p}{\partial t} (\vec{y}, \tau) dS(\vec{y}) \tag{3.47}$$

Where τ denotes the emission time ($\tau = t - r/c$), *S* is the integration surface and *p* is the hydrodynamic pressure at wall surface, p' is acoustic pressure, x_i is receiver location, y_i is source location, c is speed of sound. The subscripts *i (=1, 2, 3)* describe the coordinate (*x*,*y*,*z)* direction.

Equation 3.38 is extracted from a general solution of the Curle's model [19], where only the dipole source contribution is considered. Based on the acoustic pressure solution, the sound intensity in the far-field can be approximated as

$$\overline{p'^2} \approx \frac{1}{16\pi^2 c^2} \int_S \frac{\cos^2\theta}{r^2} \overline{\left[\frac{\partial p}{\partial t}(\vec{y},\tau)\right]^2} A_c(\vec{y}) dS(\vec{y}) \tag{3.48}$$

Where A_c is the correlation area, $r \equiv |\vec{x} - \vec{y}|$ is distance between the source to the observer, θ is the angle between $|\vec{x} - \vec{y}|$ and the wall-normal direction $\vec{n}$.

The total acoustic power emitted from the entire body surface can be computed from

$$W_S = \frac{1}{\rho c} \int_0^{2\pi} \int_0^{\pi} \overline{p'^2} r^2 \sin\theta d\theta d\psi = \int_S I(\vec{y}) dS(\vec{y}) \tag{3.49}$$

Where

$$I(\vec{y}) \equiv \frac{A_c(\vec{y})}{12\rho\pi c^3 \overline{\left[\frac{\partial p}{\partial t}\right]^2}} \tag{3.50}$$

This can be interpreted as the local contribution per unit surface of the body surface to the total acoustic power. The mean-square time derivative of the surface pressure and the correlation area are further approximated in terms of turbulent quantities like turbulent kinetic energy, dissipation rate and wall shear. The local sound power level generated by dipole power is computed by equation

$$L_w = 10\log_{10}\left(\frac{W_S}{W_{ref}}\right) \text{ (dB)} \tag{3.51}$$

3.4 Governing Equation for Fluid-Solid Interaction (FSI)

In the third steps of the computational simulation is to predict the structural vibration of the solid model under the influence of flow turbulence. The combination between the finite element analysis (FEA) and the CFD is solved through a coupling method. In general, the FEA is governed by equation of motion as shown

$$[M]\{\ddot{u}\}+[B]\{\dot{u}\}+[K]\{u\}=\{F\} \tag{3.52}$$

Where $[M],[B]$and $[K]$ are matrix of mass, damping, stiffness elements respectively. F is external excitation forces and u is displacement. For the elasticity, equations 3.52 is written in dynamic elastic form [84]

$$\rho_s \frac{\partial^2 u_i}{\partial t^2} + B_s \frac{\partial u_i}{\partial t} - \frac{\partial \sigma_{ij}}{\partial x_j} = F_i \tag{3.53}$$

For un-damped condition, equation 3.53 is written as

$$\rho_s \frac{\partial^2 u_i}{\partial t^2} - \frac{\partial \sigma_{ij}}{\partial x_j} = F_i \tag{3.54}$$

Where

$$\sigma ij = D_{ijkl}\varepsilon_{kl} \tag{3.55}$$

and

$$\varepsilon_{ij} = \frac{1}{2}\left(\frac{\partial u_i}{\partial x_j} + \frac{\partial u_j}{\partial x_i}\right) \tag{3.56}$$

In equations 3.53 to 3.56, u_i is displacement vector, D_{ij} is elastic tensor, ε_{ij} is strain tensor and F is body force vector. Equation 3.53 combines with the continuity and momentum equations in fluid domain to become governing equations for FSI methods.

3.4.1 Coupling between the solid equation and the fluid equations

In order to solve the FSI problems, coupling approaches are needed through the coupling boundary conditions, which are given as:

At the displacement boundary

$$u_i = \bar{u}_i \tag{3.57}$$

And at the force boundary

$$\sum_j \sigma_{ij} n_i = p n_i \tag{3.58}$$

Where n_i is surface normal vector, p is pressure obtained from fluid dynamics domain.

3.5 ANSYS Implementation

As this project used the ANSYS software packages, a brief discussion of the implementation of these equations in this software. Complete details implementation can be found in ANSYS theory manual [29].

In ANSYS, the Navier-Stokes (N-S) equations shown previously in this chapter are discretised with a finite volume method (FVM) in several available CFD codes such as CFX and FLUENT. In this method, the domain is discretised into a finite set of control volumes and the N-S equations are solved on this set of the control volumes. The partial differential equations are discretized into a system of algebraic equation and then solved numerically to render the solution field.

The ANSYS FLUENT software provides comprehensive modelling capabilities for a wide range of flow analysis such as 2-D and 3-D simulations; incompressible and compressible; and laminar and turbulent flows. The steady and transient simulation can also be performed. The ANSYS FLUENT software also adopted several acoustic models and offers three different approaches to compute the aerodynamically generated noise; a direct method, an integral method based on acoustic analogy and noise source models that can be utilised to predict the source locations.

Furthermore, ANSYS provides some structural simulation through its mechanical application codes such as mechanical APDL and Applications. In those mechanical applications, the dynamics structural equations is showed by finite element analysis (FEA). In this method, the elastic-plastic analysis is performed by one of the two methods using the incremental approximation.

Chapter 4: **Experimental Investigations**

4.1 Introduction

Before conducting the numerical simulations proposed in Chapter 1, it is necessary to obtain an overview of how the CPAP device generates noise and vibration during its operation. This will be done by experimental investigations. This chapter serves as a preliminary study with several objectives: (i) to obtain an overview of noise and vibration radiated from the CPAP device; (ii) to obtain boundary conditions for numerical simulations; and (iii) to validate theoretical models developed in subsequent chapters.

A series of experimental investigations on the noise and vibration characteristics of the CPAP device are conducted during the course of these investigations and are presented in this chapter. The primary focus of the experimental investigations is to independently look at how the influence of flow parameters and designed geometries on the generated noise and vibration characteristics.

The chapter consists of several sections. Section 4.2 gives an overview of designing and developing the test facility used in the experimental studies. Section 4.3 presents test equipment which includes a selection of the CPAP device, sound and vibration measurement systems. Section 4.4 discusses test procedures which includes background noise and repeatability tests, flow, noise and vibration measurements respectively. The experimental results are presented in section 4.5 with some discussions. Section 4.6

presents some investigations into noise path elements, where some case studies were developed to investigate the influence of primary elements on the overall noise level.

4.2 Test Facilities

The design for the CPAP measurement facility was setup at Fisher & Paykel Healthcare Ltd and was developed according to the ISO 3744 standard. This ISO standard is known as a free-field method over a reflecting plane and has been used for many engineering testing purposes.

Figure 4.1 shows a layout of the ISO standard used for sound measurement for the CPAP device. In this Figure, the locations of ten microphones are listed in the inserted table (4.1 a). The *x*, *y* and z are directional coordinates and *r* is a radius of a hemispherical surface. The reference box is located at the centre coordinate and is used to place tested devices. The noise pressure level (SPL) is averaged from noise pressure measured at ten microphones and calculated in the following the equation [1]:

$$\bar{L}_p = 10\log_{10}\left[\sum_j 10^{0.1(L_{pj}+A)}\right] \tag{4.1}$$

The (A) sign presents to the A-weighted scale in noise measurement techniques. The average SPL is used to calculate the noise power level (PWL)

$$L_w = \bar{L}_p + 10\log_{10}\left(\frac{S}{S_{ref}}\right) \tag{4.2}$$

Where $S = 2\pi r^2$ and S_{ref} (= 1 m^2) are the measured surface area and reference surface area respectively, *r* is radius of the spherical surface. The hemispherical surface with one meter radius in this setting will give the last term in equation 4.2 the value of 8 decibel (dB) approximately or the difference between PWL and SPL equal to 8 dB.

Microphone position	$\frac{x}{r}$	$\frac{y}{r}$	$\frac{z}{r}$
1	0,16	– 0,96	0,22
2	0,78	– 0,60	0,20
3	0,78	0,55	0,31
4	0,16	0,90	0,41
5	– 0,83	0,32	0,45
6	– 0,83	– 0,40	0,38
7	– 0,26	– 0,65	0,71
8	0,74	– 0,07	0,67
9	– 0,26	0,50	0,83
10	0,10	– 0,10	0,99

a: Coordinates of microphone positions for Sources emitting discrete tones

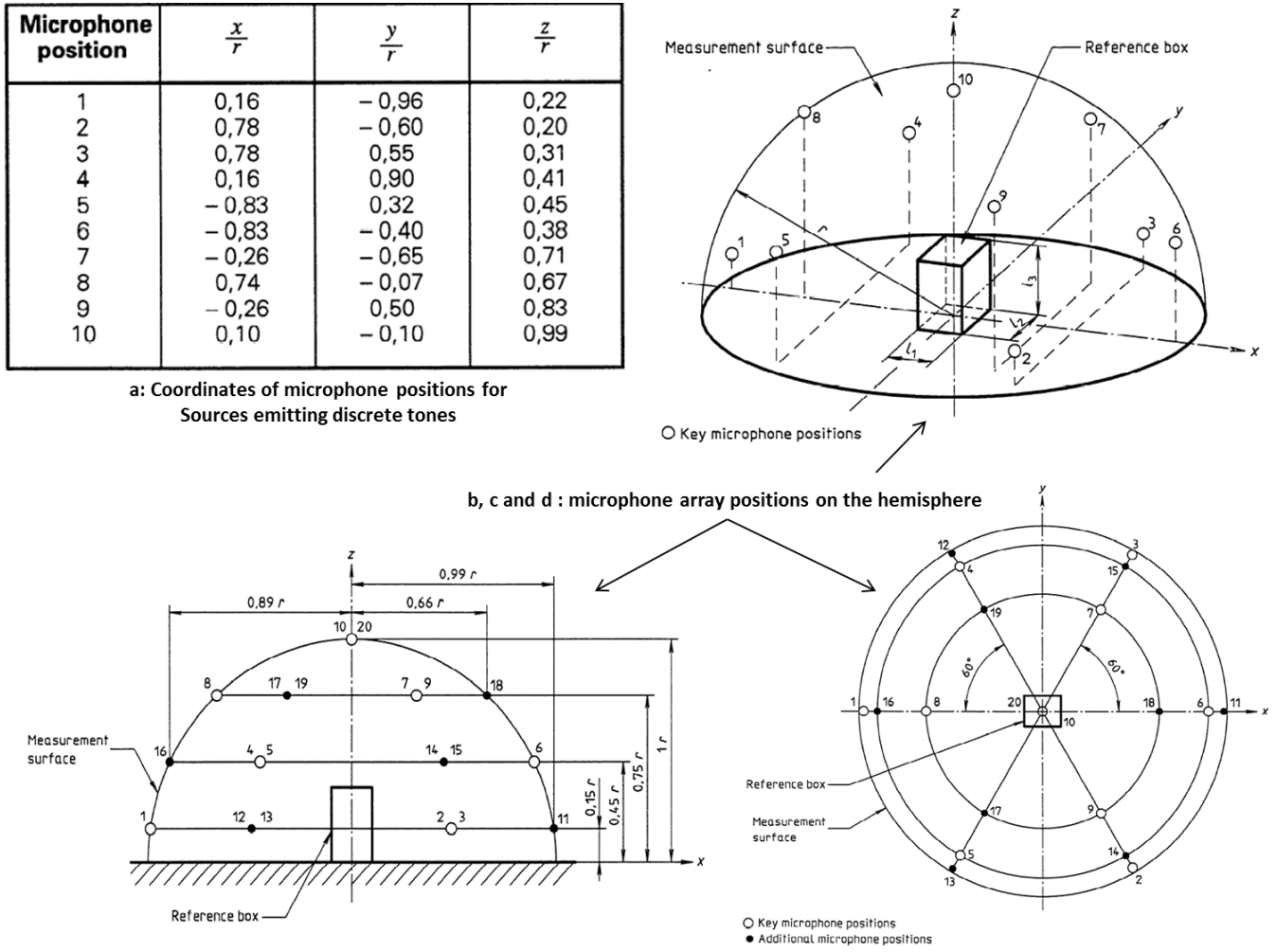

Figure 4.1: Layout of ISO 3744 standard adopted from reference [1]

Figure 4.2 shows a picture of an actual noise test room in accordance with ISO 3744 standard. The hemi-anechoic test room was designed and built in order to measure the aerodynamic performances, noise and vibration measurements. Ten microphones were placed in a custom built test rig and located on a reflecting surface. Microphones were connected to the sound measurement analysers which were placed outside the test room in the control desk, through a hub.

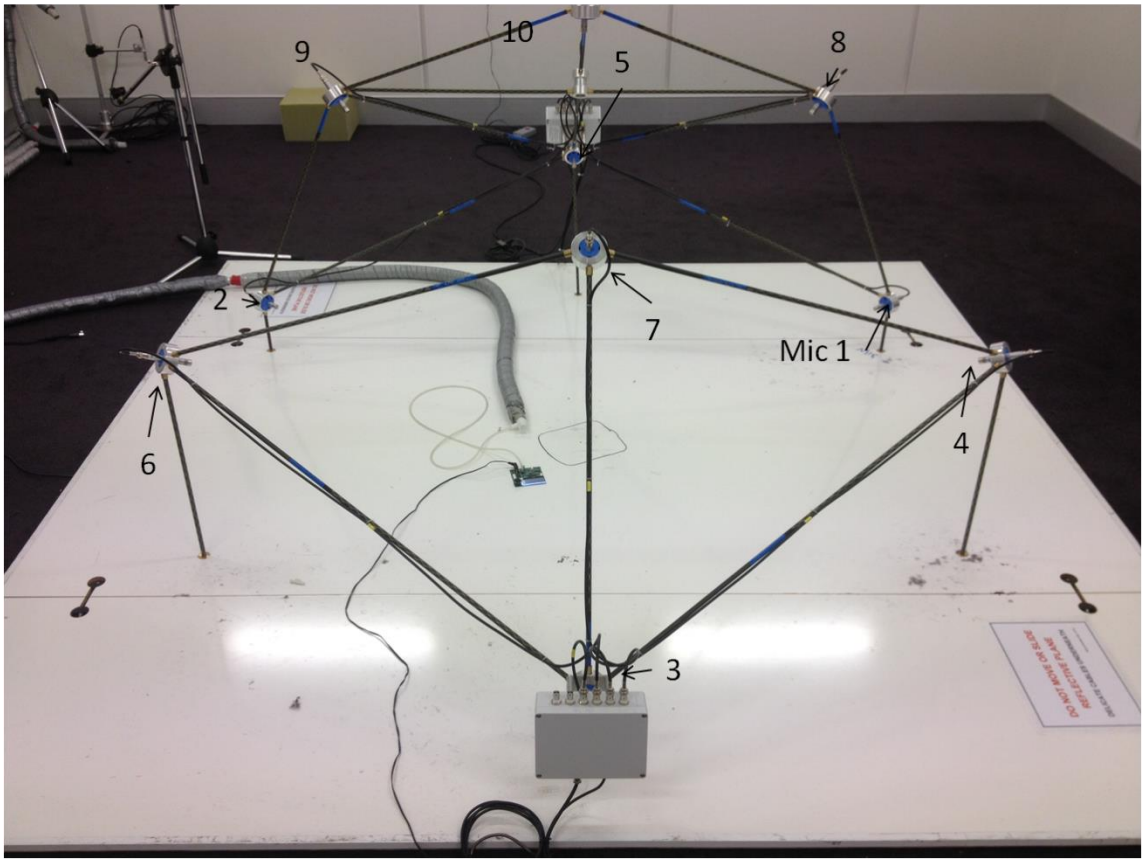

Figure 4.2: An apparatus test room

4.3 Test Equipment

4.3.1 CPAP device

At the beginning of this research project, the CPAP "ICON" devices (Figure 4.3) supplied by Fisher & Paykel Healthcare Ltd was selected for this research project. This product has already been sold in the market. The CPAP devices were designed to work under

different rotational speed and flow rate conditions. However, specific rotational speed of 14580 rpm and 50 L/min flow rate were selected for noise and vibration analysis. This condition was suggested by the manufacturer as an optimal operation speed in product specifications. Therefore, only experimental data obtained from this setting condition would be used for further analysis, other than that would only be used as references.

Figure 4.3: A CPAP "ICON" model adopted from reference [106]

4.3.2 Instrumentations

A Bruel & Kjaer (B&K) measurement system was designed for the experiment. This consists of B&K 1/2 inch free-field microphones model 4189 type. This type of microphone has a flat frequency response from 6.3 Hz to 20 kHz with a sensitivity of 50 (mV/Pa). A delta transonic B&K accelerometer type 4508 BV 002 is used for vibration measurements. These sensors were connected to a B&K real time frequency analyser.

In addition, a laser vibrometer 100 Polytec model was also used for measuring surface vibration during the CPAP operations. The measurement system used a PSV 100 manufactured by Polytec which allowed recording of the time dependent sample and presented the results in a frequency domain for further analysis.

4.3.3 Measurement Setups

The CPAP device was placed in the hemi-anechoic test room and connected to the insulated ducts which consist of pressure sensors, flow meters and a control valve. The control valve made it possible to vary the flow rate by changing the diameter of the control valve at the end of the ducts. Pressure sensors and a flow meter were placed in several locations in the insulated duct which was connected to the test object. Pressure sensors were used to obtain the pressure. A flow meter was used to record flow rate. A flow straightener was used to reduce the flow effects caused by complicated test objects that could affect the measurements. Also a silence box was added to the duct to ensure that the rebounded noise would be dampened before reaching back to the noise room. Figure 4.4 shows a schematic of the measurement setup.

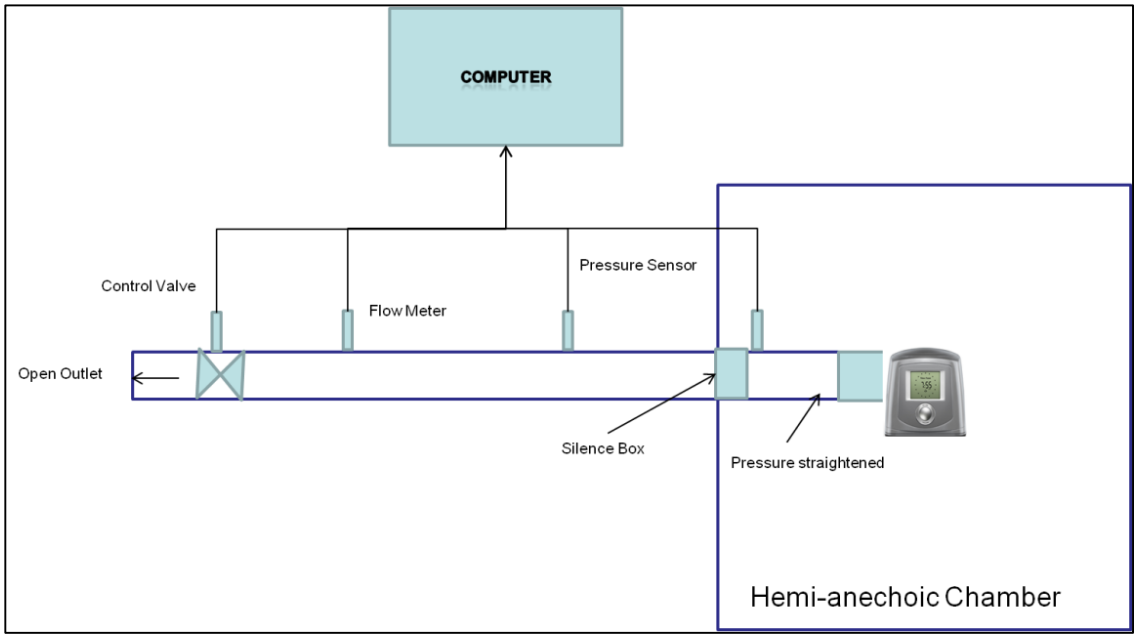

Figure 4.4: Schematic of the experimental setups

Figure 4.5 shows the actual experimental setup inside the anechoic chamber during experiments. It shows a testing object, i.e., a studied CPAP device, which is placed in the middle of the rig, faces the microphone marked number one. The CPAP device connects

to the insulated hose as the hose also connected to the wall at the other ends. Once the setups are completed, the measurements are started as described below.

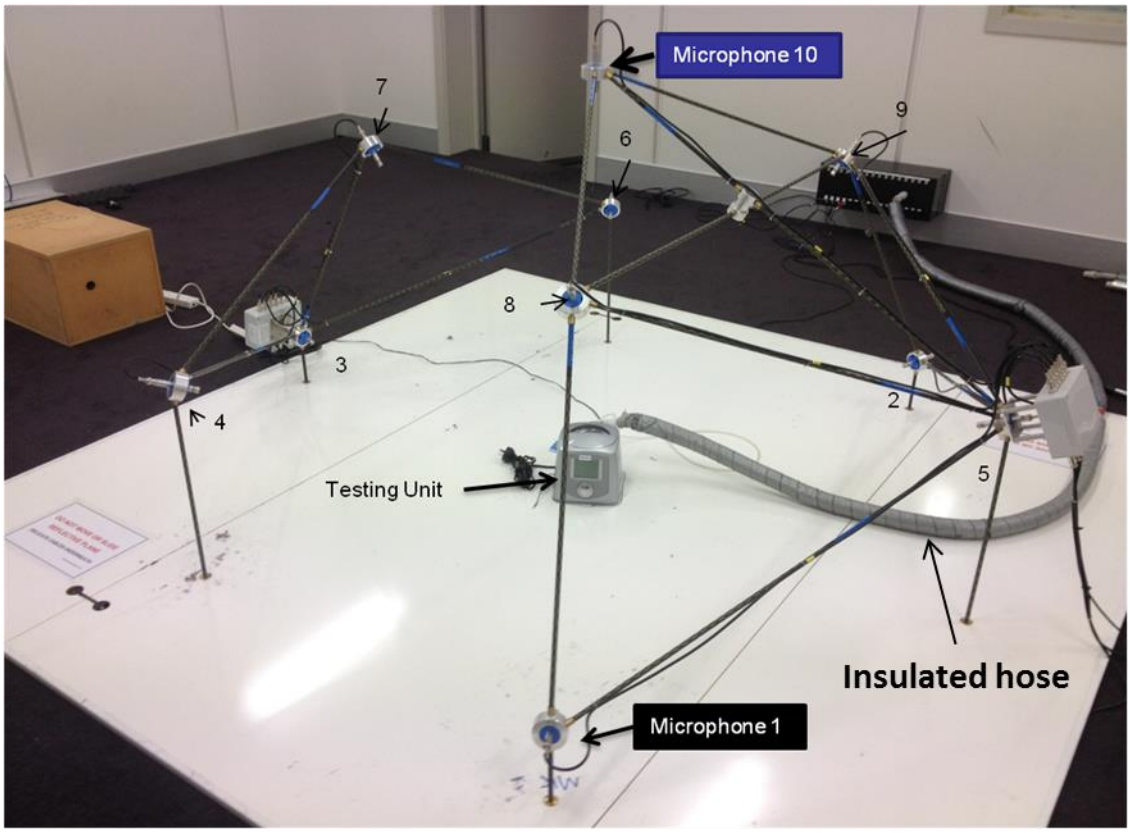

Figure 4.5: CPAP acoustics measurement settings

4.4 Test Procedures

4.4.1 Flow Tests

Despite the objectives in this chapter to investigate the noise generation and vibration characteristics of the studied CPAP devices, the experimental tests began with the assessments of fluid flow performance of the CPAP device and its elements, i.e., centrifugal fan, inlet and outlet ducts and humidifier unit. The purpose of the aerodynamic measurements can be seen as an introduction into the working conditions of the CPAP device and also it is to ensure that all the tested CPAP devices produce a similar flow performance during the experiments. Data obtained from the flow tests can also be used as the boundary conditions of the simulation process. Observations and visualisations to

the ways that the CPAP device could generate noise and vibration under working conditions would give a starting point of relationship between the aerodynamic and noise generation.

The setting of the tests for the CPAP device can be found as similar to the one showed in Figure 4.5. The CPAP device was connected to an insulated hose, which consists of flow meter, pressure sensor and a control valve as described earlier. The CPAP device was set to run at 14580 rpm speed as it was recommended by the manufacturer. When the speed reached the optimum and maintained constant, the control valve started to rotate creating blockage scenarios from free flow (totally open) to totally block or stagnation to vary the flow rates and pressure rise. During the time of the valve turning, pressure and flow rate variations were simultaneously recorded and stored by custom built software.

The flow tests were conducted with ten CPAP devices. The pressure and flow relationships were plotted to obtain the flow performance chart. Similar flow test setups and procedures were conducted for individual components such as a centrifugal fan, inlet and outlet ducts and a humidifier in the CPAP device.

4.4.2 Background Noise

Once the flow measurement is complete. The next step is to determine the background noise level of the test room. The background noise of the hemi-anechoic chamber always needs to be measured before conducting any sound measurements. This is a very important measurement step procedure to ensure that the background noise is below 20 dB (A) as an ISO standard 3744 requirement. The background noise tests were conducted at different times, i.e., during the normal working time and during the weekend. It was found that background noise varied from time to time for each measurement. However, the average background noise level was maintained at approximately 20 dB (A) during week days and about 17 dB (A) at the weekend. Therefore, it was concluded that the

background noise level will not affect the overall calculation of the SPL radiated from the CPAP device.

Figure 4.6 presents a typical background noise measured in the noise room. From this figure, the background noise has high value at a low frequency below 200 Hz. This noise is possibly due to the fan of the building ventilation system located on the roof of the building as it could be heard during the time of measurements.

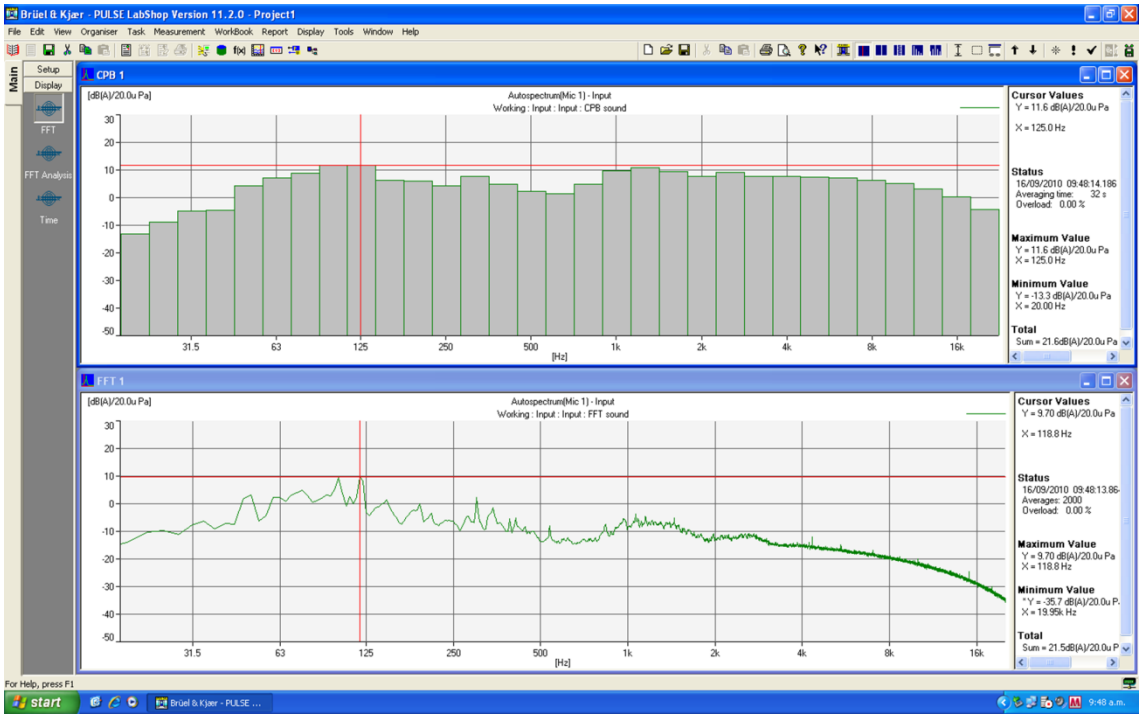

Figure 4.6: Background Noise spectrum of the Testing Room

4.4.3 Repeatability Test

As a common practice, the repeatability test is needed to ensure that all the measurement equipment could produce similar results under the same test conditions for a period of time. To calculate the repeatability of the measurement technique in this facility environment, a simple noise test was setup using a CPAP device.

A total of ten noise measurements were performed at different times over several days of the experimental periods. Between each noise measurement, the device was kept intact

and moved away and placed back in the reference box position. Also, the noise measurements were conducted at different working hours to avoid the noisiest time such as the beginning, morning break, lunch and afternoon break, etc. The SPL results were analysed statistically using a standard deviation method.

Figure 4.7 shows the standard deviation results for one-third octave bands from 50 Hz to 10 kHz. It shows the SPL generated from the CPAP device has a standard deviation of less than 2 of a decibel for the entire one-third octave bands. From the Figure, it shows that, for successive measurements of the SPL of the CPAP device, the noise generated from the CPAP device is not steady for frequencies above 500 Hz. A large variation was observed from this Figure.

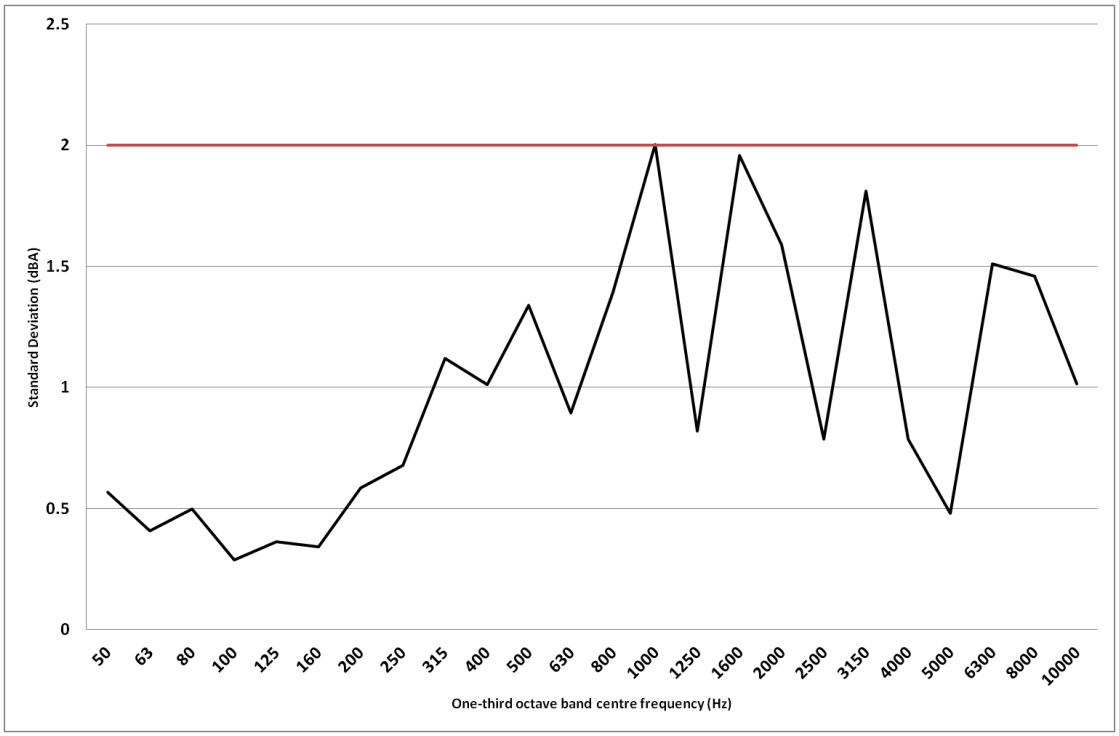

Figure 4.7: Standard deviation in measured SPL for steady CPAP noise sources

Based on the standard derivation results, it is concluded that this is the limit of accuracy of the measurement technique under current settings and environment conditions. The variation might be due to a combination of uncertainty such as equipment accuracy,

human errors, background noise variations and actual noise pressure variation of the CPAP device, etc.

4.4.4 Sound Measurements

The second test was to measure the overall noise level radiated from the CPAP device. This can be achieved by measuring the sound pressure level (SPL) in the far-field. In this test, the CPAP device was placed in the measured locations inside an anechoic chamber similar to the one shown in Figure 4.5. The CPAP device was set to operate at a constant speed of 14580 rpm, constant flow rate at 50 litres per minute (L/min) and a constant of 10 cm of water pressure. Once these conditions were reached, noise pressure signals were recorded and averaged using microphones for sixteen seconds. The sound pressure signals were transformed to the frequency resolution using the noise analysers and the overall sound pressure level (SPL) was calculated in the one-third octave band frequency.

A total of ten CPAP devices were used to measure the SPL. Furthermore, several case studies were developed to investigate the contribution of individual components on the overall noise radiated from the CPAP device. The case study is presented and discussed in section 4.6.

4.4.5 Vibration Measurements

The third test was to investigate the overall vibration characteristics of the CPAP device. In this test, vibration measurements were conducted on several surfaces of the CPAP device. The CPAP device was placed inside the test facility at a similar setting to the sound measurement. The laser vibro-meter was placed 0.5 meters away from the tested CPAP device. The CPAP was setup to run at a constant speed of 14580 rpm to generate 10 cm of water pressure and 50 L/min of flow rate. When these conditions were reached, a laser vibro-meter that was connected to the control computer was used to measure the

vibration at different selected points from the front to the back, left to right sides as well as the top of the CPAP device. At each side of the CPAP device, three measured points were marked in the middle locations from the top to the bottom. At each marked point, the vibration was measured by a laser vibro-meter through its laser beam. The vibration data was recorded and transformed into a frequency domain for analysis. A total of 15 measurements were conducted. Figure 4.8 shows a sketch of this vibration measurement.

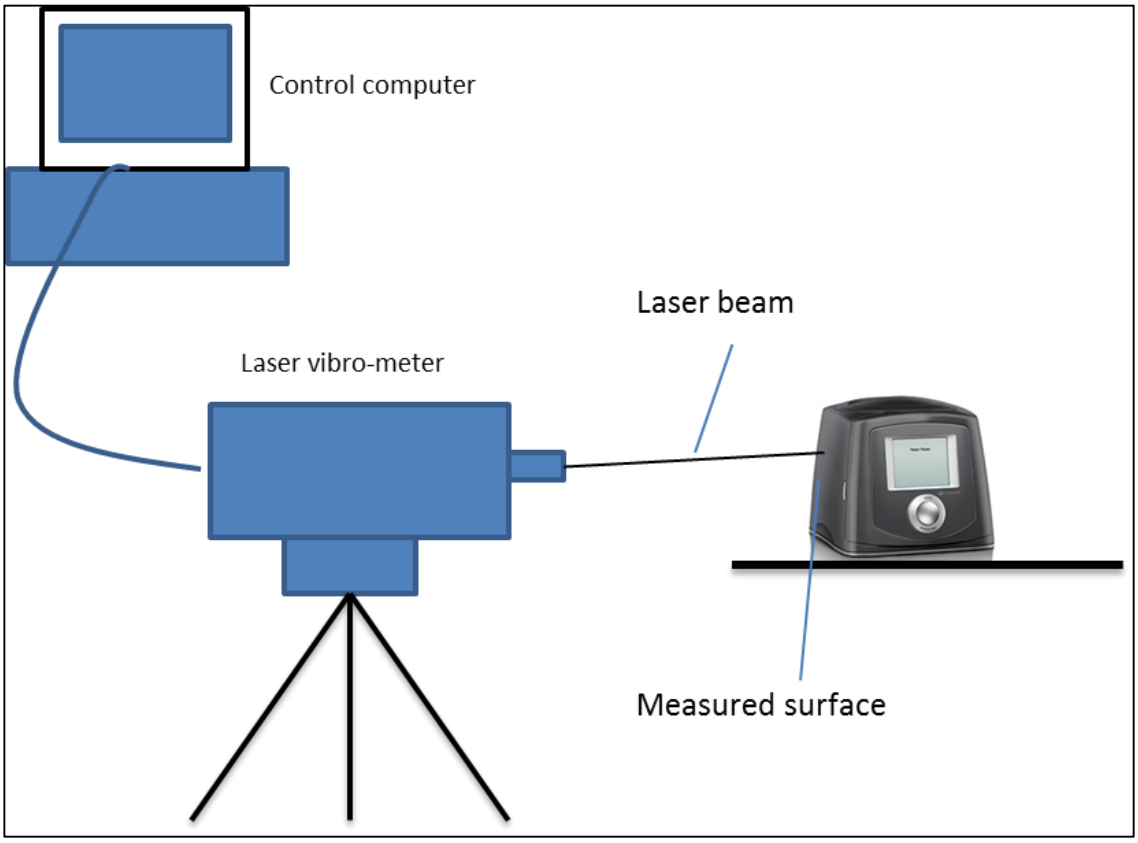

Figure 4.8: Sketch of Experimental Setup for Vibration Measurement

4.5 Experimental Results

4.5.1 Flow Analysis

Figure 4.9 shows the static pressure and flow rate performance curves of the CPAP device for the rotational speed of 14580 rpm. During the flow test, ten CPAP devices were measured and repeated several times. By comparing to each other, the results were found to be consistent and identical. Therefore only one is shown here. From this Figure, it is

found that the maximum flow rates are located around 160 (L/min). In addition, the maximum static pressure decreases as the flow rate increases. The lowest pressure difference is observed at a maximum flow or free flow condition. As the valve moves to create flow restrictions, pressure starts rising up. The maximum pressure rise is obtained between 30 to 40 L/min flow rates. From that point toward the zero flow, pressure rise tried to maintain its values as the flat curve could be seen in this Figure.

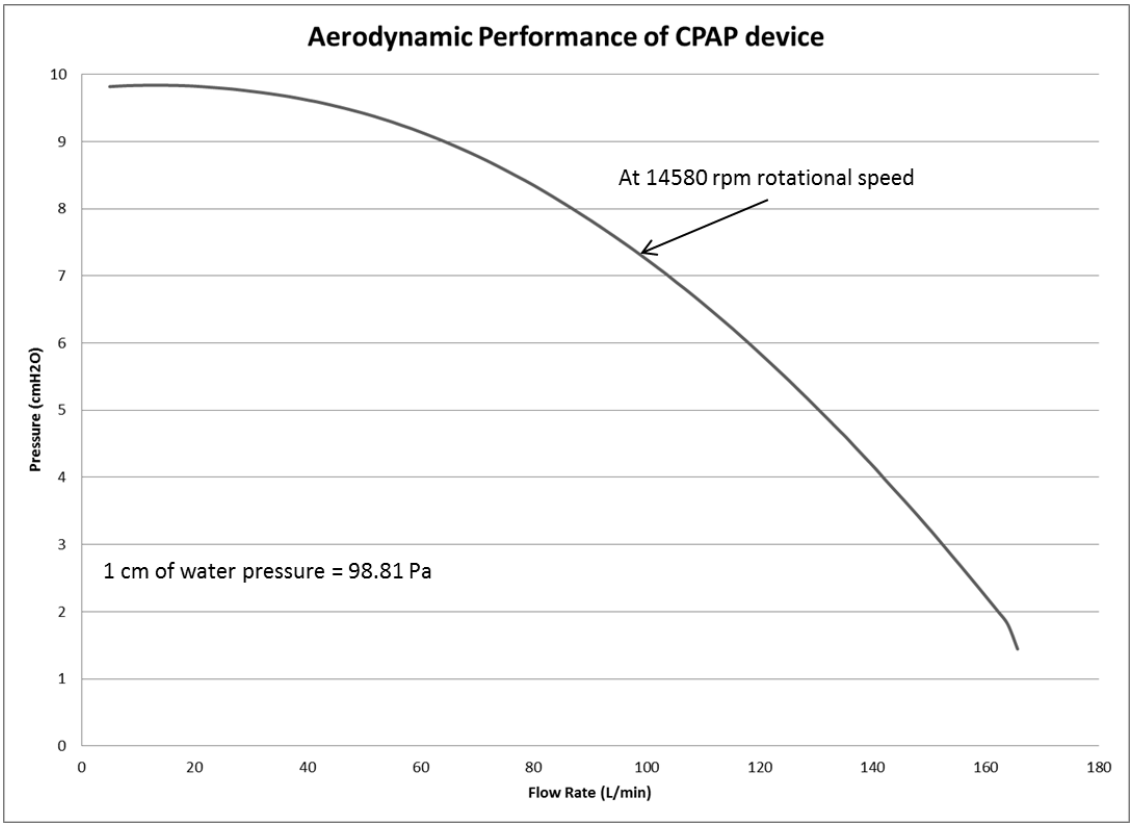

Figure 4.9: Measured volume flow-rate and static pressure diagram of a CPAP device

Figure 4.10 shows the flow chart of the centrifugal fan. A curved trend is seen as similar to the CPAP device flow curve. In this Figure, different pressure rise results at different rotational speeds of studied centrifugal fan were measured and presented. It shows the similarity curved trends for each different rotational speed. From figure 4.10, it is found that the pressure rise in the centrifugal fan is proportional to the rotational speeds. This figure also shows that the fan produces a higher pressure value than the one obtained from

the CPAP device (Figure 4.9) under a similar flow rate. The flow curves of the fan indicate that high pressure is able to be maintained throughout the flow changes.

Direct comparison between the flow curves of the centrifugal fan and the CPAP device at a rotational speed of 14580 rpm shows several observations. Firstly, the centrifugal fan produces a higher flow pressure than the pressure measured from the CPAP device under the same flow rate conditions. Secondly, at 50 L/min flow rates, pressure difference is estimated around 2 cm H_2O of pressure value. However, at a higher flow rate, significant pressure differences are observed. The centrifugal fan is seen to produce high flow pressure and yet, the pressure obtained from CPAP device seems to be much lower. The result of this comparison indicates that there is a drop of pressure throughout the entire CPAP flow system. High pressure loss could be seen at high flow rate conditions.

Figures 4.11 to 4.13 show pressure drops and flow rate curves of the inlet, outlet and humidifier components. Similar curve trends are seen throughout these Figures. As expected, the pressure drop starts to increase when the flow rate starts to increase. Under the same flow rate condition, the pressure drop at the inlet duct is seen to be mostly in the inlet duct model, followed by the humidifier and the least is seen at the outlet duct.

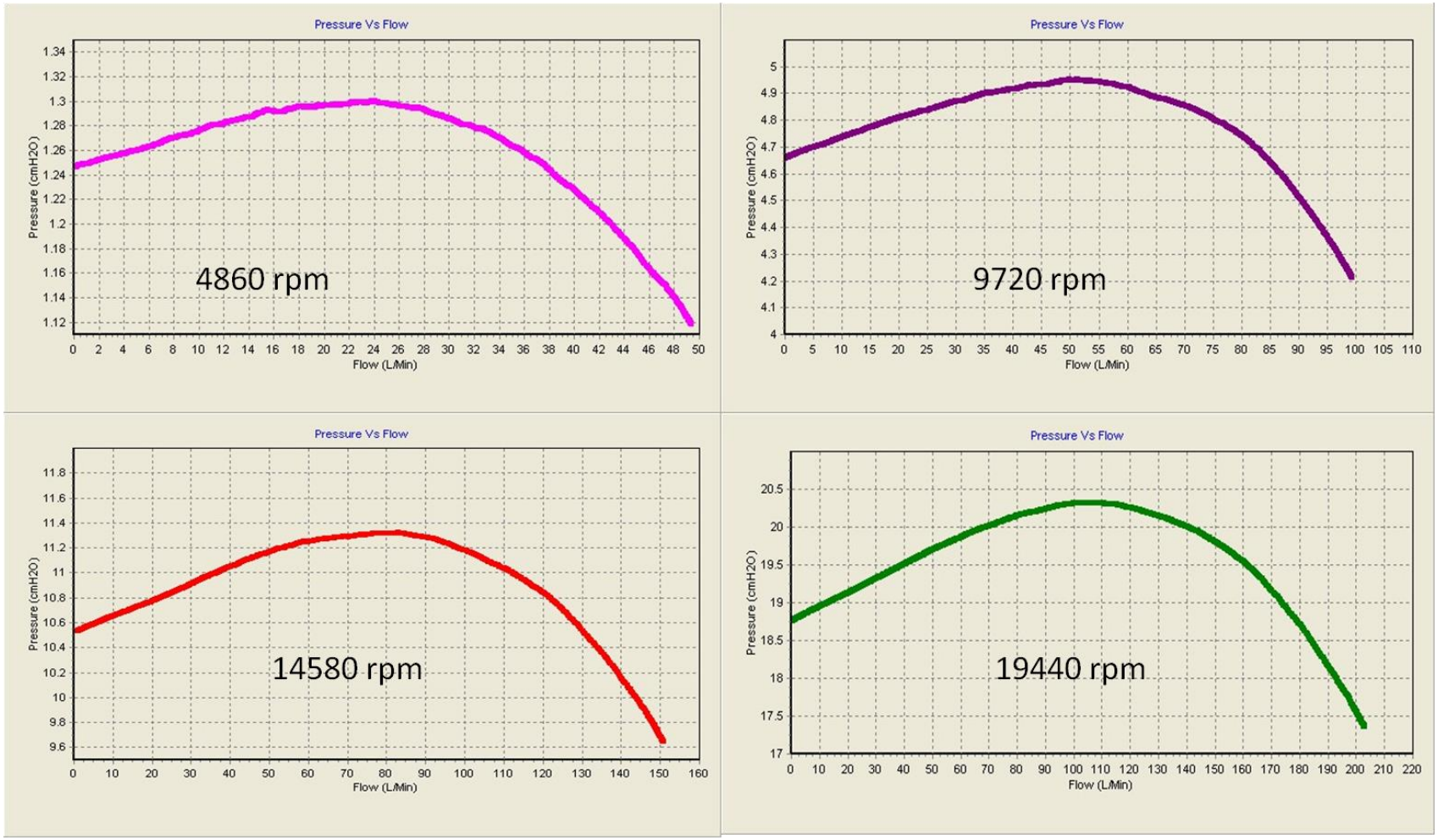

Figure 4.10: Flow Performance of Centrifugal fan measured at different speeds

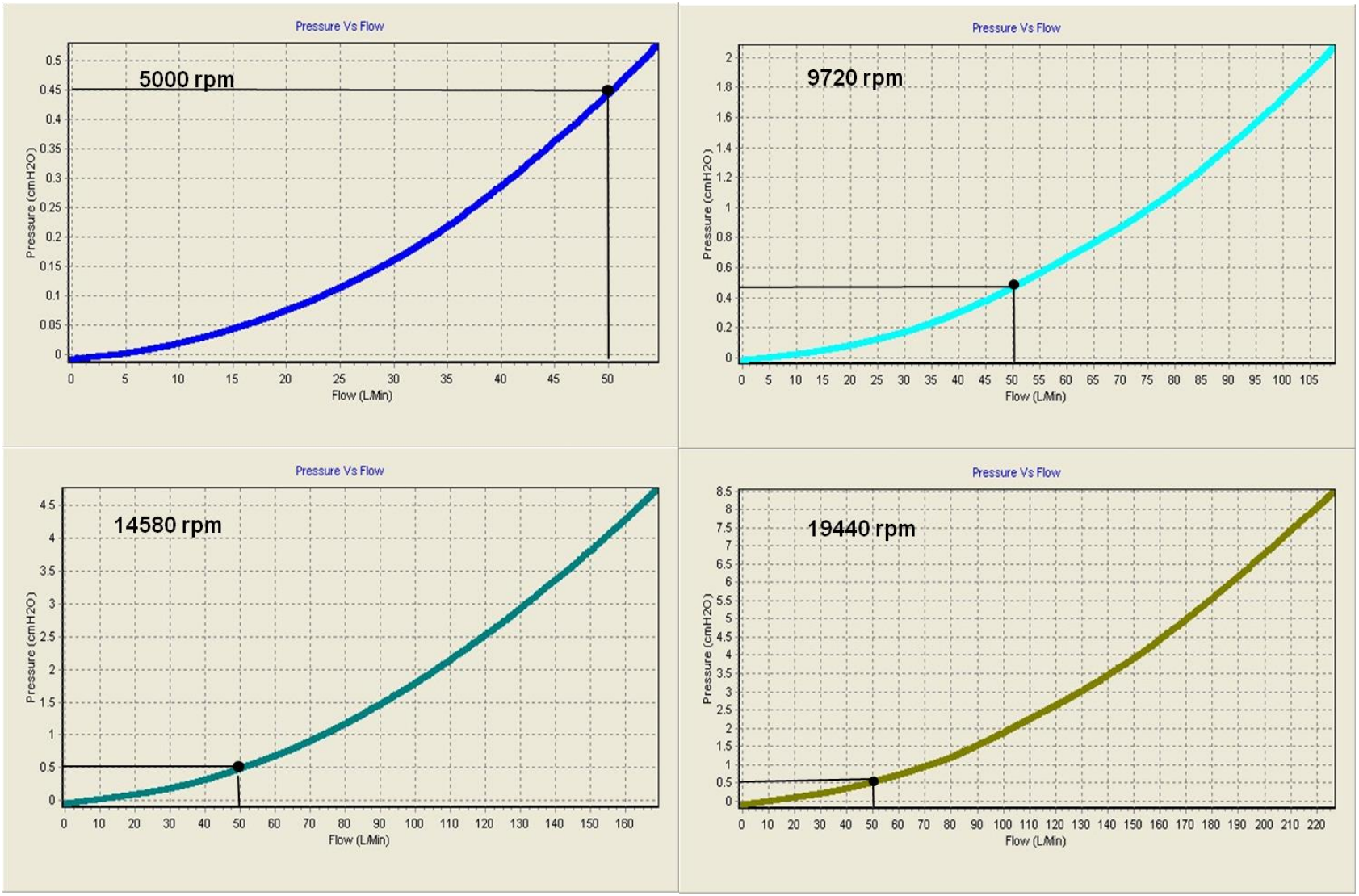

Figure 4.11: Pressure drop at inlet duct at different speeds

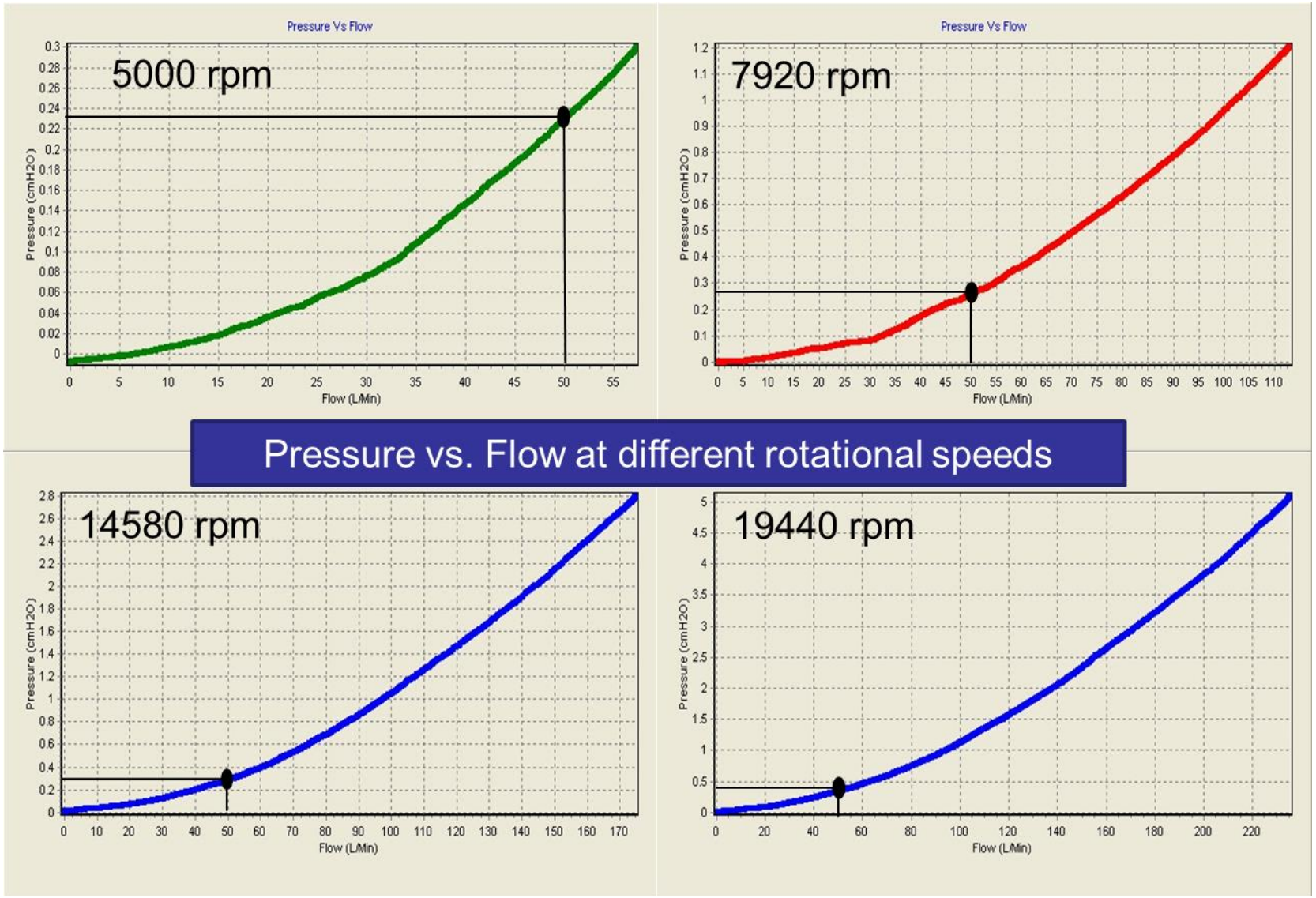

Figure 4.12: Pressure Drop at Outlet duct at different speeds

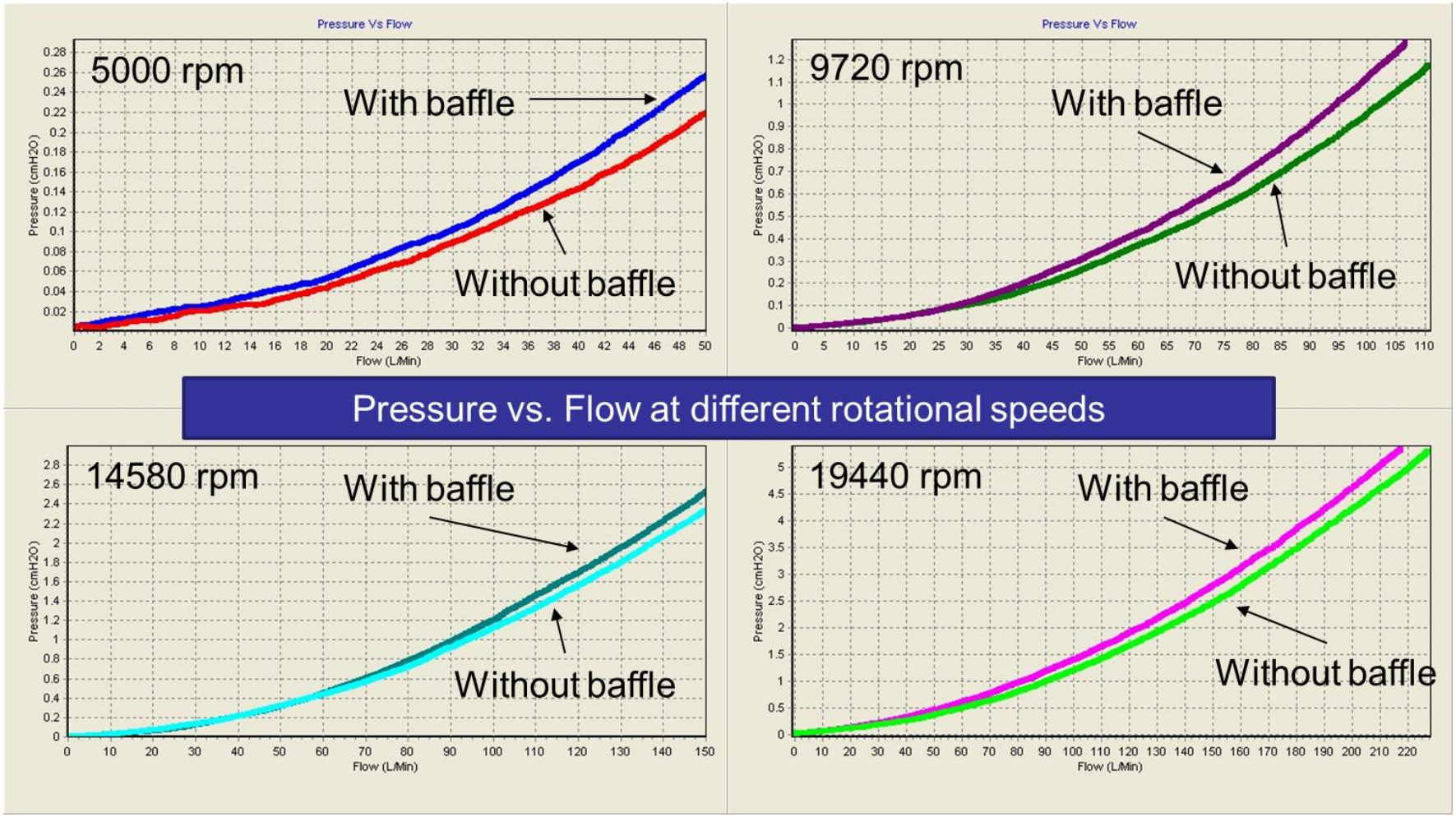

Figure 4.13: Pressure Drop at Humidifier with and without baffle

4.5.2 Sound Analysis

Noise measurements were obtained from ten CPAP devices which were provided by the company. The summary of these results are shown in Table 4.1. In this table, the sound pressure level (SPL) and the sound power level (PWL) of the CPAP devices are averaged. The average SPL result of the CPAP devices is slightly below 30 dB (A). Using equation 4.2 presented earlier in this chapter, the average sound power level (PWL) is calculated as close to 38 dB (A). The (A) sign presents to the A-weighted scale in noise measurement techniques. From measured data showed in Table 4.1, the variation of these measurements is estimated within two decibels dB:

Table 4.1: The average SPL and PWL of CPAP devices

Numbers of CPAP device	SPL dB (A)	SWL dB (A)
1	30.1	38.1
2	29.5	37.5
3	29	37
4	29.3	37.3
5	29.5	37.5
6	29.4	37.4
7	30.1	38.1
8	31	39
9	29.1	37.1
10	29.9	37.9
Average	29.7	37.7

Figure 4.14 presents the one-third octave spectrum of SPL of the CPAP device measured at ten microphone points. In addition, the SPL values at each microphone are presented in the inserted table (inserted picture in Figure 4.14). The Figure shows that the noise spectrum measured at ten microphones are consistent and largely identical. The result

shows that peaks occur at similar frequency bands. However, the magnitude of these peaks varies between microphones which can be explained using the inserted table.

Table 4-2 presents Sound pressure Level (SPL) measured at ten microphone points. Directional analysis suggests that the most noise radiated directions were mainly at the back of the device (microphones 3, 6 and 9) and at the top (microphone 10). The differences between microphone points are above 3 dB (A). By comparing each other in this table, it is suggested that there is more noise radiated from the back, the right and the top of the CPAP devices than the other direction. According to the measurement setup, this finding means that patients might probably find it nosier when the CPAP device is placed on their left or when the back of the CPAP device is facing them.

Table 4.2: The measured SPL and PWL results

Position of Unit	Level dB(A)
1	28.3
2	29.9
3	31.5
4	28.3
5	28.3
6	30.2
7	28.3
8	27.3
9	29.3
10	30.8
Average L_p	**29.4**
L_W	**37.4**

Figure 4.15 shows the SPL spectra of the CPAP devices measured at ten microphone locations. It shows the spectrums are similar in pattern and the dominant peak occurs at a third harmonic of the rotational frequency (RF). The magnitudes are varied with different microphones.

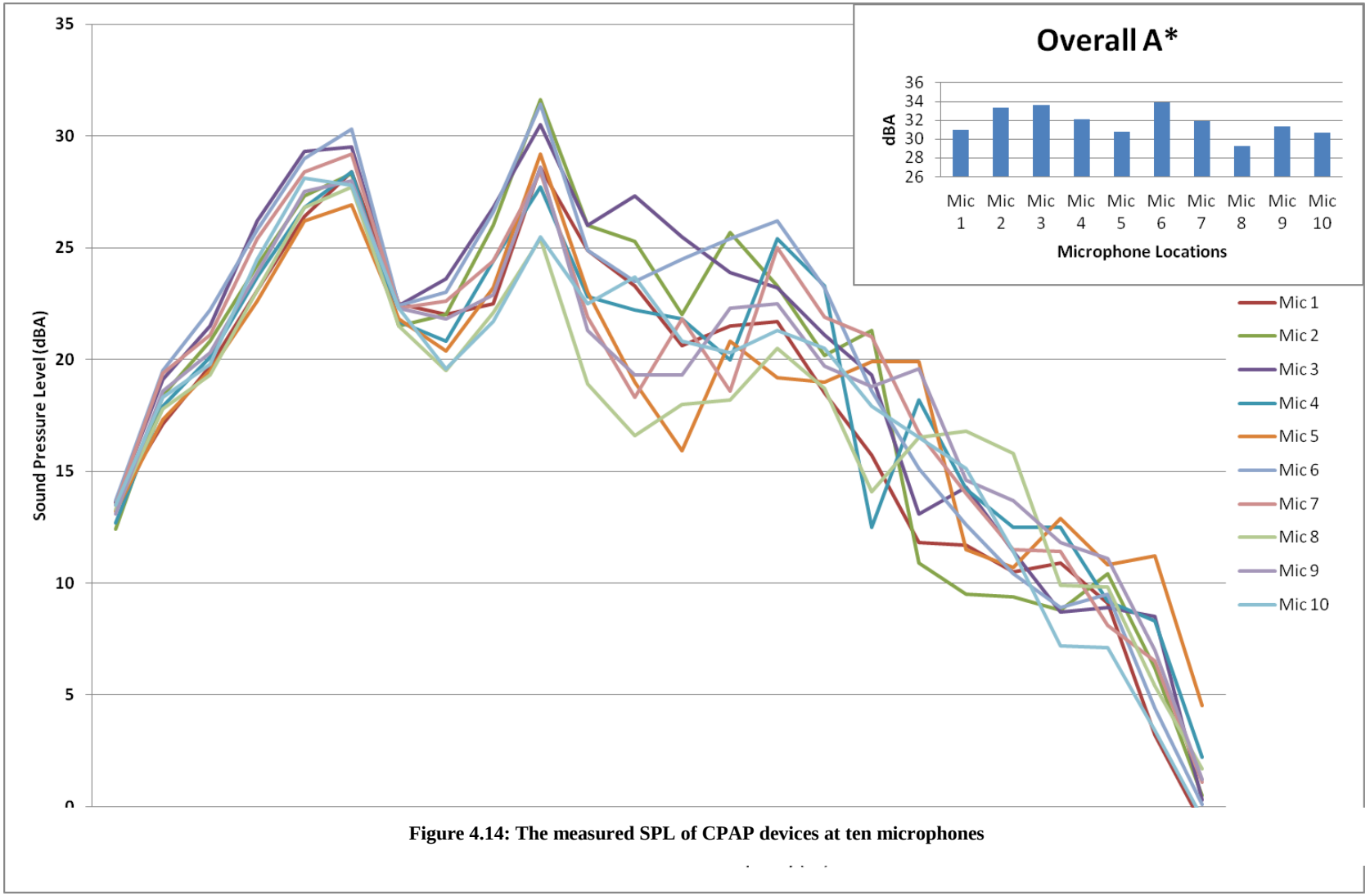

Figure 4.14: The measured SPL of CPAP devices at ten microphones

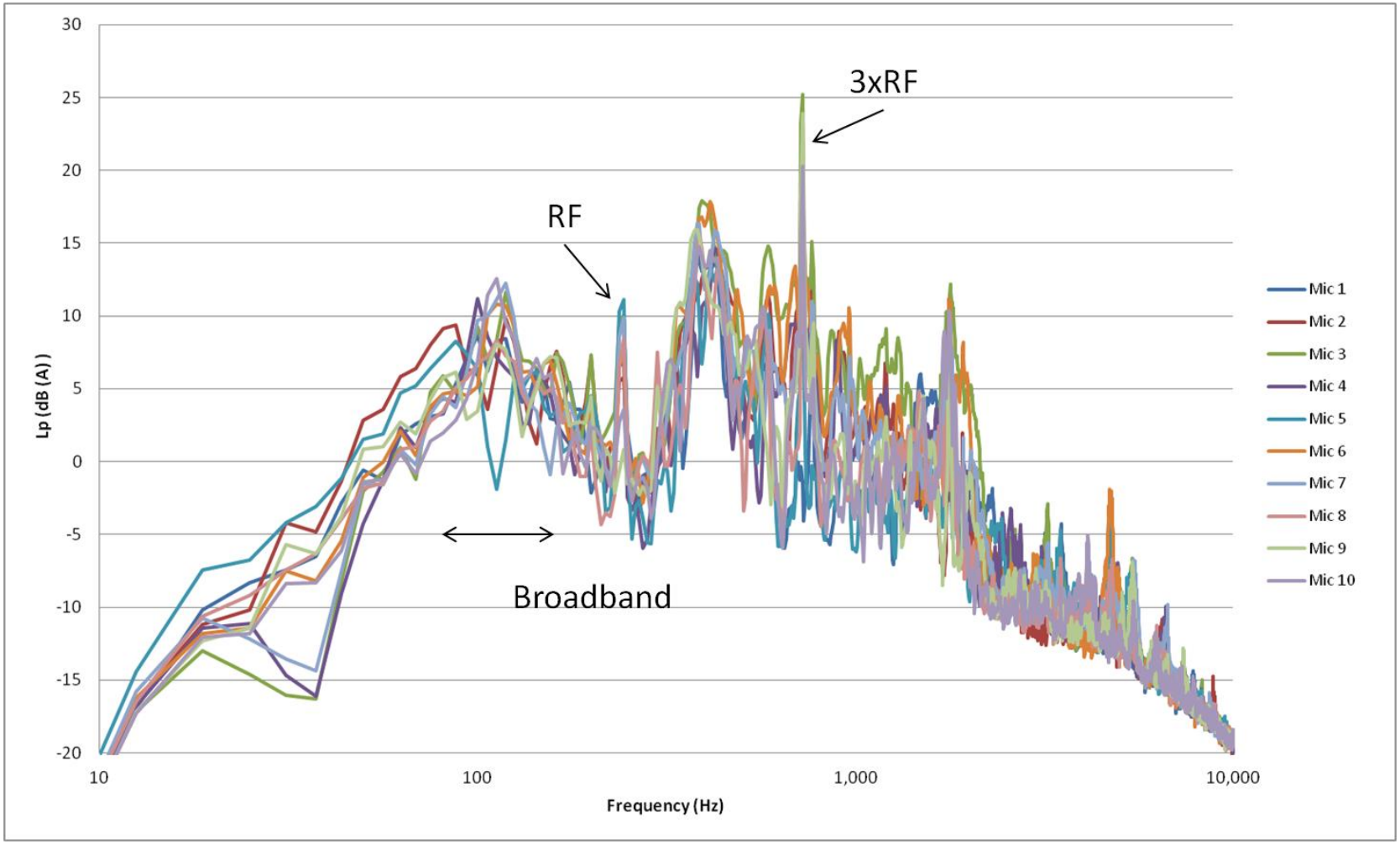

Figure 4.15: the measured SPL spectrum at ten microphones

4.5.3 Vibration Analysis

Surface vibrations on the CPAP device were measured at several locations on the top and both sides and at the front and the back of the CPAP device. High frequency resolution (FFT) vibration data was recorded and stored on the computer for analysis. The results are shown in Figures 4.16 to 4.20.

The overall observation is found that the measured vibration spectrums are identical but different magnitude. The vibration level measured at the top of the device (Figure 4.16) appeared to be higher than the others. The vibration spectrums contain a broad frequency with several dominant peaks. Using the frequency analysis technique, it is found that these peaks are related to the rotational frequency (RF) and its harmonics. This suggests that the peak components appeared in the vibration spectrums are possibly generated from the centrifugal fan and are transferred to the surface through its structural connections.

There appears to be a peak around 97 Hz and this peak is found to be the dominant one in all the vibration spectrums with the highest magnitude. This low frequency vibration could indicate the involvement of mechanical vibration and possibly coming from the centrifugal fan as well. A large broadband frequency of vibration is also dominant in the frequency spectrum range from 300 Hz to 500 Hz. This broad range has a peak of approximately 340 Hz. This suggests that the broad vibration frequency could be as a result of the flow-induced vibration.

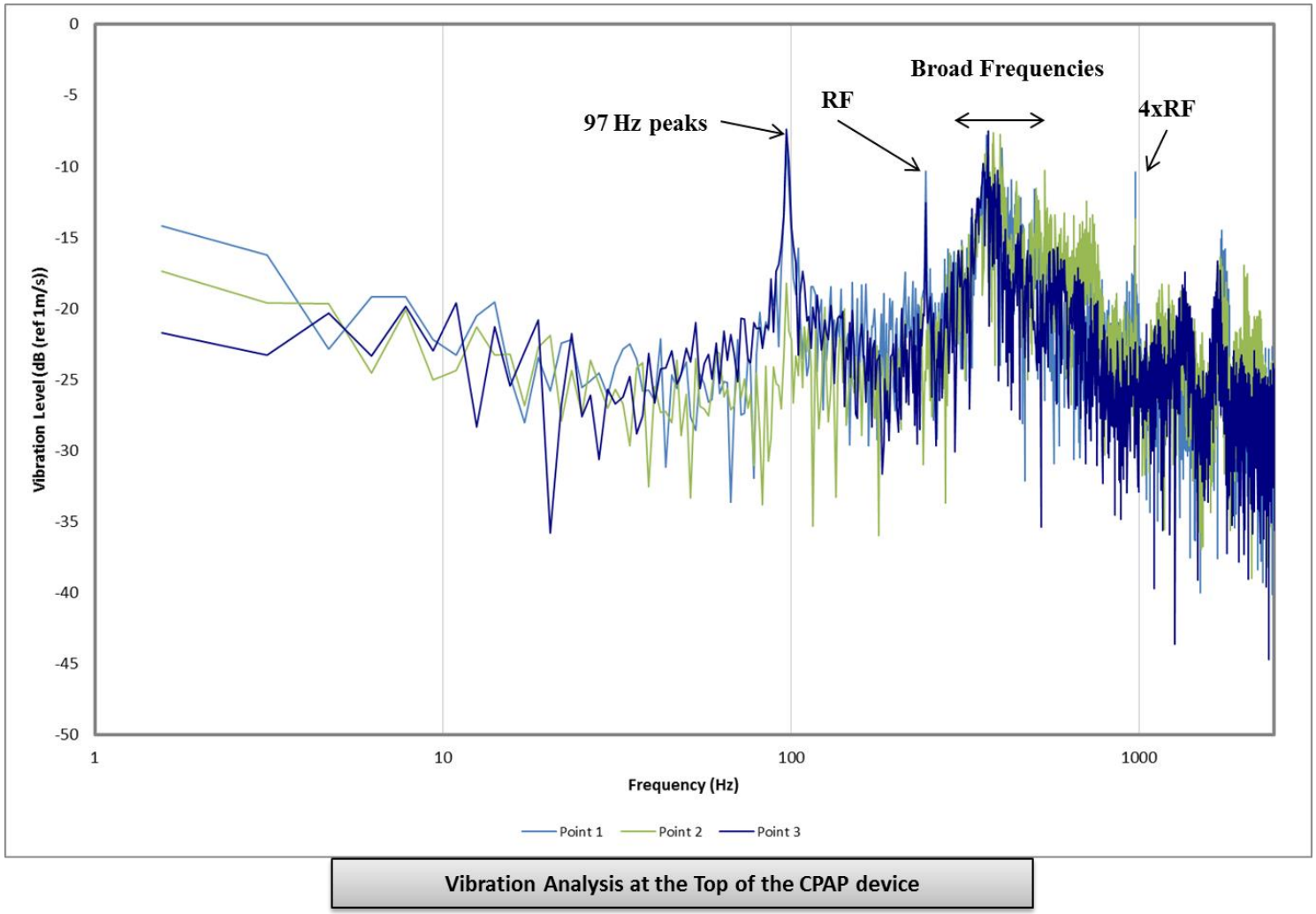

Figure 4.16: Vibration level at the top of CPAP device

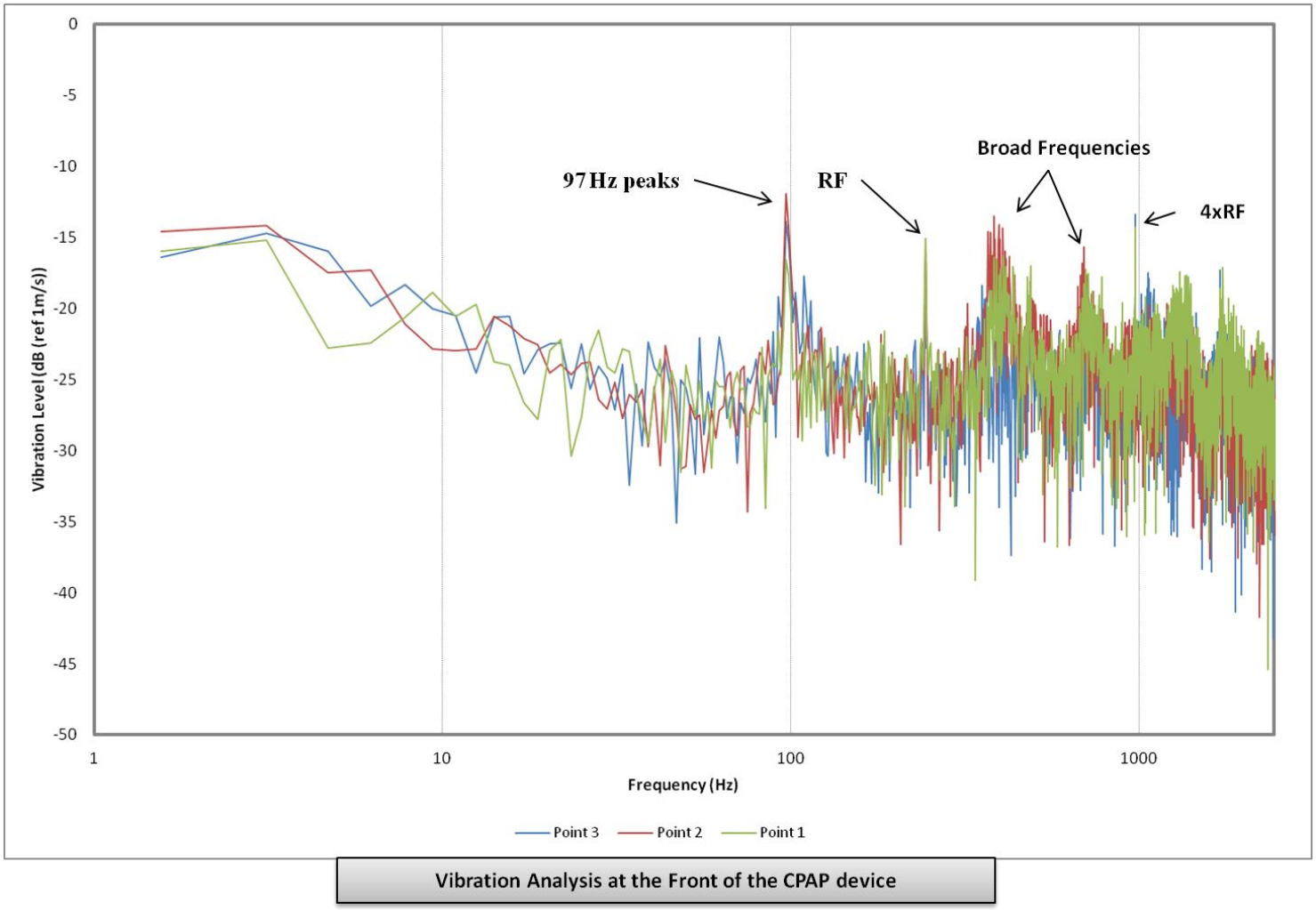

Figure 4.17: Vibration level measured at the front of CPAP device

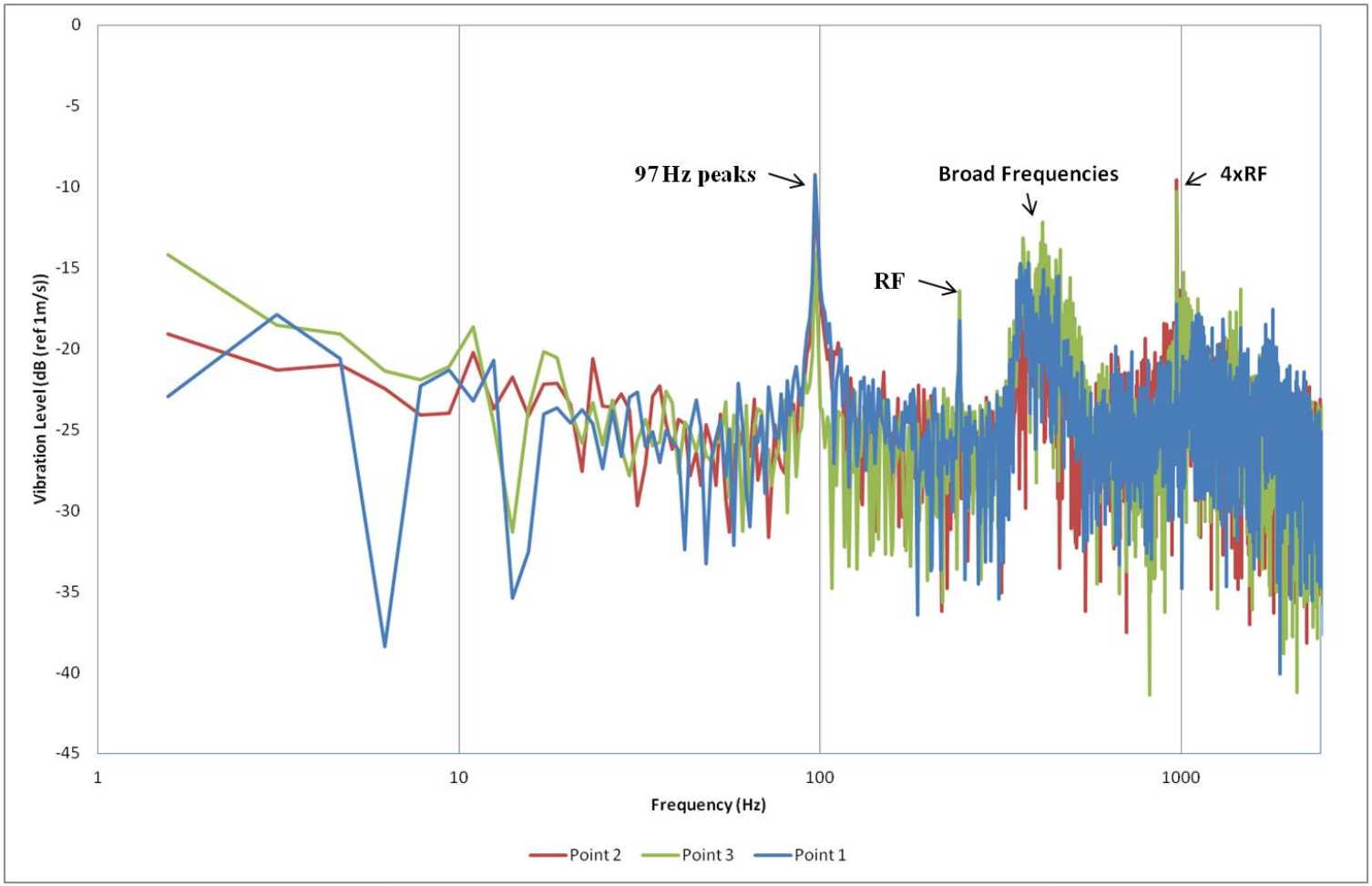

Figure 4.18: Vibration level measured at the back of CPAP device

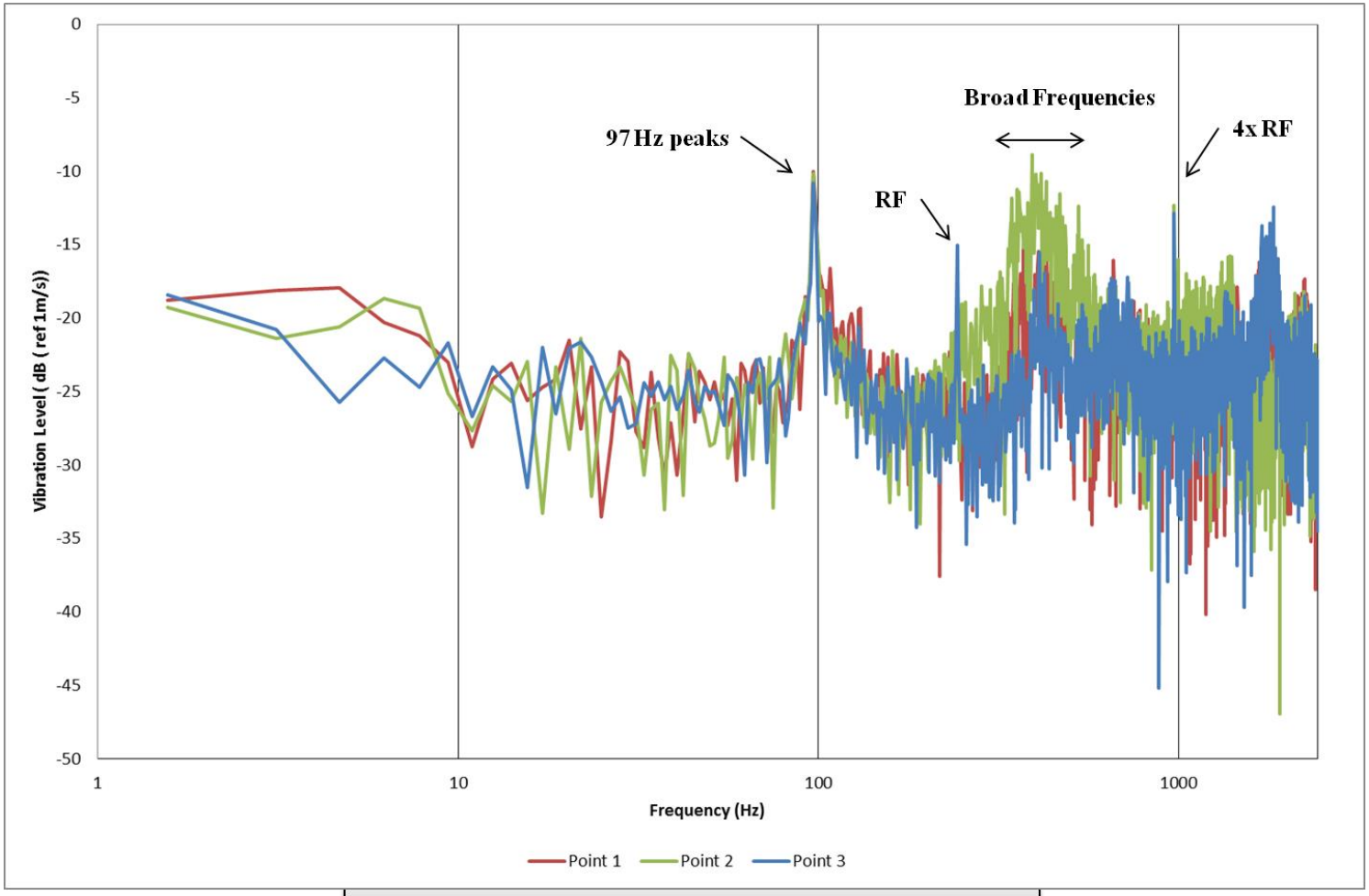

Figure 4.19: Vibration level measured at the left of CPAP device

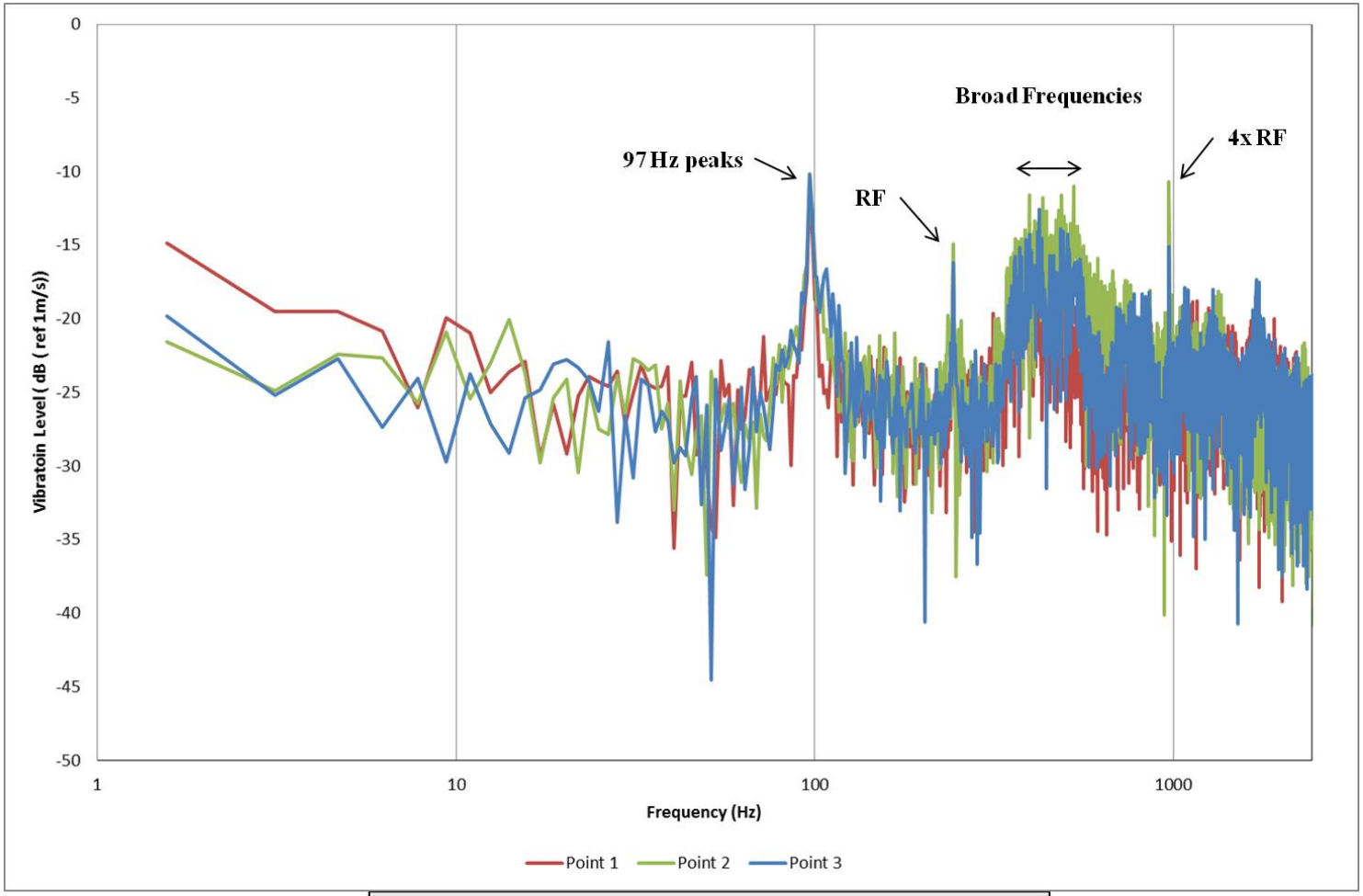

Figure 4.20: Vibration level measured at the right of CPAP device

4.6 Noise Path Elements Analysis

Previous sound and vibration analysis on the CPAP device has shown that the major noise and vibration sources of the CPAP device are possibly coming from the centrifugal fan. Also, broadband frequency suggests that additional sources may also be coming from other components such as inlet and outlet ducts, or the humidifier. The relative significance of the noise, which is generated from individual elements, needs to be understood and established before any noise reduction solution could be suggested and implemented. Therefore, further investigation is needed.

In this section, three case scenarios are developed and undertaken experimentally to study the effects of the noise generated from individual elements on the overall noise of the CPAP devices. The first involves a detailed study of the noise generation from the centrifugal fan. The second involves a study of the noise generation from the CPAP device without the inlet duct. The third involves noise generation from the CPAP device with an outlet duct and humidifier which were eliminated from the flow system.

4.6.1 Noise Measurements of the Centrifugal Fan

The first test was started with the centrifugal fan alone. In this case, the centrifugal fan was removed from the CPAP device and placed in the test room without connecting to any other components. The fan was set to operate at rotational speeds varying from 5000 rpm up to 20000 rpm. At the chosen speeds, the sound pressure level (SPL) was measured and the results were compared to each other.

Figure 4.21 shows a comparison between the SPL measured at different rotational speeds. In this Figure, the lowest SPL curve is a background noise and the highest curve is the SPL of the fan operated at the maximum speed of 20,000 rpm. From this Figure, it can be seen that a similar SPL spectrum patterns are observed. The overall spectrums indicate

that the centrifugal fan generates high broadband noise with some discrete tones related to the rotational frequency and its harmonics. The sound spectrums in this Figure shows the dominant peak is at blade passing frequency (BPF). The magnitudes of the measured SPL are increased when the rotational speed is increased. It is concluded that the noise generation from the centrifugal fan is proportional to the rotational speeds.

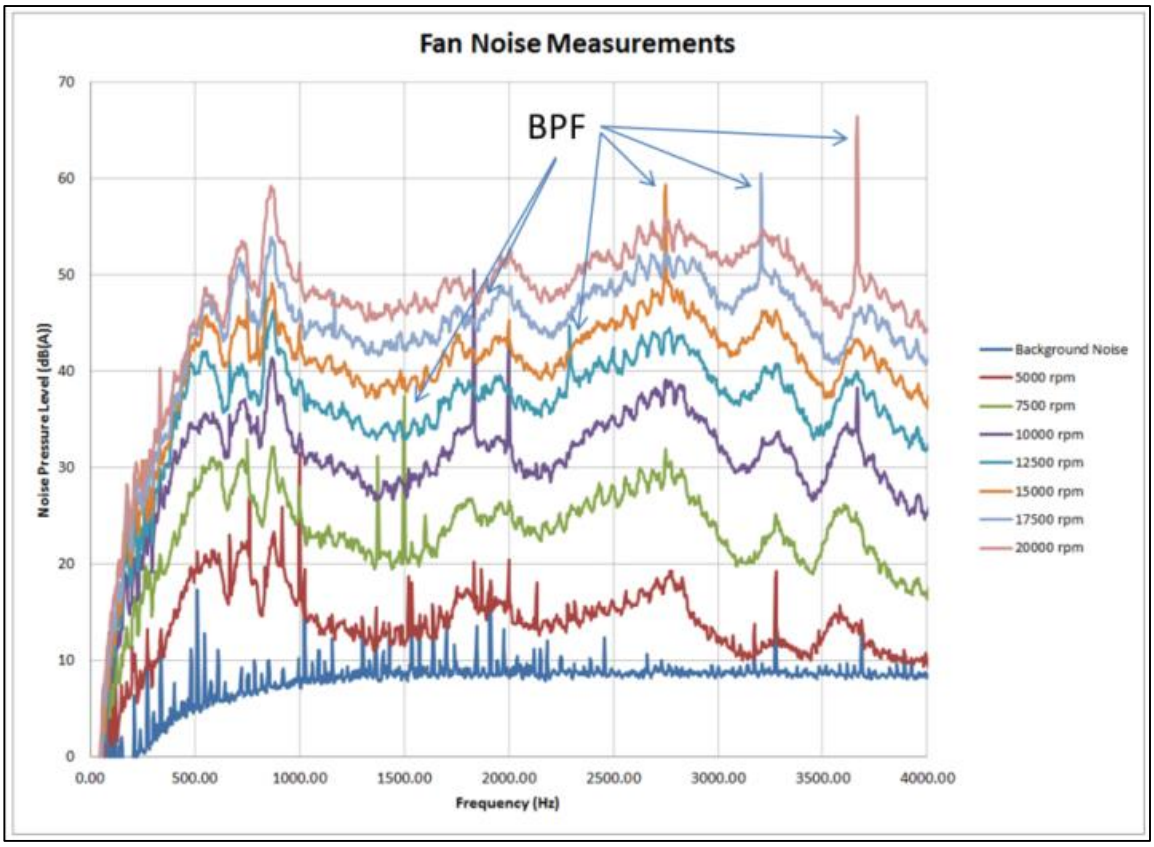

Figure 4.21: SPL spectrum of a standalone centrifugal fan

The second test was to measure the SPL generated from the centrifugal fan under different settings. The fan was set to rotate at 14580 rpm under 50 L/min flow rate and the test was conducted under three different conditions: (i) The fan outlet was connected to an insulated duct and the inlet duct was set at open space; (ii) The fan inlet was connected to the insulated duct and the fan outlet was set at open space. The purpose of this test was to observe how different the noise spectrum of the fan would be under such conditions.

Figure 4.22 shows the SPL measured at the fan inlet direction following the first condition mentioned earlier. In this test setting, the noise radiated through the fan outlet was

eliminated from the measured sound spectrum. Overall, a high broadband noise level is observed from this sound spectrum. The broadband noise with sharp peaks are observed at several frequency bands as below 1 kHz frequency band, between 1 kHz and 2 kHz and at 3 kHz band respectively. The dominant component is calculated at rotating frequency (RF) at 243 Hz at 43.1 dB (A).

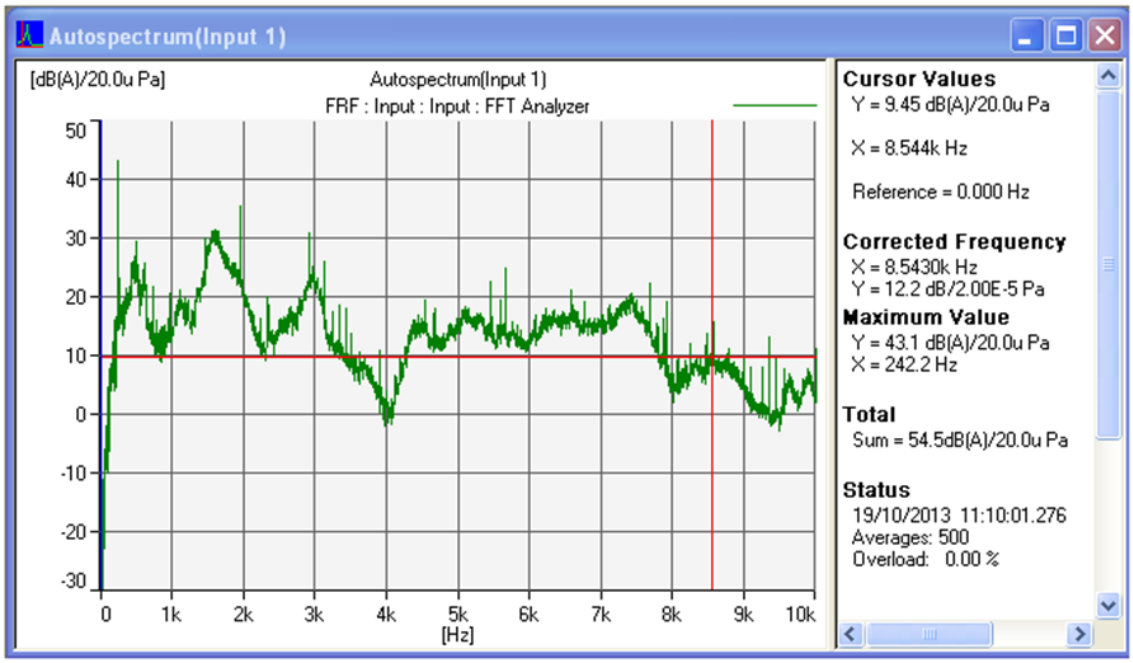

Figure 4.22: The frequency spectrum of the centrifugal fan measured at fan inlet

From this Figure, it is found that the overall SPL of the noise radiates through the fan inlet and a volute casing is calculated at 54.5 dB (A). Frequency analysis shows that the noise characteristic of the fan has changed from the broadband noise with a dominant peak at BPF in the total open space to the broadband noise with a dominant peak at RF.

Figure 4.23 shows the SPL spectrum measured at the fan outlet direction. In this test, the fan inlet was connected to the insulated duct therefore the noise radiated through the fan inlet was eliminated. From this Figure, it can be seen that the noise spectrum is broadband in nature with a dominant peak at blade passing frequency (BPF). High broadband noise is observed between 1 kHz and 3 kHz frequency range and dominated from the entire

spectrum. The dominant peak is calculated at 2672 Hz, which is a blade passing frequency (BPF). The magnitude of the BPF peak is calculated at 40.6 dB (A).

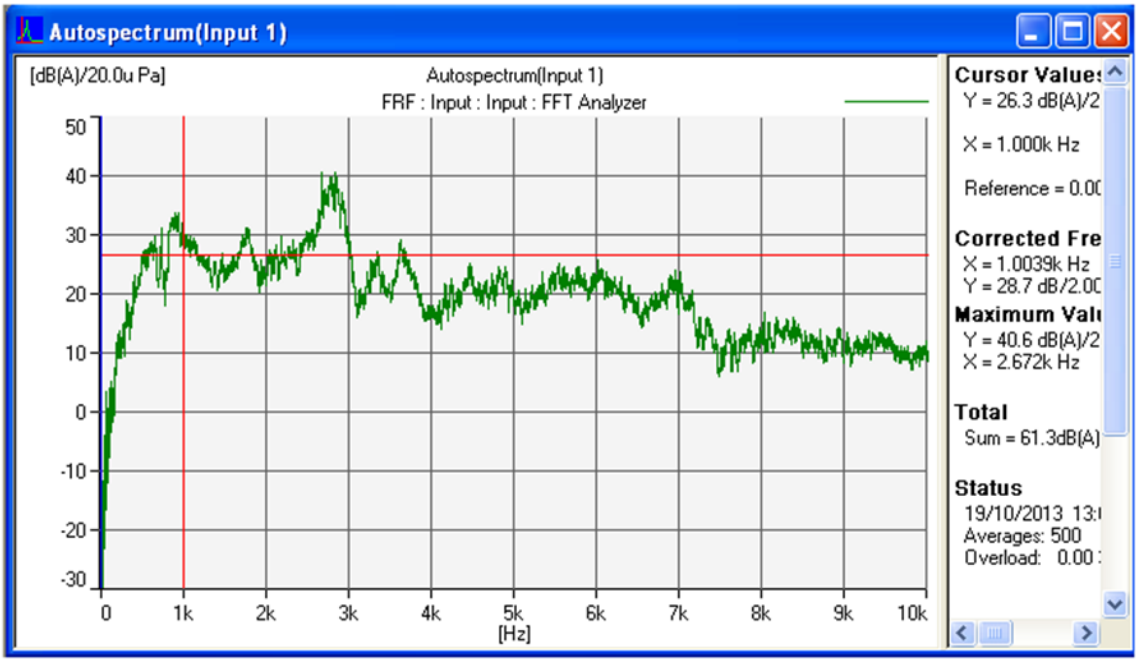

Figure 4.23: The frequency spectrum of the centrifugal fan measured at the fan outlet

In comparison, the sound pressure level (SPL) measured at the outlet direction is higher than the one measured at the fan inlet direction. The difference is about 6 dB (A). The overall SPL measured at the fan outlet direction is calculated at 61.3 dB (A) and the overall SPL measured at the fan inlet direction is calculated at 54.2 dB(A). High broadband noise between 2 kHz to 3 kHz, which is seen in Figure 4.23, is possibly generated by the turbulent flow at the fan outlet duct or at the volute tongue regions. It is to be studied numerically in subsequent chapters in this thesis.

4.6.2 The Influence of Ducts to the Overall Noise Level

The second test was to study the overall SPL of the CPAP device without involving the inlet duct. This was done by the engineers prior to this research and the results were obtained and used for analysis purpose. In this test, the centrifugal fan was reassembled back to the CPAP device. The inlet duct was removed from the CPAP device and replaced by a bypass duct which allowed the air to flow directly to the fan inlet. In this setup, the

noise generated from the inlet duct was eliminated. Therefore, the measured SPL was assumed to contain only those generated from the centrifugal fan, the outlet duct and the humidifier. The centrifugal fan was set to run at 14580 rpm at 50 L/min flow rate.

Figure 4.24 shows the compassion between the reference SPL of the CPAP device and the measured SPL without the inlet duct. The reference SPL of the CPAP device was measured before conducting the inlet isolation test.

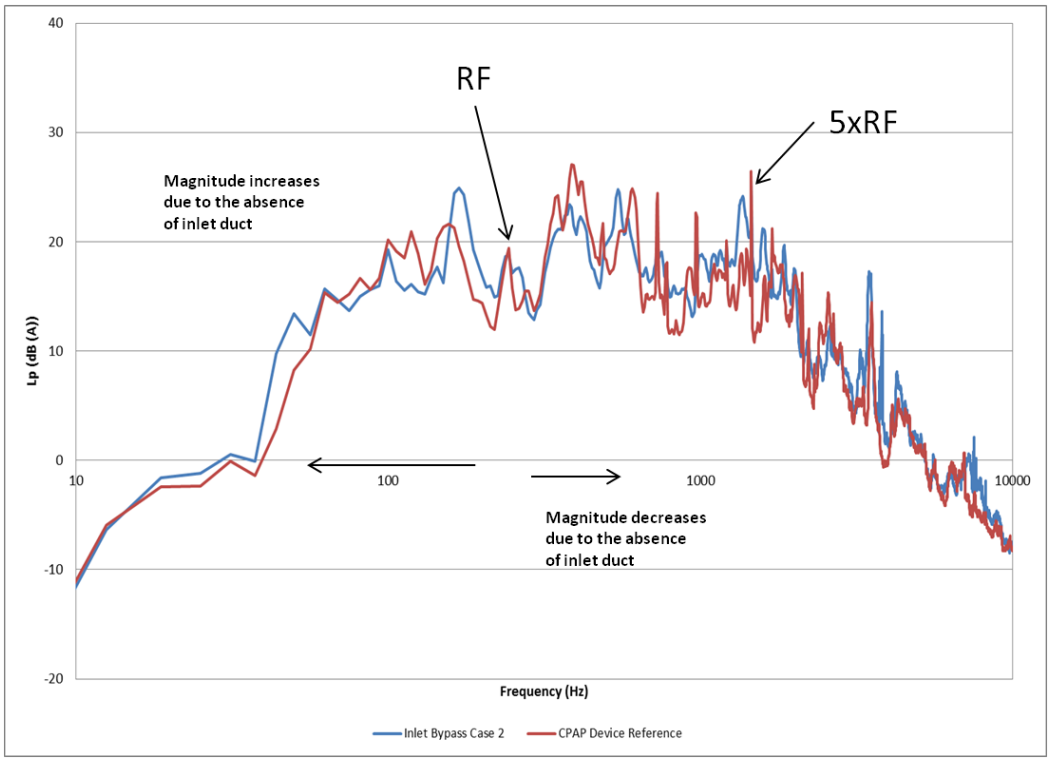

Figure 4.24: SPL of the CPAP device with bypass inlet inserted in Case 2

Overall, the similarity spectrums are observed for both SPL's. By comparison to the reference SPL of the CPAP device, one conclusion could be made that the exclusion of the inlet duct has a minor effect on the overall noise emission from CPAP device. The result in this Figure shows that both SPL spectrums are fairly identical with little differences which can be seen at low frequency bands. There are some changes at frequency ranges above and below the RF. The changes suggest that by excluding the inlet duct, the noise spectra was reduced at frequency above rotational frequency and increased at frequency range below RF. The most effects are at frequencies 200 Hz, 450

Hz. Therefore, one finding could be drawn in this case study is that the influence of the inlet duct possibly has an effect in a low frequency band of the noise generated from the CPAP device. It reduces the noise level at frequency below the RF (243 Hz) and increases the noise level at a frequency band above the RF.

4.6.3 The Influence of Outlet Duct to the Overall Noise

Figure 4.25 shows the comparison between the reference SPL of the CPAP device and the measured SPL for the second test in this section. A similar experimental approach to section 4.6.2 was used in the third test. However, in this case, the fan outlet was connected directly to a bypass duct. In this setting, the airflow from the centrifugal fan was directed to an insulated termination through an insulated bypass duct. The overall SPL measured from this test only contains the noise generated from the inlet duct and the centrifugal fan.

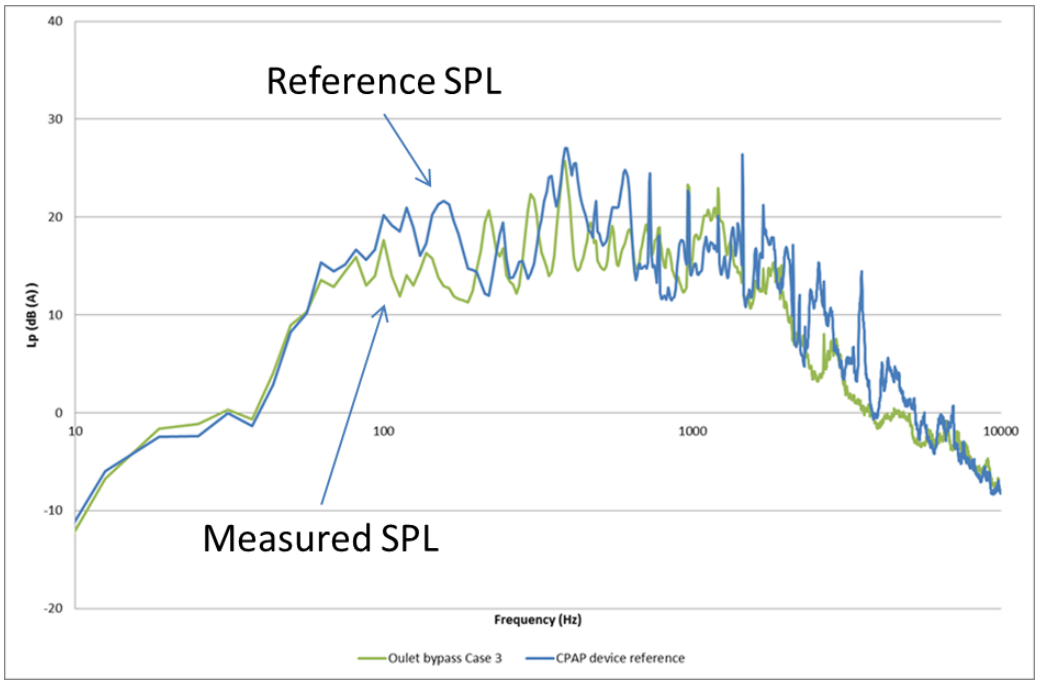

Figure 4.25: The measured SPL of the CPAP with bypass outlet inserted in Case 3

The result showed in Figure 4.25 was also done by the engineers prior to this research and was obtained and used for analysis purpose. Overall, a similar sound spectrum is seen for both spectrums. However, it is observed that without the outlet duct and the

humidifier, the noise spectrum level is reduced across the frequency spectrum. By comparing to the referenced one, it is found that at the low frequency (below 100 Hz), fairly identical curves are observed. The noise spectrum of this case study starts to reduce at frequency range from 100 to 500 Hz. Also, several peaks which are observed between 100 to 1000 Hz frequency ranges are seen to be shifted to the left in comparison to the referenced ones. At the frequency range above 1000 Hz, the broadband noise is slightly increased in comparison to the referenced one.

4.7 Summary

The experimental investigations have provided initial overviews of how the noise and vibration are generated from the CPAP devices. The study has applied several experimental techniques to measure the noise and vibration generated from the CPAP devices. Throughout this experimental excise, despite some difficulties in performing noise and vibration measurements for the CPAP device, it is found that the noise radiated from the CPAP device is broadband in nature with discrete peaks related to rotational frequency (RF) and its harmonics. These peaks are also found in the vibration spectrum. The findings during experimental investigations are summarised below:

- The noise level radiated from the CPAP devices varied in different directions. The highest level is observed mostly at the rear of the device.
- The frequency spectrum of the noise level is broadband in nature with discrete peaks related to rotational frequency and its harmonics. The appearance of these peak components has suggested that the noise generation inside the centrifugal fan has been the most likely sources of noise and vibration. The broadband noise is the main characteristics of the noise spectrum suggesting that flow turbulent possibly is main sources generation.

- Surface vibration analysis also shows evidences of rotational frequency and its harmonics. Furthermore, there is high energy in a broad frequency range between 300 to 500 Hz. This broad frequency bands possibly are generated by internal turbulent flows. The appearance of rotational frequency suggests that the vibrations of the centrifugal fan are transmitted to the CPAP surface.
- Sound measurements for the centrifugal fan in an open space has found the blade passing frequency (BPF) is a dominant component. However, when the centrifugal fan is connected to the ducts, the BPF is filtered out and the rotational frequency has become a dominant one. It can be concluded that the connection to the ducts effectively suppresses the BPF tone.
- Case studies investigate the influence of the ducts and the humidifier over the overall noise generation has also provided a brief information that the noise generated from the ducts and the humidifier could possibly be at low frequency range and broadband in nature.

Chapter 5: **Centrifugal Fan Model Simulations**

5.1 Introduction

Following on from the experimental investigations discussed in Chapter 4, the focus is directed toward numerical simulations and its potential for assisting the product design. In this chapter, the combination of CAA and FSI methods are used to conduct a full investigation on the noise and vibration generated from the centrifugal fan. Figure 5.1 illustrates a flow chart of the numerical simulations conducted on the centrifugal fan with the known boundary conditions obtained from the experimental investigations.

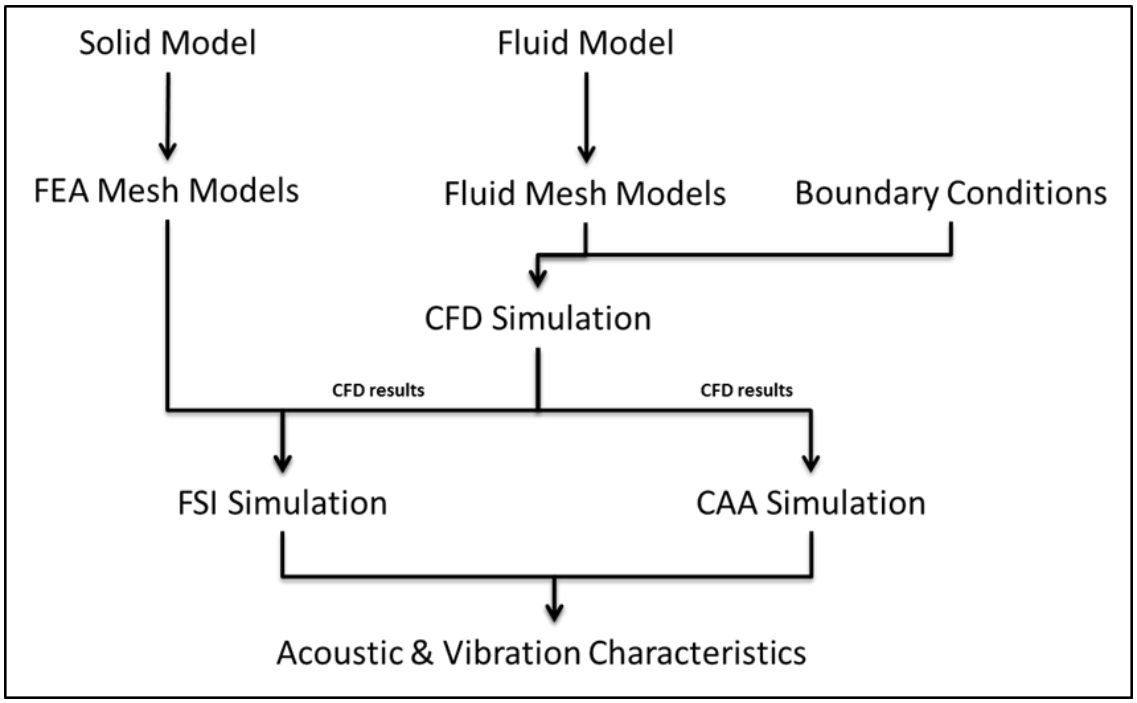

Figure 5.1: Flow chart of numerical investigation for the centrifugal fan

Two numerical simulation studies are conducted. First, the CAA simulation with hybrid approach is used to predict the noise characteristic of the centrifugal fan. Second, the FSI simulation is conducted to predict the flow-induced vibration. The simulations are conducted in ANSYS software packages.

5.2 Centrifugal Fan Models

The initial solid models of the centrifugal fan were obtained in collaboration with Fisher & Paykel Healthcare Ltd. Figure 5.2 presents an impeller assembly (a), a volute casing assembly (b) and a volute cap assembly (c). This is a high-speed centrifugal fan, which is designed specifically for the studied CPAP model in this thesis. The centrifugal fan consists of a shrouded impeller with 11 long blades and 11 splitters, an axial spiral volute casing with a constant flow channel width and a volute cap. The properties of the fan are given in Table 5.1

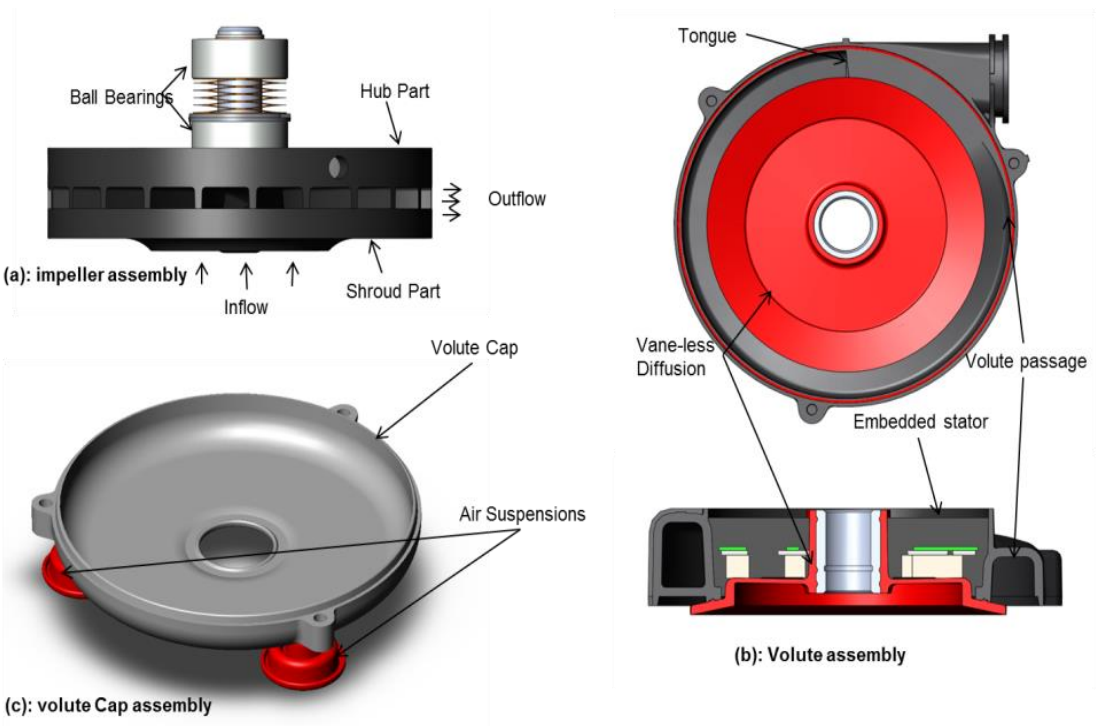

Figure 5.2: Solid Model of the studied centrifugal fan

Table 5.1: Details of the centrifugal fan geometry property

Description	Value
Impeller	
Blades Number	11
Splitters Number	11
Impeller Tip Width	2 mm
Blade Chord length	21 mm
Blade thickness	1 mm
Inlet blade angle	45º
Outlet blade angle	90º
Shape blade	Forwarded
Impeller inlet diameter	22 mm
Impeller outlet diameter	52 mm
Van-less Diffuser	
Outlet Diameter	73 mm
Inner Diameter	53 mm
Curved Angle	11°
Volute Casing	
Inlet diameter	18 mm
Outlet size	238.6 (mm^2) (appx 15x17)
Volute tongue Thickness	2 mm
Volute tongue position	42.5 mm from Fan outlet
Volute outlet Diameter	approx 20.5 mm

The solid fan models were imported into the ANSYS software environment for developing numerical models that were suitable for noise and vibration simulation. Getting the correct geometry into the software was a fundamental step in performing simulations. In this importing process, several small and minor parts were removed. Only the main parts of the centrifugal fan were kept and imported such as volute casing and impeller assemblies. Once the modelling inputs were completed, numerical simulations could be performed.

Figure 5.3 shows a simplified solid centrifugal fan after importing into the ANSYS software environment. The solid model consists of an impeller and volute casing, shaft and suspension models. The impeller was connected with the volute casing through a shaft and a bearing. The solid fan was sit on a rubber suspension system.

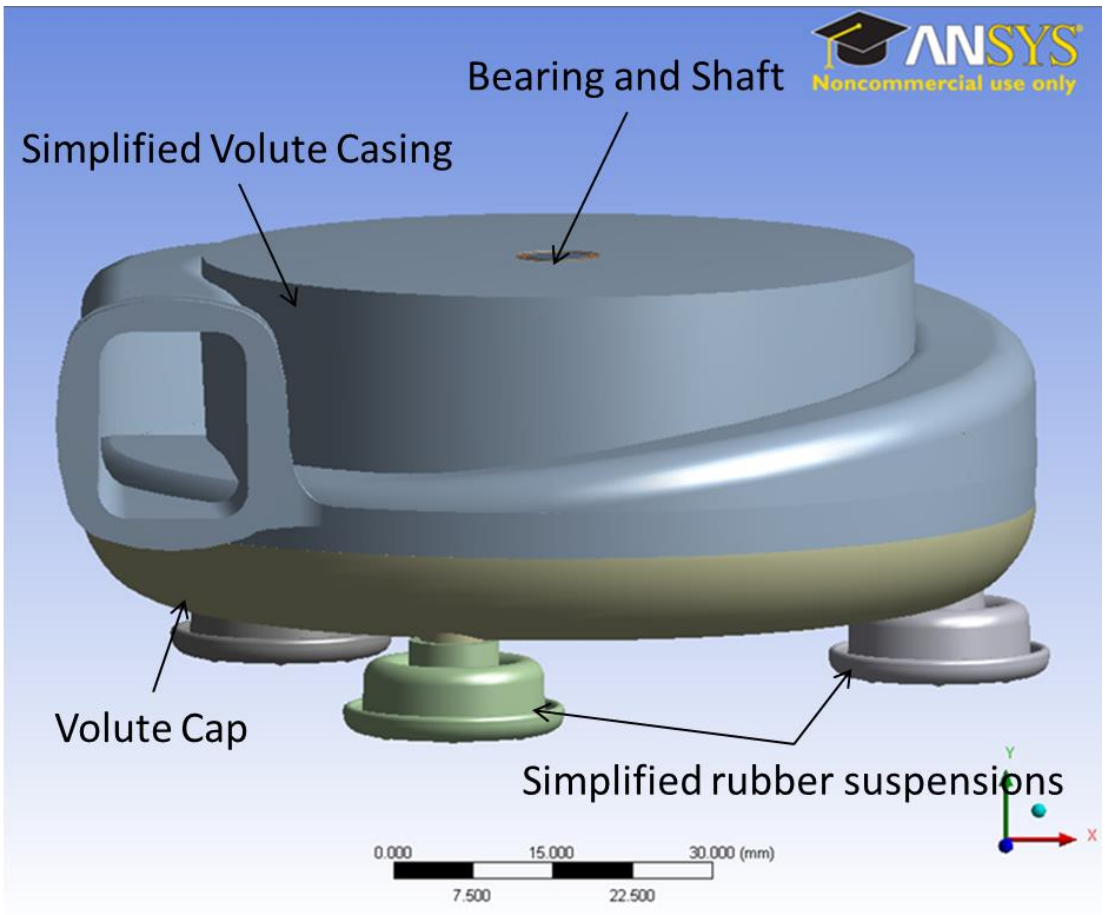

Figure 5.3: Simplified Solid Model of Centrifugal Fan

The material properties provided by the manufacturer are shown in Table 5.2. In this table, the rubber material property was applied to the rubber suspension system. The LEXAN material, which is high flow polycarbonate material, is applied to the volute casing and stainless steel material is applied to the shaft.

Table 5.2: Material properties of the solid fan model

Material	Density (Kg/m^3)	Young's Modulus (GPa)	Poison ratio
Stainless Steel	7850	200	0.3
Lexan	1190	2.35	0.35
Rubber	1280	0.01	0.45

5.2.1 Working conditions and Initial Assumptions

The operating speed of the centrifugal fan is set to vary from 5000 rpm to 20000 rpm. This rotational speed is controlled by a feedback system which is based on the measured pressure differences at the mask (called pressure controlled mode). Once a required pressure value is determined at the mask, the feedback system sends a demand allowing the centrifugal fan to operate at the necessary rotational speed. Table 5.3 presents three specific working conditions of the CPAP device obtained from the experimental investigations.

Table 5.3: Working Conditions of the CPAP device

INPUT CONDITION		OUTPUT CONDITION
Angular Velocity Approx. (RPM)	Flow Rate (L/min)	Pressure Rise at Mask (Pa)
14580	50	980
17520	100	1470
19980	150	1961

However, in this study, only one particular rotational speed is considered with the following initial assumptions:

- The fan model is assumed to operate at a constant speed of 14580 rpm, which is recommended by the manufacturer.
- A steady flow rate value of 50 L/min is chosen as the input boundary condition. This is equivalent to a mass flow rate value of 0.001 Kg/s
- Unbalance effects are negligible as the fan is assumed to be well-balanced
- There is no structural vibration affected on the fluid fields. It is assumed that the solid deformation is small enough not to influence the flow field.

- Acoustic calculation does not account for the influence of the volute casing on the noise generation.

5.2.2 Fluid Model

Figure 5.4 presents the 3-D fluid model of the centrifugal fan. The fluid model consists of a spiral volute casing fluid model (Figure 5.4 (a)), an impeller fluid model (Figure 5.4 (b)). Two external computational domains (Figure 5.4(d)) are also added. The computational domains allow turbulent flow to be fully developed within the centrifugal fan. This assists the accuracy as previously discussed in reference [107].

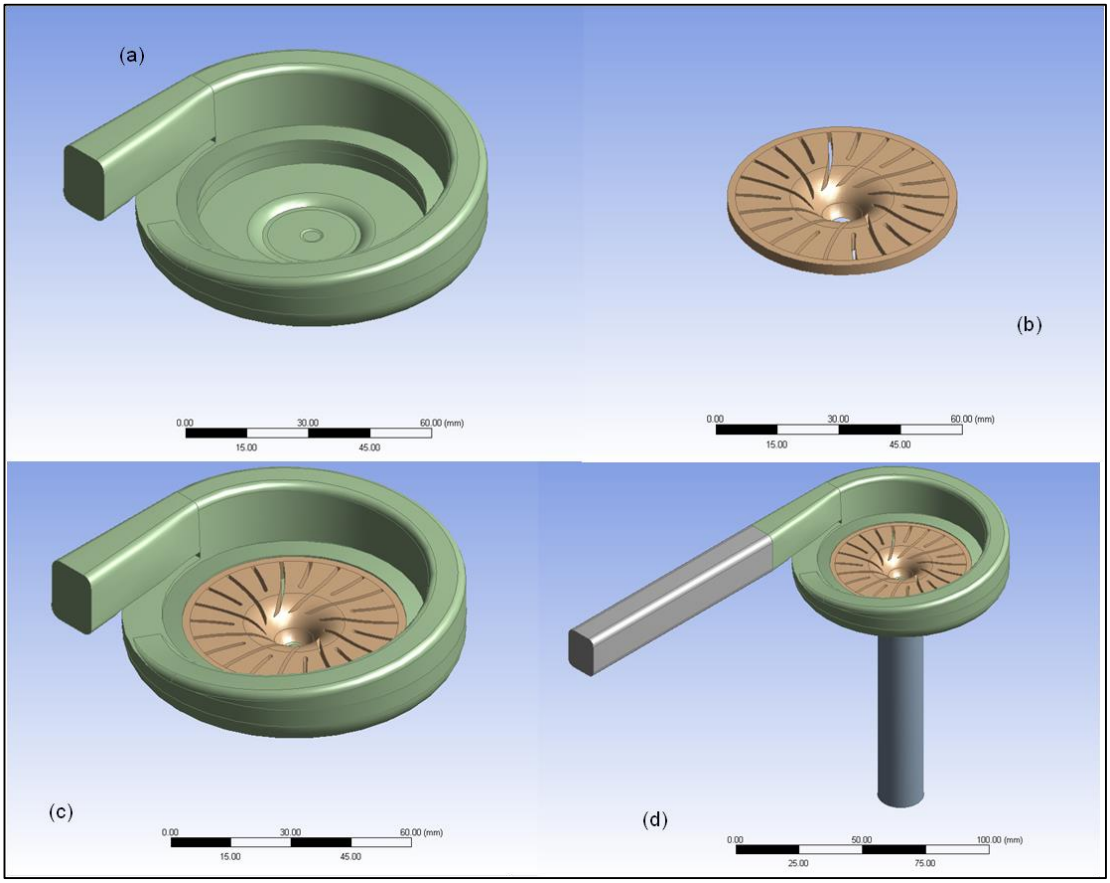

Figure 5.4: -D Centrifugal Fan Fluid Model: (a): Volute fluid, (b) Impeller, (c) 3-D fluid fan model and (c) 3-D fluid fan model with extensions

Figure 5.5 shows the details of the length of the fan extension domain. The computational domain must be long enough to avoid the boundary effect and to ensure the validity of

the numerical results. It is recommended that the length is at least ten times that of the model diameters. In this case, the extra domain lengths were 300 mm.

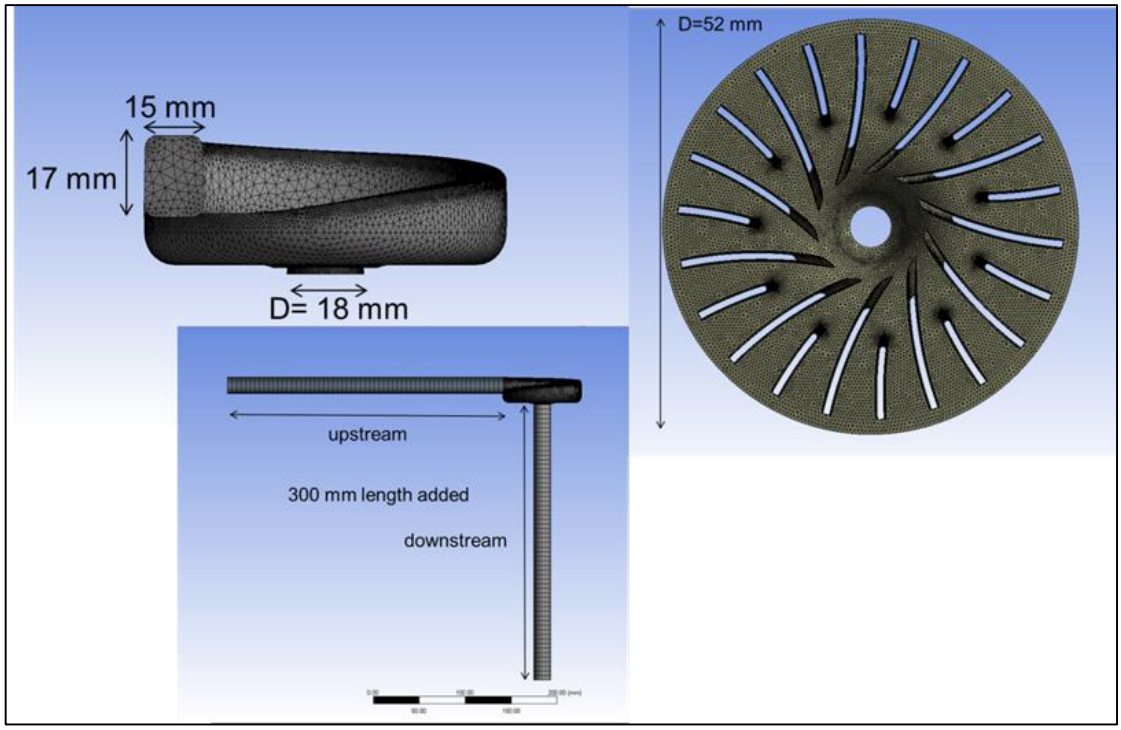

Figure 5.5: Dimension properties of the fan extensions

5.3 Computational Aero-acoustics (CAA) Simulation

The first numerical simulation in this chapter is to predict the noise generated from the centrifugal fan. In this section, the CAA simulation with hybrid approach is performed in ANSYS FLUENT software. The CAA simulation is divided into three steps: the pre-processing step where the numerical model is developed and meshed, the executing step where the model is simulated using appropriate numerical methods and the post-processing where the results are evaluated and validated by experimental results.

5.3.1 Fluid Mesh Model

Figure 5.6 shows the mesh model of the centrifugal fan. The centrifugal fan was divided into three regions, the extended domain, the rotating and the stationary regions. ANSYS FLUENT adopted several meshing methods for 3-D modelling. In general, the hexahedral

mesh method is preferable due to its connectivity and less simulation time. However, the centrifugal fan in this study had a complicated internal geometry, as a result the generated fluid model was very difficult for meshing. The tetrahedral (unstructured) meshing scheme was more suitable for volume meshing than the hexahedral (structured) scheme and was applied to the impeller and the volute casing. At the extension domains, which were not so critical for acoustic calculation, the fluid extensions were meshed using structured (or hexahedral) mesh method.

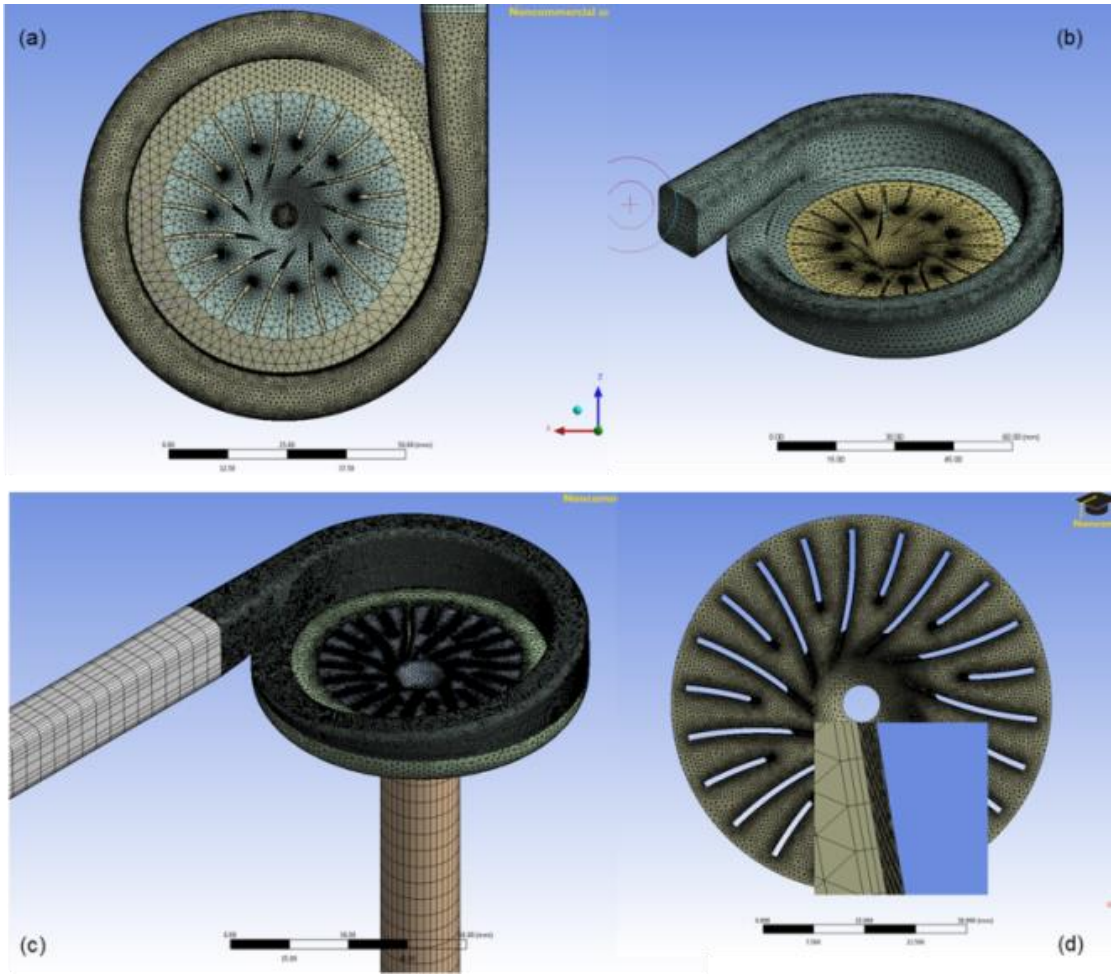

Figure 5.6: 3-D mesh model of the centrifugal fan: (a) coarsen mesh, (b) medium mesh, (c) fine mesh and (d) impeller mesh (inserted boundary layer)

The size of the surface mesh was carefully selected at the most critical regions, i.e., the blades surfaces, the hub surface, the shroud surface, the volute tongue and volute channel where small lines and surfaces were presented. A boundary layer mesh was attached to the surface of the impeller blade to resolve the boundary layer.

The centrifugal fan is set to rotate at 14580 rpm or 243 Hz frequency in this study. The blade passing frequency (BPF) is computed around 2673 Hz for 11 long-blades impeller. In order to contain this frequency, the mesh size needs to be small enough to be able to contain the BPF. In this simulation, the wavelength of the BPF is calculated around 127 mm. Minimum of 10 points are recommended to obtain a good wave length in numerical simulation, therefore at least the mesh size of 12.7 mm is required.

Table 5.4 presents mesh details of the centrifugal fan fluid model. The body volume of the fan model was meshed with a 5 mm element size. At the impeller, where the noise sources were generated, the body mesh was further reduced to 3 mm. At the impeller surfaces, mesh size of 1 mm was applied.

To ensure that the mesh model was capable for numerical prediction, several steady-state flow simulations were performed with different mesh sizes from coarse to finer mesh resolutions. It was found that the mesh size did not significantly affect the outcome such as pressure rise and flow velocity, etc. However, this study involved with acoustic prediction and required a better and finer mesh resolution than the one used for flow simulation. Therefore, the finer mesh was chosen. Total 2.6 e^6 mesh elements were generated for the fan fluid model.

Table 5.4: Mesh details of the centrifugal fan for CAA simulation

Region	Mean size (mm)	Mesh Type	Number of Elements
Upstream	5	Structured	880
Downstream	5	Structured	3220
Impeller	1 (surface), 3 (solid)	Unstructured	1,737,326
Volute	1(surface), 5 (solid)	Unstructured	885790
Total Mesh			2627216

5.3.2 Solver settings and Boundary Conditions

Table 5.5 shows solver settings and boundary conditions for steady and transient simulation of the centrifugal fan. In FLUENT, the segregated and coupled solvers are employed. However, the segregated solver is used to solve the governing equation in sequentially and the coupled solver is used to solve the governing equation simultaneously [108]. The segregated solver requires less computer memory and is quicker to obtain the convergence solution in comparison to the coupled solver. In this present CFD analysis, the segregated solver was used.

Table 5.5: Solver Settings and boundary conditions for Steady-State Simulations

Simulation Type		Turbulence Model
Steady-State		RNG k- ε
Transient		k-ω SST
Solver Settings		
Function		Settings
Solver		Segregated implicit Double precision
Time integration		Second order implicit
Pressure Discretization		Second order
Momentum Discretization		Second order
Pressure-velocity coupling		SIMPLE
Boundary	**Boundary Conditions**	**Values**
Inlet	Mass Flow Rate	0.001 (kg/s)
Fan Outlet	Constant Pressure	0 Pa (gauge)
Fan Walls	No slip wall	
Reference Pressure		101325 (Pa)

Two pressure-velocity coupling methods are recommenced and employed in ANSYS FLUENT as the modified Semi-Implicit Method for Pressure-Linked Equations

(SIMPLE) and semi-implicit method for pressure-linked equation couple (SIMPLEC). For relatively uncomplicated problems in which convergence is limited by the pressure-velocity coupling, the convergence could be achieved more quickly using SIMPLEC. The SIMPLE is dealt with a more complicated model as similar to the one used in this chapter. Therefore, in the present simulation, SIMPLE algorithm was preferred considering the complexity of the flow and mesh qualities.

At the interfaces between the rotating impeller and the stationary volute casing, ANSYS FLUENT software provides two interface solutions specifically for the turbo-machinery simulation purposes. The first one is called frozen-rotor interface. This method employed a quasi-steady algorithm, where the rotating and stationary parts are modelled at a fixed position relative to each other. Therefore, in this setting, there is no any relative shifting of the impeller mesh cells, however the centrifugal effects are included. This method is suitable for steady-state solution and was used to apply for steady-state flow simulation in this study.

The second method is called sliding mesh method. This method is used to capture the transient relative motions between the impeller and the volute casing. In this setting, the interface position is changed according to its time step as the flow variables on the interfaces are transferred to each other through the mesh interface surfaces. This method is used for transient approach and was used for transient simulation in this study.

As the inlet boundary condition was set by the mass flow rate which was obtained from the experimental investigations, the outlet boundary condition was defined by a pressure outlet at ambient pressure. All the walls were set to stationary and non-slip conditions, except to the walls at the impeller region. The wall at the impeller region, i.e., blade, hub and shroud surfaces, were set to be under rotational condition. The rotational speed was applied at 14580 rounds per minute (rpm).

5.3.3 Steady State Flow Simulation

The CFD simulation started with the steady-state condition in preparation for the transient solution. The $k-\varepsilon$ RNG turbulence model was applied in this simulation. Steady flow of 0.001 Kg/s mass flow rate was applied at the inlet boundary and static pressure outlet equivalent to atmospheric pressure was applied to the outlet boundary. The frozen rotor was used at two interfaces between the impeller and the volute regions. After 990 iterations, the steady solution was converged. The result was analysed in post-process simulation to obtain an overview of aerodynamic characteristics of the centrifugal fan.

Figure 5.7 shows the flow structure inside the fan using the velocity streamlines. A large velocity gradient is seen at the impeller as well as at the volute outlet. Rotational velocity is observed at the impeller. Flow leakage is seen at the volute casing. This is due to the high suction forces generated at the impeller inlet which resulted in the already high turbulent flow surrounding the impeller outlet in the volute region being sucked back to the impeller. The leakage process could further generate higher turbulent kinetic energy in the lower region of the volute casing.

Figure 5.8 shows the static pressure fluctuation at the volute casing surface via pressure contours. As can be seen, a large pressure fluctuation area at a lower region of the volute casing is observed. High pressure fluctuation would affect the structural vibration of the volute cover. This will be further investigated in FSI simulation later in this chapter.

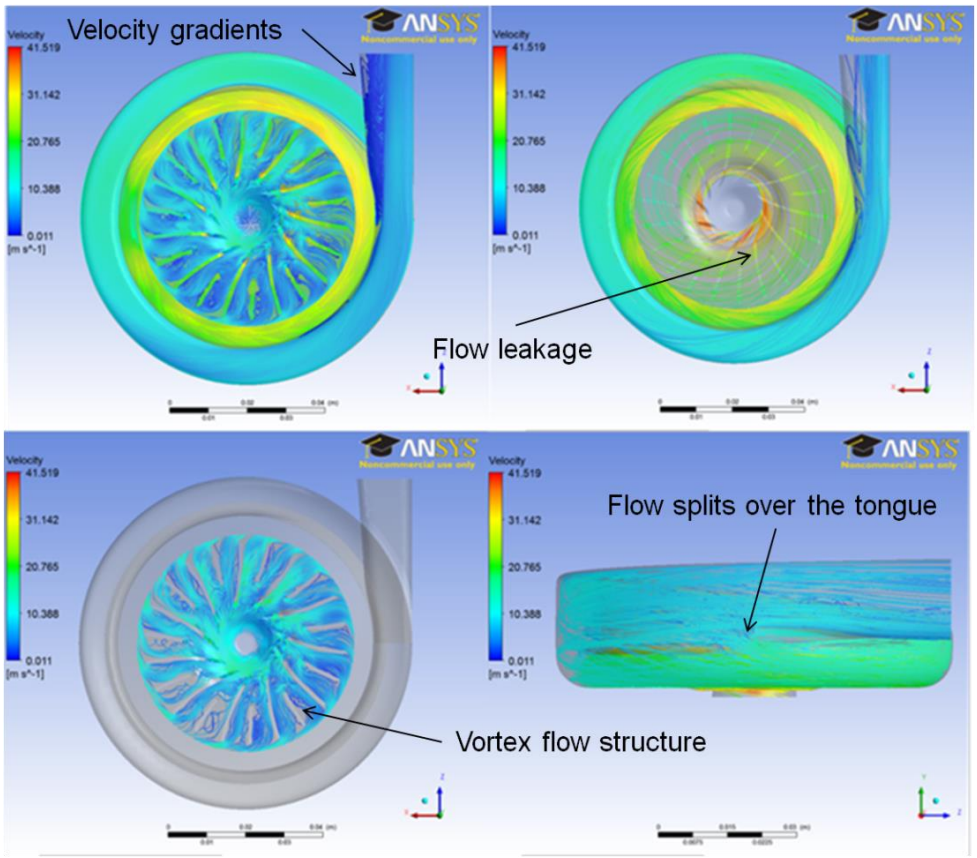

Figure 5.7: Flow Velocity of the centrifugal fan (Steady state)

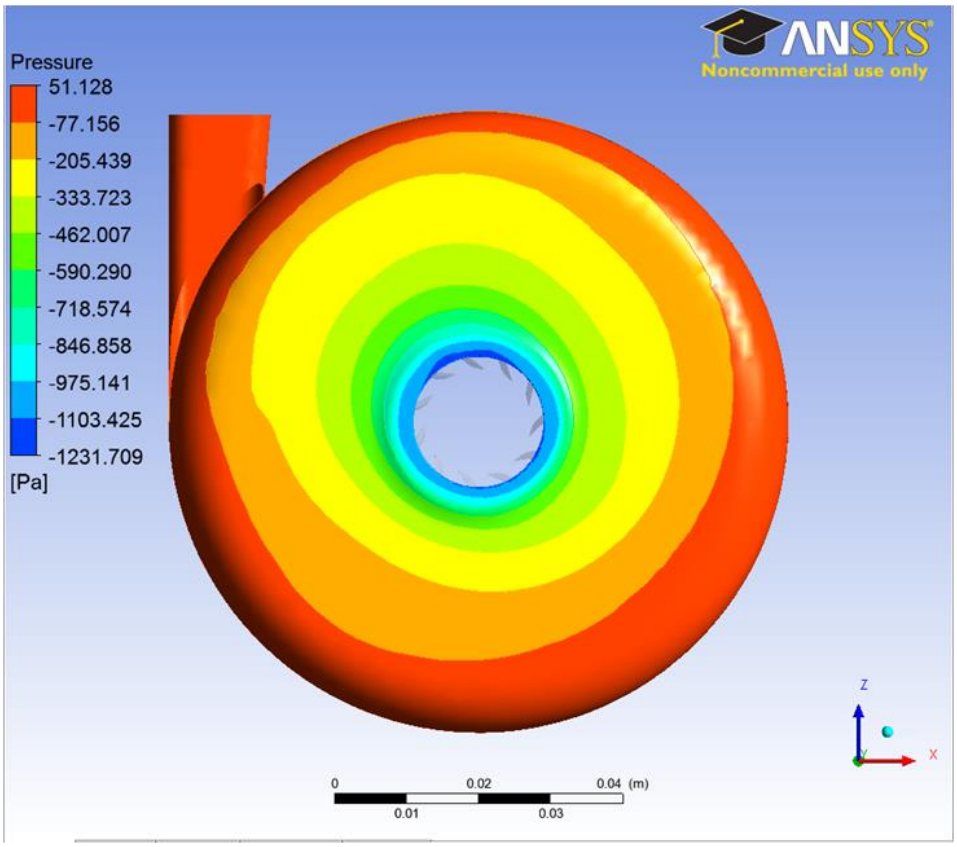

Figure 5.8: Static pressure fluctuation at volute surface

5.3.4 Unsteady Flow Simulation

Converged steady state solution was used for the transient simulation as an initial solution. The transient simulation setting can also be found in Table 5.5. In this setting, the $k-\omega$ SST (shear stress transport) turbulence model was used to obtain a better simulation of the adverse pressure gradient. Sliding mesh interfaces were applied to the impeller interfaces for modelling the rotational region. The inlet and outlet boundary conditions were kept as the same as the steady simulation. Time step was set at 1.247 e^{-5} seconds which allowed the impeller to rotate 330 times to complete one revolution. This time step was small enough in order to obtain acoustic pressure using the FW-H model. The recommended step time was a minimum of 100 step times per revolution in ANSYS FLUENT settings. Total 30 revolutions were needed to obtain periodicity conditions. The periodicity was confirmed by a monitor data point as shown in Figure 5.9. It shows the static pressure at the monitor point almost periodic.

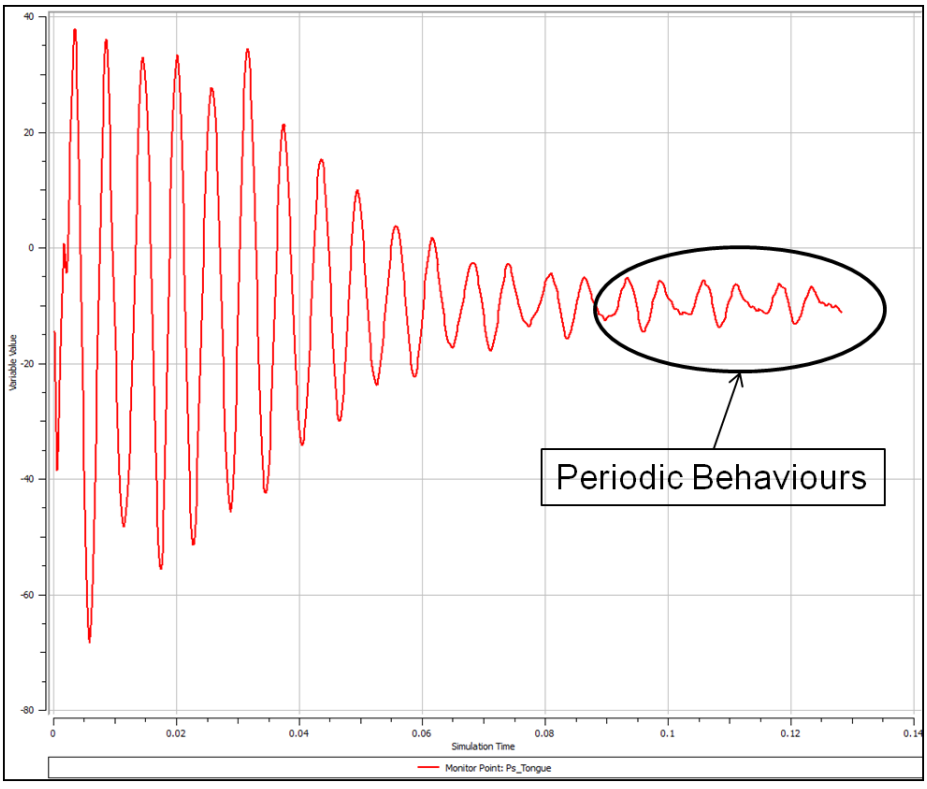

Figure 5.9: Periodic stable of unsteady fan simulation

Once the stable periodicity was observed, a further ten revolutions were obtained for acoustic calculations. During this time, the FW-H model was activated in order to record the time source variables for computing acoustic pressure.

5.3.5 Acoustic Coupling

This section utilizes the available acoustic models adopted in the ANSYS FLUENT software to compute the sound pressure level of the centrifugal fan. The FW-H acoustic model is used to predict discrete noise and the broadband noise models are used to estimate the sound power level (PWL) at the source locations. To activate the acoustic models in ANSYS FLUENT, steps were taken as followings:

- Select export acoustic sources data
- Select source surfaces. The source surface which can be a solid wall or interior wall from the available FLUENT zones setting in acoustic panel
- Select the written frequency for suitable acoustic calculation
- Specify the receivers at locations in the acoustic receiver panel
- Compute/write the acoustic signal
- Post-process the results.

A total of ten revolutions would provide a recorded time of 0.04115 seconds and 3300 simulated data points. The time step is 1.247 e^{-5} seconds which will give the maximum sampling frequency of 80190 Hz. However, the frequency target is up to blade passing frequency at 2673 Hz and its harmonics. The written frequency can be coarsened with a factor of 3, which gives a sampling frequency of 26730 Hz. This value is a sampling frequency and according to the Nyquist theorem, the highest resolved frequency will be 13365 Hz.

5.4 Fluid-Solid Interaction (FSI) Simulation

In this section, the FSI simulation is performed to investigate the influence of the turbulent flow on the fan structures. However, due to the limitation on the computer resources, the simulation only allows one coupling to simulate at a time. Also, as mentioned previously in flow analysis, there was a large surface pressure fluctuations on the volute casing that could affect the volute structure. Therefore the FSI simulation is developed with focus on only the volute casing in order to save computational time and effort.

5.4.1 Structural Mesh Model and Boundary Conditions

A simple solid model was created in ANSYS software as shown in Figure 5.10. The solid model was created based on the volute casing wall surfaces. The thin solid model was defined with a 1 mm wall thickness and meshed with Mechanical APDL solver.

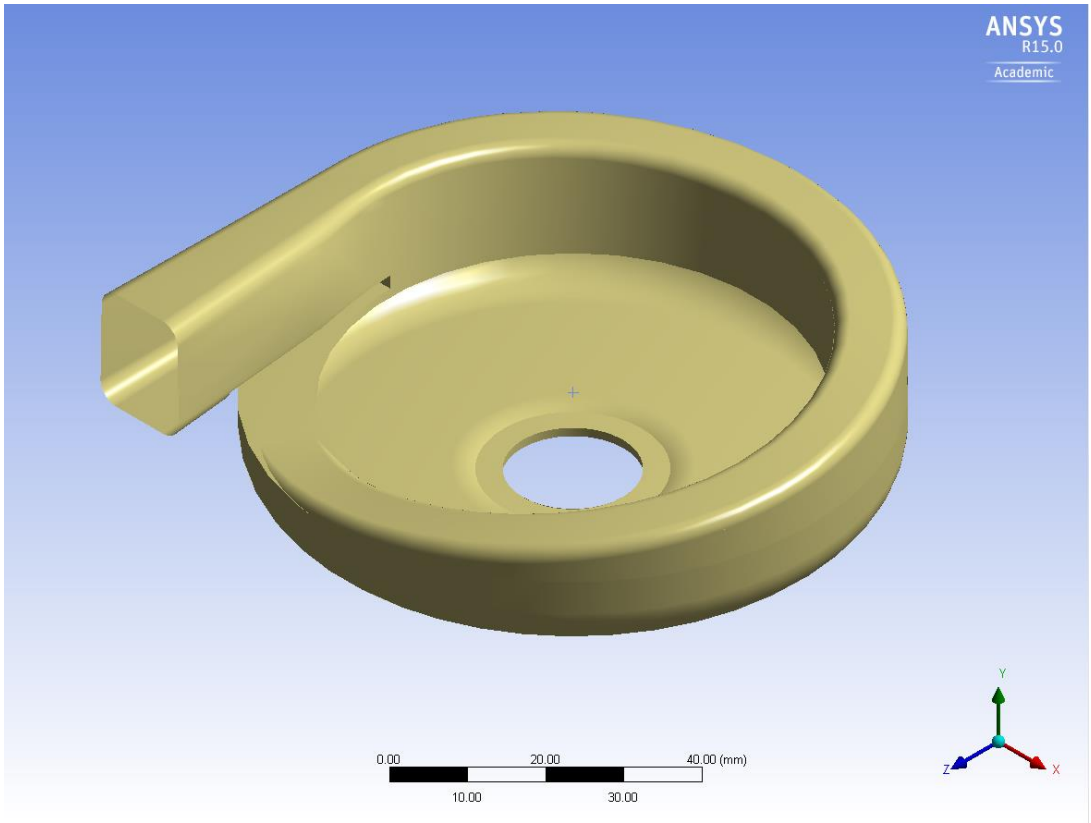

Figure 5.10: Solid thin surface model of volute casing

Figure 5.11 shows the defined solid mesh model with 1 mm of thickness. In this Figure, a total of 18629 mesh elements were generated with 18730 nodes. The statistical analysis found the maximum mesh skewness was around 0.8, which was within the recommended range for simulation. However, to ensure the structure mesh could provide a confident result, two finer mesh models were created and tested with a static structural simulation under the same applied conditions. The deformation analysis showed a small differences of less than 5 % between the mesh deformation results. Therefore, the total coarsen mesh was used to save computational time and effort.

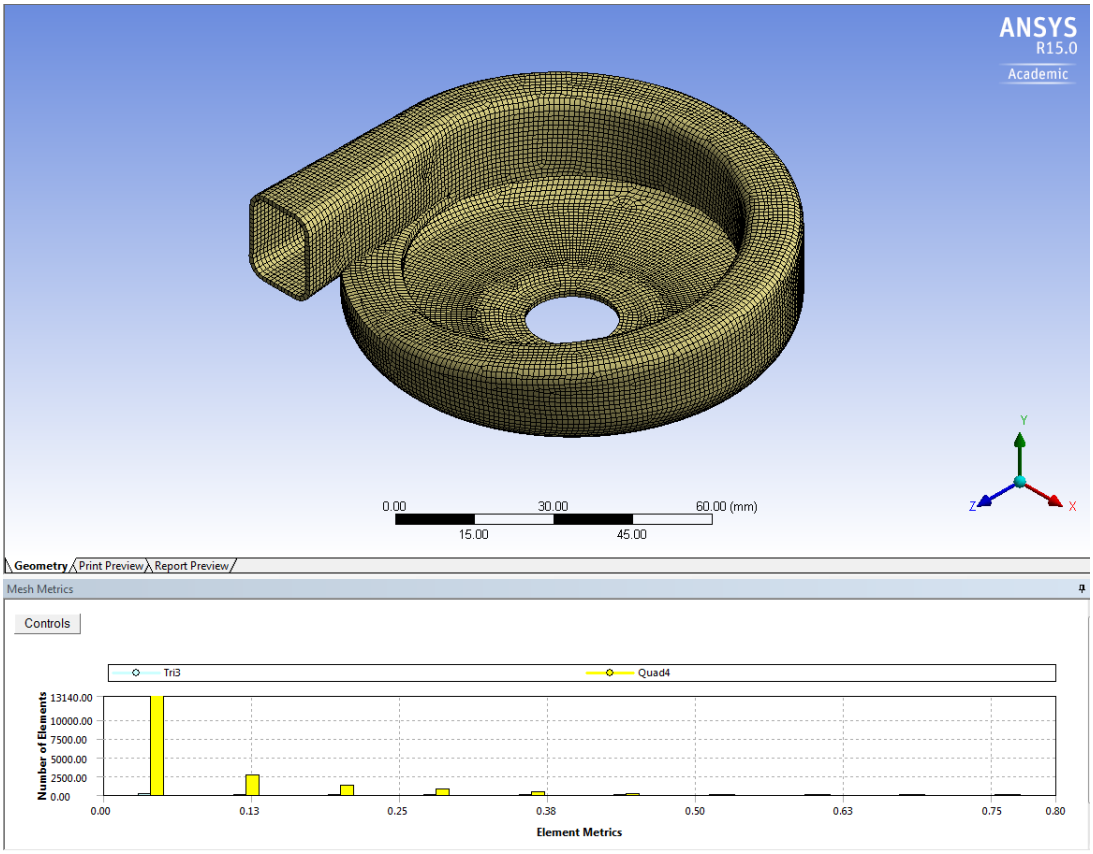

Figure 5.11: Volute casing mesh model with 1 mm of thickness

A fixed support condition was applied to the suspension and to the fan outlet as shown in Figure 5.12. These conditions allowed restriction of the fan moving in certain dimensions as it was intended to limit the vibration in vertical and horizontal directions. A fluid-structure interface condition was applied to the volute casing surface to allow the solid model to interact with the fluid model during the FSI coupling process.

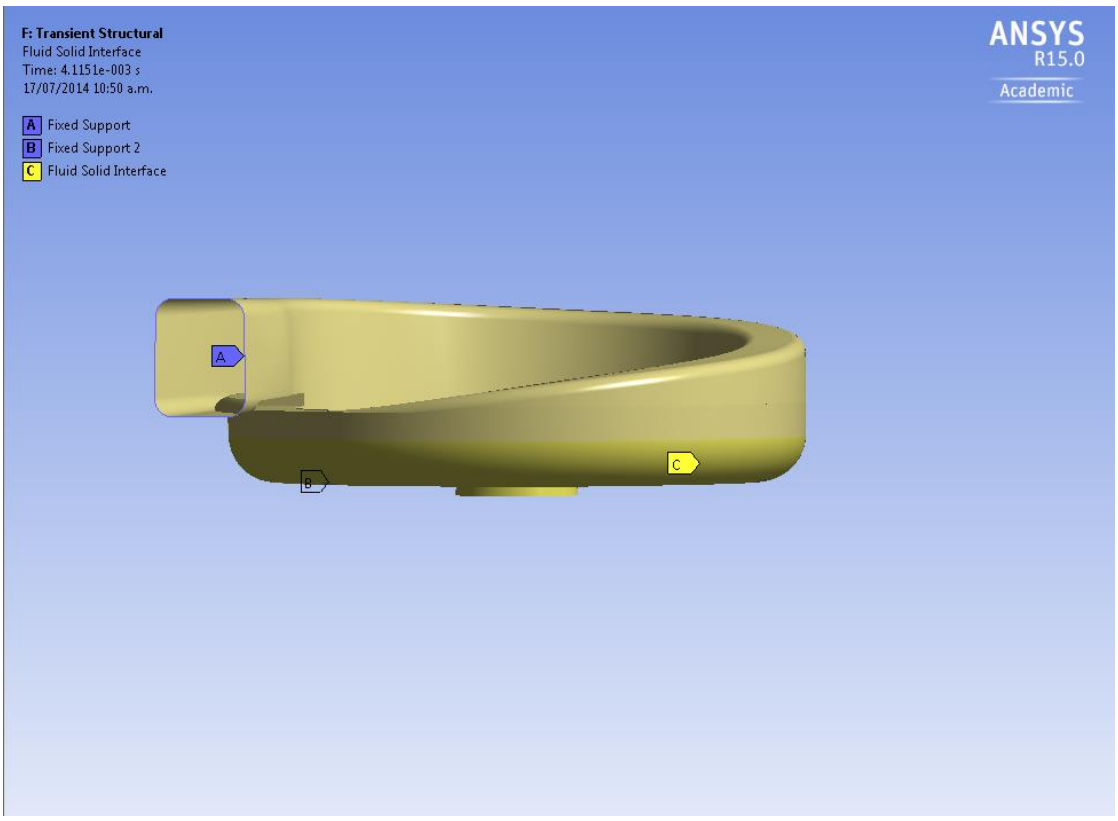

Figure 5.12: Solid boundary condition settings for the volute casing

5.4.2 System Coupling Settings

In order to perform the FSI simulation, the CFD and the structural simulations are set to connect to each other through a system coupling available in the ANSYS software. This system coupling acts as a control box, where it controls the one-way or two-way simulations, etc.

In this study, the one-way FSI study was chosen. The fluctuated forces generated from the volute casing fluid model were set to transfer to the volute solid model through its surface interfaces. The surface interfaces were well-defined in this FSI simulation, one for the solid interface, one for the fluid interface and they needed to be identical. A time step was fixed which was similar to the time step used in the transient CFD simulation at 1.247 e^{-5} seconds. This time step was valid up to 40000 Hz frequency. The frequency range was enough to cover the vibration range of interest as the frequency target was set to be up to 4000 Hz.

5.4.3 Simulation Procedures

The static structural simulation was first performed to obtain the initial solution for the transient simulation. In this simulation, a static load generated from the converged steady state CFD simulation was used to apply on the FSI surface. The static simulation was set at 20 coupling iterations per run. The simulation was set to run until the converged solution was reached.

Figure 5.13 shows the initial distribution of the applied pressure over the volute casing surface during the static simulation. It can be observed that there is a presence of high pressure fluctuation near the inlet region. Maximum pressure at the volute region is computed around 932 Pa.

Figure 5.14 shows the initial result of the solid structure responded to the generated pressure through structural deformations. The high colour contours in this Figure indicated, as expected, the maximum deformation is seen near the volute inlet region. At this region, the maximum value is computed around 0.045 mm.

The steady-state solution was used as an initial condition for the transient simulation to obtain the time varied data. During the transient structural simulation, the time step was set at 1.247 e^{-5} seconds as the same time step used in the transient fan CFD simulation. The transient time was stopped at 4.115 e^{-3} seconds. This setting allowed structural data to record 330 data points which were equivalent to one revolution in the fan CFD simulation. Only one single structural simulation data was used for analysis because the files of the results generated during the simulation were too large for a single computer to open for post processing and to extract the wall motions in the solid model.

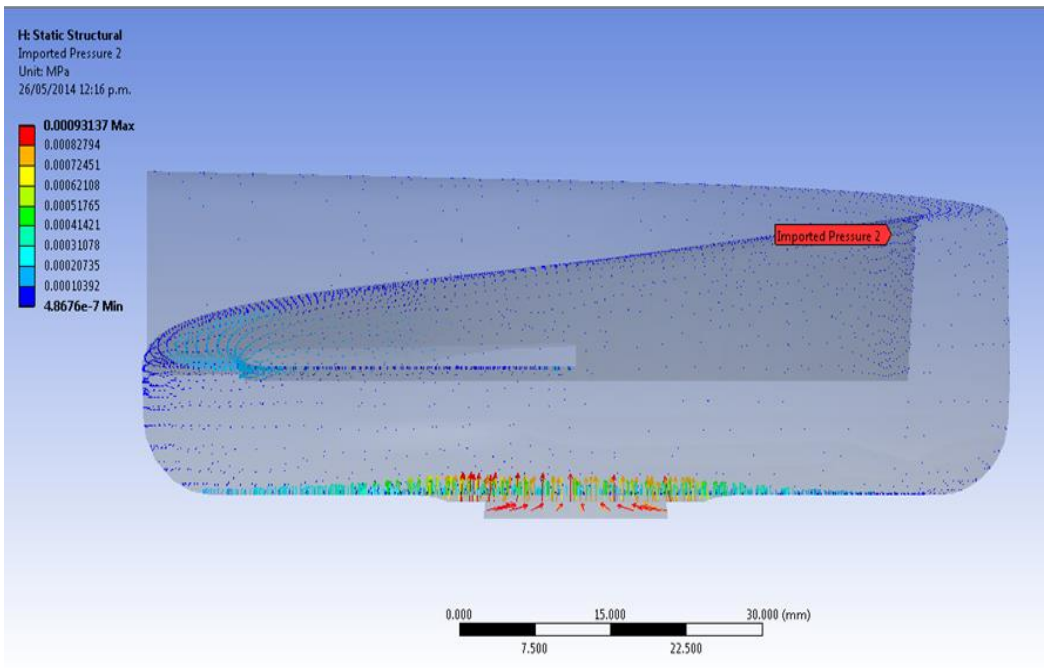

Figure 5.13: Distributed Surface Pressure on the Volute Casing

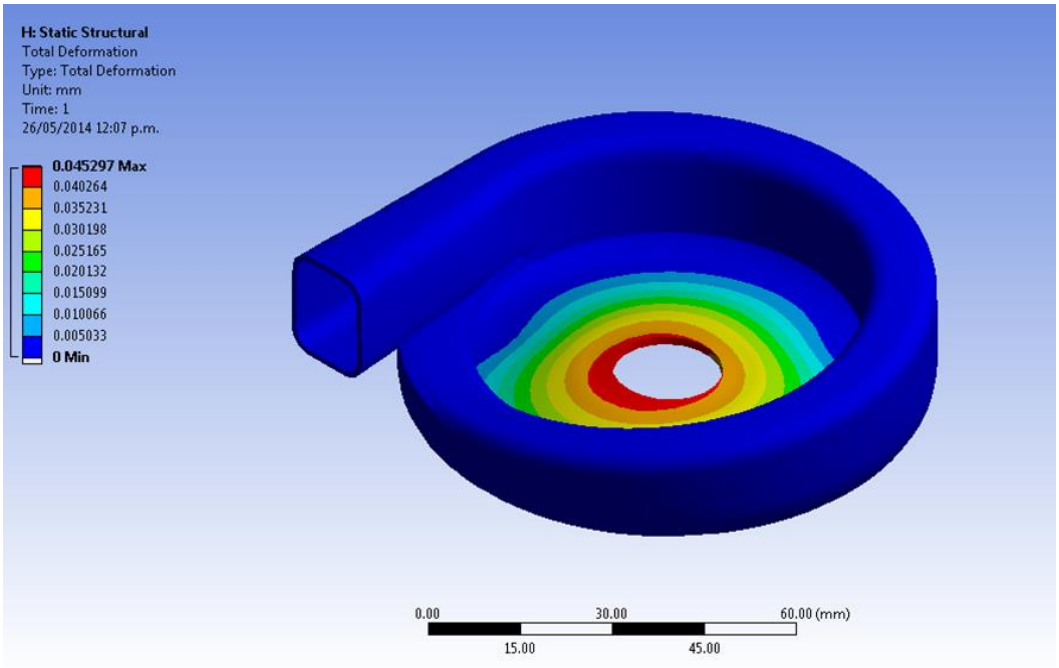

Figure 5.14: Structural Deformation of the volute casing

5.5 Results

In order to fully understand the phenomena of the flow induced noise and vibration in the centrifugal fan, this section presents numerical results of aerodynamic and aero-acoustic characteristics and the effect of the turbulent flow on the volute casing vibration.

5.5.1 Flow-field Analysis

As a partial validation of the numerical model, the flow performance curve of the centrifugal fan obtained from experimental investigation is used to compare with the numerical results. Table 5.6 shows a comparison result.

Table 5.6: Flow Performances Comparison

Flow Rates (L/min)	Predicted Pressure rise (Pa)	Experimental pressure rise (Pa)	Errors(%)
50	1077	1061	1.508
100	1038	1016	2.17
150	834	810	3

In this Table, the experimental pressure values are extracted from experimental results at different flow rates, i.e., 50 L/min, 100 L/min and 150 L/min. The pressure values are compared to numerical results. A good agreement is obtained between 3-D CFD model and experimental results. It is confirmed that the numerical simulation can be used to predict the aerodynamic performance of the centrifugal fan. However, some differences can be seen in this table and are considered minor.

The aerodynamic characteristics of the centrifugal fan are investigated graphically using the velocity and pressure contours. Figure 5.15 shows the velocity contours on the blade to blade plane views at the near hub, the mid-plane and the near shroud surfaces as well as on the meridian plane view. Uneven velocity contours are distributed over the plane view surfaces indicate a high level of unsteadiness of the flow velocity in those regions. At the same plane surface, the velocity distribution is seen very uneven. Large velocity gradients are seen at every plane surface. Large velocity gradients indicate the occurrence of large flow rotational or flow vorticity in these regions.

The unsteadiness of velocity causes high pressure fluctuations as can be seen in Figure 5.16. In this Figure, the internal static pressure shows that the pressure gradually increases

from the inlet to the outlet. Uneven pressure rise is observed at the impeller tip and is similar to what was observed in the flow structure. Whenever there is a low velocity distribution, high static pressure is observed in that location. The low pressure concentration at the impeller regions are the main cause of the flow recirculation.

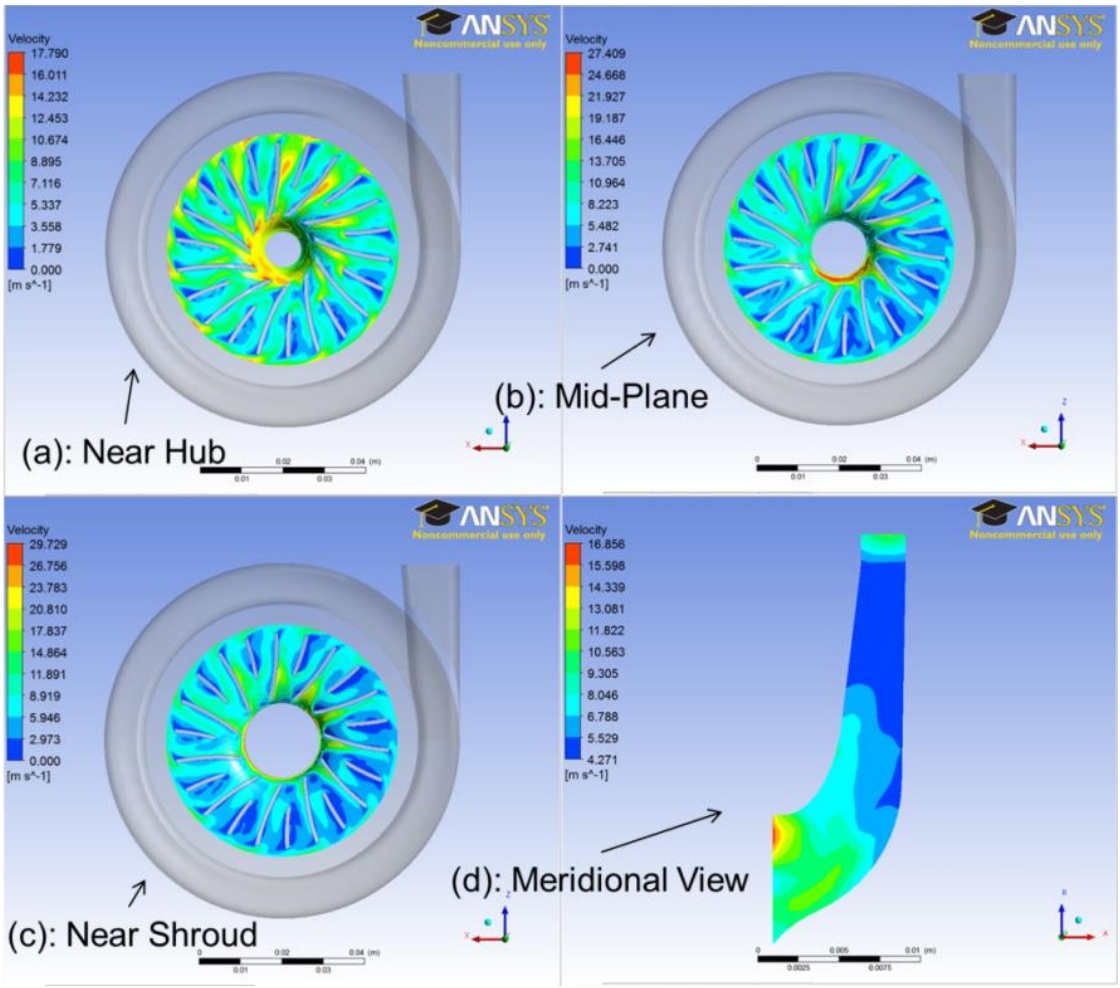

Figure 5.15: Velocity contours at the impeller surfaces

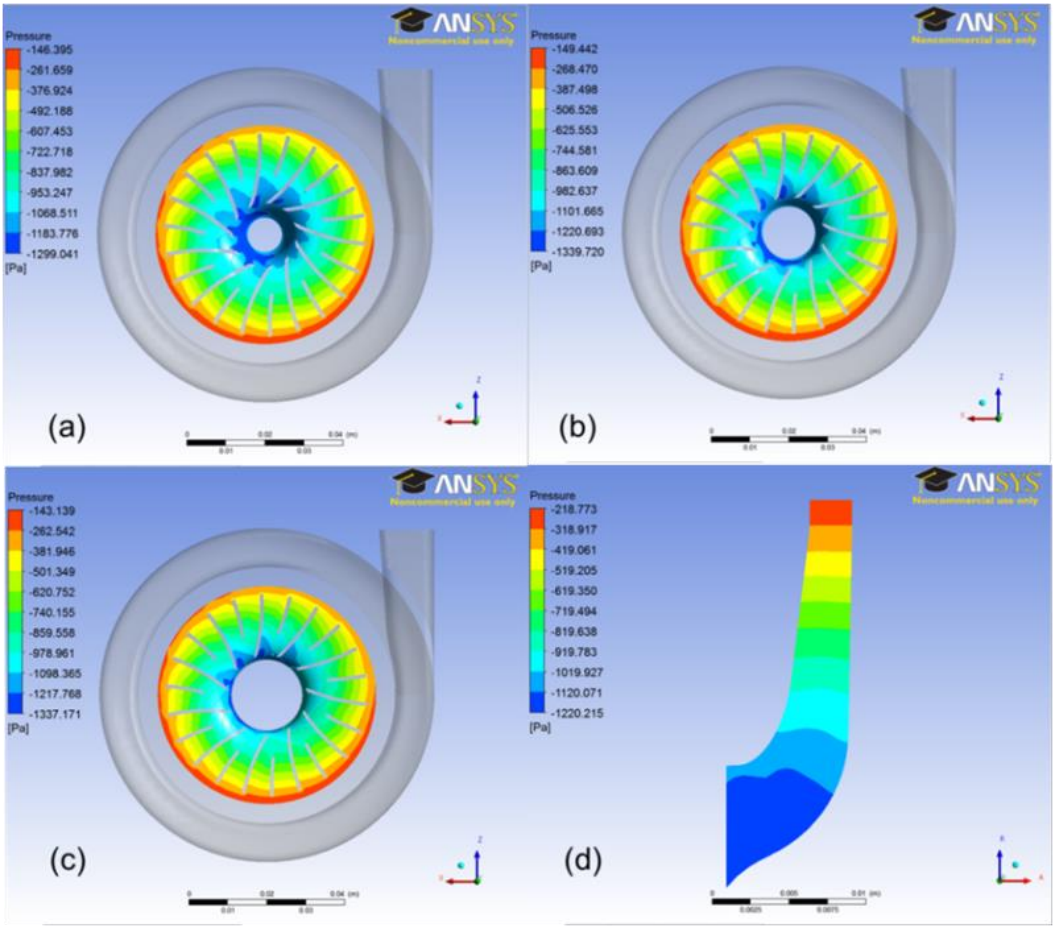

Figure 5.16: Pressure contours at impeller surface

Table 5.7 summarises the flow velocity and static pressure computed in the flow analysis.

Table 5.7: Summary of flow velocity and static pressure at impeller region

Impeller Region						
Section Plane	Velocity			Pressure		
	Min	Max	Ave	Min	Max	Ave
Near Hub Plane	0	17.79	8.885	-1299	-146.4	-687.7
Mid-plane	0	27.4	13.7	-1339.7	-149.4	-744.6
Near-Shroud plane	0	29.73	14.87	-1337.2	-143.1	-740.2

As can be seen from Table 5.7, the maximum flow velocity is computed at the surface near shroud. Zero velocity in this table indicates that there are occurrences of stall flow phenomenon in that region. Negative pressure values showed in Table 5.7 indicates that

the flow of the fan is working under suction behaviours, which mean the pressure values in that region is lower than the ambient pressure value often known as reference pressure.

Figure 5.17 shows velocity contour distribution over several internal plane views at the volute region. In this Figure, internal flow velocity is plot via its contours at several plane sections. Strong velocity gradient is seen at the volute outlet duct. Large velocity gradient results in strong flow recirculation occurred. At the lower part of the volute casing, a high but unsteady velocity is seen. The flow velocity is seen to fluctuate a lot in the lower part of the volute casing. The highest flow velocity is computed in this region up to 42 m/s. High velocity is seen to be at the volute inlet region and the surrounding region near the impeller outlet.

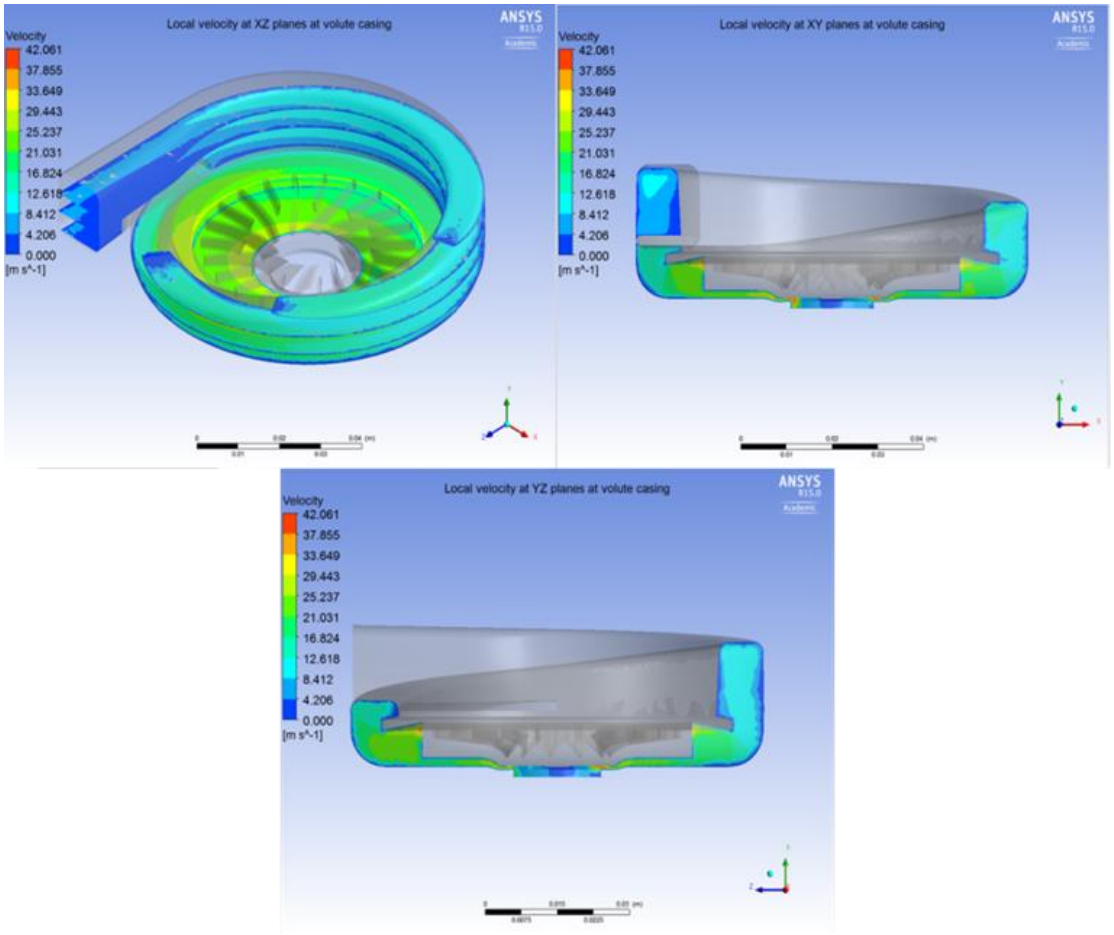

Figure 5.17: Contours of Velocity magnitude at volute regions

Figure 5.18 shows the conversion of the dynamic pressure produced by the rotation of the impeller into static pressure by volute casing and thus, maximum static pressure can be obtained at the volute outlet. However, a non-homogenous pressure distribution observed at the volute casing around the volute channel and at the lower part of the volute casing. The negative pressure is also seen at that lower part region. The negative pressure indicates large flow recirculation in that region.

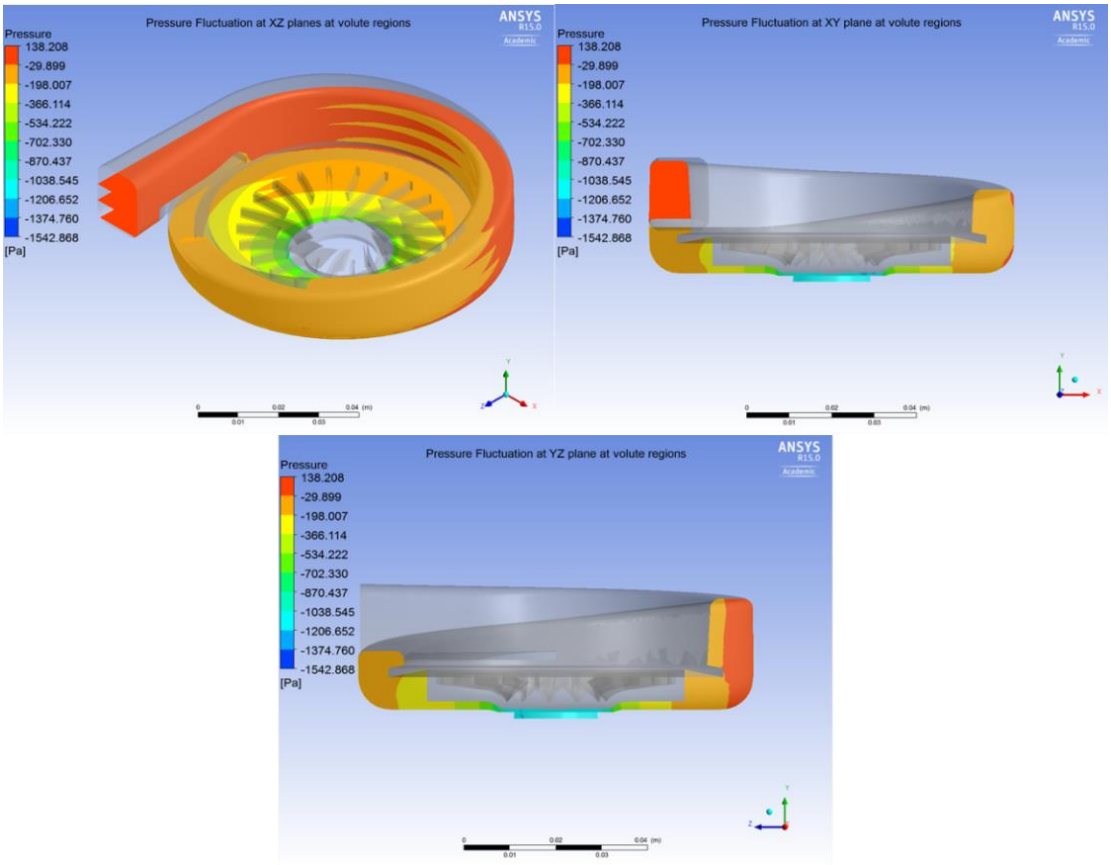

Figure 5.18: Contours of Pressure Fluctuation at Volute regions

Table 5.8 summarises the flow velocity and static pressure predicted for the volute region. Maximum velocity was computed at 42 m/s which is much higher than the maximum velocity computed at the impeller region.

Table 5.8: Summary of flow velocity and pressure at volute region

Volute Region		
	Velocity	Pressure
Max	42	138
Min	0	-1542
Ave	21	-840

The time dependent of the pressure fluctuations at blade surfaces, volute cap surface, volute tongue surfaces were also recorded during the transient simulation. The recorded signals were transformed into the frequency domain for analysis. Averaged static pressure data was first recorded in the time domain for each time step. After windowing the temporal signals using Hamming's window function, each of the recorded samples has been Fast Fourier Transform (FFT) processed and transformed into the corresponding acoustic pressure in decibel scale. The reference pressure was chosen to be 20 μPa. The frequency spectrums provide a direct measure of the amplitude of the aerodynamic pressure fluctuation at each frequency.

Figures 5.19 shows the frequency spectrum of the pressure fluctuations recorded at the impeller blade surfaces. The aerodynamic pressure spectrum shows a dominant peak at a rotational frequency (RF). There are also several smaller peaks around the RF frequency regions. The Figure suggests that the energy generated is mostly at the RF. The energy also produced at other harmonics, i.e., BPF but relatively minor in comparison to the RF.

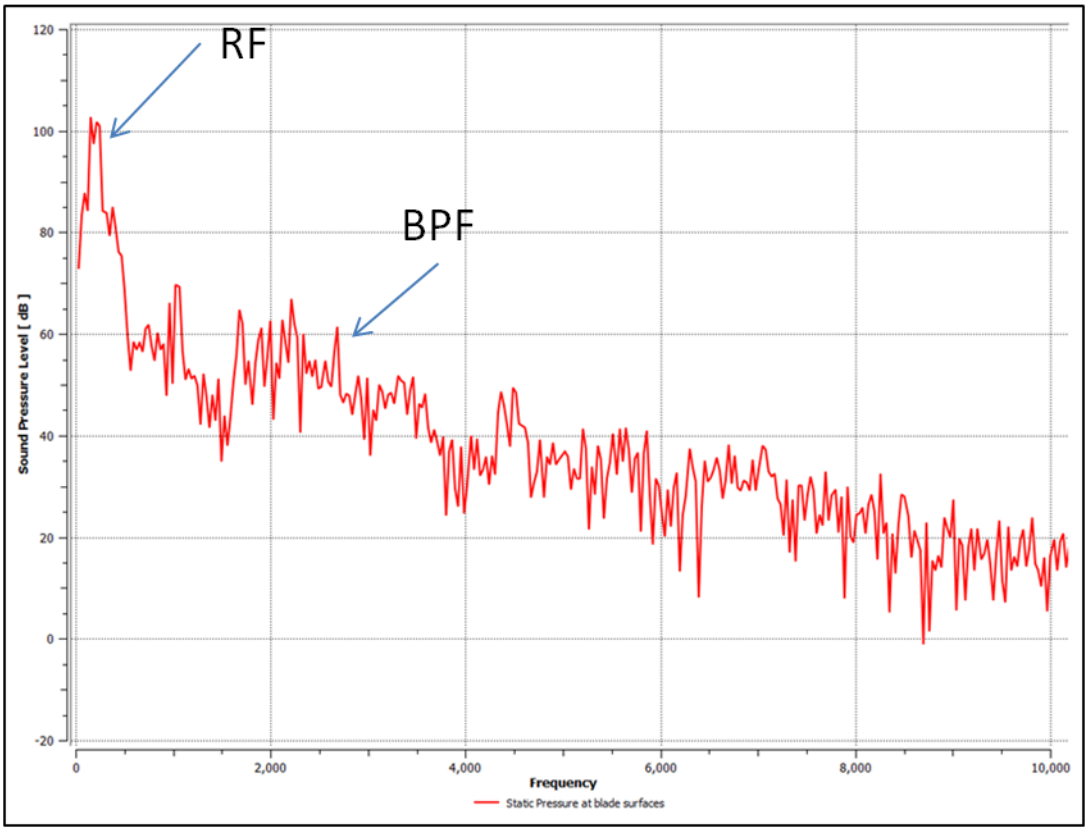

Figure 5.19: Aerodynamic pressure spectrum at the blade surfaces

Figure 5.20 shows aerodynamic pressure spectrums recorded at the volute casing and volute tongue. It is observed that the dominant peak of the frequency spectrum is seen at the rotational frequency. There are also strong energy occurring around the frequency range of 2000 Hz, where the BPF is seen. A non-dominant peak at the BPF suggests that the interaction between the rotating impeller and the stationary volute casing does generate interferences but not strong enough to have a dominant peak at BPF.

Overall, the rotational frequency (RF) is seen to be the dominant peak at all spectrums. The aerodynamic spectrum recorded at the volute tongue indicated strong energy also generated at the blade passing frequency (Figure 5.20) however, the interference was not strong enough to make the BPF dominant in the frequency spectrum. Whereas the frequency spectrum showed only the rotational frequency was dominant one. The noise level contribution by different frequency components decreased at higher frequencies.

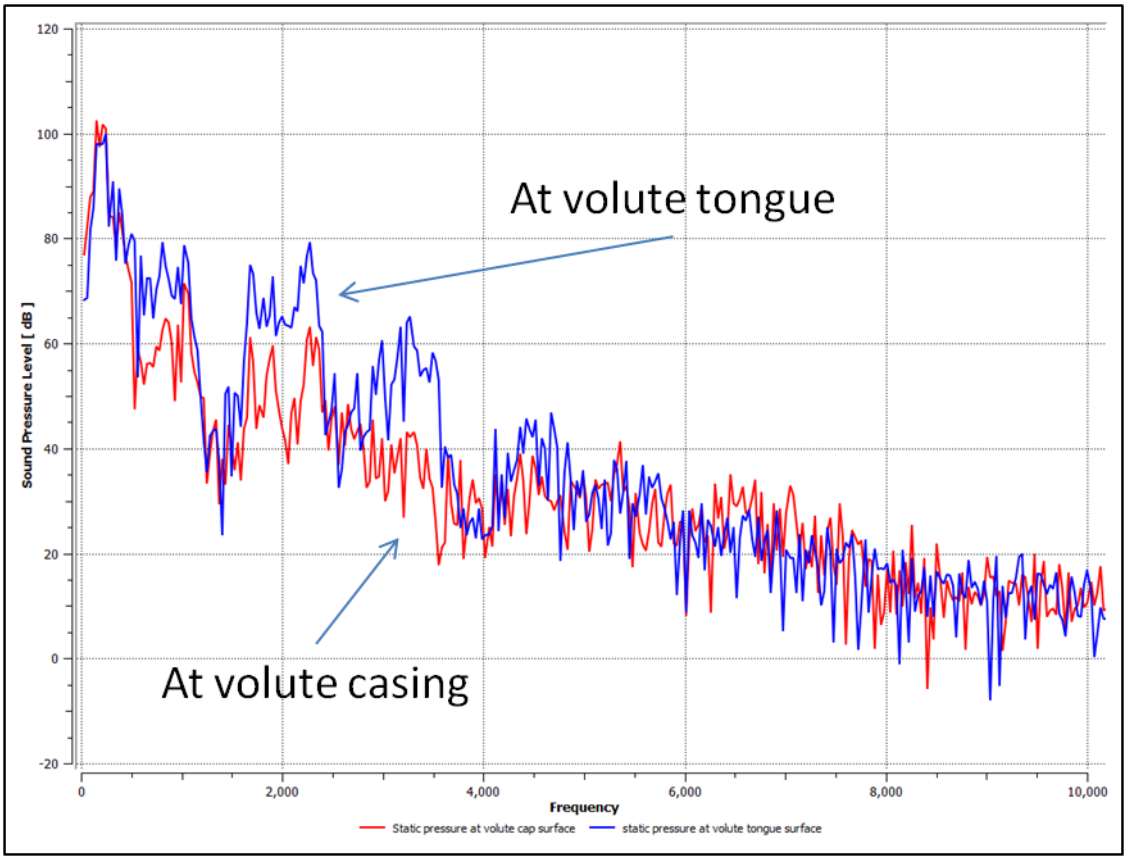

Figure 5.20: Aerodynamic pressure spectrum at the volute casing and tongue surfaces

5.5.2 Sound Analysis

The sound pressure level (SPL) obtained under the same conditions as the experimental and numerical methods are compared to each other in order to validate the numerical model.

Figure 5.21 shows that the sound pressure level spectrum of the centrifugal fan computed at a microphone point one meter away from the fan inlet. The SPL level was computed from the time dependent unsteady force signals generated by the impeller, known as monopole and dipole sources. The sound spectrum shows the dominant peak is the rotational frequency of the fan at 243 Hz. The amplitude of this peak is estimated at 55 decibels (dB). The overall sound pressure level (SPL) is estimated at 69 dB. There is a non-presence of other harmonics due to the geometrical design of the volute casing.

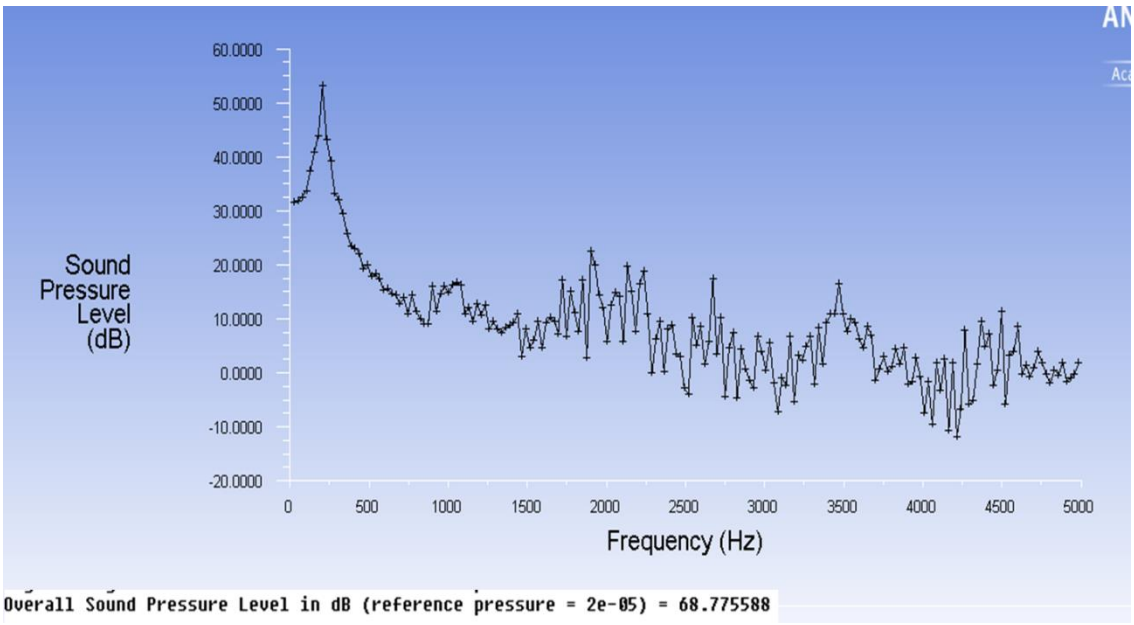

Figure 5.21: Sound Pressure Level predicted at 1 m away from fan inlet

Figure 5.22 shows a measured SPL spectrum of the centrifugal fan at similar condition to the predicted one. Maximum SPL value was computed at 42.6 dB (A) at 242.2 Hz, known as rotational frequency (RF). The total SPL was summed up at 54.3 dB (A).

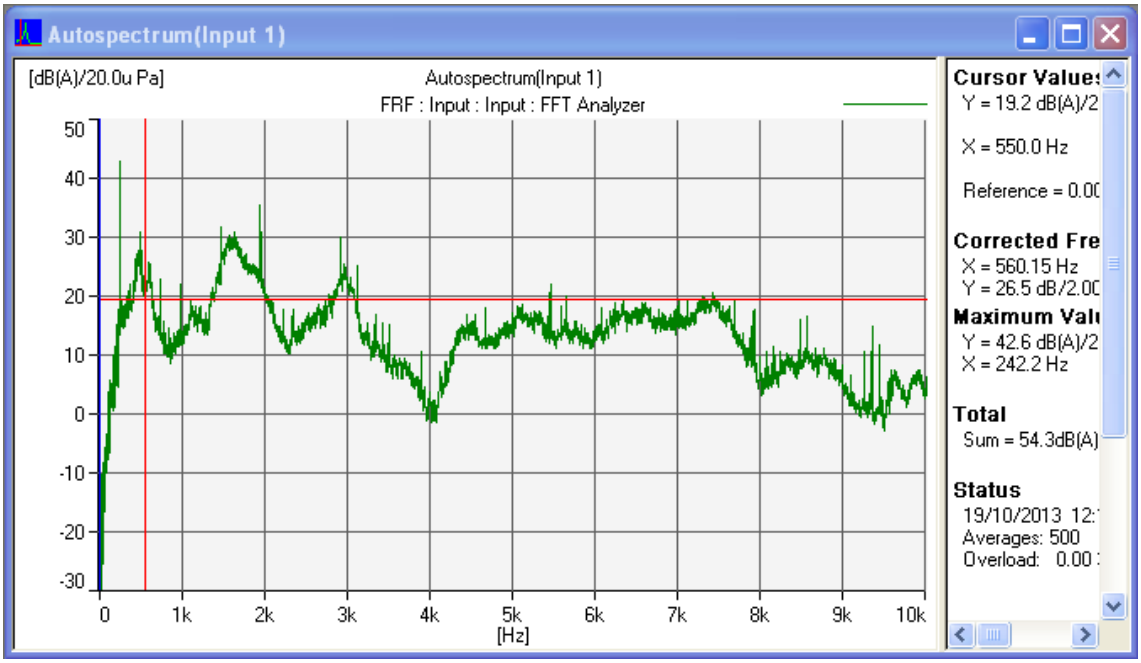

Figure 5.22: SPL of the centrifugal fan measured at the fan inlet

By comparing between these two Figures, one can conclude that the rotational frequency is dominant in both Figures. At 243 Hz peak, the SPL was measured at 42.6 dB (A). In

order to compare with the numerical value, a correction is needed. At the one third octave frequency band of 250 Hz, the correction is estimated at 8.6 dB, this will give the linear value at 51.2 (dB). The linear value corrected for the 243 Hz peak is very close to the numerical result at 55.5 (dB).

5.5.3 Vibration Analysis

Figure 5.23 shows the images of the surface deflection of the volute casing wall deformation obtained during the FSI simulation under the fan operating condition of 0.001 Kg/s mass flow rate. The images of surface deflection were randomly selected during the transient simulation. The colour contours of the mesh displacement show that most of the deflected locations are at the volute cap and near the volute inlet. Maximum deformation is estimated around 0.004 mm.

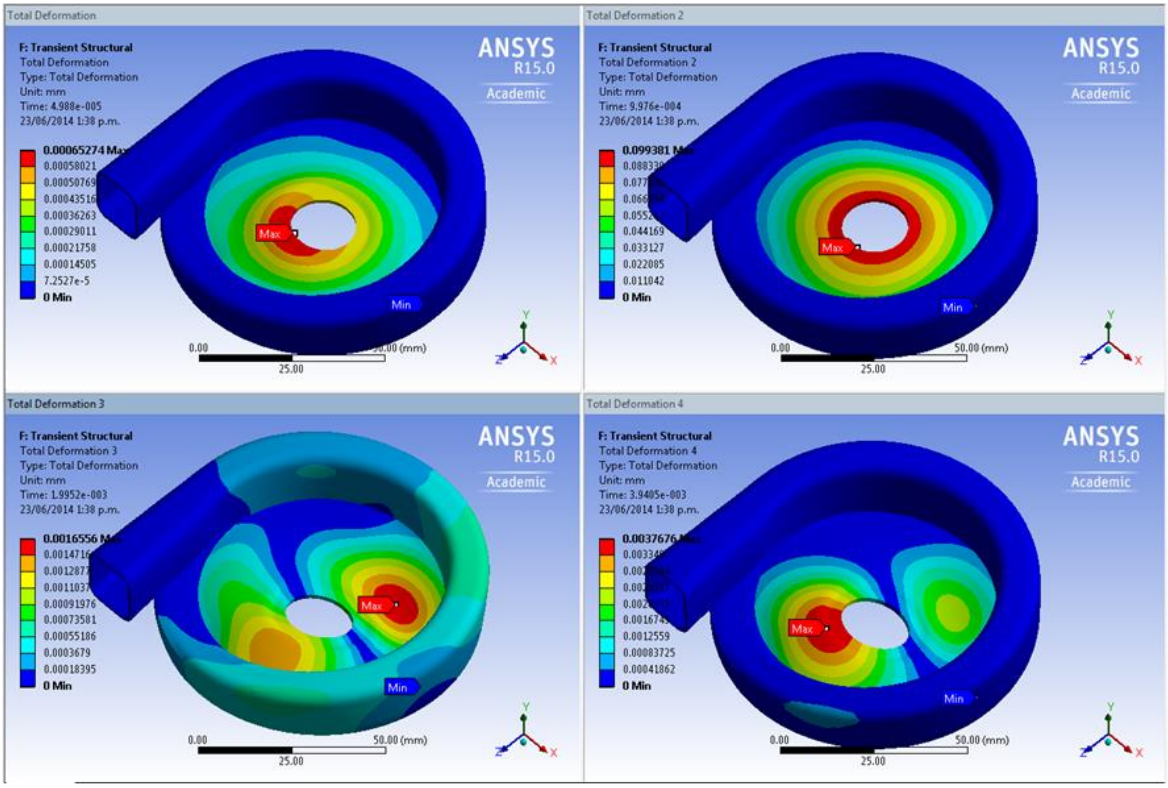

Figure 5.23: Total mesh deformation at different step times

Figure 5.24 shows a mesh deformation spectrum recorded at a maximum deformation point in the solid model. The time dependent of the displacement was recorded at a

monitor point near the volute inlet and fast-Fourier transformed to the frequency domain for analysis. From this Figure, the frequency spectrum suggests that the volute casing could vibrate in a frequency range between 200 to 1500 Hz with a large peak around 500 Hz. At this peak frequency, the maximum displacement value was estimated at $4e^{-5}$(m).

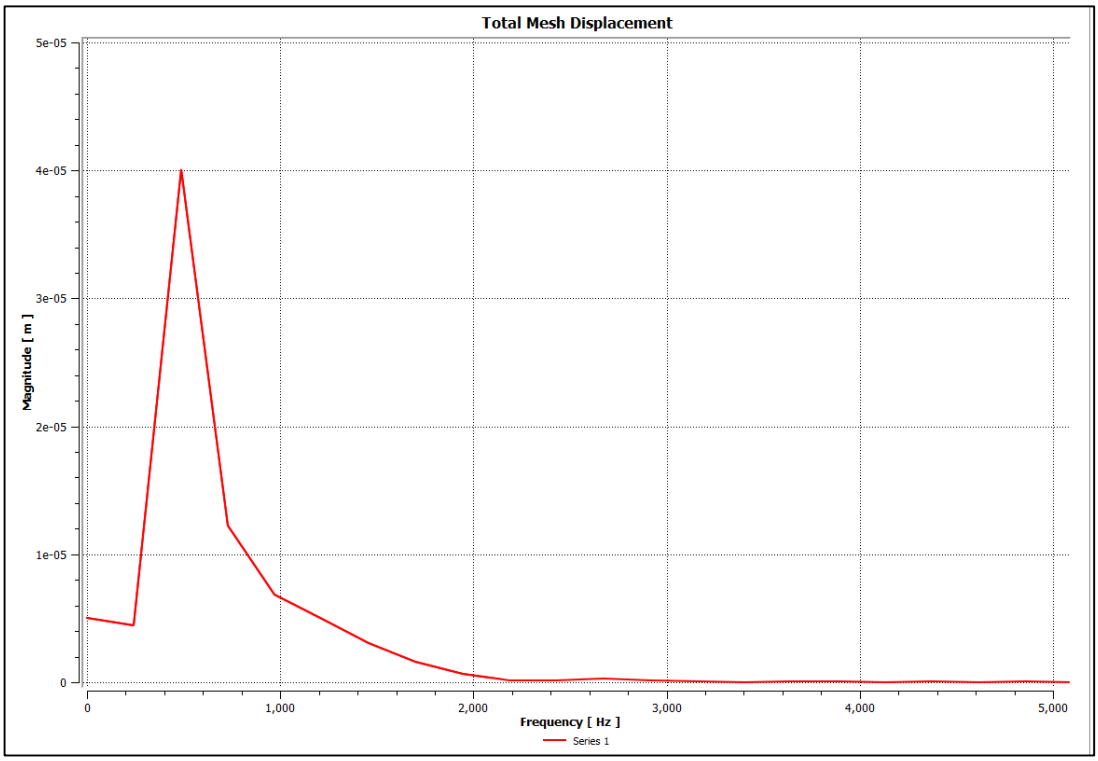

Figure 5.24: Frequency domain of the total mesh displacement

Figure 5.25 shows a vibration spectrum of the centrifugal fan measured by an accelerometer attached directly to the volute cap surface near the inlet location. The time displacement data was recorded and transformed into frequency domain for analysis. As can be seen in this Figure, multiple peaks are seen in the vibration spectrum. These peaks are related to rotational frequency and its harmonics. However, it is noticed that there is a large peak occurring between the RF and its first harmonic. This peak was measured at 381 Hz and the magnitude of this peak was measured at 4.27 e^{-5} (m).

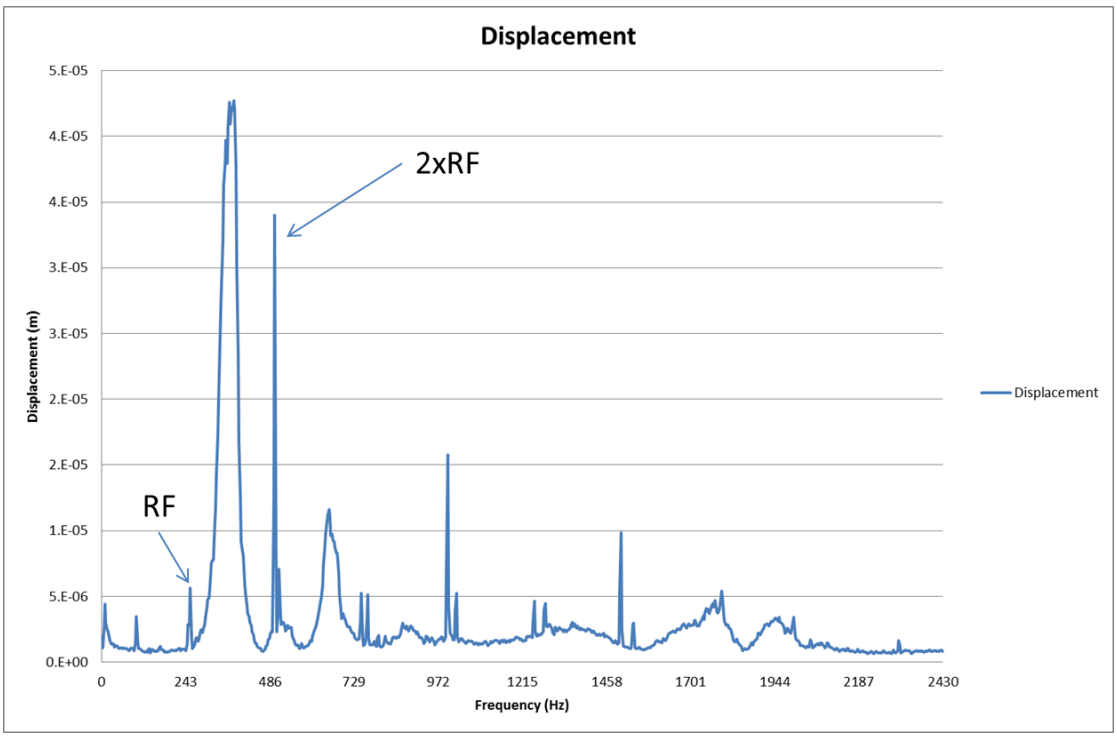

Figure 5.25: Vibration spectrum of the fan

By comparing the frequency spectrums of numerical and experimental results and ignoring those peaks related to RF and its harmonics, it is noticed that both vibration spectrums show similar trends. From observation, it suggests that the internal turbulent flow occurring at the lower part of volute casing would generate vibration around 500 Hz. The maximum predicted mesh deformation was estimated at 4x 10^{-5} (m) which was closed to the measured one estimated at 4.7 x 10^{-5} (m).

5.6 Summary

The purpose of this chapter was to investigate flow-induced noise and vibration in the centrifugal fan using the numerical simulation methods. The numerical study conducted for the centrifugal fan has served as a valuable exercise by providing some insights into noise and vibration characteristics of the centrifugal fan that may benefit product design. The study has applied the CAA and FSI simulations to investigate the flow-induced noise and vibration problems. The accuracy of the numerical simulation was validated by the experimental data. The comparisons between the numerical simulation results and the

experimental data show good agreements at discrete values. It was found that the noise characteristics of the centrifugal fan is broadband in nature with dominant peak at rotational frequency. Also, it was found that high pressure fluctuations were seen at the lower part of the volute casing that caused a large vibration in the volute cover near the inlet region.

Chapter 6: **Duct System Simulation**

6.1 Introduction

The numerical simulations are performed in this chapter to investigate the flow-induced noise and vibration in the duct system of the CPAP devices. Firstly, the CAA with hybrid approach is used to predict the flow-induced noise. Secondly the FSI simulation is used to predict the flow-induced vibration.

This chapter consists of several sections. Section 6.2 covers the introductions and developments of the duct models for numerical simulation purposes. Section 6.3 presents the CAA simulation process to predict the noise generated from the ducts. Section 6.4 presents the FSI simulation process to investigate the flow-induced vibration. Section 6.5 discusses the experimental approach for validation. Finally, the results are presented and validated in section 6.6.

6.2 Simplified CPAP Duct System

The flow path inside the CPAP device is an important system. The flow path is used to deliver the air from outside to the centrifugal fan and to transfer high pressure airflow from the centrifugal fan to the humidifier. Inside the CPAP device, the flow path is created by many solid components assembled together. The complexity of the original duct path requires a lot of rework before the duct model can be used for numerical simulation

purposes. The duct models are reconstructed and remodelled from the original dimensions. Small lines and non-important surfaces are removed to reduce the number of surfaces in order to reduce unnecessary small mesh elements that could affect the computational time.

Figure 6.1 shows simplified solid and fluid models of the inlet and outlet ducts in the CPAP device. In this Figure, the models were reconstructed and remodelled in the ANSYS environment for numerical simulation purposes. As shown, the models has small and short with many changes in size, shape and direction, etc.

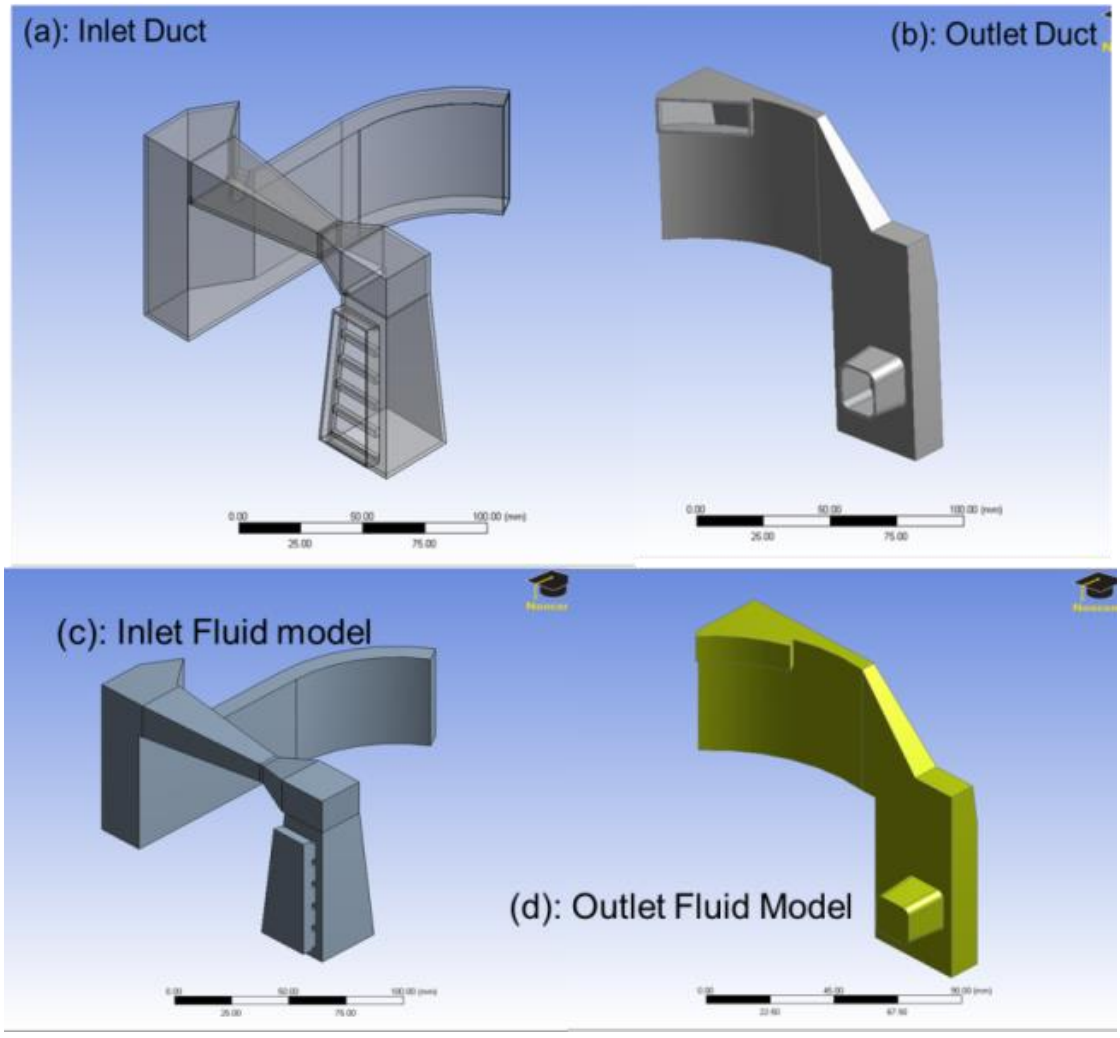

Figure 6.1: Simplified Duct Models: (a) inlet solid part, (b) outlet solid part, (c) inlet fluid model, (d) outlet fluid model

6.3 Computational Aero-acoustic (CAA) Simulation

The CAA with hybrid approach are first employed to predict the noise generated from the duct models. The CAA simulation consists of two simulated steps:

- To generate the noise sources and,
- To predict the noise generation.

6.3.1 Computational Mesh Models

Figures 6.2 and 6.3 show the 3-D fluid models of the inlet and outlet ducts. The fluid models were connected to additional computational domains to ensure that the turbulent flows were fully developed during the CFD simulations. Two long ducts and two large plenums were added at the inlet and outlet boundaries to represent the open atmosphere. The computational domain length is 300 mm length, which was long enough to prevent the reversed flow effects on the flow fields during the CFD simulations.

Figures 6.4 and 6.5 show the mesh models for numerical simulation purposes. In this Figure, the duct models were divided into five small regions or elements. The duct models were meshed with unstructured and structured mesh methods. A fine mesh resolution was maintained in regions where high flow gradients are expected, for instance, close proximity to the duct walls and a shear region in the sudden expansion and constriction inside the ducts. The mesh was created in the ANSYS FLUENT software. Near-wall treatment and turbulence length scale was considered and was satisfied for these simulations.

At the mesh bodies, the maximum mesh size was set at 5 mm length. At the mesh surfaces, the mesh size was set to 1 mm. Total 1.2 e^6 and 1.46 e^6 mesh elements were generated for the inlet and outlet models respectively.

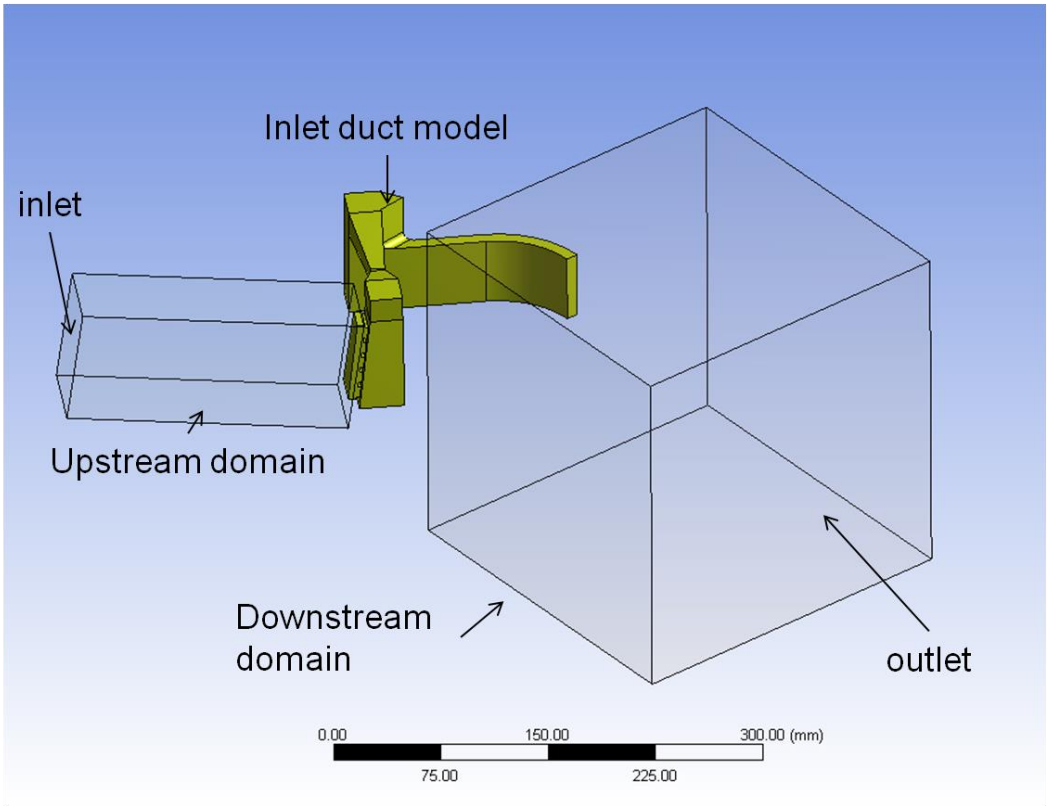

Figure 6.2: Inlet fluid model used in flow field simulation

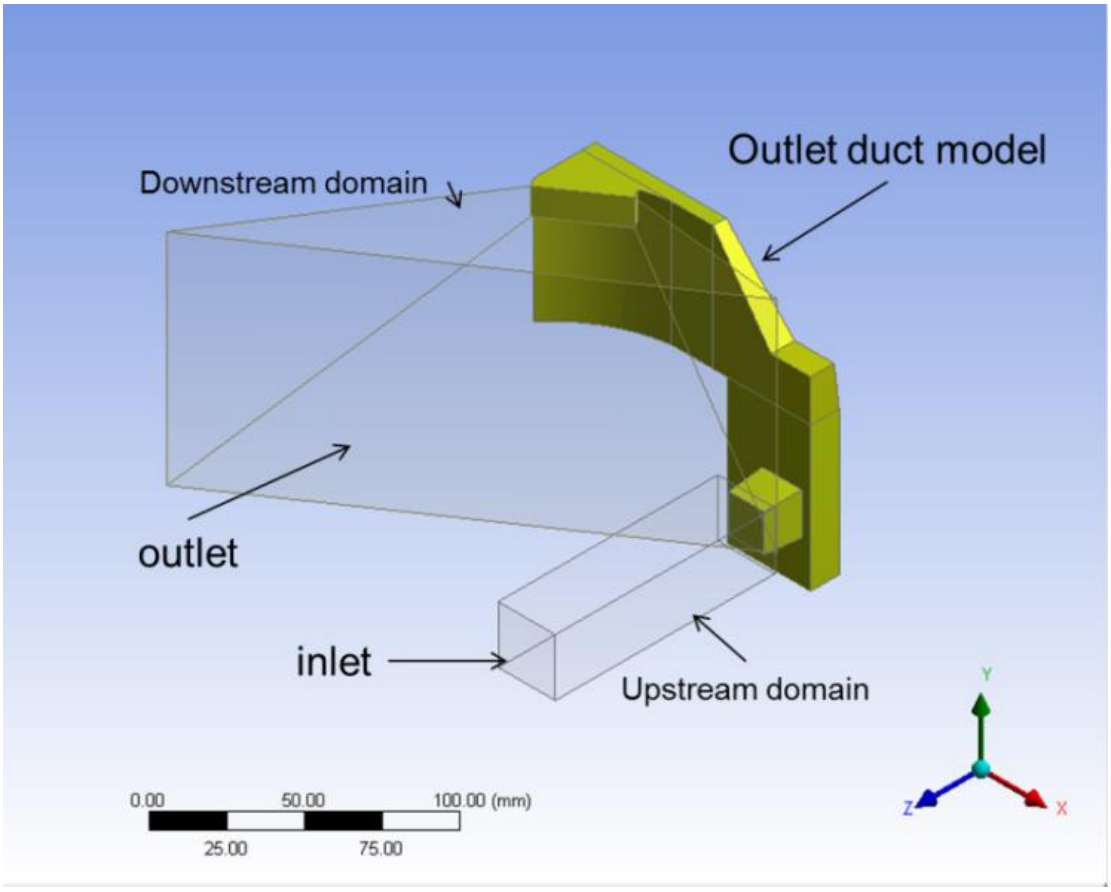

Figure 6.3: Outlet fluid model used in flow field simulation

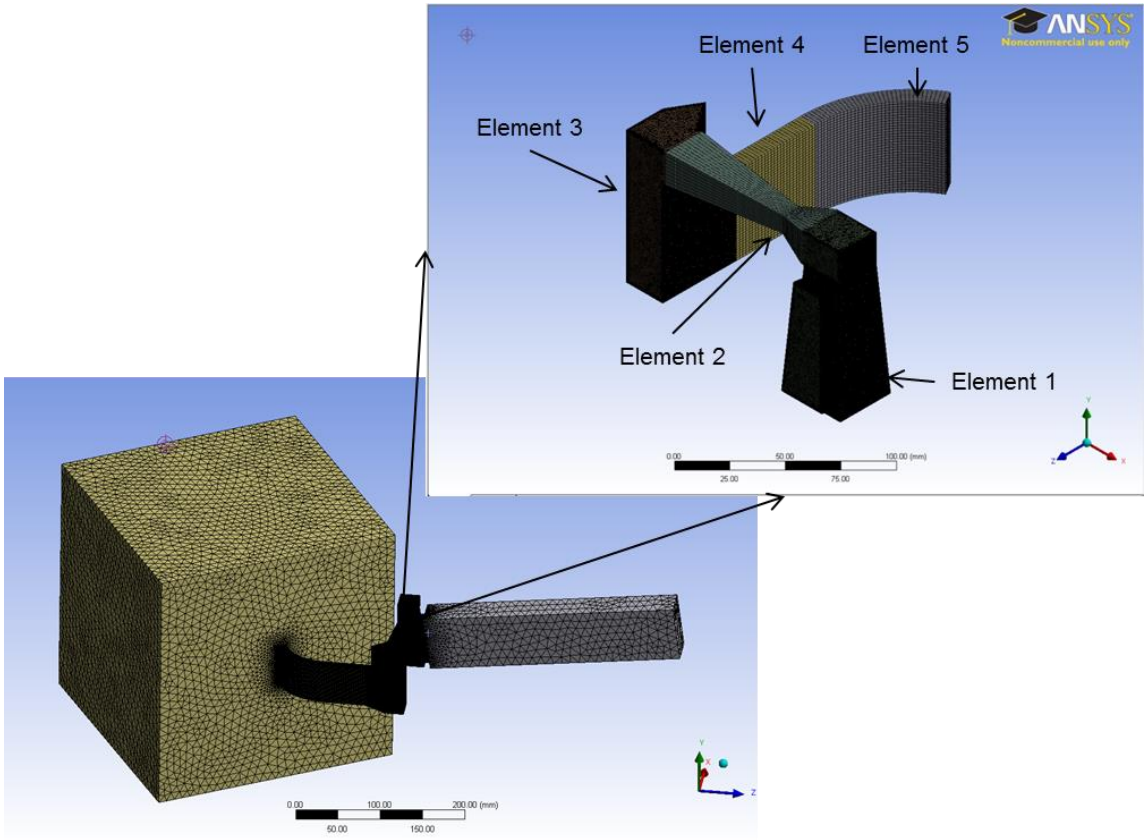

Figure 6.4: Numerical Fluid Inlet Model

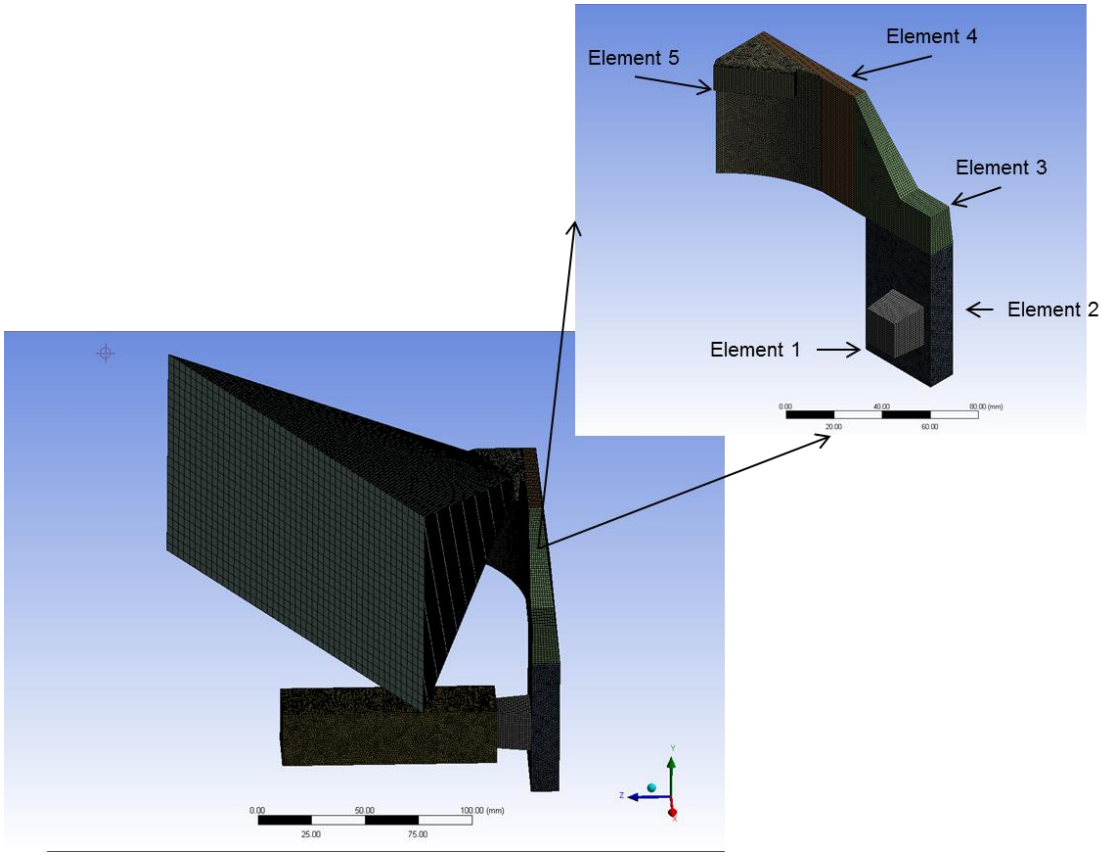

Figure 6.5: Numerical Fluid Outlet Model

In order to confidently use the mesh model for acoustic predictions, the mesh sensitivity test was performed with different mesh sizes from coarsen to finest mesh size. The test was performed with the steady-state CFD simulation. It was found that the pressure differences were insignificantly different. However, this study involved acoustic prediction and it required a better and finer mesh resolution. Therefore, the mesh sizes presented in this study were chosen and given in Table 6.1.

Table 6.1: Mesh details of the duct models

Element	Inlet Model		Outlet Model	
	Mesh Type	Number of Elements	Mesh Type	Number of Elements
Upstream	Unstructured	37620	Unstructured	220959
Element 1	Unstructured	581591	Structured	4896
Element 2	Structured	33286	Structured	144126
Element 3	Unstructured	461294	Structured	12753
Element 4	Structured	22500	Structured	31320
Element 5	Structured	31050	Unstructured	272771
Downstream	Unstructured	13500	Structured	770784

6.3.2 Solver Settings and Boundary Conditions

In order to obtain the aero-acoustic noise sources, the internal unsteady flow structures of the duct must be predicted first. A constant mass flow rate (MFR) was applied to the inlet boundary conditions corresponding to a 50 L/min flow rate of air as the same as the condition used in the centrifugal fan simulation in chapter 5. Also, the solver settings were the same as the one applied set for the centrifugal fan. The details of the solver setting can be found in Chapter 5 and will not be repeated here.

Since a 0.001 Kg/s mass flow rate (MFR) was applied to the inlet boundary, the initial velocity was calculated around 3 m/s and the Mach number was calculated around 0.009; at the low Mach number, the flow was assumed to be incompressible.

The pressure outlet was applied to the outlet boundary conditions value at 0 Pa (pressure gauge). The boundaries of the ducts and the computational domains were kept as no-slip walls. The actual inlet and outlet duct boundaries were set as interior surfaces so the air can pass freely from the computational ducts through the duct models and out to the plenums. The boundary conditions are summarised in Table 6.2

Table 6.2: Boundary conditions for the duct simulations

Boundary	Boundary Condition	Value
Inlet	0.001	(Kg/s)
Duct inlet, outlet	Interior	
Duct Walls	Non-slip Walls	
Outlet	Gauge Pressure	0 (Pa)
Computational Walls	Non-slip Walls	

6.3.3 Flow Simulation Procedures

The CFD simulation started with a steady-state simulation. In this simulation, the $k-\varepsilon$ RNG turbulence model was used to generate flow turbulences. A second order discretization scheme and non-equilibrium wall functions were used. The steady state simulation was allowed to run until statically steady. The steady-state solution converged after 3000 iterations.

The steady state solution was used as an initial solution for transient simulation to obtain the time varied source terms. The unsteady simulation was performed with the $k-\omega$ SST turbulence model. A time-step of $1.25e^{-3}$ seconds was first applied. During the transient simulation, the pressure signals at several locations were continuously monitored to ensure that the simulations reached dynamic stability. The transient simulation became dynamically stable after 3000 steps. Once the dynamic stability was established, the time-

step was reduced to 1.25 $^{e-5}$ seconds and the pressure data was recorded at different time steps. The pressure data was used as the near-field source data for acoustic analysis. The pressure data was recorded for a total number of 3000 steps.

6.3.4 Acoustic Coupling

This section utilizes the availability of the acoustic models adopted in the ANSYS FLUENT software to compute the sound pressure level of the centrifugal fan. The setting steps were the same to the ones described in section 5.3.5 in Chapter 5.

During the transient simulation, surfaces and regions are chosen for the output of dipole and quadrupole data. The time step is 1.25 e^{-5} seconds which will give the maximum sampling frequency of 80000 Hz. However, the target frequency is up to 4000 Hz. The written frequency can be coarsened with a factor of 4, which gives a sampling frequency of 20000 Hz. This value is a sampling frequency and according to the Nyquist theorem, the highest resolved frequency will be 10000 Hz. A total of 3000 data points are recorded which gives a sampling frequency of 3.333 Hz.

6.4 FSI Simulation

The second numerical simulation is performed to investigate the flow-induced vibration of the solid duct models. The FSI simulation consists of two steps:

- Static Structural Simulation is performed to obtain initial conditions and,
- Transient Structural Simulation is performed to obtain time dependent variables, i.e., displacement, velocity and acceleration, etc.

6.4.1 Solid Mesh Models and Boundary Conditions

Figures 6.6 and 6.7 show the solid mesh models of the inlet and the outlet ducts. The wall thickness of the solid models was fixed at 1 mm. The solid models were mesh with the

structural APDL mesh method. For the inlet model, a total of 42664 mesh elements and 42750 nodes was generated. For the solid outlet model, a total of 22657 mesh elements and 22718 nodes was generated. Prior to the total mesh numbers listed above, the mesh independence was performed by using two finer mesh sizes. The test was performed with static structural simulation under the same boundary conditions. The results showed that the mesh deformation differences were less than 5 %. Therefore, the coarsen mesh was chosen.

Figures 6.8 and 6.9 show the solid boundary conditions applied to the solid models. The models were placed on a hard surface during experimental tests, therefore, a fixed boundary condition was applied at the bottom surfaces of the solid models. Fixed conditions allowed restriction of the solid ducts from moving in certain dimensions as it is intended to limit the vibration in the vertical direction. This was done by limiting the degree of freedom of all the nodes at the boundary surfaces.

A fluid-solid interaction boundary condition was also applied to the wall surfaces where it is contacted with the fluid interfaces. The settings allowed communication between the solid and the fluid models at every simulated time step.

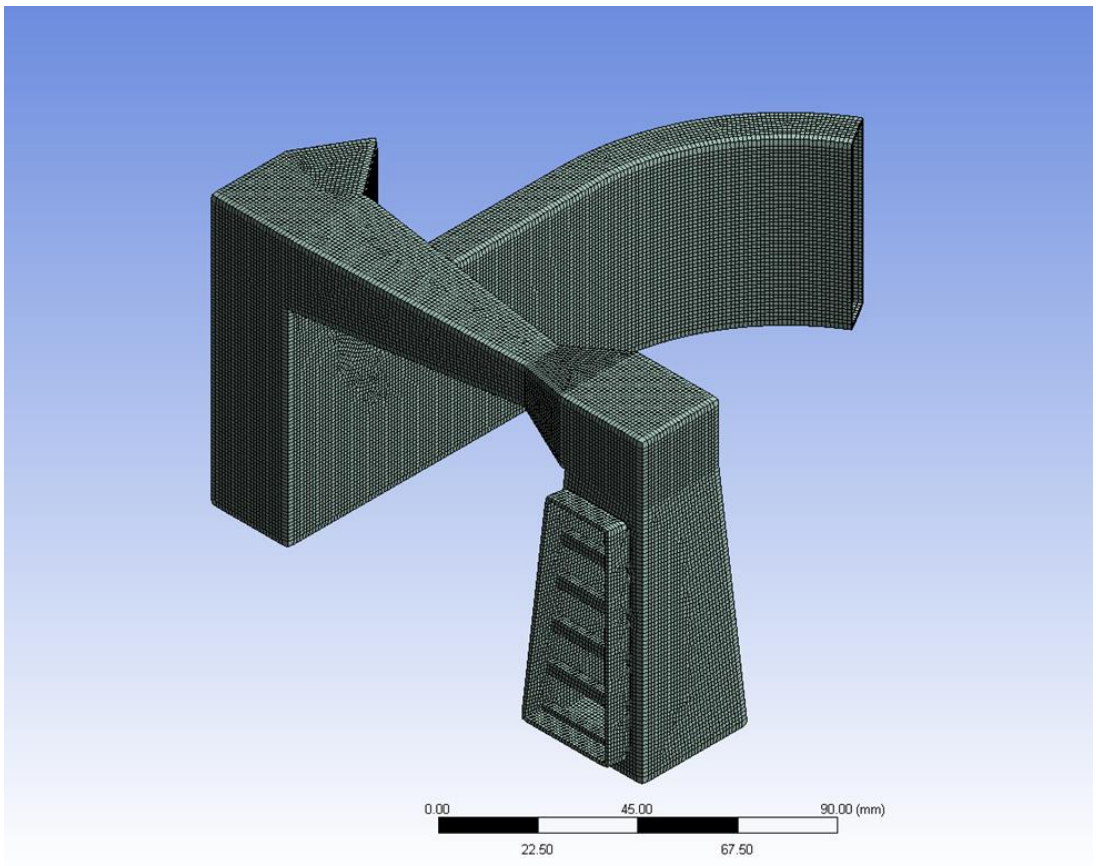

Figure 6.6: The solid mesh model of the inlet duct

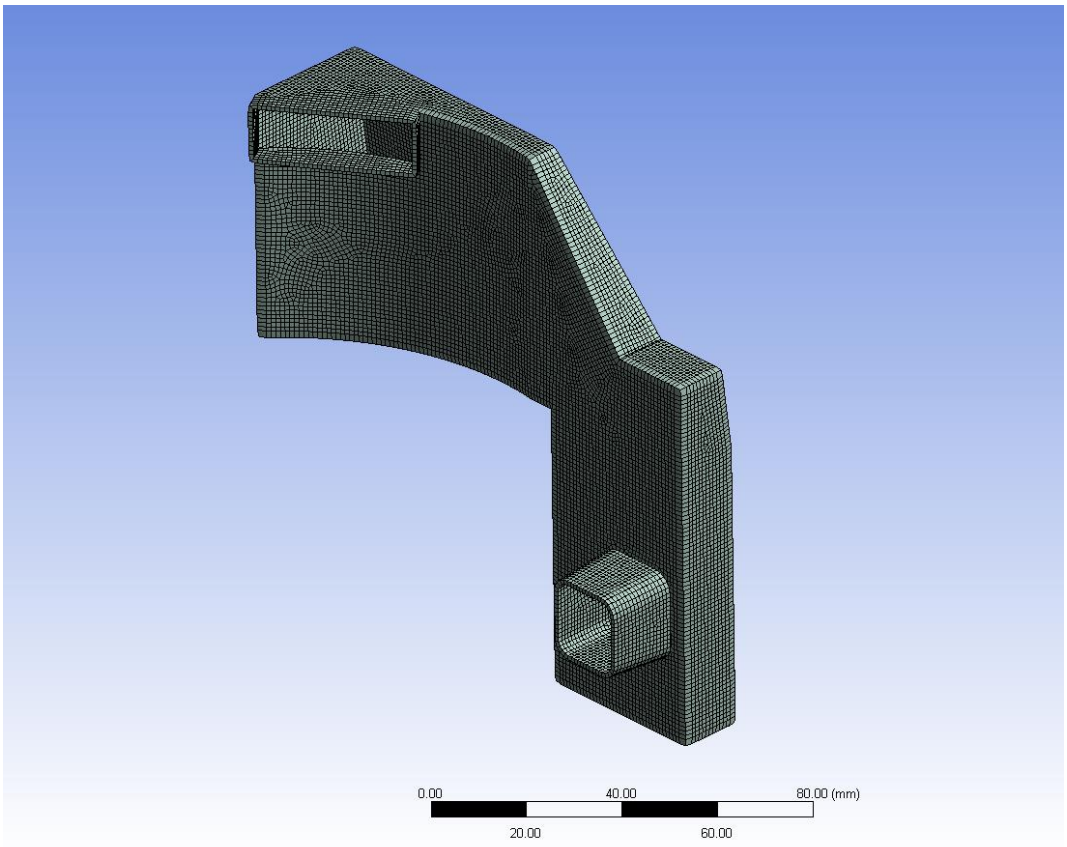

Figure 6.7: The solid mesh model of the outlet duct

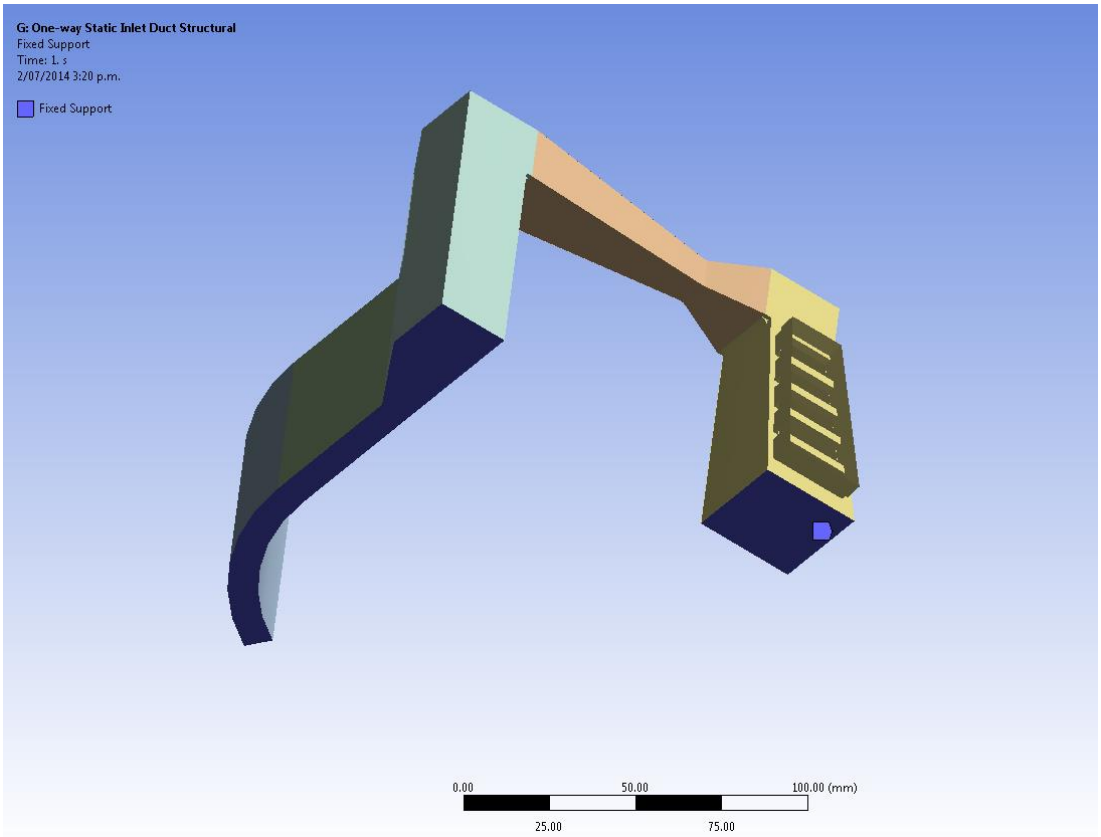

Figure 6.8: Solid boundary conditions of the inlet duct

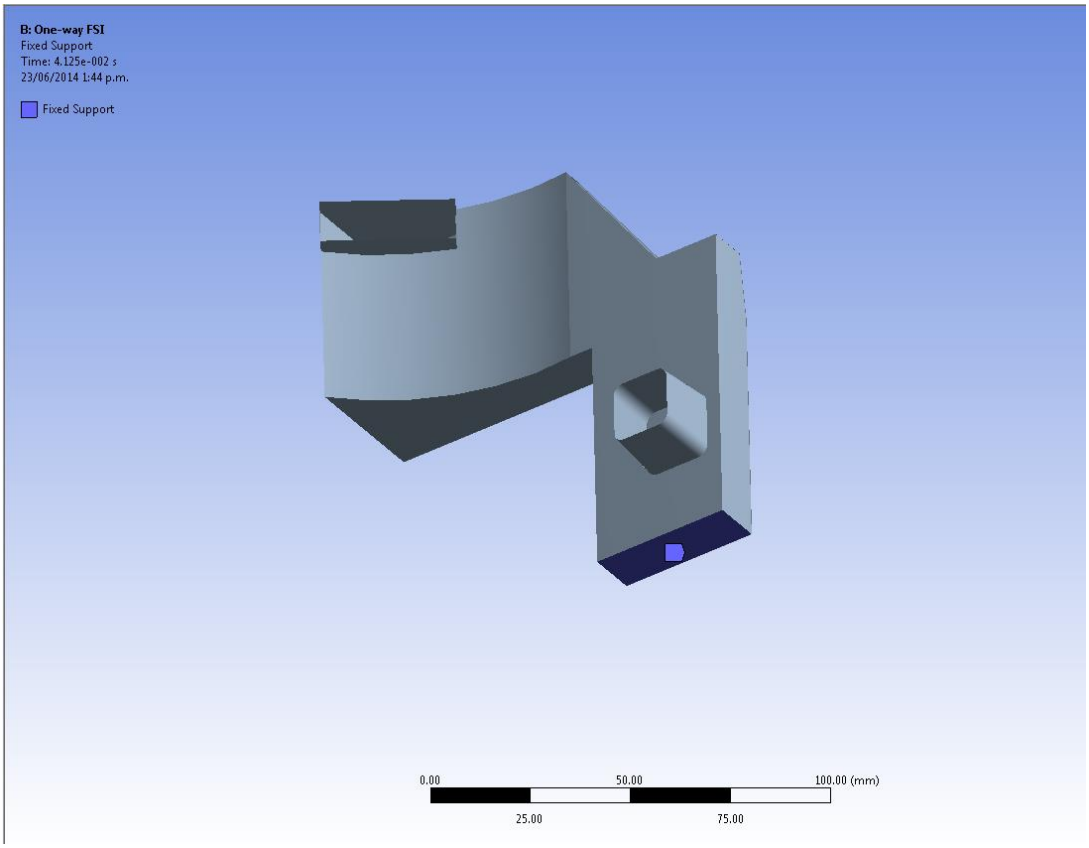

Figure 6.9: Solid boundary condition of the Outlet duct

6.4.2 Solver Settings

In order to perform the FSI simulation, the solver settings are required for both fluid and solid models. This setting allows for both models to communicate with each other during the simulation time.

For the fluid model, the solver setting can be similar as in section 6.3.2 previously. A system coupling was set at the fluid wall surface defined as FSI interface. For the solid model, the fluid-structure interface was applied to the solid surfaces where it contacted with the fluid surfaces in the fluid models. Finally, the CFD and the Structural simulations were set to connect to each other through a system coupling available in the ANSYS software. This system coupling acted as a control box, where it allowed one-way or two-way data transfer and static or transient approaches could be performed. In this study, the focus was on the flow-induced vibration problem, therefore, only one-way communication was applied.

6.4.3 Simulation Procedures

Static structural simulations were first performed to obtain initial solutions for transient FSI simulations. The converged steady state CFD results were used as initial inputs and set to interact with solid models. During the static structural simulation, the fluctuated forces from the fluid models were applied to the solid FSI wall interface. The static structural simulations were set to run until the converged solutions were reached. The converged static structural simulations were used as initial conditions for the transient solutions to obtain the time dependent data. The time steps for the transient simulation were fixed at 1.25 e^{-5} seconds similar to the CFD simulations. A total of 330 time steps were recorded during the transient FSI simulation due to the limitation of the computational resources.

6.5 Experimental Measurements for Validation

For evaluation of the numerical results, a series of noise measurements were conducted for the duct models during the experimental investigations. Two prototype duct models were developed and placed inside a noise test room as shown in Figure 6.10.

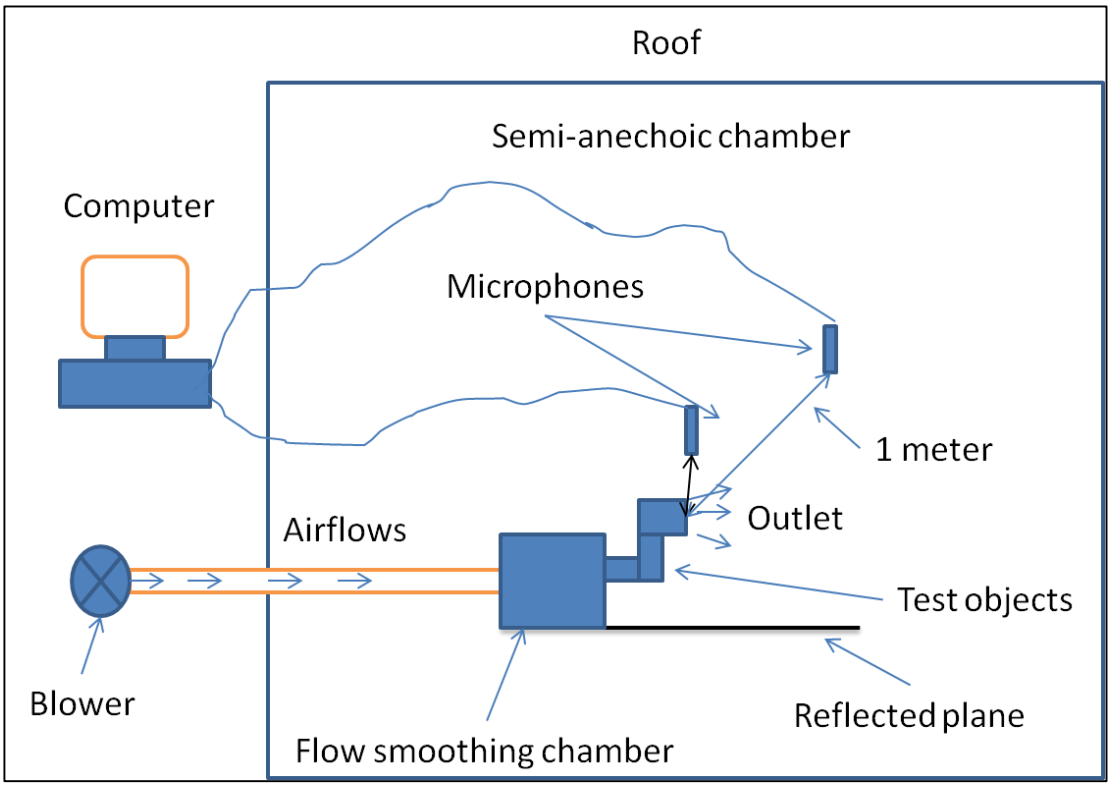

Figure 6.10: A schematic of experimental setup

From this Figure, an airflow was provided by a centrifugal fan which was placed outside the semi-anechoic test room. The tested ducts were connected to the flow smoothing chamber, which was inserted with sound proofing materials to ensure that the flow was smooth and the generated noise propagated from the centrifugal fan was dampened to the minimum.

Two microphones were placed in front of the outlet boundary to capture the noise generated from ducts. One microphone was placed in the near-field region to capture the sound power level (PWL) and one was placed in the far-field region to measure the sound pressure level (SPL).

6.6 Results

6.6.1 Flow-field Analysis

The CFD models was run with appropriate boundary conditions at 0.001 Kg/s mass flow rate which was mentioned earlier. The aerodynamic characteristics of the duct models were analysed graphically via flow velocity streamlines under vortex conditions and pressure contours. Figures 6.11 through 6.14 show contours coloured with static pressure distribution and streamlines coloured with velocity magnitude inside the duct models.

The acoustic pressure fields inside the duct models was plotted via the pressure contours as shown in Figures 6.11 and 6.12. From these Figures, it can be noticed that the locations of low pressure are seen at the constricted duct element for the inlet duct model (Figure 6.11) and at the outlet region for the outlet duct model (Figure 6.12). Overall, the distribution of static pressure shows that the change of pressure on the duct interior planes can be intense which results in strong vertex, energy loss and thus contributes to noise generation.

Figures 6.13 and 6.14 show streamlines coloured with velocity magnitude inside the duct models at several interior planes. From these Figures, it clearly shows that the specific geometries of the duct model has generated flow recirculation and velocity gradients at several locations and at turning corners. The flow travels downstream and impinges on the wall and produces vortices or flow recirculation. The vortices inside the duct models draw energy from the mean flow and as they impinge on the downstream wall, they release energy into the acoustic fields. Since the vortices impinge and dissipate on a solid wall, they cause the dipole source noise.

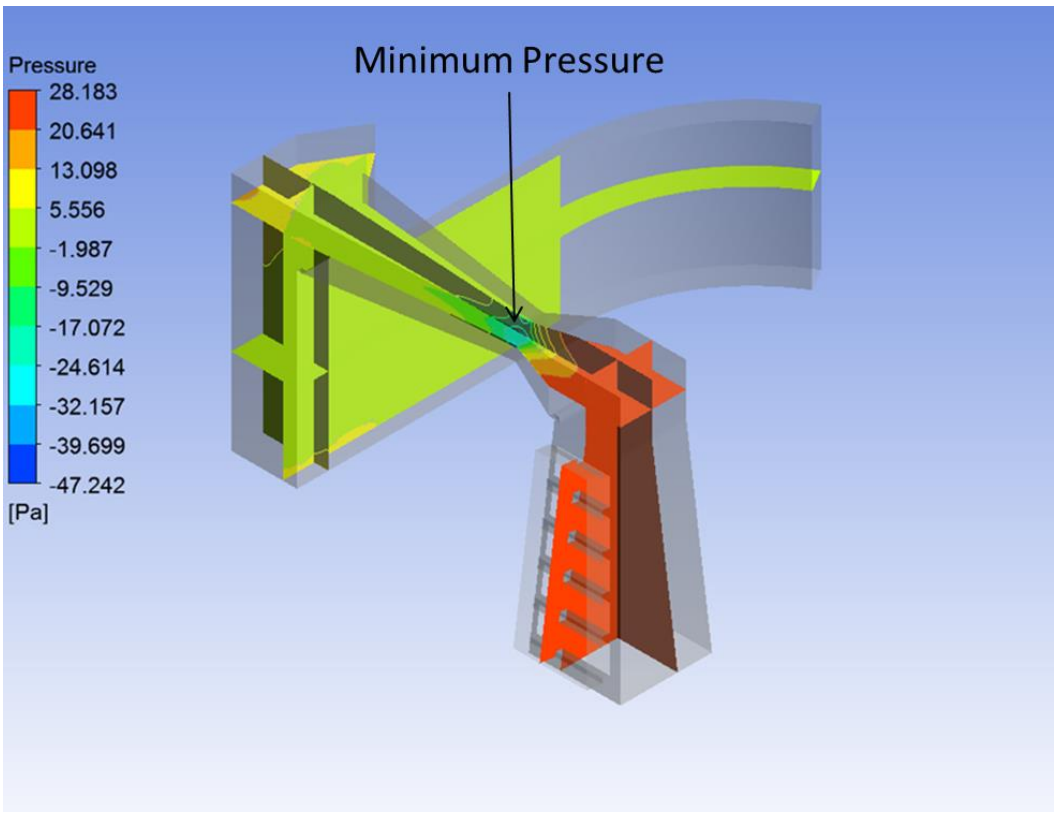

Figure 6.11: Static pressure distribution inside the Inlet duct

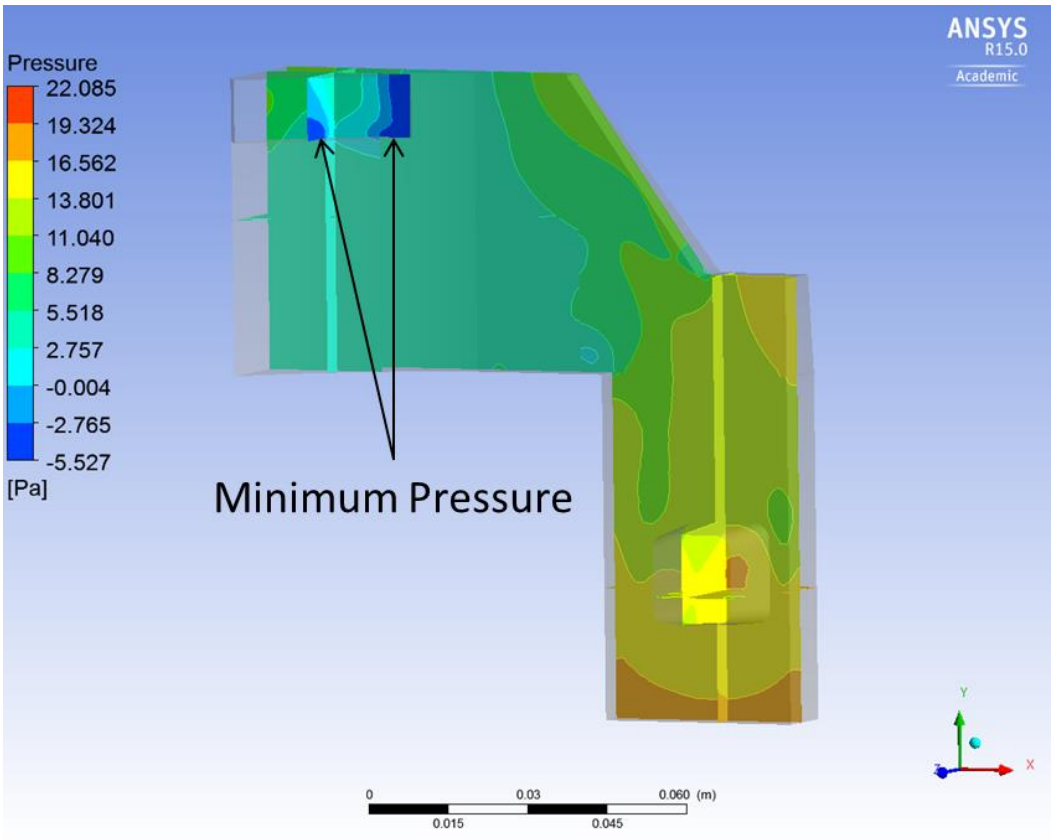

Figure 6.12: Static pressure distribution inside the outlet duct

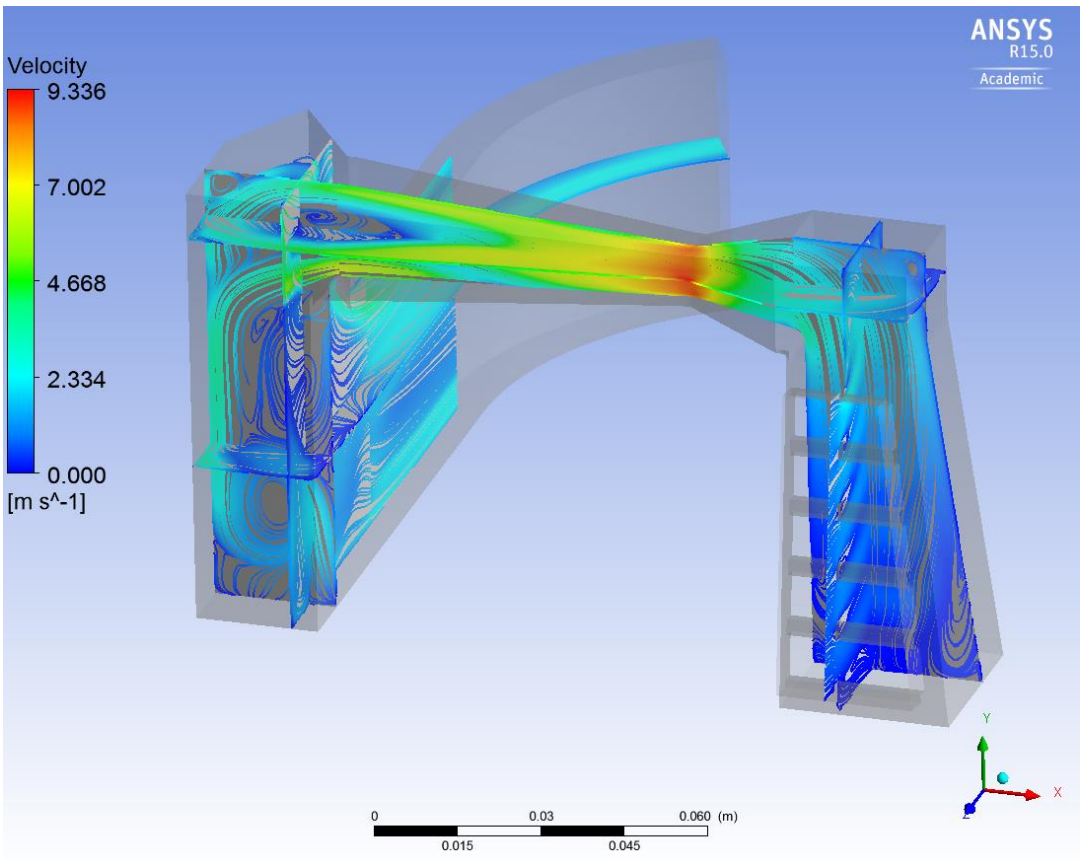

Figure 6.13: Flow velocity structure inside the inlet duct

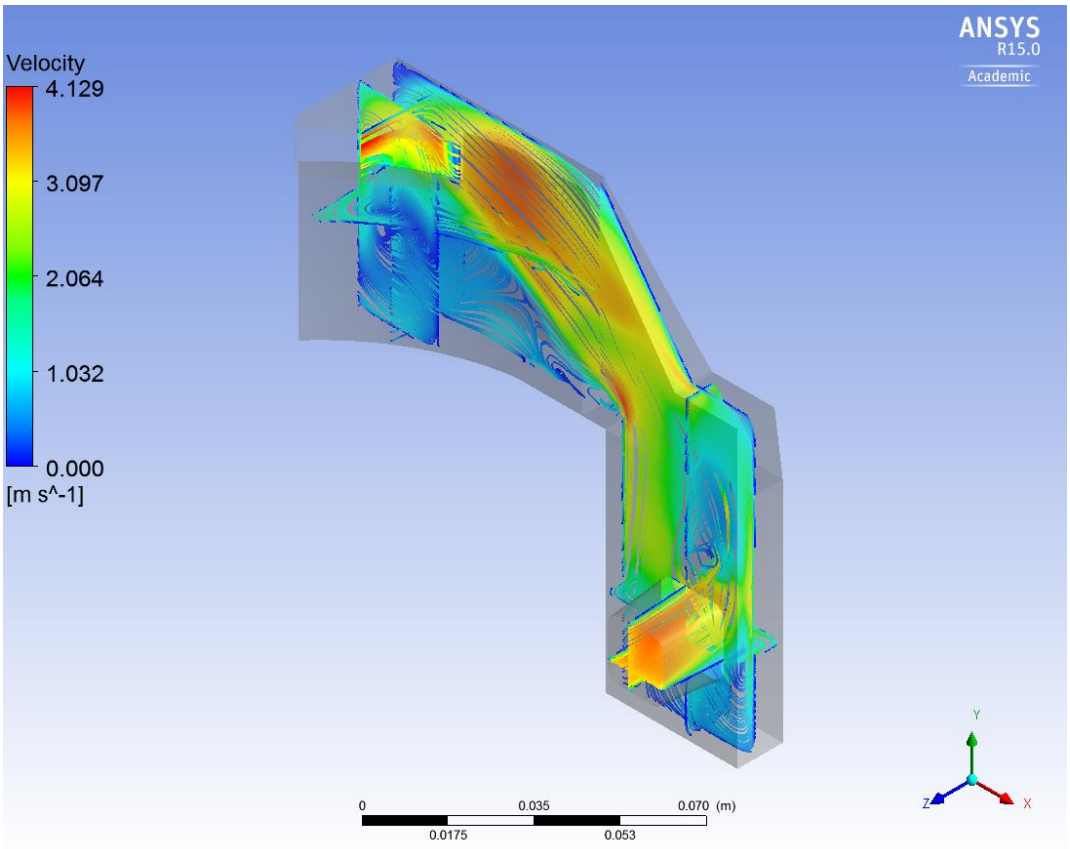

Figure 6.14: Flow velocity structure inside the outlet duct

6.6.2 Sound Analysis

The noise generated from the ducts is computed numerically and is compared with the experimental ones. Previously, a set of sound measurements were conducted by two microphones placed in the near field and far-field respectively. However, at the far-field, the noise generated from the tested ducts was weak as the pick-up SPL was similar to the background noise level under the 50 L/min flow rate conditions. Therefore, only the near-field SPL was measured and utilised as the sound power level produced from the ducts. The measured results are used to validate the numerical results.

Figures 6.15 and 6.16 show the near-field SPL computed for the inlet and outlet duct models. In these Figures, the acoustic pressure fluctuations were recorded at microphone points for both inlet and outlet models at 200 mm away from the outlet boundary surfaces. The time signal of the acoustic pressure is transformed to the frequency domain to compute the SPL and the overall SPL. Overall, the frequency spectrum shows the noise generated from the duct model is broadband with several peaks below 200 Hz. The overall SPL level is computed at 48 dB and 34.6 dB for the inlet and outlet models respectively.

Figures 6.16 and 6.17 show the near-field SPL of the inlet and outlet models and are used to compare with the numerical results. From these Figures, it is observed that the measured SPL results also produce the broadband noise with no specific dominant peak. A-weighted SPL also shows that the SPL band is similar to the ones seen in the numerical predictions.

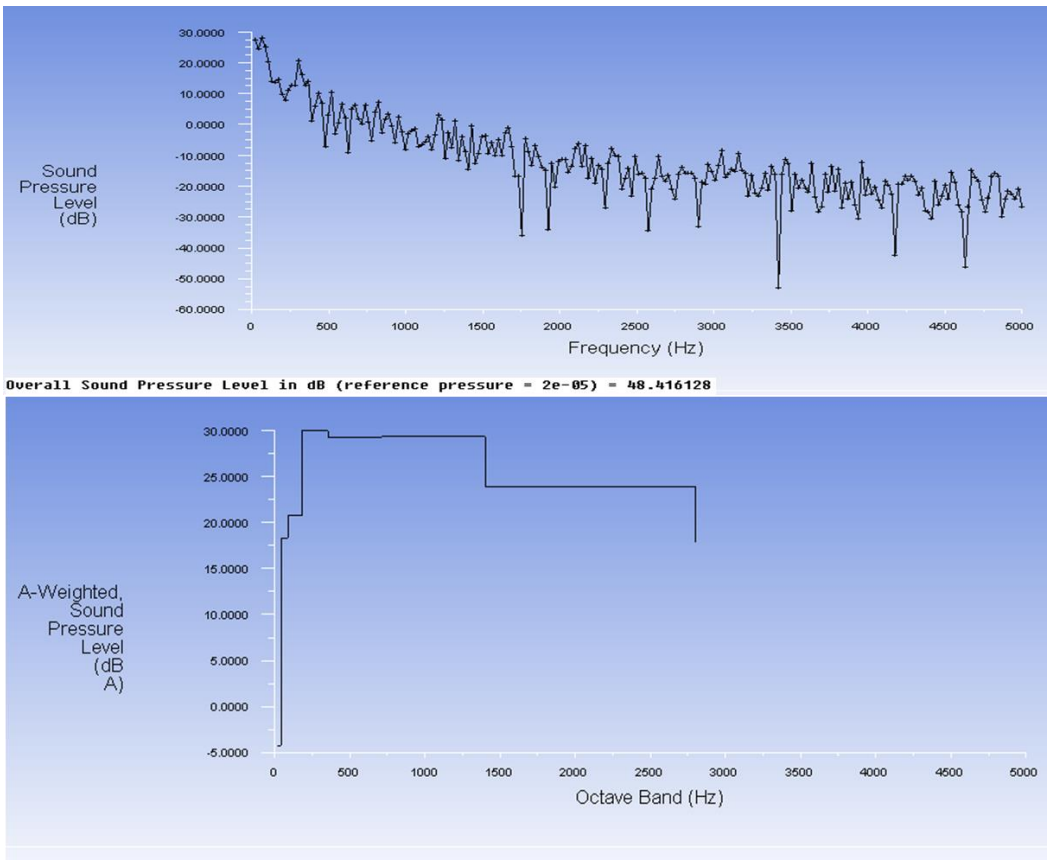

Figure 6.15: The Inlet Duct SPL computed at a monitor point

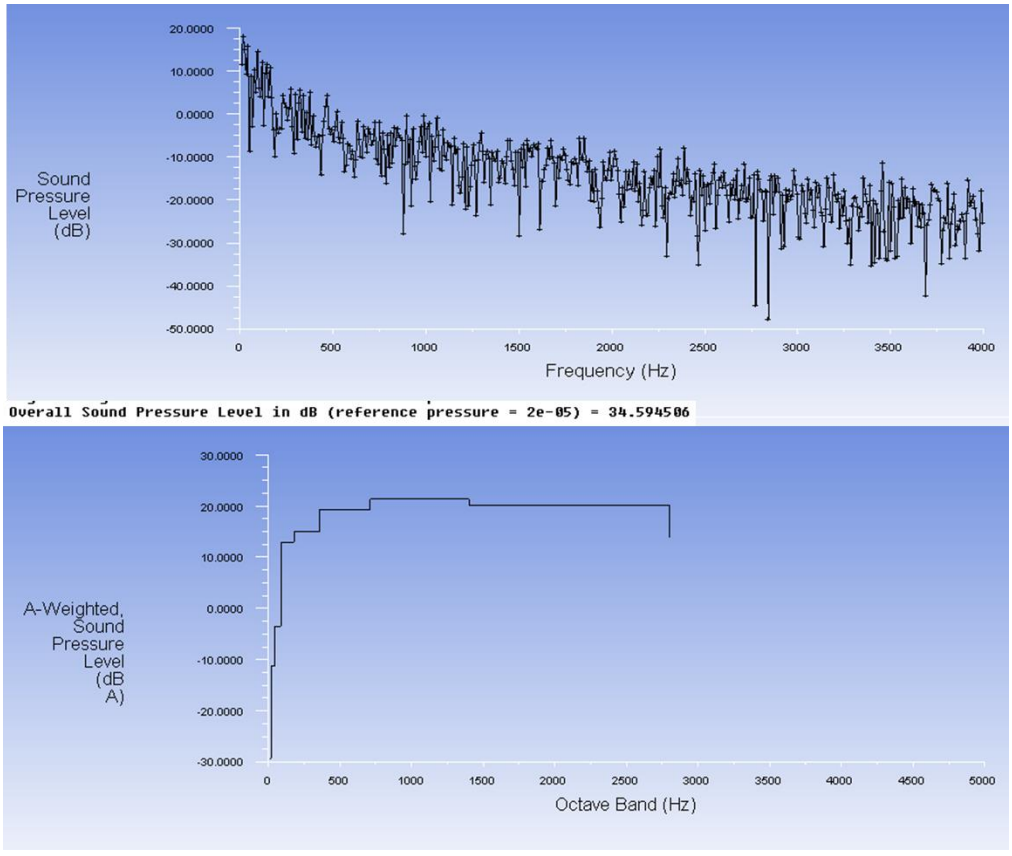

Figure 6.16: The Outlet Duct SPL computed at a monitor point

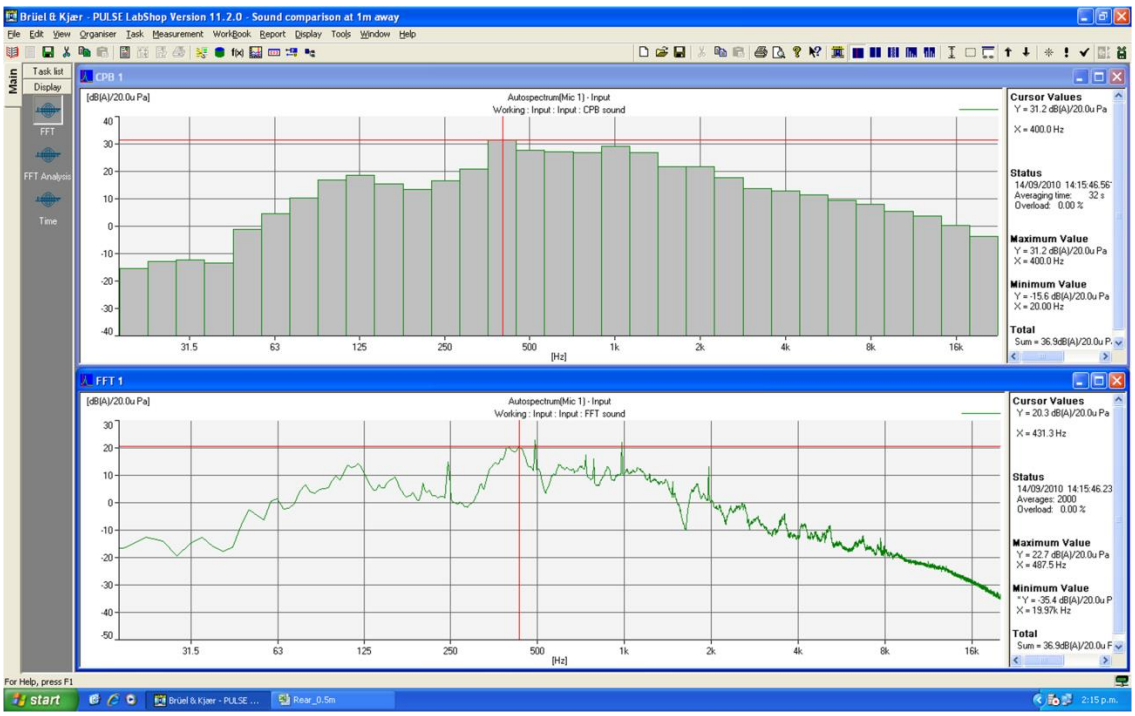

Figure 6.17: The Near-field SPL measured at the inlet duct

Figure 6.18: The Near-field SPL measured at the outlet duct

Table 6.4 summarises the sound pressure level (SPL) comparison of the inlet and outlet ducts. In this table, the overall SPL of the inlet duct and outlet duct were calculated experimentally and numerically.

Table 6.3: SPL Comparison of the duct models

	Inlet Duct		Outlet Duct	
	Near-field	Far-field	Near-field	Far-field
Predicted SPL (dB)	48	23.5	34.6	10
Experimental SPL (dB)	37	-	32	-

It is clear that the predicted results are not adequately reproducing the expected results. The difference from this comparison may be resulted from the assumptions of the way of the sound measurement was conducted for the ducts, or from the deficiencies in the way the numerical simulations has been conducted in this study.

6.6.3 Vibration Analysis

Figures 6.19 to 6.20 shows the mesh deformations of the inlet and outlet solid models respectively. The mesh deformations were randomly selected at several time steps for observation. High colour contours from these Figures suggest that high vibration is obtained in those regions. Maximum deformation was estimated around 0.004 mm for the solid inlet duct model and about 0.001 mm for the solid outlet duct model. The time dependent data was computed at the predicted maximum locations and transformed into the frequency domain as shown in Figures 6.21 and 6.22.

Figures 6.23 and 6.24 shows that the vibration spectrum obtained from the experimental investigations are used to compare with the numerical results.

In comparison to the numerical results, a similar vibration spectra is observed for both experimental and numerical results. The predicted results show dominant peaks around 50 to 100 Hz. These peaks are also seen in experimental ones. However, the magnitude of these peaks in the numerical results are under-predicted.

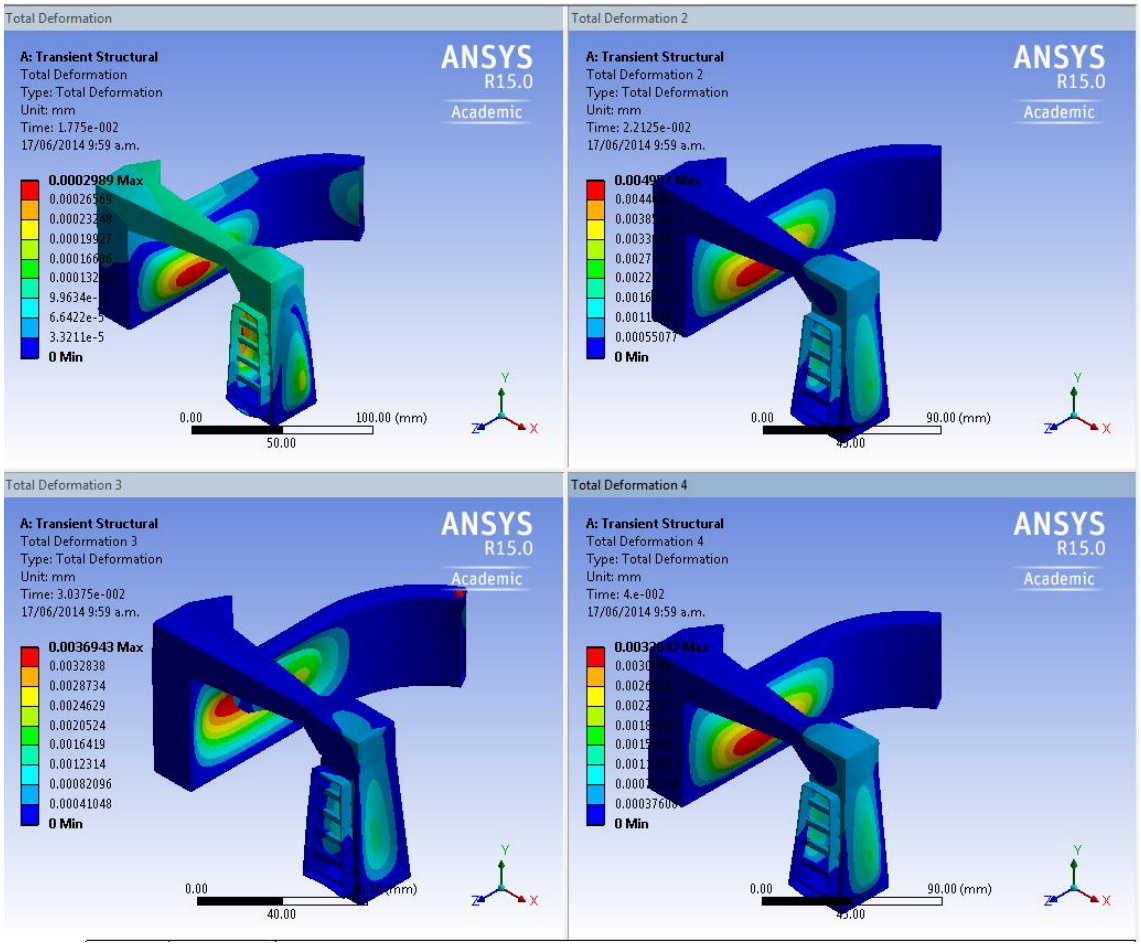

Figure 6.19: Total Deformation at the inlet duct model

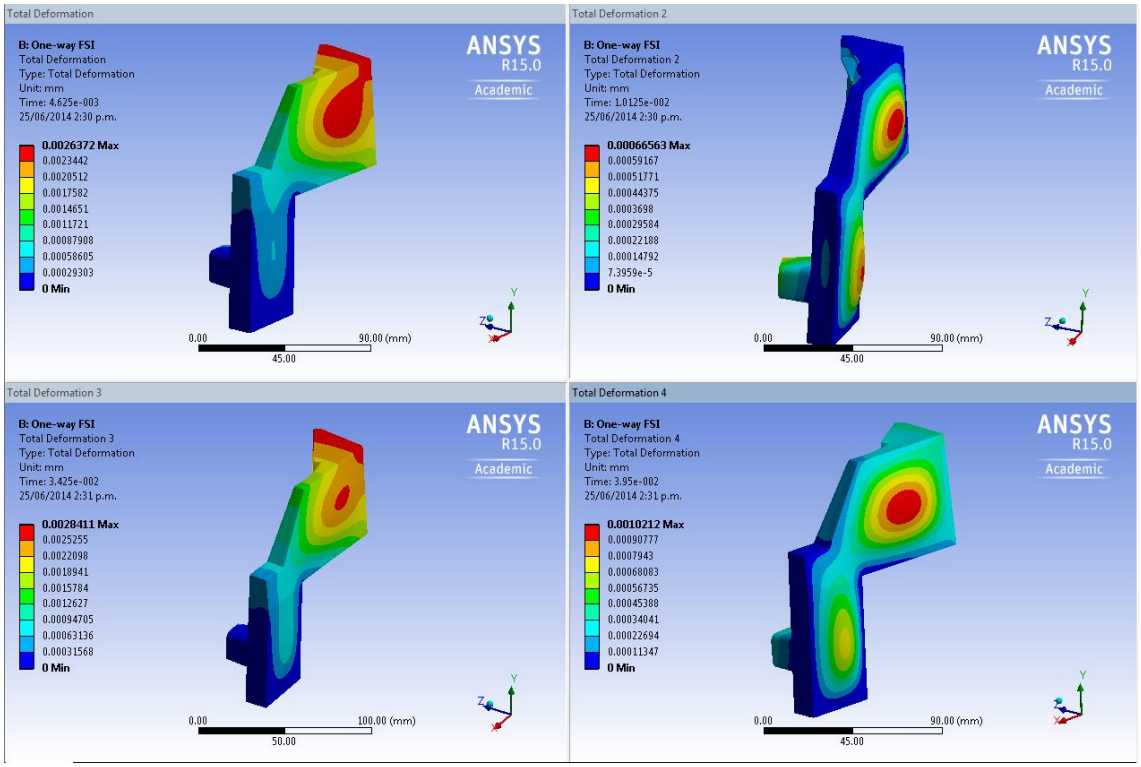

Figure 6.20: Total Deformation at the outlet duct

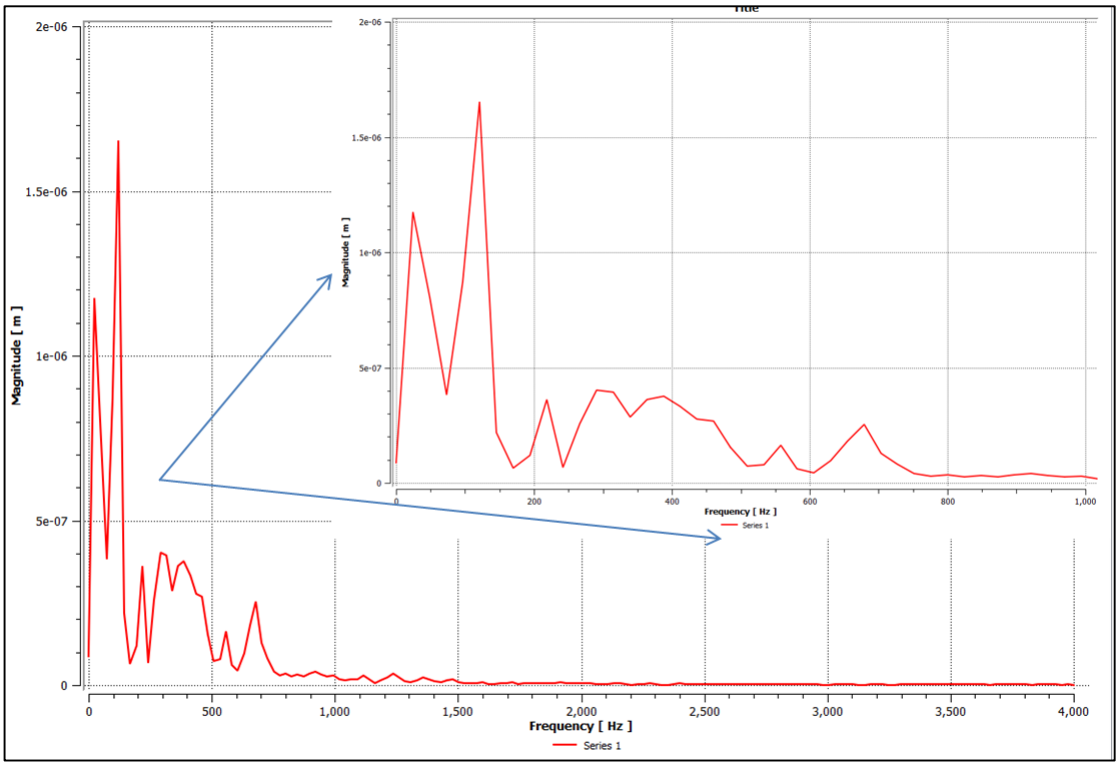

Figure 6.21: Frequency Spectrum of the inlet duct deformation

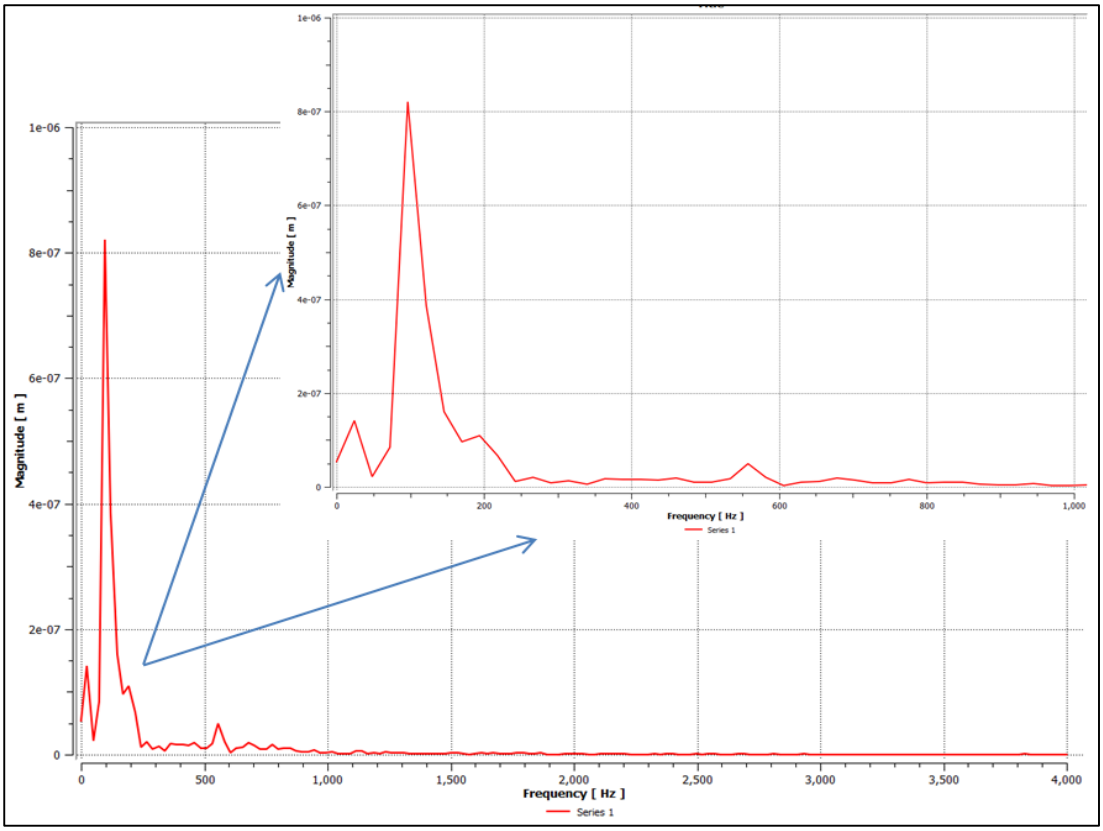

Figure 6.22: Frequency spectrum of the outlet duct deformation

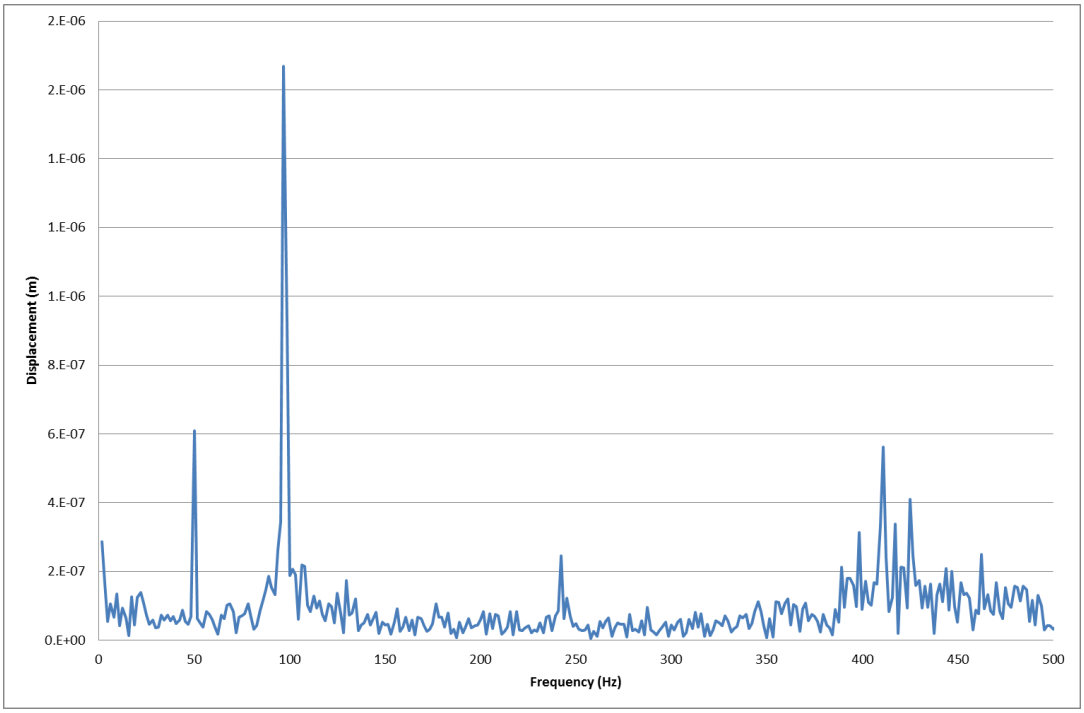

Figure 6.23: Frequency spectrum of the vibration measured at the inlet surface

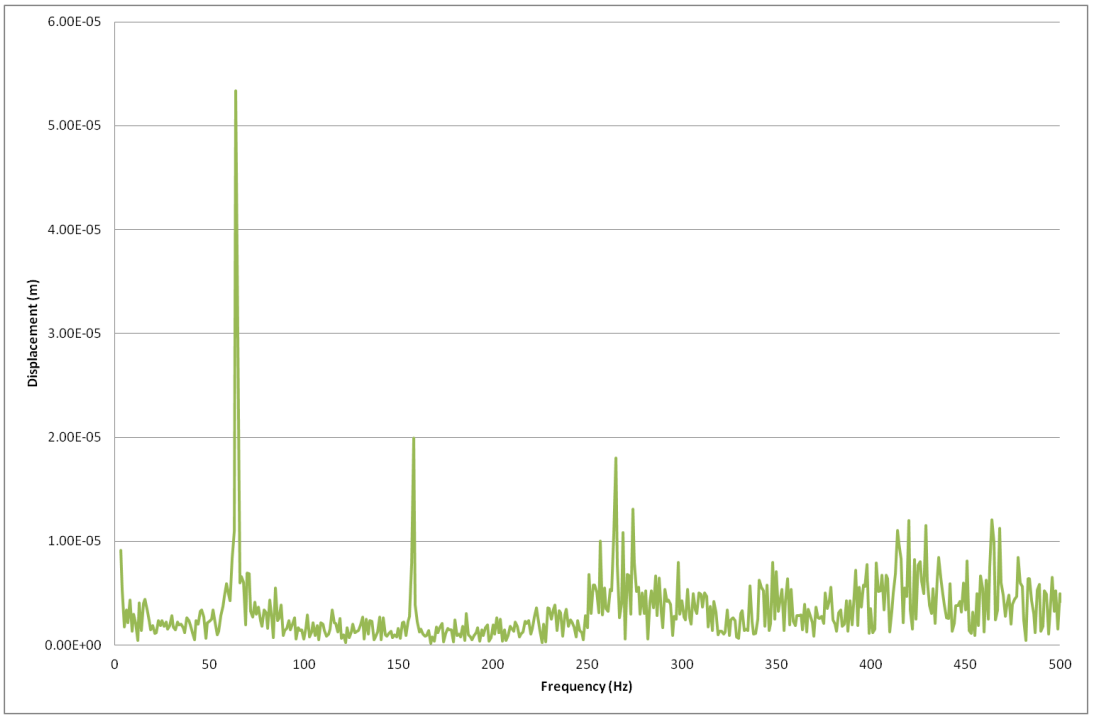

Figure 6.24: Frequency spectrum of vibration measured at the outlet surface

6.7 Summary

The purpose of this chapter was to investigate flow-induced noise and vibration generated from the duct system of the CPAP device. The combined CAA and the FSI simulation methods were adopted in this chapter. The accuracy of the numerical simulation was validated by the experimental data. The comparisons between the numerical simulation results and the experimental data has showed good agreements. It is found that the noise characteristics of the ducts is broadband in nature with dominant peaks existing at low frequency.

Flow field analysis has indicated that the flow characteristics are vertex flows due to many changes in the dimensions and directions in the duct geometries. The vertex flows are resulted in high static pressure fluctuation at the wall surface which is known as dipole source strength for aero-acoustic generation. The sound analysis has shown that the noise generated from the duct models is broadband and contains a low peak frequency. Surface pressure fluctuation has also generated structural vibration. The vibration analysis has found the solid duct models vibrated around 100 Hz.

Chapter 7: **Humidifier Model Simulation**

7.1 Introduction

Following on the numerical simulations conducted in chapter 6, the numerical simulations are performed in this chapter to investigate flow-induced noise and vibration in the humidifier component. Firstly, the CAA with hybrid approach is used to predict the noise generation. Secondly, the one-way FSI simulation is used to determine the structural vibration due to the flow turbulence.

This chapter consists of several sections. Section 7.2 covers the introductions and the development of the humidifier models for numerical simulation purposes. Section 7.3 presents the CAA simulation and section 7.4 presents the FSI simulation approach. Section 7.5 discuss the experimental approach for validation. Finally, the results are presented and validated in section 7.6.

7.2 Humidifier Models

The humidifier is a special component unit in the CPAP devices. The main purpose of this component is to improve the air quality in the CPAP devices. Figure 7.1 shows a reconstructed and simplified solid model of a humidifier unit. The solid model consists of a water chamber which contains a baffle, a lid and a round elbow. Figure 7.2 shows a humidifier fluid model developed in the ANSYS environments.

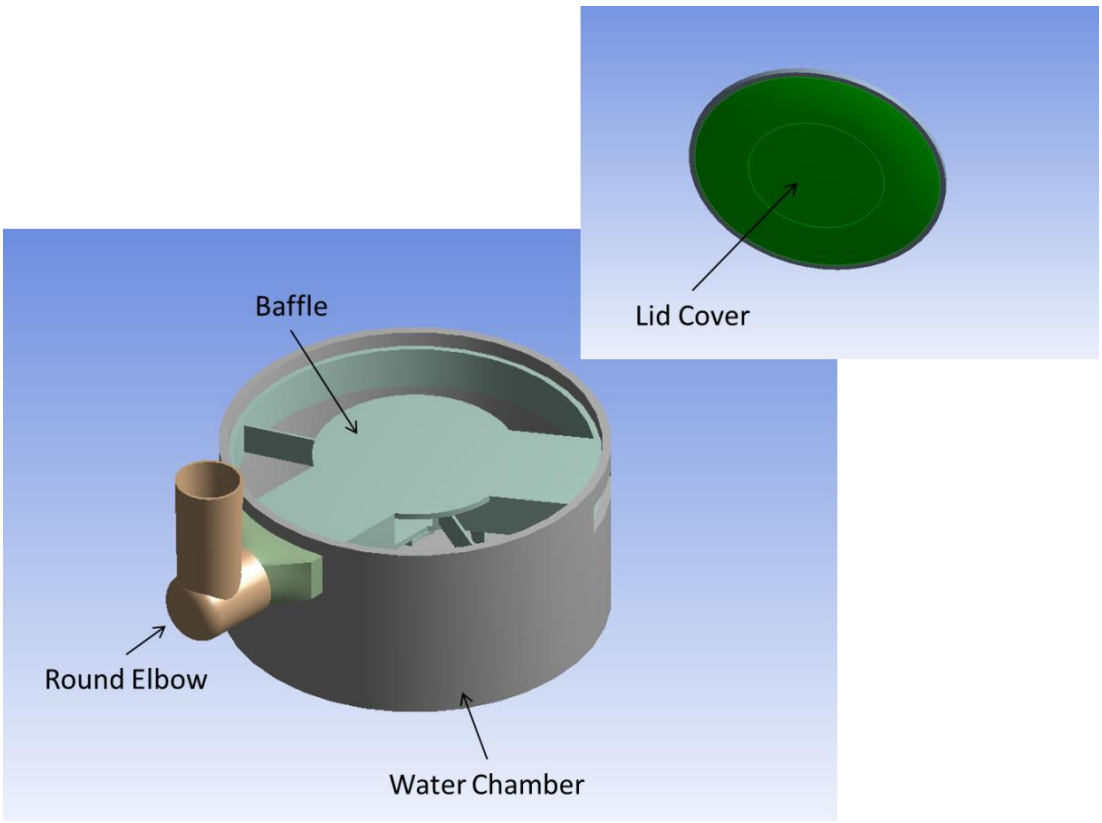

Figure 7.1: A simplified Humidifier Solid Model

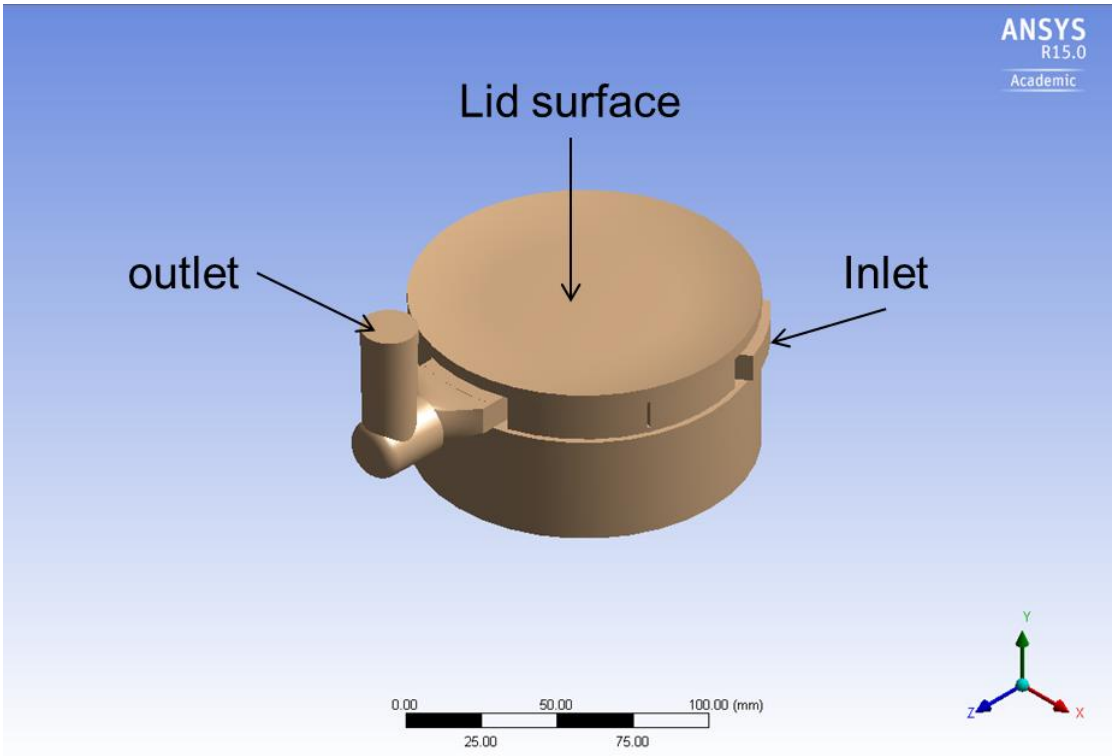

Figure 7.2: A simplified Humidifier Fluid Model

7.3 CAA Simulation

The CAA with hybrid approach is first performed in this section. This consists of two simulated steps: (i) to generate the noise sources and; (ii) to predict the noise generation.

7.3.1 Fluid Mesh Model

In order to conduct numerical simulation for the humidifier model, two extra domains were added at the inlet and the outlet of the humidifier fluid model as open atmosphere. Figure 7.3 shows the humidifier fluid model connected to an external domain. A large plenum was added at the outlet boundary and a long duct was added at the inlet boundary. The external domain is to ensure that the flow turbulence is fully developed during the simulation in order to obtain accurate results. Some dimensions of the CFD model are shown in Figure 7.4. The mesh model is shown in Figure 7.5.

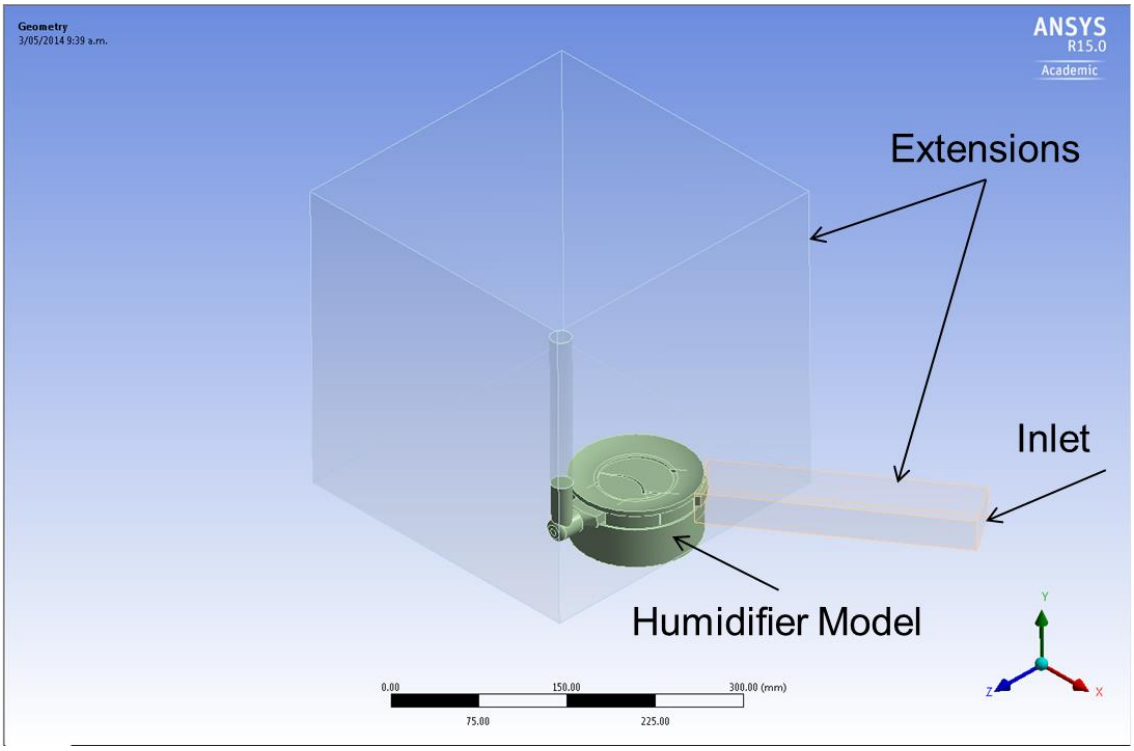

Figure 7.3: The humidifier fluid model with extensions

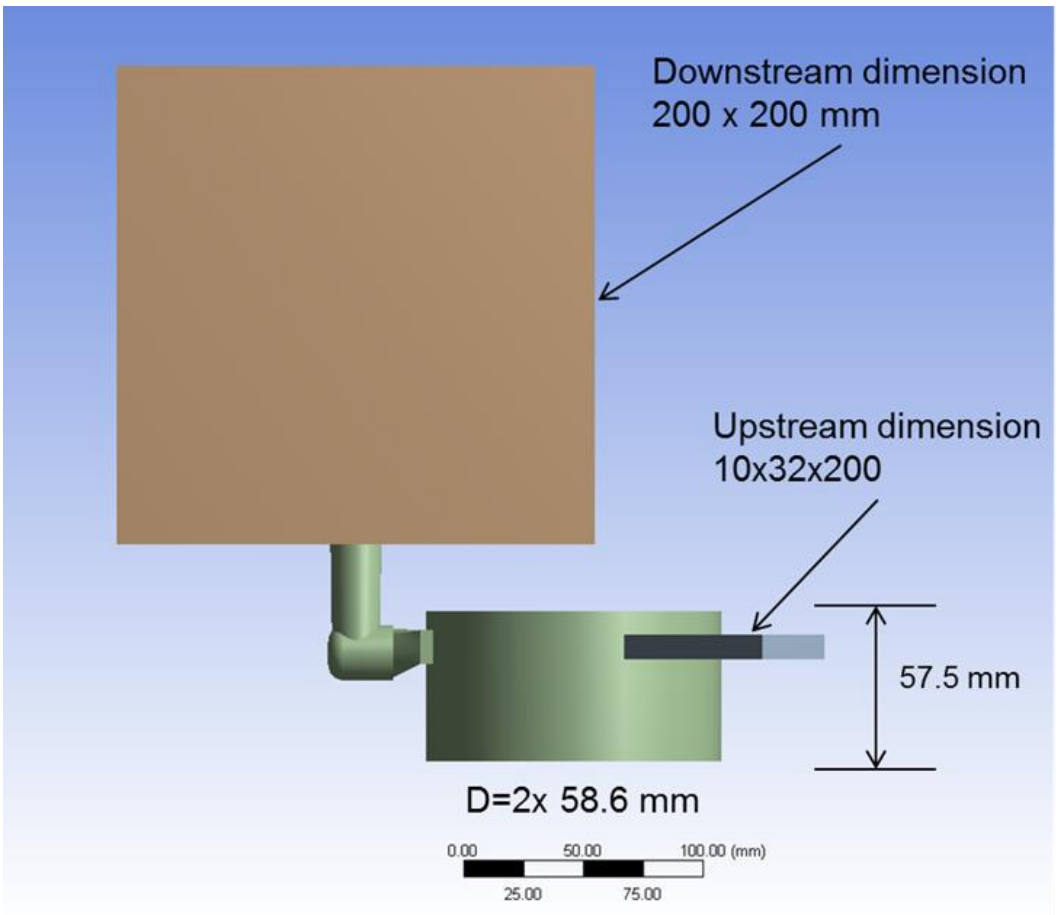

Figure 7.4: General dimensions of the humidifier model

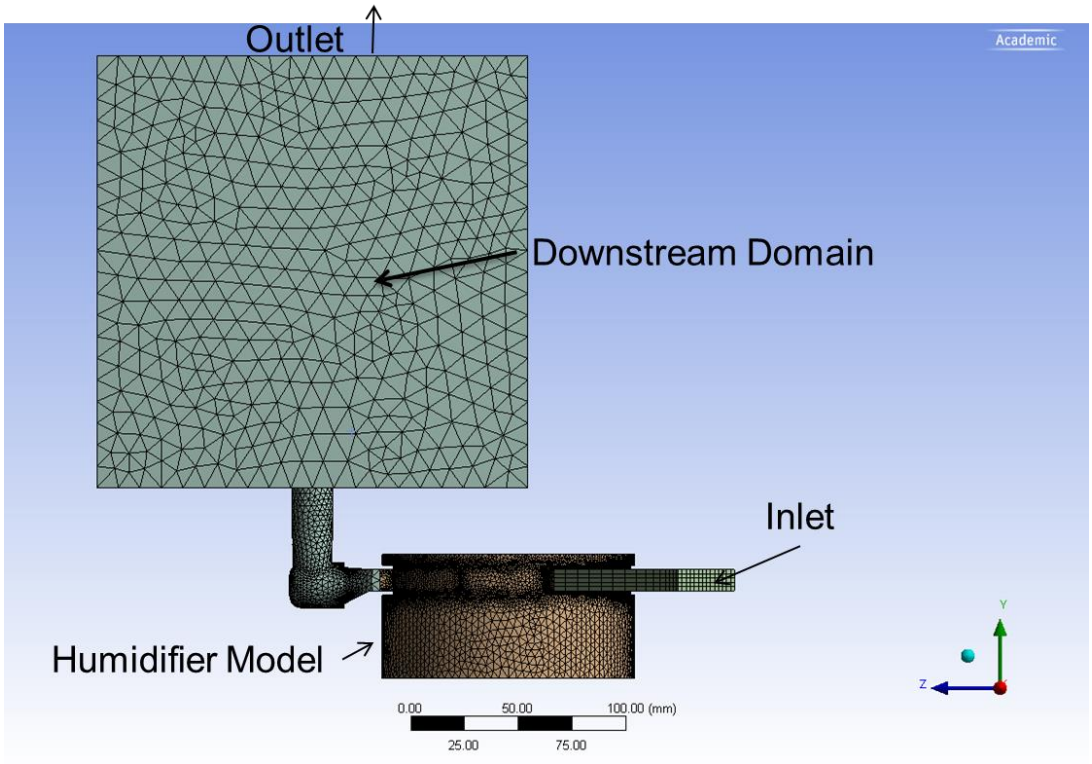

Figure 7.5: The humidifier mesh model

The humidifier fluid model was meshed with the unstructured and structured mesh methods. The unstructured mesh was applied to the humidifier fluid domain because of the complicated geometry. The mesh sensitivity tests were performed for the humidifier mesh model under different mesh sizes, from coarsen to finer meshes. The tests were performed using the steady-state CFD simulation. It was found that the aerodynamic values, i.e., pressure, velocity, were insignificantly different. However, the finer mesh size was chosen to ensure that the numerical model could well-delivered the noise predictions. Table 7.1 details the humidifier mesh model.

Table 7.1: Mesh details of the humidifier fluid model

Mesh details			
Elements	Mesh Type	Mesh Size (mm)	Element Numbers
Upstream	Structured	5	66760
Humidifier Fluid	Unstructured	1 mm(surface) 5 mm (body)	893833
Elbow Fluid	Unstructured	2 mm(surface) 5 mm (body)	76126
Downstream	Hybrid	5 mm (interior) 20 mm (exterior)	26546
Total Mesh			1063265

In this study, the acoustic target was set to be up to 4000 Hz. Therefore, the mesh size was generated and valid for acoustic simulation up to 8000 Hz. Considering the Nyquist effects, the time step was set at 1.25 e^{-5} seconds.

7.3.2 Solver Settings and Boundary Conditions

The CFD simulation was first performed to obtain the sources. A similar setting to the setting applied in chapter 6 was applied in this section. A constant 0.001 Kg/s mass flow

rate was applied at the inlet boundary and a gauge pressure was applied at the outlet boundary, representing to the open pressure. The entire wall in the CFD model was applied as non-slip conditions. The details of the solver settings can be found in Table 5.5 in Chapter 5 and will not be repeated here. Table 7.2 summarises boundary conditions applied to the humidifier model.

Table 7.2: Boundary conditions of the humidifier simulation

Boundary	Boundary Condition	Value
Inlet Boundary	0.001	(Kg/s)
Humidifier inlet and outlet	Interior surfaces	-
Humidifier Walls	Non-slip Walls	-
Outlet Boundary	Gauge Pressure	0 (Pa)
Computational Walls	Non-slip Walls	-

7.3.3 Flow Simulation Procedures

The steady-state CFD solution was first performed to obtain the initial solution for the unsteady simulation. The flow turbulence was modelled by the $k-\varepsilon$ RNG turbulence model. The steady-state simulation converged after 5000 iterations.

The converged steady state solution was used as an initial condition for the transient simulation. The unsteady simulation was performed with the $k-\omega$ SST turbulence model. During the transient simulation, a time step was set at 1.25 e^{-5} seconds. The simulation was set to run until a stable periodic condition was reached. Periodic condition was obtained after 5000 runs. Once the periodicity was reached, the transient simulation was set to run for further 5000 steps. During this time, the acoustic analogy was activated to record acoustic source data for calculating acoustic pressure.

7.3.4 Acoustic Coupling

The acoustic pressure was recorded at two different monitor points at different locations. One monitor point was placed inside and near the centre bottom of the humidifier to record pressure fluctuation due to the flow circulation. Another monitor point was placed outside the humidifier model near the outlet interior boundary to record the near-field aerodynamic pressure.

The time step is applied at 1.25 e^{-5} seconds which will give the maximum sampling frequency is 80000 Hz. However, the target frequency is set to be up to 4000 Hz. The written frequency can be coarsened with a factor of 4, which gives a sampling frequency of 20000 Hz. According to the Nyquist theorem, the highest resolved frequency would be 10000 Hz.

7.4 FSI Simulation

In this section, the FSI simulation is performed to investigate the influence of the turbulent flow on the humidifier structure. Due to the limitation on the computer resources, only the humidifier cap is chosen in this study to save computational time and effort.

7.4.1 Structural Mesh Model and Boundary Conditions

Figure 7.6 shows the numerical mesh model for the solid humidifier model. A thin solid model was developed and mesh with structured method. The round elbow was acquitted in the solid model in order to save computational time and resource.

The mesh size was fixed with 1 mm thickness as similar to other previous models. A total of 21141 mesh element and 21068 nodes was generated to obtain a good mesh quality for structural simulation. The mesh quality was performed by static structural simulation. In this test, three different mesh sizes from coarsen to finer mesh were generated and performed. The mesh deformation comparison showed a little difference in magnitude.

Therefore, the coarsen mesh size was chosen. The material used for the structural simulation was similar to the one used in Chapter 5. This material belongs to polycarbonate family and often being used in medical device.

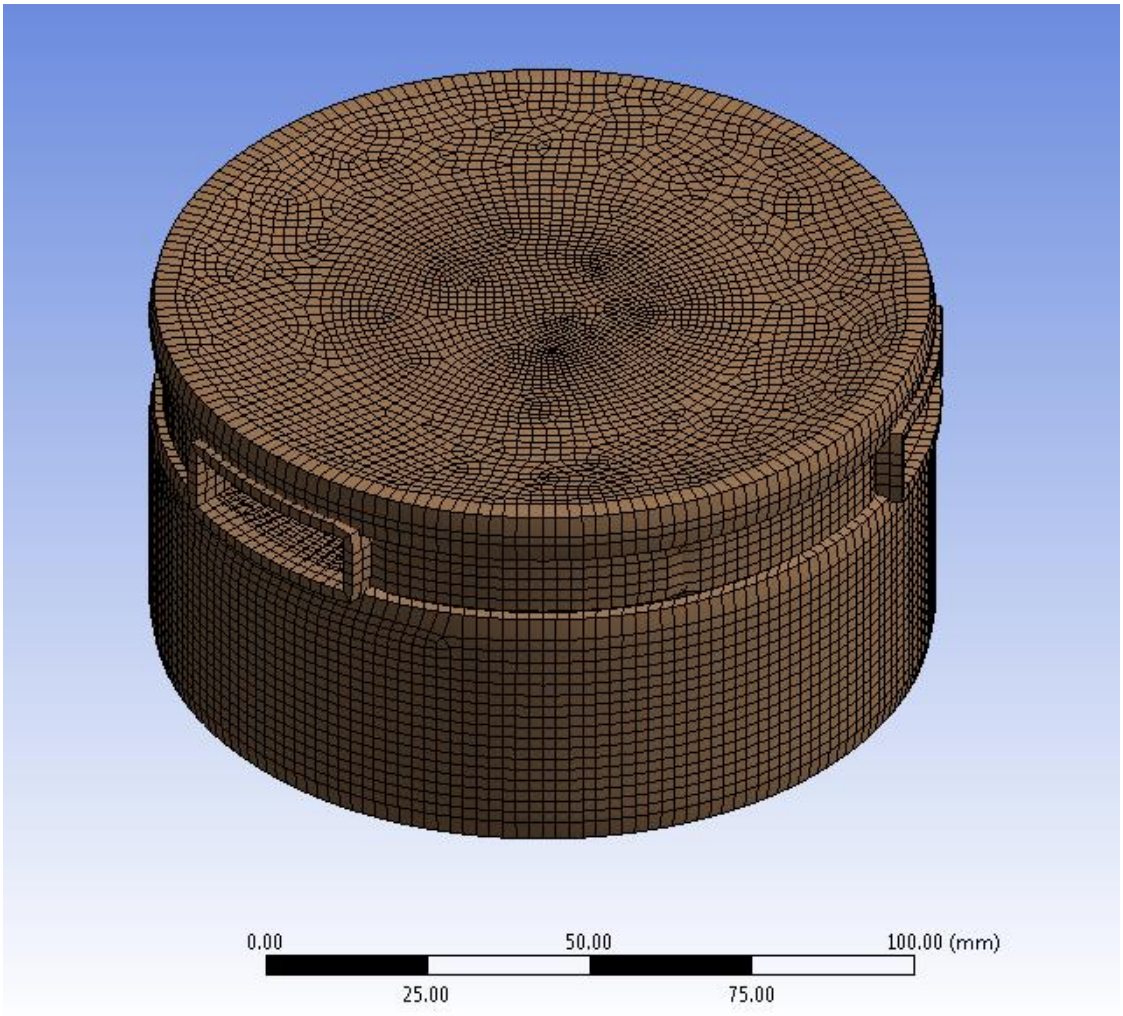

Figure 7.6: the solid humidifier model

Figure 7.7 shows a fixed support condition applied to the solid model. Inside the solid model, contact conditions were applied at several contacts locations as frictionless and no-separation conditions. These conditions restricted the solid model from motion at several directions. Only the vertical vibration at the volute cap surface is considered in this simulation.

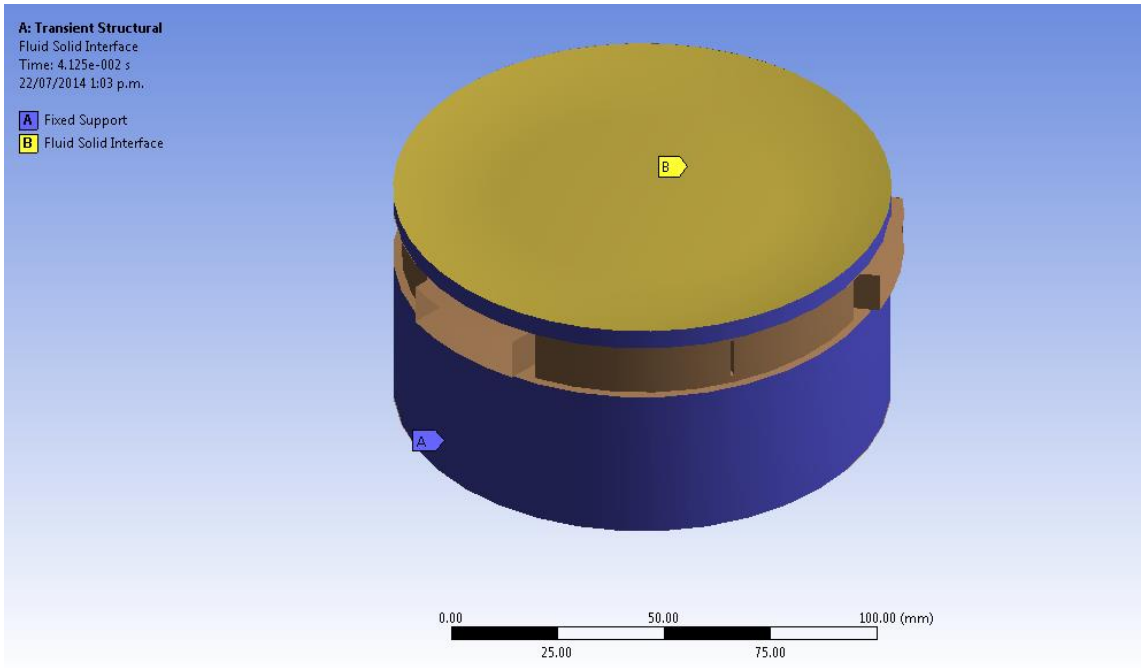

Figure 7.7: A fixed support boundary applied to the solid model

7.4.2 Simulation Procedure

The static structural simulation was first performed to obtain an initial solution. In this simulation, the converged steady state CFD solution was used as an initial input and applied to the structural simulation through FSI interfaces. The static structural simulation was set to run until converged the dynamic structure was reached. The converged static simulation solution was continued to run under the transient FSI simulation. The transient one-way FSI was performed for the 330 coupling steps under 1.25 e^{-5} seconds time steps.

7.5 Experimental Measurement for Validation

The noise generated from the humidifier was also measured during the experimental investigation for validation purposes. A similar setup was discussed in section 6.5 previously and was used for this experiment. The humidifier was connected to the flow smooth chamber. Air flow was provided by a centrifugal fan placed outside the tested room. During the experiment, a portable microphone was used to measure SPL at different measured points, i.e., near the bottom of the humidifier, near the outlet boundary

and one meter away from outlet boundary. Acoustic pressure data was recorded and transformed to the frequency domain to calculate the sound pressure level (SPL). The results were used to compare with the numerical results for validations.

7.6 Results

7.6.1 Flow-field Analysis

The aerodynamic characteristics of the humidifier model were studied graphically via the flow velocity streamlines, the iso-surface turbulent kinetic energy and the pressure contours.

Figure 7.8 shows the streamlines coloured with the velocity magnitude of the humidifier. From this figure, the flow enters the humidifier at the inlet with constant velocity. The flow is redirected by a baffle placed inside the humidifier to create a chaotic flow scenario. The flow velocity is accelerated to the outlet boundary and reached the maximum value at the round elbow element. The flow trajectory indicates that the chaotic incurred inside the chamber is due to the complicated baffle. High vortex flows are seen in the region surrounding the wall of the baffle.

The chaotic of the flow structure inside the humidifier chamber caused high turbulence kinetic energy level as shown in Figure 7.9. The turbulence kinetic energy is computed and presented via iso-surface contours. A very large energy level is seen in one side of the model where the flow impacted on the wall.

Figure 7.10 shows the static pressure fluctuation at the surfaces of the humidifier. High, uniform and stable pressure is seen at the inlet boundary and at the surrounding chamber. However, pressure fluctuation is seen at the outlet region. Surface pressure fluctuations indicate that the noise is likely to be generated in this region.

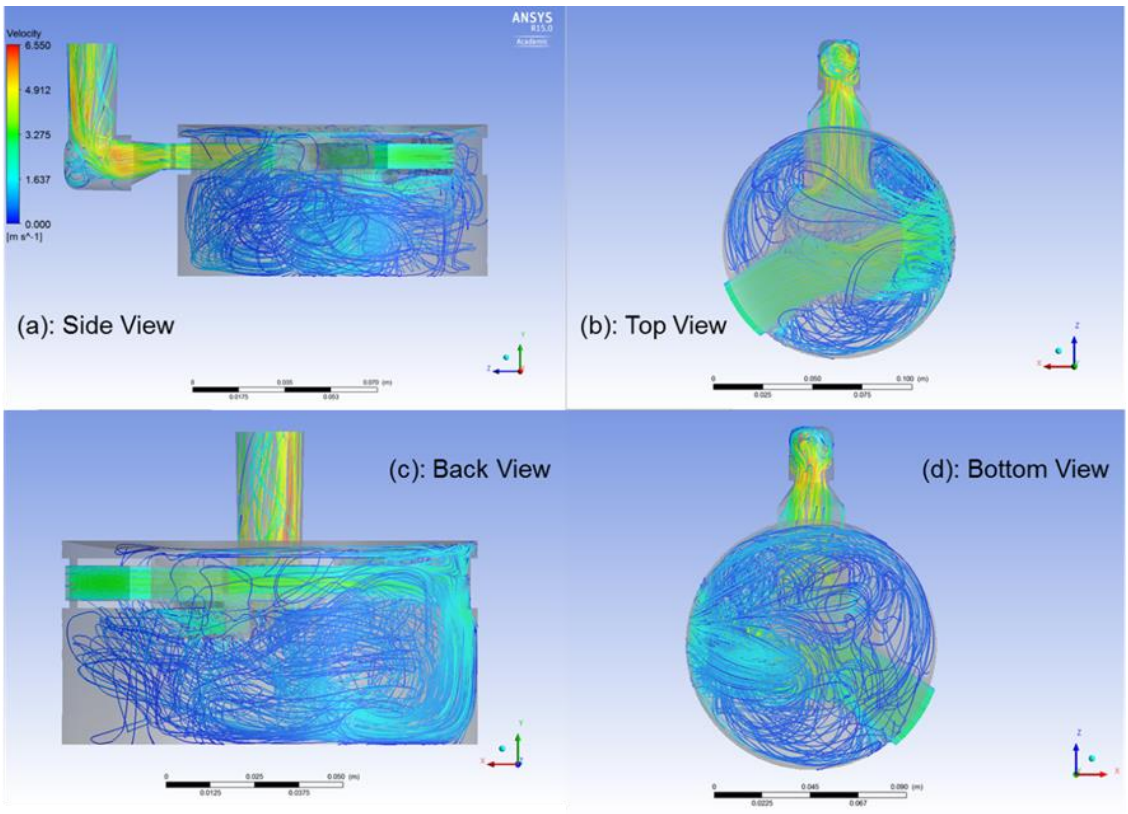

Figure 7.8: Flow velocity structure inside the humidifier unit

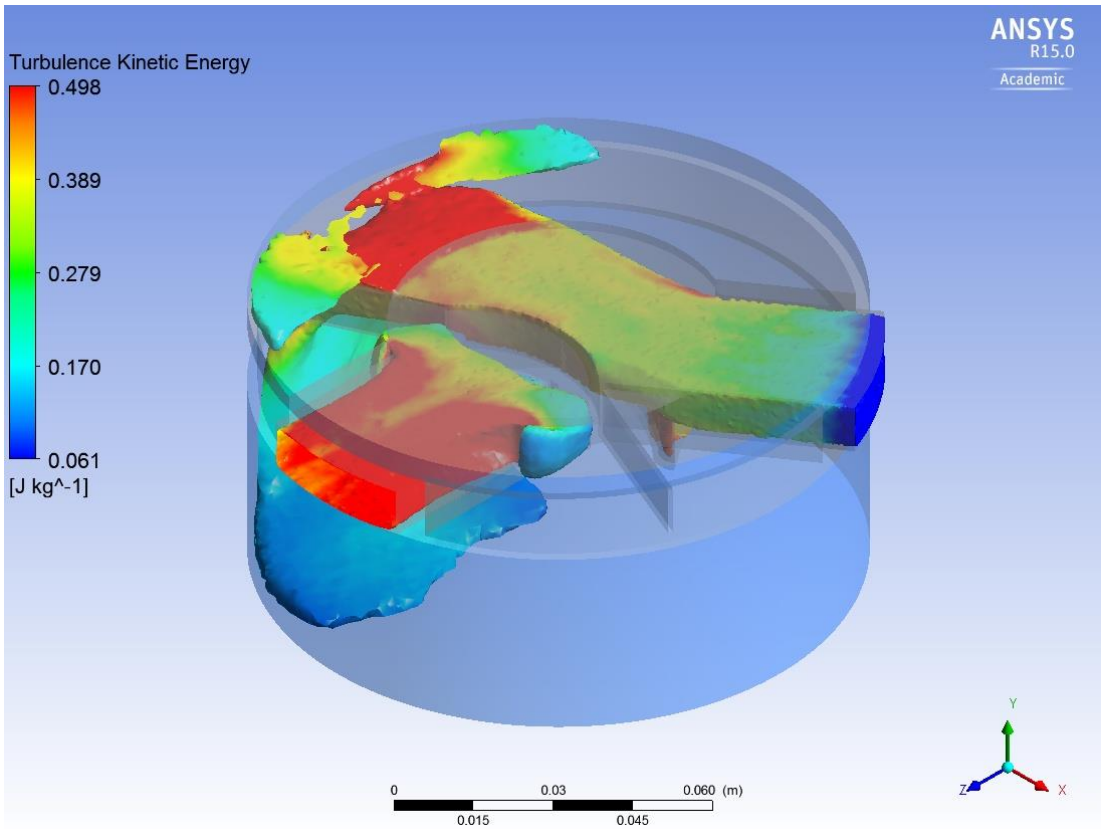

Figure 7.9: Turbulence Kinetic Energy distribution inside the humidifier

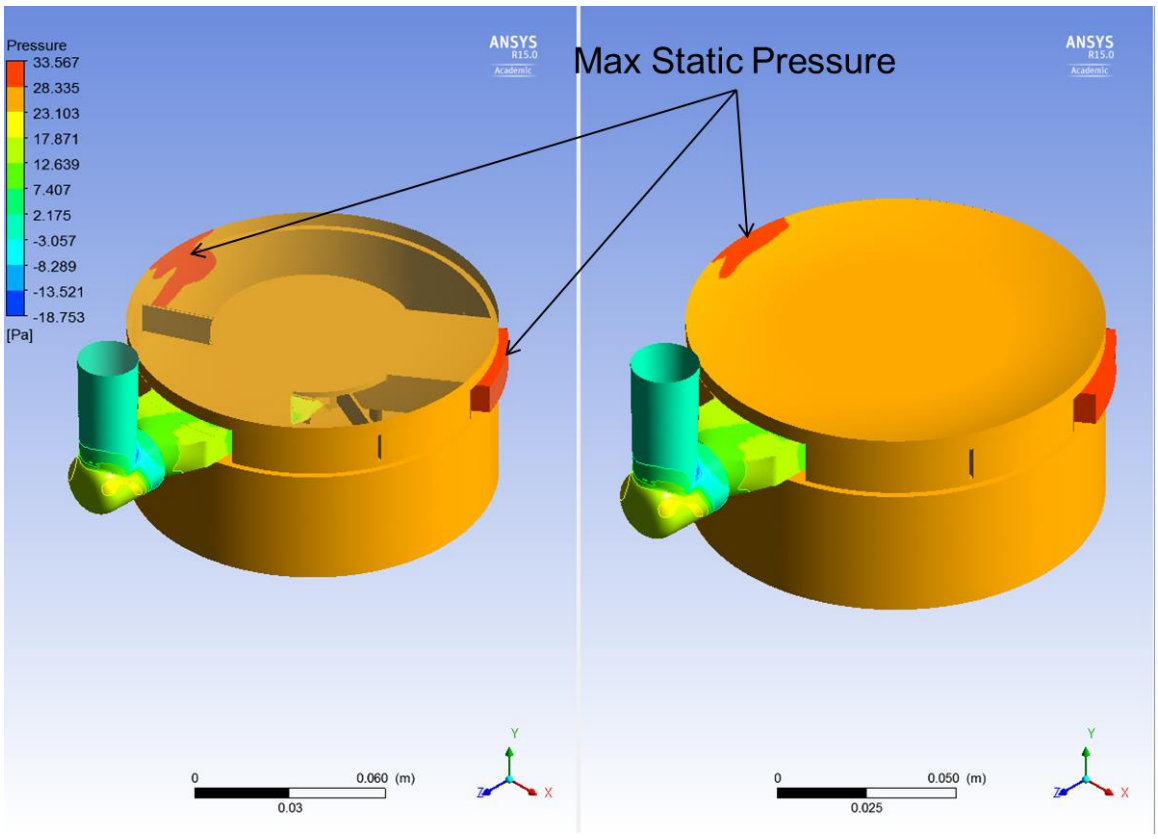

Figure 7.10: The contour of static pressure fluctuation at the humidifier

7.6.2 Sound Analysis

Figure 7.11 shows near-field and A-weighted SPL is predicted for the humidifier model. A low broadband noise level is observed in this Figure. The overall sound pressure level is computed at 37 dB with a high peak magnitude of 20 dB at 100 Hz. A-weighted SPL indicates that the high noise level is possibly in the range of 1000 Hz to 1500 Hz.

The predicted SPL is compared with the experimental one as shown in Figure 7.12. The experimental SPL was conducted with a microphone placed in front of the humidifier model to measure the sound power level. Similar flat curve is observed from the A-weighted SPL. However, the highest SPL is measured at frequency below 500 Hz frequency bands. The overall SPL measured from the humidifier is 34.1 dB, which is close to the predicted one.

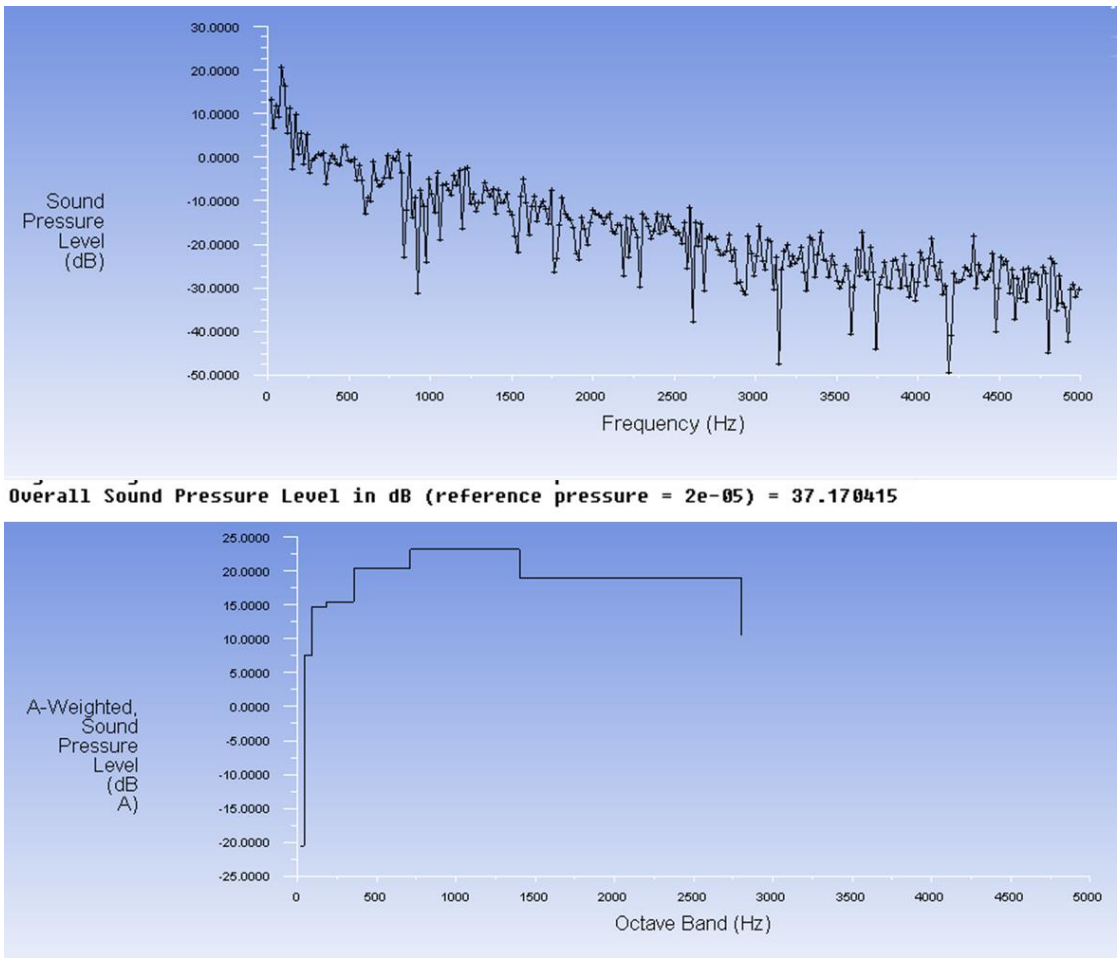

Figure 7.11: Near-field SPL computed for the humidifier

Figure 7.12: Near-field SPL measured for the humidifier

7.6.3 Vibration Analysis

Figure 7.13 shows the mesh deformation contours obtained at several random time steps. From this Figure, the cover surface of the humidifier is found to be vibrated the most. The time dependent of the mesh deformation is recorded at the maximum deformation point and transformed into the frequency domain as shown in Figure 7.14. Several peaks are seen below 500 Hz frequency. The maximum mesh deformation is computed at 1.45 e^{-8} (m). The predicted spectrum is used to compare with the experimental data obtained previously during the experimental investigations for validation.

Figure 7.17 shows a measured vibration spectrum at the volute cap. A broad vibration frequency occurred between the frequencies ranges of 200 to 600 Hz. The vibration spectrum contains both related and non-related to the fan vibration.

In comparison, it is clearly that the frequency spectrum does not agree with the each other. The magnitude of the predicted results is under-predicted. The maximum values is around 1.45 e^{-8} (m) while the maximum of the measured one is 9 e^{-8} (m). The difference from this comparison would possibly due to several assumptions of the way of vibration measurements were conducted and also the way of the numerical simulation was conducted.

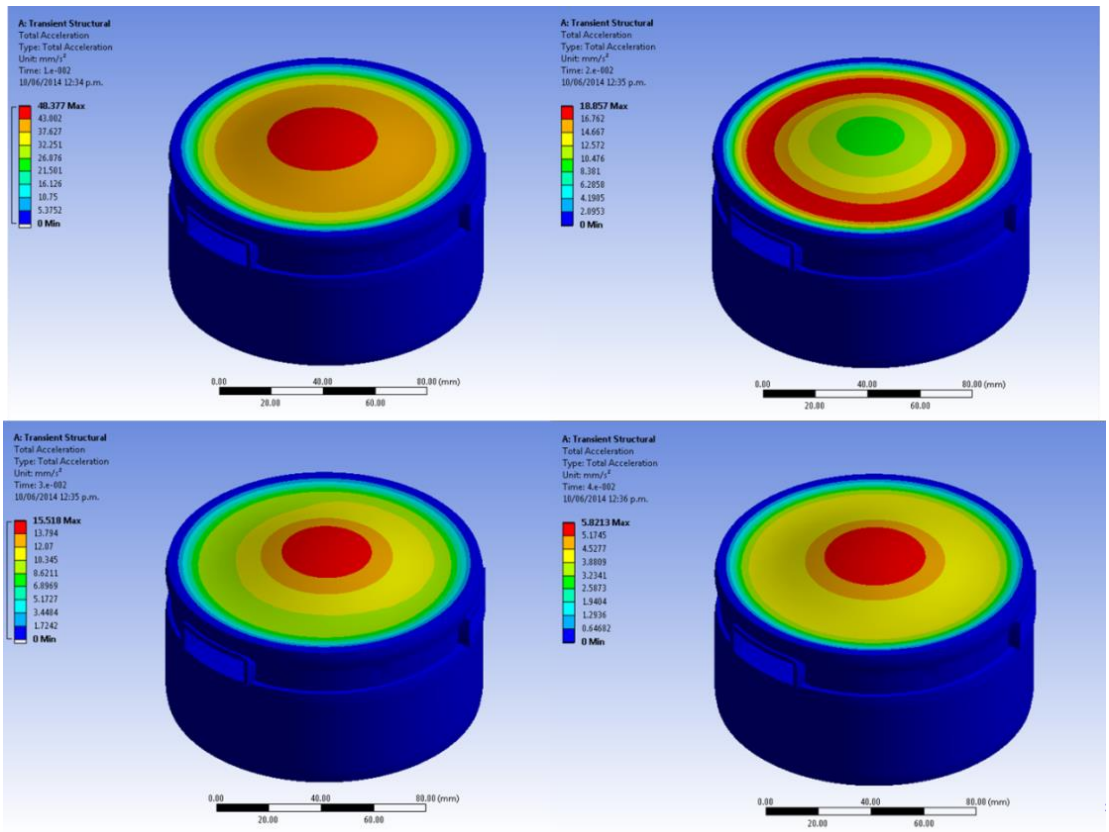

Figure 7.13: Total Acceleration distributed at the cap surface

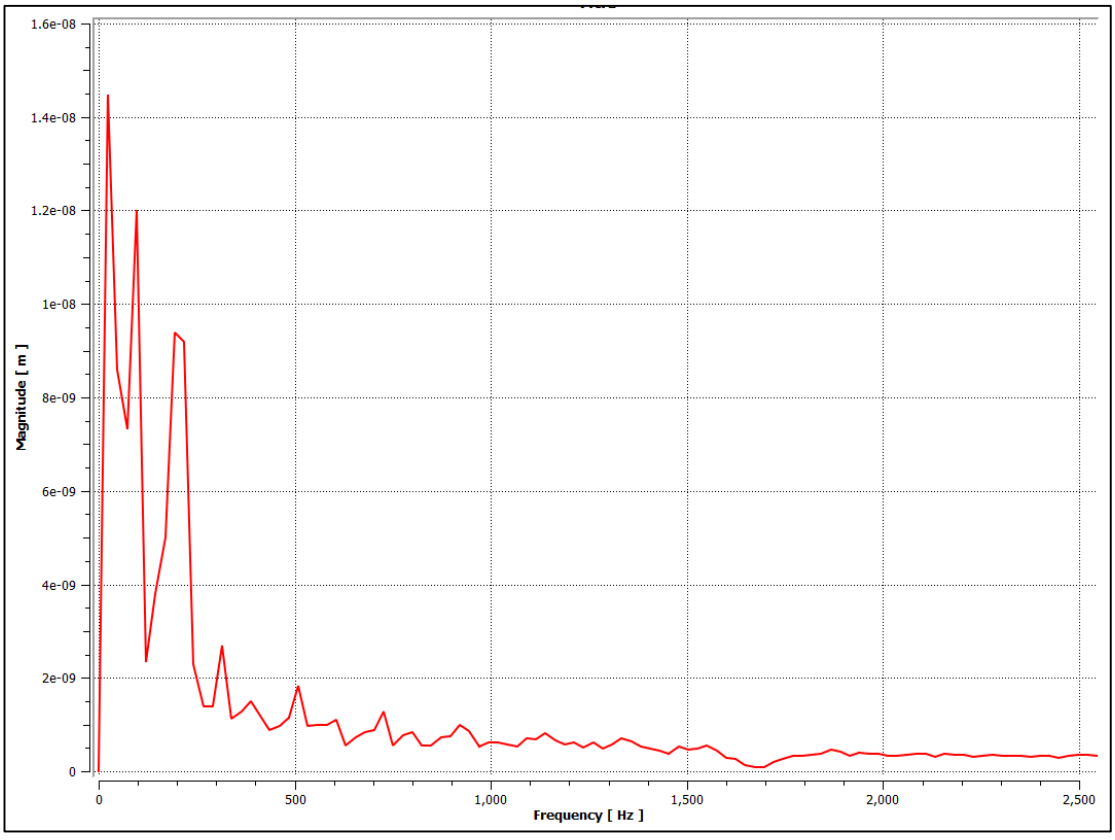

Figure 7.14: Frequency spectrum of mesh displacement at the cap surface

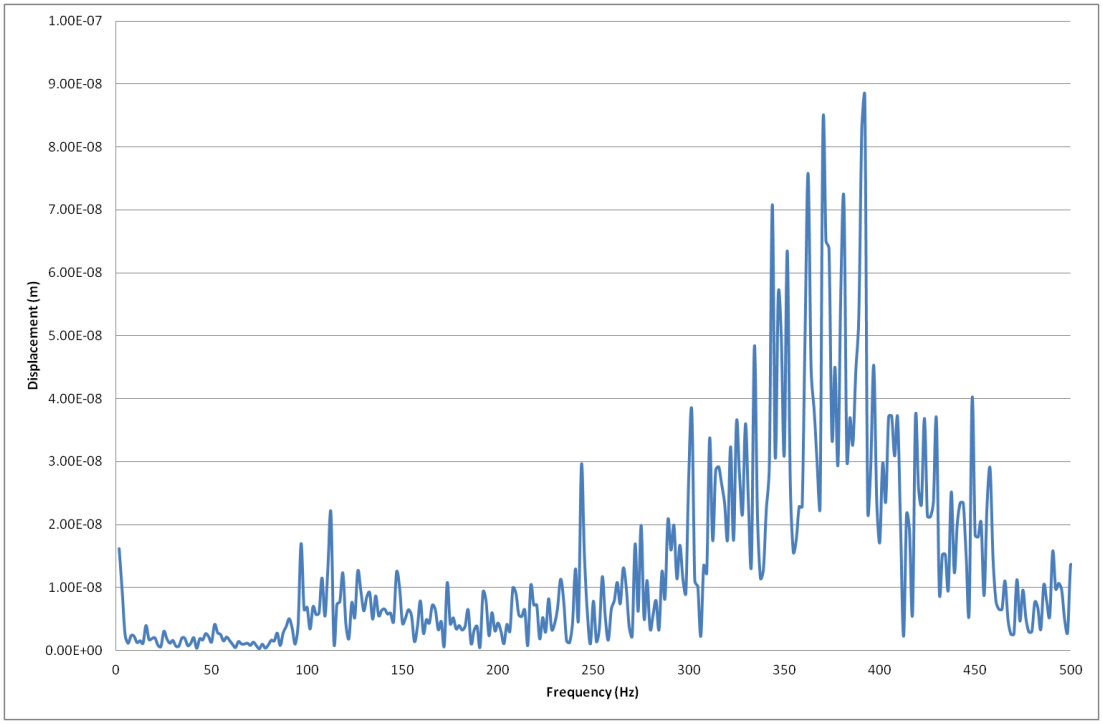

Figure 7.15: Vibration measurement at the cap surface

7.7 Summary

The purpose of this chapter was to investigate flow-induced noise and vibration from the humidifier of the CPAP devices. In this chapter, a combination of the CAA and the FSI simulation methods are used. The numerical analysis has shown chaotic flows inside the model. The flow rotating and scattering are seen at one side of the humidifier mode, which has created high level of turbulent and pressure fluctuations in that region, those variables are known as the quadrupole and the dipole sources from the aerodynamic noise generation perspective. The pressure fluctuations are also generated the structure vibration at the volute cap surface.

The predicted results are validated by the experimental ones. It shows some differences in the frequency spectrum. However, in principle, some agreements are made as they both shows a similarity in the curve spectrums, especially at the lower range of the frequency.

Chapter 8: Noise Source Locations and Contributions

8.1 Introduction

In previous chapters, the noise and vibration generated by individual components of the CPAP device were numerically investigated and validated by experimental results. However, it is still not possible to identify the individual contributions of the fan, duct and humidifier noise. In order to clarify this issue, one can compare the sound power level (PWL) at sources altogether. In this chapter, the noise source locations and the sound power level are predicted and estimated for each components. The contribution of the PWL of each individual component to the total PWL can be determined.

8.2 Noise Source Location Prediction and Power Estimation

In this section, the noise source locations and its powers are predicted and compared with each other. The ANSYS FLUENT software provides both the quadrupole and the dipole source models as post-processing tools to compute the sound power level at sources. As discussed in chapter 3, the physical quantities such as turbulence velocity, turbulence length scale and mean-square surface pressure need to obtain from the CFD solutions and use to compute the acoustic power and the surface acoustic power at sources. The results provide an approximate measure of the local contribution to the total noise generated from the CPAP devices. The accuracy of these source models are strongly dependent on the accuracy of the CFD simulation results.

8.2.1 Combining Noise Sources

The combination of noise level from many sources contribute to the total noise can be obtained by the equation

$$L_{p\_overall} = 10\log_{10}(10^{L_{p,1}/10} + 10^{L_{p,2}/10} + ...10^{L_{p,n}/10}) \quad (8.1)$$

Where $L_{p\_overall}$ is the overall sound pressure level and $L_{p,n}$ is the sound pressure level of an element source, where n is number of elements. From equation 8.1, the total acoustic pressure can be obtained by:

$$p_{t,rms}^2 = p_{1,rms}^2 + p_{2,rms}^2 + ... + p_{n,rms}^2 \quad (8.2)$$

Where

$$p_{rms}^2 = p_{ref}^2 . 10^{L_p/10} \quad (8.3)$$

The contribution of each individual acoustic pressure over the total acoustic pressure can be estimated by the pressure ratio.

8.2.2 Fan Noise Source Location and Power Estimation

Figure 8.1 shows the contour of the sound power level distributed over the centrifugal fan surfaces. The figure shows that most of the dipole noise is generated from the lower region of the centrifugal fan near the volute inlet. The lowest sound power level is estimated at the fan outlet duct. Average sound power level (PWL) of the centrifugal fan is estimated to be varied between 62 to 73 decibels (dB).

The average PWL is used to estimate and compare with each other in order to determine the PWL contribution of each component to the overall PWL noise. This is done by

following the fundamental of sound quantification as similar to the equations in sections 8.2.1.

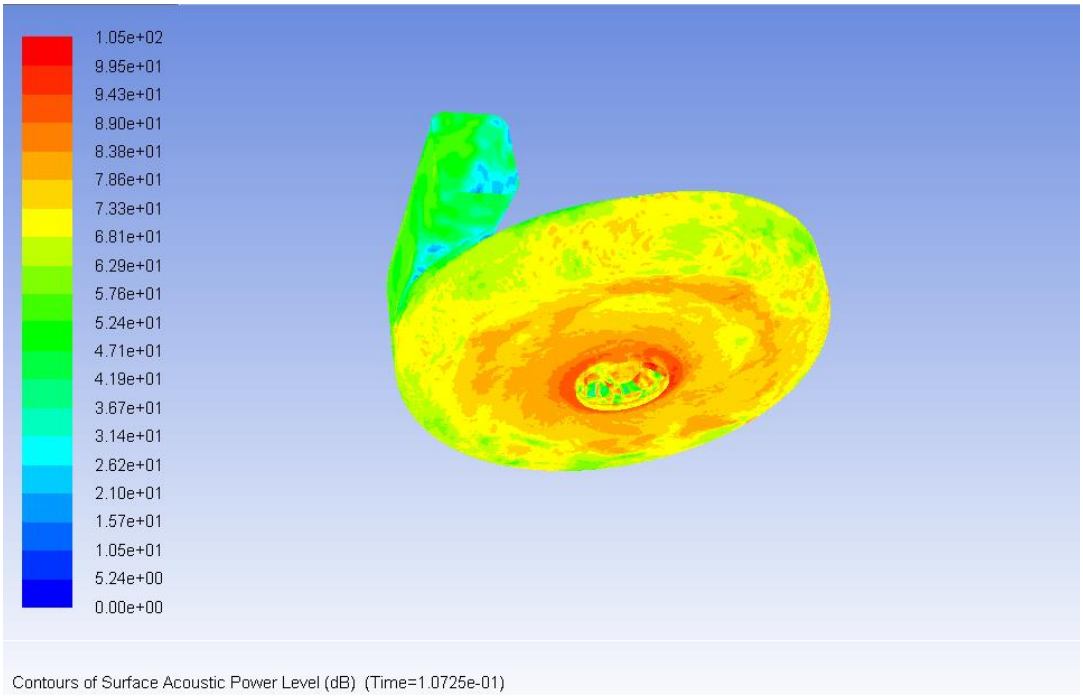

Figure 8.1: The surface PWL of the centrifugal fan

Table 8.1 shows the estimated PWL of individual components of the centrifugal fan. In this table, the maximum and the average PWL of each component is presented in the first two column. It shows most of the dipole noise was generated from the impeller region. At the impeller region, the maximum value of the PWL is computed at the surface of the impeller blades, however the averaged values of the PWL show that the highest average PWL is computed at the shroud surface.

The average PWL is used to estimate the contribution of individual components in the centrifugal fan. The contribution is approximated and presented in the third column of the Table 8.1. By comparing to each other, it is found that the PWL generated at the shroud impeller contribute approximately 87 % to the total PWL generated by the centrifugal fan. It is followed by the PWL generated from the volute cap surface which is close to 5 %. The contribution of the blade the hub surfaces is also close to 4 %. The contributions

from other components are considered to be minor and not presented as the pressure ratio is found to be very small.

Table 8.1: The surface PWL computed for centrifugal fan

Fan Elements	Sound Power Level Estimation at Source (dB)		
	Maximum (dB)	Average (dB)	Contribution (%)
Blades	105	70	≈ 4 %
Hub	101.9	69.6	≈ 4 %
Shroud	101	82.9	≈ 87 %
Volute cap	93.1	70.3	≈ 5 %
Volute tongue	72.3	36	-
Diffuser	90.4	53.6	-
Volute casing	80	40	-
Overall	108	83.5 (dB)	100%

8.2.3 Duct Noise Source Location and Power Estimation

Similar approach is applied to the inlet duct models to predict the noise locations and estimate the contribution of individual components to the total sound power level.

Figures 8.2 and 8.3 show the contours coloured with the local sound power level distributed at the inlet and the outlet duct surfaces. The local PWL is computed from the local dipole source which is identified as dominant one. High colour contours suggest that there is a strong noise generation in that region. High dipole source is due to the high velocity recirculation in that region, which in turns, causes high pressure fluctuations. From these Figures, it is observed that high PWL is generated at the constricted element for the inlet duct (Figure 8.2) and also at the large chamber element for the outlet duct (Figure 8.3). The average PWL generated from the inlet is estimated to be varied from 40 to 55 dB. The average PWL generated from the outlet duct is estimated to be varied from

59 to 70 dB. In comparison between the duct models, the outlet model seems to produce higher noise level.

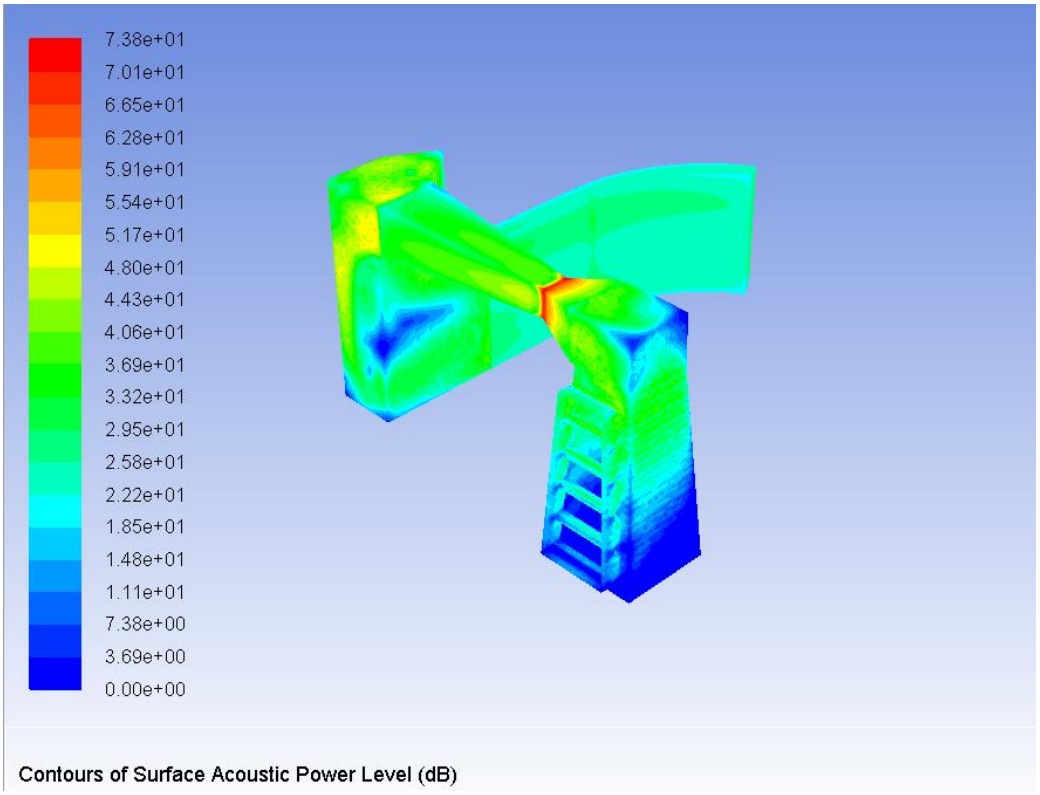

Figure 8.2: The PWL distributed over the inlet surface

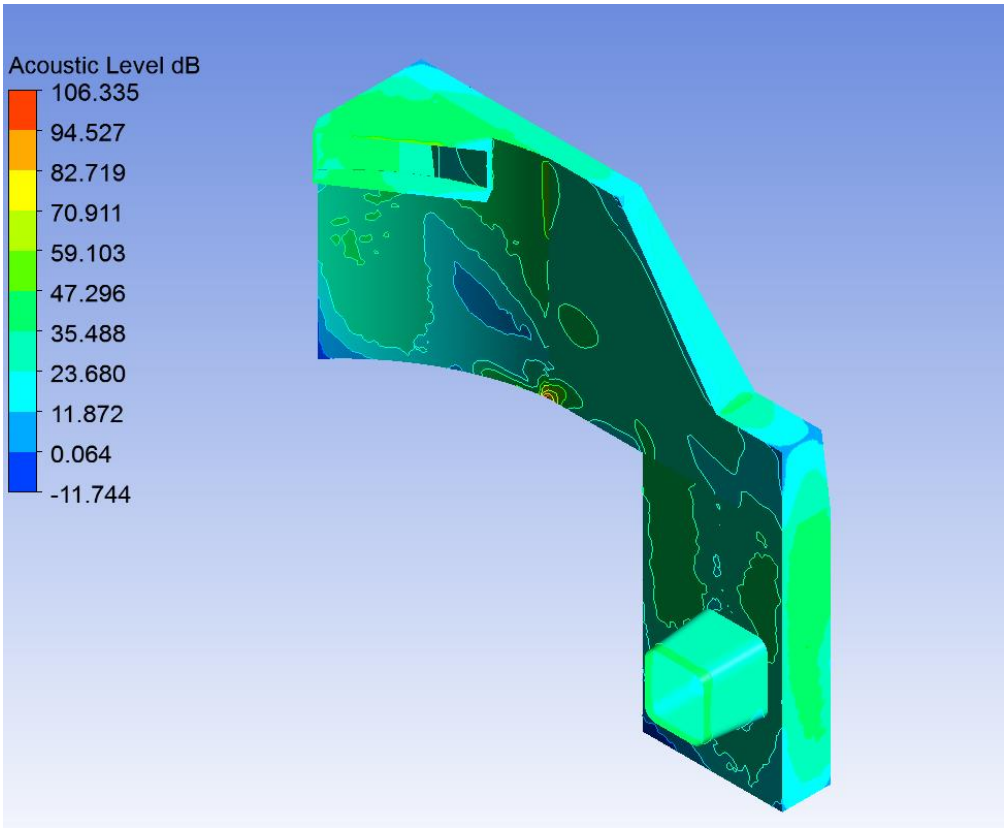

Figure 8.3: The PWL distributed over the outlet surface

Tables 8.2 and 8.3 show the local PWL estimated for individual elements of the inlet and outlet ducts. In these tables, the maximum PWL and the average PWL are computed and presented. The average PWL is used to estimate the contribution of the local element to the total PWL. The estimated results are shown in the third column in these tables.

At the inlet model (Table 8.2), the estimated result shows that the element 2 (the constricted duct element) contributed 74 % approximately to the total PWL generated from the inlet duct. It is followed by the element 3, which is a complicated shape corner, by 19 % approximately. A narrow rectangular duct (element 4) contributes close to 6 %. Elements 1 and 5 contribute the least PWL to the total PWL of the inlet duct.

At the outlet model, elements 4 and 5 contributed the most to the total PWL generated from the outlet duct as closed to 45 % and 54 % approximately. High level of PWL

computed in these regions are due to high level of flow circulation seen from the flow analysis.

Table 8.2: Surface PWL computed at inlet duct elements

Inlet Duct Elements	Sound Power Level Estimation at Source (dB)		
	Max (dB)	Ave (dB)	Contribution (%)
Element 1	54.8	27.4	≈ 1%
Element 2	73.8	44.8	≈74 %
Element 3	57.5	38.8	≈19 %
Element 4	49.5	33.7	≈6 %
Element 5	30.8	24.4	≈1 %
Overall	74	45	100 %

Table 8.3: Surface PWL computed at outlet duct elements

Outlet Duct Elements	Sound Power Level Estimation at Source (dB)		
	Max (dB)	Ave (dB)	Contribution (%)
Element 1	40	30.5	-
Element 2	49	35.5	≈1%
Element 3	38	31.5	-
Element 4	81.3	54.7	≈45%
Element 5	106	55.5	≈54%
Overall	106	58.2	100%

8.2.4 Humidifier Noise Source Location and Power Estimation

Figures 8.4 and 8.5 show the contours coloured with the sound power level distributed over the humidifier surfaces. The PWL is computed from the dipole source generated during the numerical simulation. A high colour indicates that there is a strong sound energy generated in that region. As can be seen, the high level of sound power is predicted at one side of the humidifier. Inside the humidifier (Figure 8.5), high PWL is seen at several locations and mostly at the baffle surfaces. The average PWL generated from the humidifier is estimated to be varied from 30 to 45 dB.

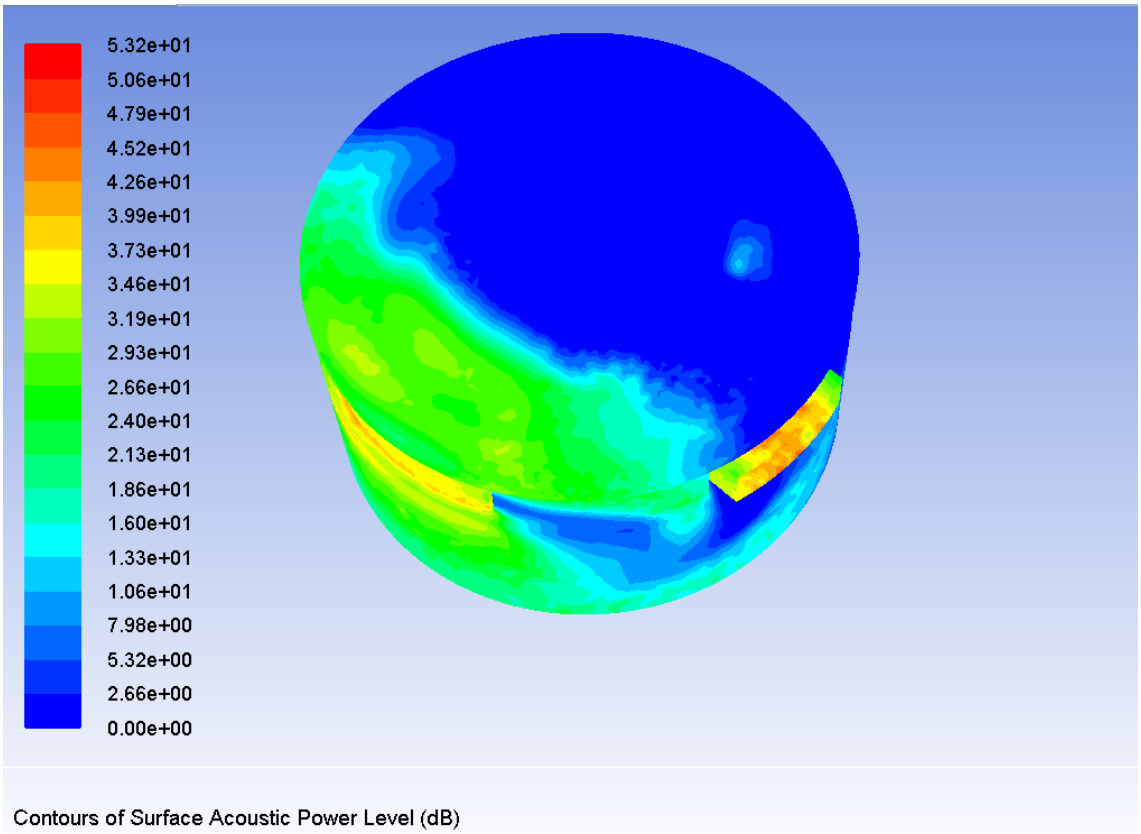

Figure 8.4: PWL distributed over the humidifier surface (1)

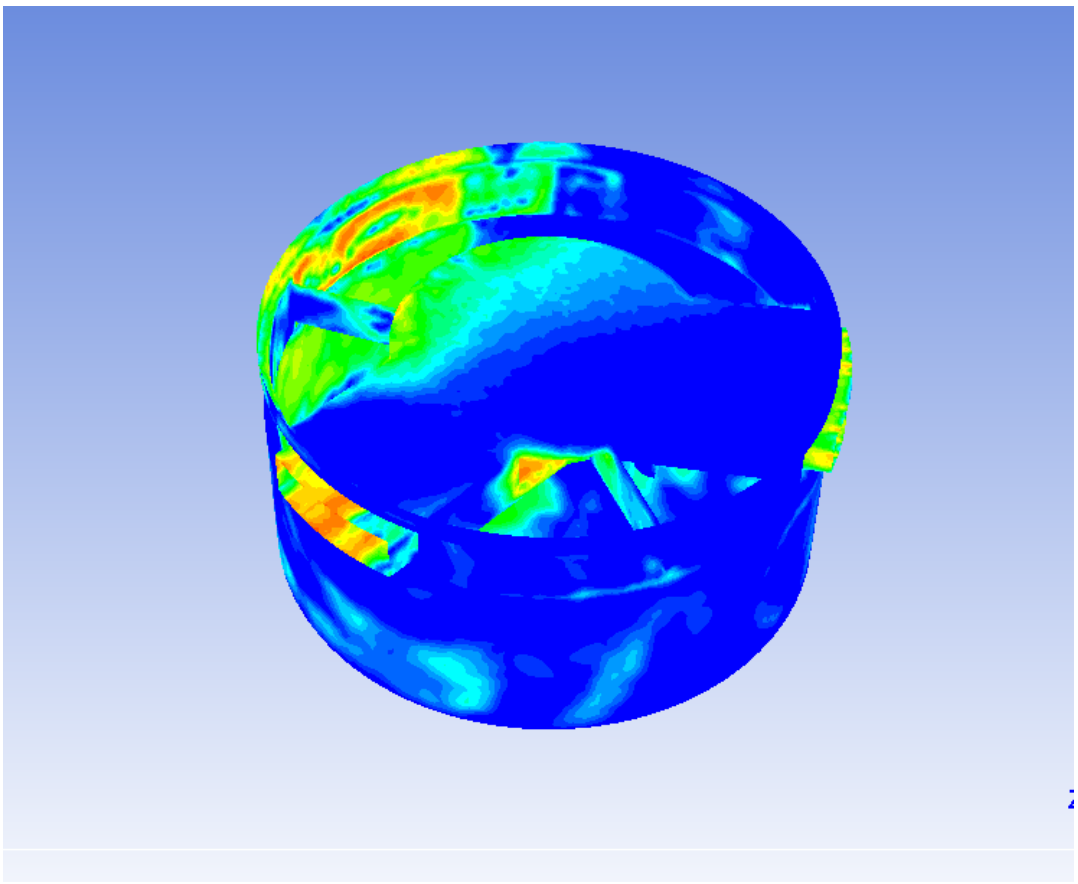

Figure 8.5: PWL distributed over the humidifier surface (2)

Table 8.4 shows the local sound power level estimated for individual elements of the humidifier. In this table, the local sound power level of each element is estimated and presented under the maximum and average values. The average PWL values is used to estimate the contribution of the local elements to the total PWL generated from the humidifier.

By comparing with each other, it is found that the sound power level PWL generated from the baffle is estimated to contribute almost 80 % to the overall PWL. It is followed by the PWL generated from the chamber surface around 14 % approximately. The PWL generated by the cap surface is seen to contribute the least around 7 %.

Table 8.4: Surface PWL computed for Humidifier elements

Humidifier Elements	Sound Power Level Estimation at Source (dB)		
	Max (dB)	Ave (dB)	Contribution (%)
Baffle	53.2	37.1	≈80 %
Cap	33	26.5	≈7 %
Chamber	37.7	29.4	≈14 %
Overall	53	38	100 %

8.3 Contribution of various Components

In previous section, the noise source locations and its power were estimated. The PWL was calculated by the dipole source and the average overall PWL of each component was estimated. In this section, the contribution of various components in the CPAP flow system is compared to each other.

Table 8.1 shows the comparison of the total PWL computed for individual components in the CPAP flow system. Two different values are used to compare with each other such as the overall maximum PWL and the overall average PWL.

Table 8.5: PWL and SPL contribution of CPAP flow system

Components	Overall Maximum PWL (dB)	Contribution (%)	Overall Average PWL (dB)	Contribution (%)
Centrifugal Fan	108	≈ **61**	83.5	≈ **100**
Inlet Duct	74	-	45	-
Outlet Duct	106	≈ **39**	58	-
Humidifier Unit	53	-	38	-
Overall	**110 (dB)**	**100 %**	**83.5 (dB)**	**100 %**

From Table 8.5, it is observed that by far the highest contribution to the overall noise level comes from the centrifugal fan. It follows by the outlet duct, inlet duct and the humidifier respectively. The comparison using the maximum values has shown that the centrifugal fan contributes 61 % and the outlet duct contributes 39 %. However, the comparison using the average values has shown that the noise generated from the centrifugal fan is contributed the most.

8.4 Summary

In this chapter, the sound power level (PWL) generated at sources is estimated for each individual component of the CPAP flow system. At each component, the PWL is computed and compared to each other to identify the contribution of the local to the total PWL.

The total PWL of each component of the CPAP device is compared with each other. It is found that the PWL generated from the centrifugal fan is the highest contribution. The PWL generated from the outlet duct is also seen to have a minor contribution to the overall noise as well. The PWL generated from the inlet duct and the humidifier is seen have the least contribution to the total PWL estimated from the CPAP system.

Chapter 9: **Conclusions and Future Works**

9.1 Conclusion

This is the first systematic and fully validated model which has been developed for noise and vibration prediction in the CPAP devices. The significance of this research is to provide a simple but innovative solution that easy to use and apply in a complicated flow system such as the CPAP devices. Although the nature of this work allows solving noise and vibration problems involving an airflow system, the implementation of this work could be extended as a tool for solving similar problems in various industrial applications.

In conclusion, the numerical work presented in this thesis which is motivated by the need for research industry to use more efficient prediction tools to aid in the product design for quieter CPAP devices. The main objectives setups for this thesis have been met. In this thesis, the numerical simulation methods is successfully adopted and applied to investigate the flow-induced noise and vibration of the CPAP device. The numerical methodology is used as the combination of the CAA with hybrid approach and the one-way FSI simulation.

The numerical simulation was performed for each individual component and presented in separate chapters. The numerical results were compared with experimental data for validations. Useful insights into the performance characteristics of the fan, the duct and the humidifier to the same flow conditions and the consequent acoustic generation were obtained from the acoustic analysis.

The numerical study conducted for the centrifugal fan has found that the uneven or asymmetrical air flow was the main cause of the high level of static pressure fluctuations and high level of turbulent kinetic energy inside the centrifugal fan. These were the sources that generated aerodynamic noise as well as some structural vibrations. The aerodynamic noise generated from the centrifugal fan was predicted by using the Ffowcs-Williams and Hawkings (FW-H) acoustic model. The tonal noise from the fan blade surface was simulated and computed. The comparison between the predicted sound pressure level (SPL) and the measured SPL has shown an agreement. Structural vibration was also investigated using the one-way fluid-structure interaction (FSI) method. It was found that high deformation in the volute cap region due to the pressure fluctuations. A similar numerical study was also performed for the inlet and outlet ducts as well as the humidifier. The numerical analysis found the main cause of the noise generation in these models was the flow recirculation or flow rotation.

Furthermore, the noise power level at individual models were predicted and compared with each other to estimate their contributions toward the overall noise level. It was found that under the same conditions and without the influence to each other, the sound power level generated from the centrifugal fan was the most contributed component to the total sound power level estimated for the CPAP flow system.

Despite the thorough investigation of this work, the noise prediction of the duct models and the humidifier does not take into account the influence of high level of the turbulent flow. This is very complicated and time consuming which is left for future investigation process. Also, the numerical investigation in this work is only valid to individual components of the CPAP devices and does not include the continuity of the system.

9.2 Recommendations for Future Works

This thesis has introduced a novelty of methodology that can be used to solve the noise and vibration problem in a complex flow system by breaking it down into several components. The noise and vibration of each component are simulated and analysed independently. Therefore, the cause and locations of noise and vibration sources are identified immediately.

However, this work has only taken the first step towards the application of numerical simulation approaches in product development. It provides a framework for using the combined numerical simulation approaches for predicting the flow-induced noise and vibration in the CPAP device as well as similar flow systems. The numerical studies in this thesis are simple in nature, each element in the CPAP device is investigated under the same conditions. Based on the numerical results obtained from this thesis, suggestions for future product improvement could implemented to improve the flow path characteristics. The optimal study can be performed for each individual components as similar to those studies in this thesis. Despite of the successful of this thesis, these simple cases does not reflect the reality in practise. Therefore, the extension of this work will involve modelling a full flow system is needed. Also, for the future use, the future improvement of the numerical modelling is suggested as:

- Consider a better turbulence model, i.e., large eddy simulation for CFD simulation. Even though the RANS turbulence models were used in this thesis and applied successfully, however a better turbulence model is needed to investigate the high level of vorticity observed in this thesis.
- Consider the interaction between individual elements in the CPAP devices. In this study, the physical variables, such as pressure, velocity and turbulent kinetic energy, etc., are transferred from one to another components.

REFERENCE

1. ISO-3744, *Acoustics-Determination of sound power levels of noise sources using sound pressure-Engineering method in an essentially free field over a reflecting plane*. 1994.
2. Al-Jumaily, A.M., Reddy, P.I., Medical Devices for Respiratory Dysfunctions: Principles and Modelling of Positive-Pressure Lung Support Devices. In press, ASME Press 2011, ISBN: 978-0-7918-5977-3.
3. Sun, Y.-C., *CPAP system modelling*. 2005, Auckland University of Technology.
4. Zhen, Z.F., *CPAP mask thermo-fluid dynamic for carbon dioxide and condensation reduction*. 2005, Auckland University of Technology.
5. Li, C., *The Effects of CPAP Tube Reverse Flow*. 2008, Auckland University of Technology.
6. Wang, M., Freund, J.B., and Lele. S.K., *Computational Prediction of Flow-Generated Sound.* The Annual Reviews of Fluid Mechanics, 2006. **38**: p. 483-512.
7. Wells, V.L., *computing aerodynamically generated noise.* Annu. Rev. Fluid. Mech, 1997. **29**(1): p. 61-99.
8. Xue-min, L., *Computational aeroacoustics using Lattice boltzmann model*. 2006, The Hong Kong Polytechnic University.
9. Rembold, B., *Direct and large-eddy simulation of compressible rectangular jet flow*. 2003, Swiss Federal Institute of Technology Zurich.
10. Liu, Q., Qi, D., and Tang, H., *Computation of aerodynamic noise of centrifugal fan using large eddy simulation approach, acoustic analogy, and vortex sound theory.* Proceedings of the Institution of Mechanical Engineers, Part C: Journal of Mechanical Engineering Science, 2007. **221**(11): p. 1321-1332.
11. Francescantonio, P.D., *A New Boundary Integral Formulation for the Prediction of sound radiation.* Journal of Sound and Vibration, 1997. **202**(4): p. 491-509.
12. Casalino, D., *An advanced time approach for acoustic analogy predictions.* Journal of Sound and Vibration, 2003. **261**(4): p. 583-612.
13. Tang, H., Lui, X., Qi, D., and Mao,Y., *Numerical prediction of aerodynamic tonal noise radiated from a centrifugal fan.* Proceedings of the Institution of Mechanical Engineers, Part A: Journal of Power and Energy, 2008. **222**(8): p. 831-842.
14. Lighthill, M.J., *On Sound Generated Aerodynamically. I. General Theory.* Proceedings of the Royal Society A: Mathematical, Physical and Engineering Sciences, 1952. **211**(1107): p. 564-587.
15. Lighthill, M.J., *On Sound Generated Aerodynamically. II. Turbulence as a Source of Sound.* Proceedings of the Royal Society A: Mathematical, Physical and Engineering Sciences, 1954. **222**(1148): p. 1-32.
16. Williams, J.E.F., *Aeroacoustics.* Journal of Sound and Vibration, 1995. **190**(3): p. 387-398.
17. Wright, M.C.M. and Morfey, C.L., *Extensions of Lighthill's acoustic analogy with application to computational aeroacoustics.* Proceedings of the Royal Society A:

Mathematical, Physical and Engineering Sciences, 2007. **463**(2085): p. 2101-2127.

18. Proudman, I., *The Generation of Noise by Isotropic Turbulence.* Proceedings of the Royal Society A: Mathematical, Physical and Engineering Sciences, 1952. **214**(1116): p. 119-132.
19. Curle, N., *The Influence of Solid Boundaries upon Aerodynamic Sound.* Proceedings of the Royal Society A: Mathematical, Physical and Engineering Sciences, 1955. **231**(1187): p. 505-514.
20. Powell, A., *Theory of Vortex Sound.* The Journal of the Acoustical Society of America, 1964. **36**(1): p. 177-195.
21. Howe, M.S., *Sound generated by fluid-structure interactions.* Computers & Structures, 1997. **65**(3): p. 433-446.
22. Lowson, M.V., *The Sound Field for Singularities in Motion.* Proc. R. Soc. Lond. A, 1965. **286**: p. 559-572.
23. Williams, J.E.F. and Hawkings, D.L., *Sound Generation by Turbulence and Surfaces in Arbitrary Motion.* Philosophical Transactions of the Royal Society A: Mathematical, Physical and Engineering Sciences, 1969. **264**(1151): p. 321-342.
24. Farassat, F., *Theory of noise generation from moving bodies with an application to helicopter rotors.* NASA Technical Report, 1975. **R-451**.
25. Farassat, F., *Linear Acoustic Formulas for Calculation of Rotating Blade Noise.* AIAA, 1981. **19**: p. 1122-1130.
26. Farassat, F. and Sussi, G.P., *The Prediction of Helicopter Discrete Frequency Noise.* Vertica, 1983. **7**(4): p. 309-320.
27. Farassat, F., *Derivation of Formulations 1 and 1A of Farassat.* NASA Technical Report, 2007. **NASA/TM 2007-21483**.
28. Farassat, F. and Myers, M.K., *Extension of Kirchhoff's Formula to Radiation from Moving Surfaces.* Journal of Sound and Vibration, 1988. **123**(3): p. 451-461.
29. *ANSYS FLUENT Therory Guide*. 2011, ANSYS, Inc: Southpointe, Cannosburg, PA 15317.
30. Bailly, C., Bogey, C., and Gloerfelt, X., *Some useful hybrid approaches for predicting aerodynamic noise.* Comptes Rendus Mécanique, 2005. **333**(9): p. 666-675.
31. NEISE, W., *Noise reduction in centrifugal fans- a literature survey.* Journal of Sound and Vibration, 1976. **45**(3): p. 375-403.
32. Choi, J.-S., *Aerodynamic Noise generation in Centrifugal turbomachinery.* KSME Journal, 1994. **8**(2): p. 161-174.
33. Choi, J.-S., McLaughlin, D.K., and Thompson, D.E., *Experiments on the unsteady flow field and noise generation in a centrifugal pump impeller.* Journal of Sound and Vibration, 2003. **263**(3): p. 493-514.
34. Velarde-Suarez, S., Santolaria-Morros, C., and Ballesteros-Tajadura, R., *Experimental Study on the Aeroacoustic Behavior of a Forward-Curved Blades Centrifugal Fan.* Journal of Fluids Engineering, 1999. **121**(2): p. 276-281.

35. Velarde-Suárez, S., Ballesteros-Tajadura, R., Pablo Hurtado-Cruz, J., and Santolaria-Morros, C., *Experimental determination of the tonal noise sources in a centrifugal fan.* Journal of Sound and Vibration, 2006. **295**(3-5): p. 781-796.

36. Cho, Y. and Moon, Y.J., *Discrete Noise Prediction of Variable Pitch Cross-Flow Fans by Unsteady Navier-Stokes Computations.* Journal of Fluids Engineering, 2003. **125**(3): p. 543-550.

37. Mao, Y., Qi, D., Lui, X., and Tang, H., *Numerical prediction of aerodynamic tonal noise radiated from a centrifugal fan.* Proceedings of the Institution of Mechanical Engineers, Part A: Journal of Power and Energy, 2008. **222**(8): p. 831-842.

38. Mao, Y. and Qi, D., *Computation of rotating blade noise scattered by a centrifugal volute.* Proceedings of the Institution of Mechanical Engineers, Part A: Journal of Power and Energy, 2009. **223**(8): p. 965-972.

39. Langthjem, M.A. and Olhoff, N., *A numerical study of flow-induced noise in a two-dimensional centrifugal pump. Part I. Hydrodynamics.* Journal of Fluids and Structures, 2004. **19**(3): p. 349-368.

40. Langthjem, M.A. and Olhoff, N., *A numerical study of flow-induced noise in a two-dimensional centrifugal pump. Part II. Hydroacoustics.* Journal of Fluids and Structures, 2004. **19**(3): p. 369-386.

41. Lu, H.Z., Huang, L., So, R.M.C., and Wang, J., *A computational study of the interaction noise from a small axial-flow fan.* The Journal of the Acoustical Society of America, 2007. **122**(3): p. 1404-1415.

42. Sun, H. and Lee, S., *Numerical prediction of centrifugal compressor noise.* Journal of Sound and Vibration, 2004. **269**(1-2): p. 421-430.

43. Sun, H., Shin, H., and Lee, S., *Analysis and optimization of aerodynamic noise in a centrifugal compressor.* Journal of Sound and Vibration, 2006. **289**(4-5): p. 999-1018.

44. Khelladi, S., Kouidri, S., Bakir, F., and Rey, R., *Flow Study in the Impeller--Diffuser Interface of a Vaned Centrifugal Fan.* Journal of Fluids Engineering, 2005. **127**(3): p. 495-502.

45. Khelladi, S., Kouidri, S., Bakir, F., and Rey, R., *Predicting tonal noise from a high rotational speed centrifugal fan.* Journal of Sound and Vibration, 2008. **313**(1-2): p. 113-133.

46. Younsi, M., Bakir, F., Kouidri, S., and Rey, R., *Numerical and experimental study of unsteady flow in a centrifugal fan.* Proceedings of the Institution of Mechanical Engineers, Part A: Journal of Power and Energy, 2007. **221**(7): p. 1025-1036.

47. Younsi, M., Bakir, F., Kouidri, S., and Rey, R., *Influence of impeller geometry on the unsteady flow in a centrifugal fan: numerical and experimental analyses.(Research Article)(Technical report).* International Journal of Rotating Machinery, 2007: p. NA.

48. Jeon, W.H. and Lee, D.J., *An analysis of the flow and aerodynamic acoustic sources of a centrifugal impeller.* Journal of Sound and Vibration, 1999. **222**(3): p. 505-511.

49. Jeon, W.-H., *A numerical study on the effects of design parameters on the performance and noise of a centrifugal fan.* Journal of Sound and Vibration, 2003. **265**(1): p. 221-230.

50. Jeon, W.-H., Baek, S.-J., and Kim C.-J., *Analysis of the aeroacoustic characteristics of the centrifugal fan in a vacuum cleaner.* Journal of Sound and Vibration, 2003. **268**(5): p. 1025-1035.

51. Jeon, W.-H. and Lee, D.-J., *A numerical study on the flow and sound fields of centrifugal impeller located near a wedge.* Journal of Sound and Vibration, 2003. **266**(4): p. 785-804.

52. Jeon , W.-H. and Lee, D.-J, *An analysis of the flow and aerodynamic acoustic sources of a centrifugal impeller.* Journal of Sound and Vibration, 1999. **222**(3): p. 505-511.

53. Choi, H.-L. and Lee,D.J., *Development of the numerical method for calculating sound radiation from a rotating dipole source in an opened thin duct.* Journal of Sound and Vibration, 2006. **295**(3-5): p. 739-752.

54. Liu, Q., Qi, D., and Mao, Y., *Numerical calculation of centrifugal fan noise.* Proceedings of the Institution of Mechanical Engineers, Part C: Journal of Mechanical Engineering Science, 2006. **220**(8): p. 1167-1177.

55. Moon, Y.J., Cho, Y., and Nam, H.-S., *Computation of unsteady viscous flow and aeroacoustic noise of cross flow fans.* Computers & Fluids, 2003. **32**(7): p. 995-1015.

56. Lee, S., Heo, S., and Cheong, C., *Prediction and reduction of internal blade-passing frequency noise of the centrifugal fan in a refrigerator.* International Journal of Refrigeration, 2010. **33**(6): p. 1129-1141.

57. Suaraz, S.V., Tajadura, R.B., Morros, C.S., and Francos, J.F., *Numerical prediction of the aerodynamic tonal noise in a centrifugal fan.* In Proceedings of the ASME Fluids Engineering Division Summer Meeting, Montreal, Canada, 2002: p. 1-8.

58. Velarde-Suárez, S., Ballesteros-Tajadura, R., and Hurtado-Cruz, J.P., *A predictive maintenance procedure using pressure and acceleration signals from a centrifugal fan.* Applied Acoustics, 2006. **67**(1): p. 49-61.

59. Velarde-Suárez, S., Ballesteros-Tajadura, R., Santolaria-Morros, C., and Pereiras-García, B., *Reduction of the aerodynamic tonal noise of a forward-curved centrifugal fan by modification of the volute tongue geometry.* Applied Acoustics, 2008. **69**(3): p. 225-232.

60. Velarde-Suárez, S., Ballesteros-Tajadura, R., Pérez, J.G., and Pereiras-García, B., *Relationship between volute pressure fluctuation pattern and tonal noise generation in a squirrel-cage fan.* Applied Acoustics, 2009. **70**(11-12): p. 1384-1392.

61. DOAK, P.E., *Fundamentals of aerodynamic sound theory and flow duct acoustics.* Journal of Sound and Vibration, 1973. **28**(3): p. 527-561.

62. Tam, C.K.W., Kurbatskii, K.A., Ahuja, K.K., and Gaeta, R.J., *A numerical and experimental investigation of the dissipation mechanisms of resonant acoustic liners.* Journal of Sound and Vibration, 2001. **245**(3): p. 454-557.

63. Tam, C.K.W., Ju, H., and Walker, B.E., *Numerical Simulation of a slit resonator in a grazing flow under acoustic excitation.* Journal of Sound and Vibration, 2008. **313**(3-5): p. 449-471.

64. Humbad, N., *Automotive HVAC Flow Noise Prediction Models.* SAE International, 2001. **01**: p. 1498.

65. Ashok, D.K., Sandeep D. Sovani, and Kim, S.-E.., *On Predicting Aero-acoustics Perfromance of Ducts with Broadband Noise Sources Model.* SAE International, 2005. **01**: p. 2495.

66. Ayhan Ayar, Raymond Ambs, Christoph Capellmann, Balthasar Schillemeit, and M. Matthes., *Prediction of Flow-Induced Noise in Automotive HVAC Systems Using a Combined CFD-CA Approach.* SAE International, 2005. **01**: p. 0509.

67. Venkatesh Kannan, David Greeley, Sandeep D. Sovani, and A.D. Khondge., *Computational Aero-acoustics Simulation of a Whistle Noise in An Automotive Air-Intake System.* SAE International, 2005. **01**: p. 2364.

68. Omar M.Mohamud and Johnson, P., *Broadband Noise Source Models as Aeroacoustics Tools in Designing Low NVH HVAC Ducts.* SAE International, 2006. **01**: p. 1192.

69. Julien Manera, Yves Detandt, and D. d'Udekem., *Aero-Acoustic Predictions of Automotive Instrument Panel Ducts.* SAE International, 2009. **01**: p. 2237.

70. Dongkon Lee, Myung Han Lee, Kang-Duck ih, and M.-S. Kim., *Aeroacoustics Predictions of Automative HVAC Systems.* SAE International, 2010. **01**: p. 0415.

71. Chen, J., Gu, Z., and Wang, Y., *Numerical Simulations of Noise Induced by Flow in HVAC Ventilation Ducts.* SAE International, 2011. **01**: p. 0505.

72. Ashcroft, G.B., Takeda, K., and Zhang, X., *A numerical investigation of the noise radiated by a turbulent flow over a cavity.* Journal of Sound and Vibration, 2003. **265**(1): p. 43-60.

73. Yu, Y., Yang, Q., and Wang, X., *Finite element analysis of fluid–structure interaction for the design of MAV aerodynamic shape.* Computers & Fluids, 2013. **76**: p. 50-57.

74. Sonntag, S.J., Kaufmann, T.A.S., Büsen, M.R., Laumen, M., Linde, T., Schmitz-Rode, T., and Steinseifer, U., *Simulation of a pulsatile total artificial heart: Development of a partitioned Fluid Structure Interaction model.* Journal of Fluids and Structures, 2013. **38**: p. 187-204.

75. Wang, X. and Li, X., *Computational simulation of aortic aneurysm using FSI method: influence of blood viscosity on aneurismal dynamic behaviors.* Comput Biol Med, 2011. **41**(9): p. 812-21.

76. Dailey, H.L. and Ghadiali, S.N., *Fluid-structure analysis of microparticle transport in deformable pulmonary alveoli.* Journal of Aerosol Science, 2007. **38**(3): p. 269-288.

77. Pei, J., Dohmen, H.J., Yuan, S.Q., and Benra, F.K., *Investigation of unsteady flow-induced impeller oscillations of a single-blade pump under off-design conditions.* Journal of Fluids and Structures, 2012. **35**: p. 89-104.

78. Ismaier, A. and Schlücker, E., *Fluid dynamic interaction between water hammer and centrifugal pumps.* Nuclear Engineering and Design, 2009. **239**(12): p. 3151-3154.

79. Nicolici, S. and Bilegan, R.M., *Fluid structure interaction modeling of liquid sloshing phenomena in flexible tanks.* Nuclear Engineering and Design, 2013. **258**: p. 51-56.

80. Anghileri, M., Castelletti, L.-M.L., and Tirelli, M., *Fluid–structure interaction of water filled tanks during the impact with the ground.* International Journal of Impact Engineering, 2005. **31**(3): p. 235-254.

81. Campbell, R.L., *FSI and Inverse design simulations for flexible turbomachinery*, in *Mechanical Engineering*. 2010, The Pennsylvania State University.

82. Hasnedlová, J., Feistauer, M., Horáček, J., Kosík, A., and Kučera, V., *Numerical simulation of fluid–structure interaction of compressible flow and elastic structure.* Computing, 2012. **95**(S1): p. 343-361.

83. Yamada, T. and Kikuchi, F., *An arbitrary Lagrangian-Eulerian finite element method for incompressible hyperelasticity.* Computer Methods in Applied Mechanics and Engineering, 1993. **102**(2): p. 149-177.

84. Jiang, Y.Y., Yoshimura, S., Imai, R., Katsura, H., Yoshida, T., and Kato, C., *Quantitative evaluation of flow-induced structural vibration and noise in turbomachinery by full-scale weakly coupled simulation.* Journal of Fluids and Structures, 2007. **23**(4): p. 531-544.

85. Teich, M. and Gebbeken, N., *Analysis of FSI effects of blast loaded flexible structures.* Engineering Structures, 2013. **55**: p. 73-79.

86. Hart, J.D., Peters, G.W.M., Schreurs, P.J.G., and Baaijens, F.P.T., *A three-dimentional computational analysis of fluid-structure interaction in the aortic valve.* Journal of Biomechanics, 2003. **36**: p. 103-112.

87. Zwaan, R.J. and Prananta, B.B., *Fluid-structure interaction in numerical aeroelasitc simulation.* International Journal of Non-Linear Mechanics, 2002. **32**: p. 987-1002.

88. Chouly, F., Van Hirtum, A., Lagrée, P.Y., Pelorson, X., and Payan, Y., *Numerical and experimental study of expiratory flow in the case of major upper airway obstructions with fluid–structure interaction.* Journal of Fluids and Structures, 2008. **24**(2): p. 250-269.

89. Nobili, M., Morbiducci, U., Ponzini, R., Del Gaudio, C., Balducci, A., Grigioni, M., Maria Montevecchi, F., and Redaelli, A., *Numerical simulation of the dynamics of a bileaflet prosthetic heart valve using a fluid-structure interaction approach.* J Biomech, 2008. **41**(11): p. 2539-50.

90. Liang, Q.W., Rodríguez, C.G., Egusquiza, E., Escaler, X., Farhat, M., and Avellan, F., *Numerical simulation of fluid added mass effect on a francis turbine runner.* Computers & Fluids, 2007. **36**(6): p. 1106-1118.

91. Dilin, T., Sakai, T., Wilson, M., and Whitfield, A.. *A computational and experimental evaluation of the performance of a centrifugal fan volute*. in *Proceedings of the Institution of Mechanical Engineers*. 1998. IMechE 1998.

92. Matsumoto, S., Ohba, H., and Miyamoto, H., *An Analysis of Flow in a Centrifugal Impeller by FEM with k--e Model.* Journal of Thermal Science, 2000. **10**(1).

93. Lin, S.-C. and Huang, C.-L., *An integrated experimental and numerical study of forward-curved centrifugal fan.* Experimental Thermal and Fluid Science, 2002. **26**: p. 421-434.

94. Asuaje, M., Bakir, F., Kouidri, S., Noguera, R., and Rey, R.. *Computer-aided design and optimixation of centrifugal pumps*. in *IMechE 2005*. 2005. Paris, France: J. Power and Energy.

95. Lee, Y.-T., Ahuja, V., Hosangadi, A., Slipper, M.E., Mulvihill, L.P., Birkbeck, R., and Coleman, R.M., *Impeller Design of a Centrifugal Fan with Blade Optimization.* International Journal of Rotating Machinery, 2011. **2011**: p. 1-16.

96. Lin, S.-C. and Tsai, M.-L., *An integrated performance analysis for a backward-inclined centrifugal fan.* Computers & Fluids, 2012. **56**: p. 24-38.

97. Oro, J.M.F., Diaz, K.M.A., Morros, C.S., and Vega, M.G., *Numerical simulation of the unsteady stator-rotor interaction in a low-speed axial fan including experimental validation.* International Journal of Numerical Methods for Heat & Fluid Flow, 2011. **21**(2): p. 168-197.

98. Zhao, X., Sun, J., and Zhang, Z., *Prediction and measurement of axial flow fan aerodynamic and aeroacoustic performance in a split-type air-conditioner outdoor unit.* International Journal of Refrigeration, 2013. **36**(3): p. 1098-1108.

99. Hu, B.-b., OuYang, H., Wu, Y.-d., Jin, G.-y., Qiang, X.-q., and Du, Z.-h., *Numerical prediction of the interaction noise radiated from an axial fan.* Applied Acoustics, 2013. **74**(4): p. 544-552.

100. Shojaeefard, M.H., Tahani, M., Ehghaghi, M.B., Fallahian, M.A., and Beglari, M., *Numerical study of the effects of some geometric characteristics of a centrifugal pump impeller that pumps a viscous fluid.* Computers & Fluids, 2012. **60**: p. 61-70.

101. Li, J., Zeng, Y., Liu, X., and Wang, H., *Optimum design on impeller blade of mixed-flow pump based on CFD.* Procedia Engineering, 2012. **31**: p. 187-195.

102. Jin, J., Fan, Y., Han, W., and Hu, J., *Design and Analysis on Hydraulic Model of The Ultra -low Specific-speed Centrifugal Pump.* Procedia Engineering, 2012. **31**: p. 110-114.

103. Menter, F.R., *Two-Equation eddy-viscosity turbulence models for engineering applications.* AIAA, 1994. **32(8)**: p. 1598-1605.

104. Farassat, F., *The acoustic far-field of rigid bodies in arbitrary motion.* Journal of Sound and Vibration, 1974. **32**(3): p. 387-405.

105. Brentner, K.S. and Farassat, F., *an analytical comparison of the acoustic analogy and Kirchhoff formulation for moving surfaces*, in *American Helicopter Society 53 th Annual Forum*. 1998: Virgina Beach, VA.

106. http://www.fphcare.co.nz/sleep-apnea/cpap-devices/f-p-icon/.

107. Rey, R., Kouidri, S., Bakir, F., and Younsi, M., *Numerical and experimental study of unsteady flow in a centrifugal fan.* Proceedings of the Institution of Mechanical Engineers, Part A: Journal of Power and Energy, 2007. **221**(7): p. 1025-1036.

108. FLUENT, *FLUENT USER GUIDELINES.* FLUENT, Release 14, Documentations, 2012.